PHOTOVOLTAICS OF SELENIDE KESTERITE DOPED WITH NANOSCOPIC IRON AND CERIUM OXYSELENIDES

By

SHANE TIMOTHY WERRY

(BSc Honours, *Summa Cum Laude*, UWC)

A mini-thesis submitted in partial fulfilment of the requirements for the degree

of

MAGISTER SCIENTIAE IN NANOSCIENCE

In the

Faculty of Science
University of the Western Cape, South Africa

Supervisor: Prof Emmanuel I. Iwuoha

Co-supervisors: Dr Miranda M. Ndipingwi and Dr Suru V. John-Denk

September 2021

ABSTRACT

As the demand for energy is constantly increasing, researchers are looking at various methods of energy production. Following the rise of solar energy becoming a major player, researchers are looking at kesterite materials, $Cu_2ZnSn(S,Se)_4$ (CZTS) for photovoltaic applications as they demonstrate many excellent characteristics making them highly suitable for use in thin-film solar cells. Consequently, there are major drawbacks of using kesterite materials for photovoltaic applications such as their point defects and secondary phases. Cerium and iron oxyselenides ($Ce_2O_2Fe_2OSe_2$) are a member of the chalcogenide family and by introducing this chalcogenide into the kesterite structure there would be an improvement in the semiconducting property of the kesterite material. The focus of this research is to dope the kesterite material with nanoscopic cerium and iron oxyselenides in order to reduce the band gap of the kesterite material, thereby improving its light absorption, thus, resulting in a more efficient photovoltaic effect. The X-ray Diffraction (XRD) result confirms the presence of the kesterite phase in the synthesized kesterite and doped kesterite nanoparticles with the crystal sizes being 10.30 nm, 11.03 and 9.45 for the $Ce_2O_2Fe_2OSe_2$, kesterite and doped kesterite nanoparticles respectively. The High-Resolution Scanning Electron Microscopy (HRSEM) and the High-Resolution Transition Electron Microscopy (HRTEM) indicated that there were high levels of agglomeration across all nanoparticles with the $Ce_2O_2Fe_2OSe_2$ nanoparticles having an irregular inhomogeneous composition, the kesterite nanoparticles having a general rod shape with homogeneous composition and the doped kesterite nanoparticles having a general rod shape with inhomogeneous composition resulting from the $Ce_2O_2Fe_2OSe_2$. Small Angle X-ray Scattering (SAXs) was used to study the internal structure of the synthesized nanoparticles. The overall shape of all the synthesized nanoparticles were a mix of core shell hollow sphere and flat disk. The optical band gaps for the nanoparticles were 1.59 eV, 2.25 eV and 2.20 eV for the $Ce_2O_2Fe_2OSe_2$, kesterite and doped kesterite nanoparticles, respectively. The Cyclic Voltammetry (CV) results indicated an electrochemical band gap of 0.48 eV, 0.67 eV and 0.46 eV for the $Ce_2O_2Fe_2OSe_2$, kesterite and doped kesterite nanoparticles respectively. I-V curves for the synthesized nanoparticles as well as the fabricated solar cells were analyzed, with the electrochemical efficiencies being 8.62%, 3.26% and 5.79% for the $Ce_2O_2Fe_2OSe_2$, kesterite and doped kesterite nanoparticles respectively. For the fabricated solar cells, the efficiencies were 0.48% and 0.003% for the pristine kesterite and doped kesterite solar cells respectively.

KEYWORDS

Auxiliary phases (secondary phases)

Cerium and Iron oxyselenide

Chalcogens

Cyclic voltammetry

Electrochemistry

Energy production

Kesterite

Optical band-gap

Photovoltaic cell

Photovoltaics

Renewable energy

Ultra-violet visible spectroscopy

ABBREVIATIONS

CdTe: Cadmium Telluride

CE: Counter electrode

Ce_2O: Cerium oxide

$Ce_2O_2Fe_2OSe_2$: Cerium and Iron oxyselenide

CIGS: Copper Indium Gallium Selenium

CL: Cathodoluminescence

CO_2: Carbon dioxide

$CuCl_2$: Copper chloride

$CuInSe_2$: Copper Indium Selenium

CV: Cyclic voltammetry

CZFTS: Ferrokesterite

CZTS: Kesterite

DEG: Diethylene glycol

ECB: Conduction band

Ef/η: Conversion efficiency

E_g: Bandgap

EIS: Electrochemical impedance spectroscopy

EVB: Valance band

$FeCl_2$: Iron chloride

FF: Fill factor

GB: Grain boundaries

GW: Gig watt

HOMO: Highest occupied molecular orbital

HRSEM: High resolution scanning electron microscopy

HRTEM: High resolution transmission electron microscopy

I_{sc}: Short circuit current

I-V: Current-Voltage

J_{sc}: Short-circuit current density

LUMO: Lowest unoccupied molecular orbital

mm: Millimetres

mmol: Millimole

Na_2S: Sodium sulfide

$NaBH_4$: Sodium borohydride

nm: Nanometres

PBS: Phosphate-Buffered Saline

PCEs: Power conversion efficiencies

P_{max}: Peak power

PV: Photovoltaics

R_{ct}: Charge transfer resistance

RE: Reference electrode

R_s: Solution resistance

SAX: Small-angle X-ray scattering

Se: Selenium

SEM: Scanning electron microscopy

$SnCl_2$: Tin chloride

TEM: Transmission electron microscopy

TGA: Thermogravimetric analysis

UV-Vis: Ultraviolet–visible spectroscopy

V_{oc}: Open circuit voltage

WE: Working electrode

XRD: X-ray diffraction/crystallography

ZnCl$_2$: Zinc chloride

DECLARATION

I declare that **Photovoltaics of Selenide Kesterite doped with nanoscopic Iron and Cerium Oxyselenides** is my own work, that it has not been submitted before for any degree or examination in any other university, and that all the sources I have used or quoted have been indicated and acknowledged as complete references.

Signature ----------------------------------

Shane Timothy Werry   **31/08/2021**

DEDICATION

This work is dedicated to my family, Jenifer Werry (mother) and Jarryd Werry (brother) as well as Gavin and Brendon Ryan, who have been by my side offering moral and emotional support, prayers and love throughout this process.

ACKNOWLEDGEMENTS

Prof Emmanuel Iwuoha, has my sincerest gratitude and humble thanks for not only giving me this amazing opportunity to be a part of the nanoscience program but being part of the SensorLab family as well. His guidance as my supervisor and constant want for me to keep improving has made me a better scientist and researcher.

I would like to thank my co-supervisors Dr Miranda M. Ndipingwi and Dr Suru V. John-Denk. I would like to extend a massive thanks to Miranda for always being there to assist me with everything and guide me through each aspect of this study. She has made me a researcher that constantly looks to gain further knowledge. This project would have been an almost impossible task without her.

I would like to thank my family, my mother Jenifer Werry and my younger brother Jarryd Werry for their continued support throughout my masters. I would also like to thank Dylan Dixon and Jamie-Lee de Bruyn for their support when times got difficult, without them I may not have completed my masters.

My appreciation goes to the entire SensorLab family for looking out for me and always assisting me when I need help or had stupid questions. A special thanks goes to Kelechi Nwambaekwe and Sodiq Tolulope Yussuf for being my go-to guys who have acted as additional co-supervisors throughout my work, they have assisted and guided me through almost everything and I can't thank them enough.

My thanks also go to Mrs V. Jamalie and Mrs C. Abrahams for their assistance, support and encouragement, who are a part of the Nanoscience and Nanotechnology Postgraduate Teaching and Training platform. As well as the Department of Science and Technology for awarding me the MSc Nanoscience scholarship.

I would also like to thank the chemistry department for providing the laboratories and equipment which enabled me to perform my research.

LIST OF PUBLICATIONS

Oxyselenides a path to improve kesterite efficiency

TABLE OF CONTENTS

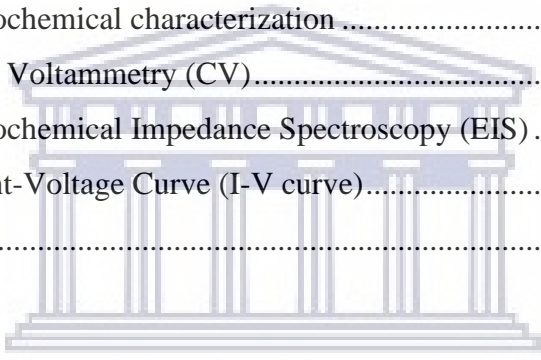UNIVERSITY of the

WESTERN CAPE

LIST OF FIGURES

UNIVERSITY *of the*

WESTERN CAPE

LIST OF TABLES

UNIVERSITY *of the*

WESTERN CAPE

CHAPTER 1

INTRODUCTION

Chapter overview

This first chapter presents a brief description of the reasoning and impact of the switch towards the use of solar energy, highlighting their advantages and general operation. This chapter then further describes general PV and the need to move away from them and toward safer forms of PV such as kesterite PV. Finally, the chapter discusses the research impetus, aims, objectives and outline.

1.1   General Background

In this day and age, there is a huge international demand for clean, safe and useable energy. This demand and need acts as a burden to almost all countries and will never cease to be fulfilled. With the rise of global warming resulting from the use of greenhouse gasses, new forms of energy must be used. A very popular method way of generating and obtaining energy is through the use of solar energy a form of renewable energy generated from the sun. It is known that solar energy possesses several advantages over currently used fossil fuels such as reduce carbon emissions, clean the air and the main aspect is that it is renewable [1,2].

The advancements of photovoltaics (PV) are staggering with promises of being a major participant in the current energy transition. The PV industry has been expanding globally at a rapid rate of 35% over the last decade, with the worlds cumulative PV capacity being 591 GW at the end of 2019 [3]. Looking at the "Levelized Cost of Energy (LCOE)", for the utility scale PV is $32 to $44 USD per MWh, which is starting to rival conventional fuels as the natural gas combined cycle plants LCOE is between $44 to $68 USD per MWh. Analysing multiple forecasts, there has been dramatic growth over the last several years in PV. Predictions from both the prudent and aggressive forecasts from the World Energy Outlook (WEO) and the International Renewable Energy Agency (IRENA), indicate that in

the next 20 years, several terawatts of PV capacity would be developed and operational. Each of which having approximately 5 TW of cumulative PV capacity by 2040 forecasted by both IRENA and WEO, in spite of the IRENA 'REMap' framework being more aggressive than the IEA's 'Sustainable Dev. Scenario' [3,4].
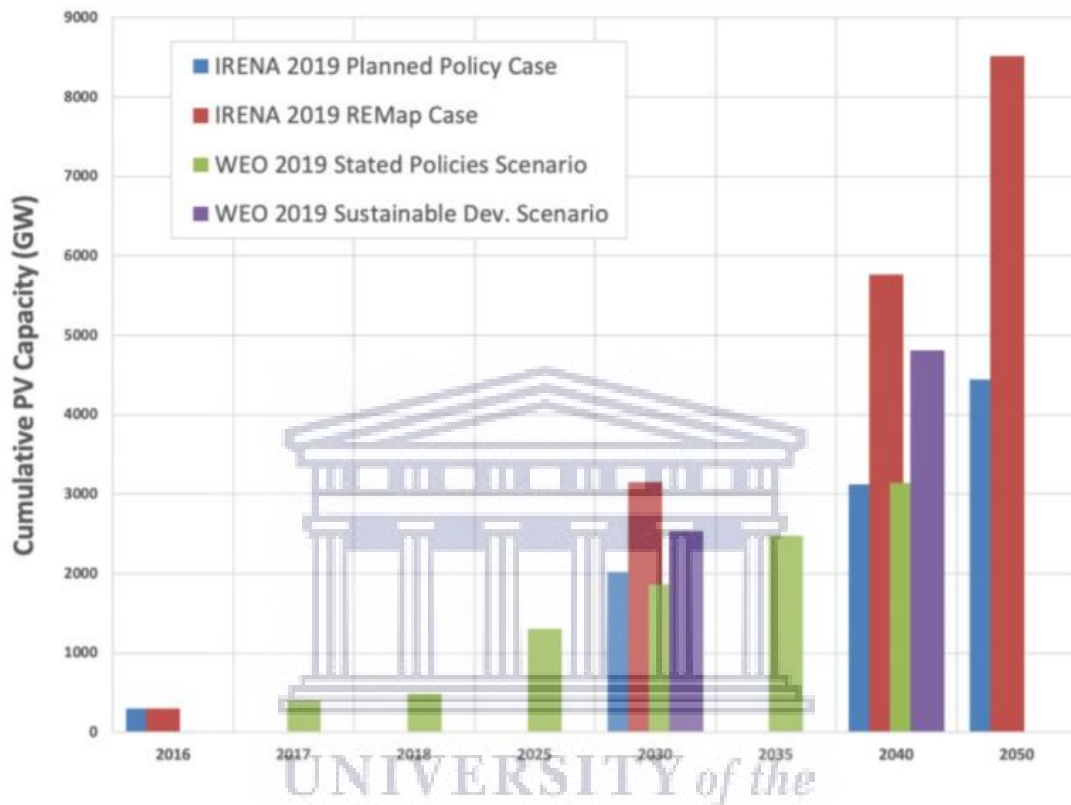
Figure 1.1.1: A comparison of PV capacity projections between IRENA 2019 and WEO 2019 scenarios [3].

"The photovoltaic effect is identified as the surfacing of electric voltage in a system exposed to solar radiation, via charge carriers being excited into the conduction band through the absorption of photons". This process leads to the creation of solar energy. The photovoltaic effect and the photoelectric effect share a similar mechanism of light induced electron transitions, where an electron is freed from the surface of a metal by a photon carrying adequate amounts of energy. Photovoltaics takes solar radiation and transforms it into electrical energy; solar cells is the name given to devices which take advantage of the photovoltaic effect, other names include photovoltaic devices [5].

PV cell efficiency is the outcome of; electron-hole separation efficiency, thermodynamic efficiency, conductive efficiency and reflectance efficiency. This overall PV cell efficiency is a function of successful electron-hole generation and separation. There are many factors that can decrease this efficiency mainly. Prominent among these factors are poor conductivity and hole electron recombination. It is difficult to measure all these parameters but it is possible to estimate their effects by measuring electric parameters such as voltage, current, and resistance. "The fill factor, quantum efficiency, shunt resistance, and series resistance are derived parameters which are used to characterize solar cell performance" [6].

The current generated by the cell due to illumination without implementation of external potential is the short-circuit current. Potential differences occurring between the two terminals of solar cells under illumination without the flow of current through the terminals is defined as the open circuit voltage (V_{oc}). The solar cell generated quotient of maximum power (PM) with the product of open-circuit voltage and short-circuit current produces the fill factor (FF). "At the maximum power density, current density is denoted with J_m and voltage with V_m. The load attached to the solar cell circuit, has an optimum resistance given by V_m/J_m. J_m and V_m should be as near to J_{SC} and V_{OC} as possible". The fill factor is defined by [5,7,8]:

$$FF = \frac{J_m V_m}{J_{sc} V_{oc}} \quad (1.1)$$

"The power conversion efficiency (η), is the ratio of the maximum power generated by the solar cell to the incident radiant energy":

$$\eta = \frac{J_m V_m}{P_i} = \frac{J_{sc} V_{oc} FF}{P_i} \quad (1.2)$$

Where P_i is the incident power. A light beam with a specific a power and wavelength coming towards the cell together with the quotient of the current coming out of the cell defines the spectral responsivity. "Quantum efficiency (ηQE) is determined by the number of electron-hole pairs collected per incident photon", the resulting short circuit photocurrent density depends upon quantum efficiency [5,7].

$$J_{sc} = q \int B_s(W) \eta QE(W) dW \quad (1.3)$$

"Where, q is unit charge, W denotes energy of photons and B_S is the incident spectral photon flux density (the number of photons with energy between W and W + dW falling on a cell per unit area and per unit time)". It is required to have a high ηQE between wavelengths of 400 and 1300 nm, where the solar photon flux density is high, the quantum efficiency is also directly influenced by wavelength as seen in Figure 1.1.2 [5].
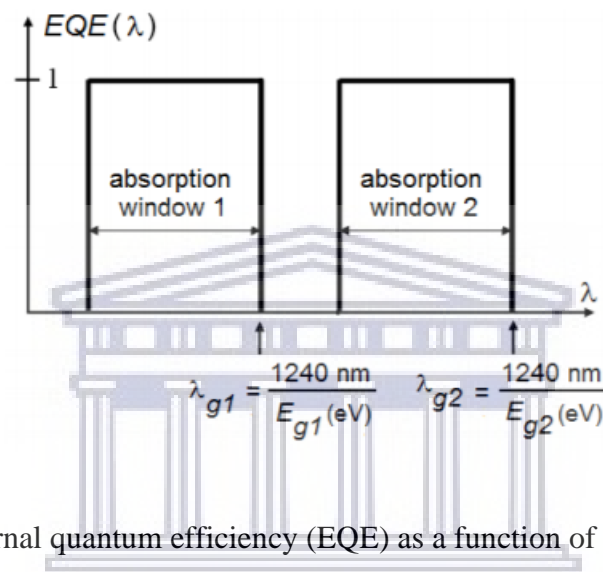
Figure 1.1.2: "External quantum efficiency (EQE) as a function of the wavelength λ" [9].

The most popular and efficient solar cell technologies are solar cells made from thin wafers of silicon. Using materials with a high sunlight absorbance in comparison to silicon requires the use of less material, thus having a significant cost reduction while allowing for greater possibilities of constructing building with built in solar cell modules. A great way of utilizing solar energy in an economically feasible and malleable manner is through the use thin-film photovoltaic (PV) technologies. Thin-films which are preferred and ideal for PV applications include copper indium gallium selenium (CIGS) films, as a result of their ideal optical absorption coefficient. An ideal method of fabricating these cells is by electrode deposition due to the low economical cost and generally good output. Despite these benefits only a handful of thin-film technologies commercially available have obtained power conversion efficiencies (PCEs) greater than 20%, some of which are cadmium telluride (CdTe) and CIGS solar cells that each possess a PCE of 21% [10]. Although the large-scale utilization of these cells does contain hindering factors, some of which are cadmiums toxicity levels as well as indium availability [6,10,11].

As the severity of the energy crises increases, a growing amount of research and development in low-cost solar cells with a high effective efficiency has been implemented. The initial iteration of these thin-film solar cells boomed with the CdTe and CuInSe$_2$ solar cells having major success as a result of their low cost and great output. While the CdTe and CuInSe$_2$ materials have these major benefits, it is still necessary to obtain alternative solar cell materials resulting from the lack of indium and cadmium availability as well as cadmiums toxicity levels. The alternatives lean towards absorber materials with a high availability and supporting the terawatt scale photovoltaic industry [12]. Vital progressive development has been made in the search for different materials that can replace the use of CdTe and CIGS solar cells for thin film photovoltaics. Extensive research has found a good potential replacement for CdTe and CIGS cells due to the discovery of kesterite materials, offering a wide selection of unique properties for PV applications.

In this study, selenide kesterites materials doped with nanoscopic iron and cerium oxyselenides will be quantitatively evaluated for their electrochemical and photovoltaic efficiencies. Up to now, these materials have however not been used for the absorption of solar energy from sunlight. A substantial amount of data has only been collected at the laboratory scale with an isolated focus on several applications of iron and cerium oxyselenides, let alone photovoltaic applications. Thus, this study focused on how doping the kesterite material with nanoscopic iron and cerium oxyselenides will influence the photovoltaics of the kesterite materials. A substantial amount of data has only been collected at the laboratory scale on the topic of iron and cerium oxyselenides.

1.2   Problem Statement

As the world is aiming to dive into the use of renewable energy, many scientists have considered many different types of renewable energy sources, but almost all agree that solar energy is the best way to go as it's the most freely available form of energy. In order to harness solar energy, solar cells are required. Challenges facing the production of solar cells is the high toxicity levels of the materials, while being extremely expensive or extremely rare. The development and fabrication of low-cost materials with an extremely low toxicity level for PV applications has been a major challenge as the focus has shifted onto the use of kesterites which has many inefficiencies accompanying their use in

photovoltaics, these inefficiencies can be improved making kesterites extremely competitive in photovoltaics.

1.3   Rationale and justification for the research

One of the biggest challenges of a country's energy sector is the harnessing of renewable energy, this being solar energy in South Africa. The fabrication of solar cells for the generation of solar energy is another major challenge for scientists as they must develop new non-toxic and cost-effective materials, which abide by the country's strict environmental laws. Many governments have imposed stringent environmental regulations on industries. These regulations compel them to limit their use of fossil fuels and start incorporating the use of renewable energy to power their industries. As a result, there is a drive to search for and develop new technologies that can economically ensure high-quality renewable energy. There is currently research looking at kesterite materials and various doped kesterite materials for photovoltaics, but there is very little to no research looking into selenide kesterites doped with nano iron and cerium oxyselenides and comparing them to kesterites for use in photovoltaics.

Enough information on each kesterite and oxyselenide materials has been accumulated through laboratory studies and has been found to be very competitive, but there is very little to no information on them together. Thus, the aim of this study is to therefore, synthesise selenide kesterites doped with nanoscopic iron and cerium oxyselenides and to determine their photovoltaic and electrochemical efficiencies.

1.4   Research aims and objectives of the study

The aim of this work is to evaluate the influence of doping selenide kesterite with nanoscopic cerium and iron oxyselenide on its photovoltaic and electrochemical properties.

This research project was undertaken with the following specific objectives:

To synthesise iron and cerium oxyselenides ($Ce_2O_2Fe_2OSe_2$) precursor for use in the synthesis of selenide kesterites doped with nanoscopic iron and cerium oxyselenides by solid state reaction.

To use the $Ce_2O_2Fe_2OSe_2$, to synthesize the final product, the selenide kesterites doped with nanoscopic iron and cerium oxyselenides, $Cu_2,Ce_2(Zn,Fe)SnSe_4$.

To evaluate the morphological and structural properties of the synthesised $Cu_2,Ce_2(Zn,Fe)SnSe_4$ materials using: "Transmission electron microscopy (TEM), Scanning electron microscopy (SEM) and X-ray diffraction/crystallography (XRD)".

To evaluate the spectroscopic and optical properties of the synthesised $Cu_2,Ce_2(Zn,Fe)SnSe_4$ materials using: "Ultraviolet–visible spectroscopy (UV-Vis)".

To evaluate the photovoltaic and electrochemical properties of the synthesised $Cu_2,Ce_2(Zn,Fe)SnSe_4$ materials using: "Cyclic voltammetry (CV), electrochemical impedance spectroscopy (EIS) and current-voltage curves (I-V curves)".

To apply the synthesised $Cu_2,Ce_2(Zn,Fe)SnSe_4$ materials for use in photovoltaic applications.

1.5 Thesis Outline

This outline shown below describes the structure and topics that will be discussed in the chapters.

Chapter 2

This chapter gives intensive literature of the overall study. Detailed literature on cerium and iron oxyselenides and kesterites is discussed. Current photovoltaic devices and solar cells are also reviewed in this chapter. The limitations of these photovoltaic devices are given and an alternative device which is the kesterite technology is discussed in detail. Also, literature on photovoltaics in general is discussed in this section of the thesis.

Chapter 3

This chapter deals with the synthesis of cerium and iron oxyselenide dopant, kesterite and doped kesterite materials as well as the fabrication of the pristine kesterite and doped kesterite solar cells. The analytical methods and experimental procedures are explained.

Chapter 4

The experimental, results and discussion on the characterization, electrochemical and photovoltaic efficiencies of the cerium and iron oxyselenide dopant, kesterite and doped kesterite material are discussed in detail in this chapter.

Chapter 5

The results and discussion on the electrochemical and photovoltaic efficiencies of the kesterite solar cell and cerium and iron oxyselenide doped kesterite solar are discussed in detail in this chapter.

Chapter 6

This chapter sums up the conclusions from the individual chapters and recommendations are also made.
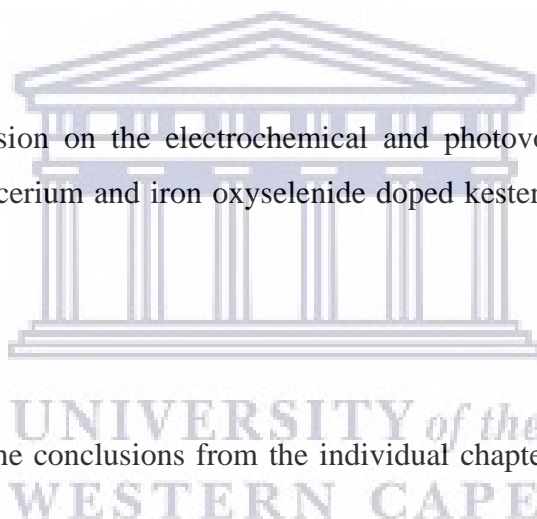
References

[1]   R. Larmae, T. Gimpaya, Solar Energy Technology Assessment, J. Res. Technol. Eng. 1 (2020) 67–75. https://www.researchgate.net/publication/342610877_Solar_Energy_Technology.

[2]   O. Peter, C. Mbohwa, Renewable energy technologies in brief, Int. J. Sci. Technol. Res. 8 (2019) 1283–1289.

[3]   G.M. Wilson, M. Al-Jassim, W.K. Metzger, S.W. Glunz, P. Verlinden, G. Xiong, L.M. Mansfield, B.J. Stanbery, K. Zhu, Y. Yan, J.J. Berry, A.J. Ptak, F. Dimroth, B.M. Kayes, A.C. Tamboli, R. Peibst, K. Catchpole, M.O. Reese, C.S. Klinga, P. Denholm, M. Morjaria, M.G. Deceglie, J.M. Freeman, M.A. Mikofski, D.C. Jordan, G. Tamizhmani, D.B. Sulas-Kern, The 2020 photovoltaic technologies roadmap, J. Phys. D. Appl. Phys. 53 (2020). doi:10.1088/1361-6463/ab9c6a.

[4]   Lazard, Lazard's Levelized Cost of Energy Analysis Version 13.0, Lazard Freres Co. 11 (2020) 1–21. https://www.lazard.com/media/451086/lazards-levelized-cost-of-energy-version-130-vf.pdf.

[5]   K. Vozel, Solar Cells, in: Semin. -1st Year, 2nd Cycle Sol. Cells, Ljubljana, 2011: p. 15. https://www.yumpu.com/s/OIddAW4rZ0w3j4nP.

[6]   Mahfouz Saeed, Electrochemical fabrication of thin film photovoltaic devices (CIGS & CIGSS), Case Western Reserve Univirsity, 2014.

[7]   O.A. Abdulrazzaq, V. Saini, S. Bourdo, E. Dervishi, A.S. Biris, Organic solar cells: A review of materials, limitations, and possibilities for improvement, Part. Sci. Technol. 31 (2013) 427–442. doi:10.1080/02726351.2013.769470.

[8]   A. Mohammad Bagher, Types of Solar Cells and Application, Am. J. Opt. Photonics. 3 (2015) 94. doi:10.11648/j.ajop.20150305.17.

[9]   B. Minnaert, P. Veelaert, Guidelines for the bandgap combinations and absorption windows for organic tandem and triple-junction solar cells, Materials (Basel). 5 (2012) 1933–1953. doi:10.3390/ma5101933.

[10]   K. Ranabhat, L. Patrikeev, A.A. evna Revina, K. Andrianov, V. Lapshinsky, E. Sofronova, An introduction to solar cell technology, J. Appl. Eng. Sci. 14 (2016) 481–491. doi:10.5937/jaes14-10879.

[11]   S.K. Wallace, D.B. Mitzi, A. Walsh, The Steady Rise of Kesterite Solar Cells, ACS Energy Lett. 2 (2017) 776–779. doi:10.1021/acsenergylett.7b00131.

[12]   T. Shibuya, Y. Goto, Y. Kamihara, M. Matoba, K. Yasuoka, L.A. Burton, A. Walsh, From kesterite to stannite photovoltaics: Stability and band gaps of the $Cu_2(Zn,Fe)SnS_4$ alloy, Appl. Phys. Lett. 104 (2014). doi:10.1063/1.4862030.

CHAPTER 2

OXYSELENIDE: PATH TOWARDS KESTERITE EFFICIENCY IMPROVEMENTS

Chapter overview

A comprehensive review of the fundamentals of chalcopyrite and kesterite materials is discussed in this chapter, explaining their differences and similarities. This chapter goes into the detailed background, benefits and synthetic strategies for the chalcopyrite material cerium and iron oxyselenides as well as for the kesterite martial, followed by a comparison of the different martials. Then finally describes the process and benefits of doping the kesterite material with the cerium and iron oxyselenide chalcopyrite material. The literature contained in this section provides crucial significance to research as is provides integral context to the work that will be performed on the cerium and iron oxyselenide and kesterite material.

2.1   Introduction

The photovoltaic effect is the generation of electric voltage in a system that came into contact with solar radiation. The photovoltaic effect gives rise to solar energy. This electric voltage generated by charge carries being excited into the conduction band is due to photon absorption. The French physicist, Alexandre Edmond discovered the photovoltaic effect in 1839, he realised that conductance increases with illumination as he was experimenting with metal electrodes and electrolyte. The photovoltaic effect has a similar mechanism to electron transitions to higher energy states as a result of light induction, where an electron breaks free from a metals surface in the presence of a photon containing enough light energy. Photovoltaics takes solar radiation and transforms it into electrical energy; solar cells is the name given to devices which take advantage of the photovoltaic effect, other names include photovoltaic devices [1]. There are three basic attributes required for photovoltaic operation:

❖ The creation of electron-hole pairs or excitations resulting from light absorption.

❖ Opposite charge carries being segregated.

❖ Individual extraction of the opposite carriers to an external circuit.

In order to understand the basic operation of photovoltaic cells, these attributes must be explored and explained, starting with semiconductor material. A semiconductor is a material with a band gap i.e., a discontinuity in the allowed energetic states of electrons in the solid. This band gap property of semiconductors prevents the relaxation of electrons once excited by a photon, thus is key for photovoltaic activity. The larger the band gap; the more potential energy/ voltage a device provides. However, fewer photons can be absorbed, this specific parameter determines electrical current. Although photons of lower or higher energy than the bandgap cannot be utilized [2–4]. The power of a cell is dictated by the voltage and current. The optimal absorber band gap, was first determined by Shockley and Queisser, and occurs at a photon energy of around 1.34 electron volts [5], thus providing a convenient screening parameter for potential photovoltaic materials. Naturally, band gaps can be direct or indirect and for the band gap to be direct, an electron must be able to travel across the gap with no change in crystal momentum, if this does not occur then the gap is indirect. Direct band gap photovoltaic materials are desirable as the indirect band gap materials require light and heat to promote electrons across the gap, with an associated weaker optical absorption and loss of device efficiency [6–8].

Semiconductor solar cells are ultimately simple devices. A semiconductor is a material possessing the capacity to absorb light, a portion of this absorbed photon energy is then delivered to electrons and holes which are carriers of electrical current [9]. An illuminated semiconductor absorbs a photon and an electron is excited and moves from the full valence band to the empty conduction band where it moves away from its original position, leaving behind a positive charge since the species was originally neutral. This electron 'hole' is then filled by a neighbouring electron, creating another hole on the adjacent space. This mechanism is repeated resulting in the migration of the electron vacancy in the opposite direction to the electrons filling the previous holes. Therefore, for every absorbed photon, two mobile charge carriers are produced, one positive and one negative. This binary

species is called an exciton, with a lifetime of femtoseconds before the electron ejects a photon that corresponds to the energy of the band gap and recombines with the hole it left behind, a process termed radiative recombination, which is undesirable for PV applications as it results in a loss thereby reducing the efficiency. The exciton is stabilized by the dielectric constant of the material and it is possible to cause the bound hole and electron to migrate away from each other by applying an electric field across an exciton [6,10]. Essentially this process is seen as the production of an electric voltage betwixt a cathode and an anode which are connected to either a solid or liquid system in the presence of light on the system [11].

A potential gradient can be generated by using crystal defects, without any externally applied bias, in what is called a p-n junction [12]. All crystals generally contain impurities or imperfections, which introduces a localised empty state somewhat higher in energy than the valence band. Thus, this localised empty state is able to accept an electron from the valence band, leaving behind a hole that acts as a charge carrier. This material is termed p-type "(where p stands for positive)" when a significantly large amount of these defects is present in a material. Whereas if the defects have a filled state slightly lower in energy than the conduction band, then the electrons from the dopant can be easily promoted to the empty band, resulting in the conduction occurring predominantly with the electron charge carrier, and is called n-type materials (where n stands for negative) [6]. A depletion zone is formed by the recombination of the charge carries at the interface between a p-type and n-type material when they are placed together. This depletion zone charges the interface between the p-type substrate negative (as the holes have been filled by electrons) and the n-type substrate positive (as the electrons have moved across the interface to fill the holes). Photovoltaic cells make use of this phenomena in order to create a natural electric field, thus when excitons are created by photons, the charge carriers can separate across this field and produce a working current. Extrinsic dopants are intentionally introduced defect states, which provides a means of controlling conductivity. A p-n junction can be created across a single material by doping opposing sides differently [6,13,14].

2.2   Photovoltaic sustainability and competitiveness

Currently energy is one of the most important concerns needing to be discussed, studied, reviewed, and researched in further detail than currently being done. Energy depletion is of major concern worldwide and the depletion of non-renewable reserves is causing an imbalance in nature. Currently 10 terawatts (TW) per year is the world's energy consumption and is estimated to be around 30 TW by 2050 [15]. One way to combat this energy crises it by the implementation solar energy, a form of renewable energy which is in abundance. The configuration of a photovoltaic system is genuinely quite simple; photovoltaic systems are built up of four components; PV modules producing electrical energy from sunlight. The battery for energy storage and delivery of electrical energy in a form that can be used. The charge controller which regulates the level of charging the battery receives. Then finally devices including the lamps and computers [16]. PV does not result in any harmful impacts to nature and the environment, and by using this form of renewable energy, pollution will be reduced [17].

PV modules are known as solar panels which contain constituents of independent solar cells. Despite the light source being natural or artificial, solar cells are photovoltaic. There are many uses of photovoltaics such as a photo detector, water pumping, lighting, traffic signals or cold storage [18,19]. In essence the name of the semiconducting material used to produce the solar cells is the name given to these cells, and some are designed to work with sunlight reaching the earth while others are designed for space. Single-junction solar cells consist of a single light-absorbing material layer, multi-junction solar cells consist of several physical configurations which exploit several absorption and charge separation mechanisms. First generation cells produce a lab-based efficiency of 24.7% with a module-based efficiency of 22.7%. Second generation with lab-based and module-based efficiencies of 18.4% and 13.4% respectfully. The third generation have a very high efficiency of > 30% [20]. The first-generation cells are made of crystalline silicon. Amorphous silicon, CdTe and CIGS cells populate the second-generation cells, while thin-film technologies identified as emerging photovoltaics, generally most of them are researched based or only in the development phase [7,21,22].

Four types of PV installations are available; grid-tied centralized, grid-tied distributed, off-grid commercial and off-grid, with the grid-tied centralized and off-grid commercial used for large scale industrial and power generation buildings [23]. In recent years, the research, development, and manufacturing of solar cells has seen a massive spike due to the growing demand for clean energy resources. Silicon solar cells along with other inorganic and heterojunction solar cells are mature and known technologies with PCEs reaching record highs of 24.7%. [24]. Despite being the face of solar cell technology, silicon-based solar cells possess a complex fabrication process consisting of several important steps which drive up the cost of these panels and in comparison, to fossil fuels the energy production of these panels don't compete at all. The silicon wafer processing technology has limitations thus, rendering the silicon cells rigid and large-scale fabrication of these cells is non-feasible. Along with their disadvantages, their limitations in generating cost-effective energy have led many researchers to find different route for solar energy production, despite silicon PVs potentially still occupying more than 50% of the PV production [24,25]. In comparison to silicon, using strong light absorbing materials requires the use of less material, thus having a significant cost reduction while allowing for greater possibilities of constructing buildings with solar cell modules incorporated in the building. Thin-film PV technologies provide a low cost and malleable method for exploiting solar energy [26]. Right now, only three types of the thin film solar cells have reached industrialization, including cadmium telluride (CdTe) solar cells, amorphous silicon (a-Si) solar cells and copper indium gallium diselenide (CIGS) solar cells [27]. CIGS are group I–III–VI2 ternary compound p-type absorber materials that possess a tetragonal chalcopyrite crystalline structure ideal for PV applications, resulting from their record optical absorption coefficient [28]. An ideal method of fabricating these cells is by electrode deposition due to the low economical cost and generally good output. Despite these benefits only a handful of thin-film technologies commercially available have obtained power conversion efficiencies (PCEs) greater than 20%, some of which are cadmium telluride (CdTe) and CIGS solar cells that each possess a PCE of 21% [29–31]. The overall efficiency of a photovoltaic cell is the outcome of; electron-hole separation efficiency, thermodynamic efficiency, conductive efficiency and reflectance efficiency [29]. This overall PV cell efficiency is a function of successful electron-hole generation and separation. There are many factors that can decrease this efficiency mainly, poor conductivity and hole electron recombination.

2.3   Chalcogenide and chalcopyrite crystallographic analysis

2.3.1   Chalcogenide and chalcopyrite morphology

There is a lot of focus on the use of chalcogenides in photovoltaics, of which the CIGS films fall under. The $Cu(In,Ga)Se_2$ (CIGS) material has become known as the thin-film solar cell technology with the greatest efficiencies and has demonstrated a record efficiency of 20.0% [20,32]. Chalcogenides are a well-known group of inorganic glassy materials consisting of one or more chalcogen elements: elements of group sixteen of the periodic table such as Sulphur, Selenium and Tellurium. Generally, the phases existing amongst the systems, M-S, M-Se, M-Te and M-O (M = transition metal) differ considerably in their chemical and physical structure as well as their compositions, resulting from the differences between the oxygen atom and the S, Se, Te atoms [33,34]. The chalcogens are usually alloyed with electropositive elements such as Arsenic and Germanium, and with elements like Phosphor, Antimony and Bismuth, to form chalcogenide glasses that exhibit fascinating properties. The potential of transition metal chalcogenides has become recognised considerably due to the advanced applications of these metals or solar energy generation and microelectronic devices. The family of the transition metal dichalcogenides (TMDCs) forming TX_2 is composed of the transition metals, T, chalcogenides, X. When looking at the properties of transition metal chalcogenides and chalcogenides in general, chalcogenide glasses (CG) can be regarded as a soft semiconductor due its flexible and viscous atomic structure, while possessing a band gap energy (~2 eV) characteristics of semiconductor materials (1-3eV) [35]. Several early transition metal dichalcogenides structures resembles graphite due to their layered structures, the two most frequently observed structures of these compounds are CdI_2 and MoS_2. Both these chalcogenides exhibit a six-fold coordination of the metal, the CdI_2 exhibits an octahedral structure and the MoS_2 exhibits a trigonal prismatic structure. If the polyhedrons are joined at their edges, X–M–X, it will form sandwich layers (M = Cd, Mo; X = I, S). The x-layers of MoS_2 are in registry (ABA). Several polytypes can be formed by stacking the layers perpendicular to the layer plane in different sequences [36].

2.3.2   Electrical and optical properties

When looking at their electronic properties, these, CGs are considered amorphous semiconductors with electrical and optical band gaps of 1-3 eV. Their band gap decreases in the order of S, Se and Te, present enhanced metallic character. TMDC form a group of compounds known for their layered structure, where this term layered is referring to the existence of parallel planes, possessing bonds much weaker than inside the region of the limit, making these materials highly anisotropic and in extreme cases two dimensional. Electrical resistivity of solids, excluding superconductivity, may vary in the order of 10^{32} which may be the widest of any common physical properties of solids. There are many factors that influence the temperature dependence of the electrical resistivity such as, phonon scattering, impurity and defect scattering and mutual scattering of electrons, which are involved in the electrical transport in different temperature ranges [35,37]. CGs are extensively incorporated in photonic applications due to their ideal optical properties, including their ideal refractive index, high photosensitivity and huge optical nonlinearity [35]. The optical band gap (E_g) of materials is a crucial optical parameter, it's been found that the E_g of any single crystal solar cells should be between 1.0 eV to 1.4 eV for maximum solar energy conversion. Therefore, semiconducting materials that possess a band gap close to this optimum value are considered optimal for use in photovoltaic operations. The optical properties of the group IVA trichalcogenides are in contrast to the valence bands (VB) compounds [37].

2.4   Kesterite crystallographic analysis

2.4.1   Kesterite and Ferrokesterite structures

A kesterite (CZTS) is a chalcogenide material belonging to the AI2BIICIVXVI4 compound family and are natural p-type I2-II-IV-VI4 semiconductors showing a great amount of promise as absorber layers in thin film photovoltaic solar cells [38,39], thus its anion is a chalcogen from Group 16 in the periodic table. These CZTSSe materials have gained a significant amount of research interest for thin-film PV applications due to them containing many desired aspects such as being earth abundant and nontoxic, possessing band gaps around 1.0 and 1.5 eV which are very near to the ideal band gaps for single-

junction solar cells, additionally they possess huge light absorption coefficients > 104 cm^{-1} [40–42]. The Cu_2ZnSnS_4, $Cu_2ZnSnSe_4$ and $Cu_2ZnSn(S,Se)_4$ compounds are represented as structural models of two naturally occurring minerals: stannite (space group I-42m) and kesterite (space group I-4) according to literature [43–45]. The kesterite group of materials is linked to the older $Cu(In,Ga)(S,Se)_2$ (CIGSSe) technology quite closely. The kesterite structure can be obtained by substituting the two indium (In^{3+}) or gallium (Ga^{3+}) atoms found in the CIGSSe structure with one tin (Sn^{4+}) atom and one zinc (Zn^{2+}) atom. The kesterite system can take the form of three structural forms which differ slightly namely the kesterite, stannite or primitive mixed Cu–Au material, with the kesterite being the most stable structural polytype [46,47]. The kesterite and stannite minerals are acknowledged as individual species resulting from their different Fe to Zn compositional ratios, their distinct optical and physical properties as well as their difference in the position of the chalcogen atoms [48–50]. A major key aspect supporting the manufacturing and fabrication of extensible thin-film PV technology is the CZTS material, considering the abundancy and low-cost of the essential elements of the CZTS material [51].
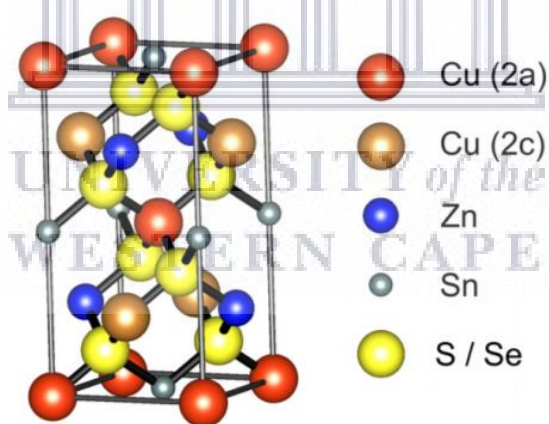
Figure 2.4.1: Kesterite, $Cu_2ZnSn(S,Se)_4$, elemental structure [49]

The crystal structure is made up of the periodic array of ordered elements and the CZTS occurs in four different phases: stannite, kesterite, wurtz-stannite, and wurtz-kesterite. All crystal structures appear in the Inorganic Crystal Structure Database (ICSD) [50]. The kesterite mineral can exist in two main structural forms, the kesterite (CZTS) and the stannite/ ferrokesterite (CZITS). Looking at the crystal structure of the kesterite compound it has a tetragonal (diamond) structure. The Cation ordering ($z = 0$, ¼, ½, ¾) of the CZTS

is as follows; CuSn, CuZn, CuSn, CuZn. The energy (meV/atom) and the energy (meV/cell) are both 0. The A (Å) is 5.427, the C (Å) is 10.871 and the c/a is 2.003. The band gap (exp.) (eV) is between 1.45-1.51 and the band gap (theo.) (eV) is between 1.47-1.65. The absorption coefficient (cm^{-1}) is $> 10^4$. Looking at the crystal structure of the stannite compound it has a tetragonal (diamond) structure. The cation ordering (z = 0, ¼, ½, ¾) of the CZITS is as follows; ZnSn, Cu2, ZnSn, Cu2. The energy (meV/atom) is 2.8 and the energy (meV/cell) 50. The A (Å) is 5.450, the C (Å) is 10.878 and the c/a is 1.996. The band gap (theo.) (eV) is between 1.27-1.42 [50]. The most stable kesterite structure is (I$\overline{4}$), whereas the stannite (I$\overline{4}$2m) and the kesterite structures (P$\overline{4}$2c and P$\overline{4}$2m), which are tetragonal structural modifications, are marginally greater in energy (ΔE = 2.8 meV/atom for stannite, and ΔE = 3.2 meV/atom for P$\overline{4}$2m). Earlier work has provided information on the vibrational frequencies of the three individual kesterite structures (I$\overline{4}$, I$\overline{4}$2m, and P$\overline{4}$2m) [52,53]. The kesterite and stannite crystal structures contain different crystallographic unit cells, with the relative difference lying in the cation position. The kesterite has Cu in each plane, while stannite has Zn-Sn at the z = 0 and z = ½, and Cu2 at the z = ¼ and z = ¾. Sn is located at the same site in both structures. "Density functional theory" (DFT) calculations have given the total energy of the CZTS system, and the kesterite crystal structure is found to be in the ground state, while the stannite is only 2.8 meV/atom above it. The wurtz-kesterite is 6.0 meV/atom and wurtz-stannite 7.2 meV/atom. Thus, the kesterite crystal has a total energy per primitive cell that is 50 meV lower than the stannite crystal, therefore has a slightly higher stability [49,50].

2.4.2 Intrinsic defects of the Kesterite material

Along with the several different structures of the kesterite compounds, secondary phases including ZnS, Cu$_2$S, and Cu$_2$SnS$_3$ are almost guaranteed in the films due to the kesterite being thermodynamically stable in a slim section of the phase diagram. The performance of the device is heavily influenced by the existence of these phases due to variance in the band alignment or a mismatch in the crystal structure. The steady array of chemical potentials of CZTSSe versus the secondary phases is incredibly low and the simple formation of Zn(S,Se) or Cu$_2$Sn(S,Se)$_3$ due to the chemical potential of Zn being within a shallow section results in a limit as seen in the phase inhomogeneity, shown that by Chen et al [54]. The generation of secondary phases in CZTSSe solar cells with high efficiencies developed in nonstoichiometric conditions is unavoidable. As secondary phases may

potentially intensify the recombination as a result of their unsuitable band gap and electrical properties, they are known to be detrimental to the device performance. A smaller band gap than that of the kesterite (Cu_2SnS_3, Cu_2S, and SnS in a pure sulfide and Cu_2SnSe_3 in a pure selenide) attributed to the secondary phases can limit the V_{oc}, while secondary phases with larger band gap can impede the charge transport. Therefore, detecting the secondary phases in CZTSSe at the atomic level by analyzing the component uniformity is vital [41,55–57]. ZnS and CTS which are key secondary phases, are not easily identified by XRD due to their incredibly similar patterns. The CdTe and CIGS devices are very efficient and exhibit a minority carrier lifetime of 1–2 orders of a magnitude longer than state-of-the art CZTS device, which suffer from crystallographic defects that are negatively influencing the carrier transport and lifetime of the absorber layer [51]. Several different types of point defects are allowed within the kesterite crystal structure, resulting in the appearance of discrete energy levels, allowing p-type doping. An enormous group of shallow acceptor-like defects consisting of Cu vacancies (V_{Cu}) and CuZn antisites, result in the p-type conductivity [41,58]. Doping is generally achieved through stoichiometry variations rather than extrinsic doping, similar to doping in CIGS materials. According to deep defect measurements of the kesterites, the Sn-Se bond is superior in strength compared to the Zn-Se and Cu-Se bond resulting in a higher energy of formation of V_{Sn}. In kesterite materials, the conversion efficiency is still limited to 12.6%, this limitation mainly resulting from the open circuit voltage (V_{oc}) losses correlated to the optical band gap. The minority carrier's brief lifetime occurring in the deep defects of the bulk or at GB could be vastly damaging to the performance. This is largely due to the multivalent characteristic of Sn resulting from its capability to form +II and +IV oxidation states, as Sn^{2+} creates deep recombination centres, assisting the dismal open circuit voltage [59,60]. The large V_{oc} loss of kesterite devices are mainly due to copious point defects and defect clusters; including cation disordering, associated severe band tailing and band fluctuations as a result of micro inhomogeneities in composition and anion substitution, un passivated junction interfaces as well as undesirable conduction band offset (CBO) [57,61–63]. In order to achieve high-efficiency kesterite devices, it is vital to acquire an off-stoichiometric kesterite composition, with the material being copper-poor and zinc-rich. During a general kesterite synthesis, ZnS/Se is the first species formed, accompanied by the creation of the other binary or ternary compounds, resulting in the compound being poor in Zinc from the onset of its formation. Thus, zinc-rich reaction conditions are

required to compensate for this deficit. Common disorders are Zn and Cu disorders due to their analogous chemical structures, like ionic radii, with both atoms easily being able to swop at reduced enthalpic cost to form CuZn acceptor and ZnCu donor antisite defects. The main point defect acceptors are V_{Cu}, CuZn and the main point defect donor is ZnCu. Defect complexes formed from the conjugated defects, of [CuZn + ZnCu] and [V_{Cu} +ZnCu], which are self-compensating with analogously reduced CuZn energy of formation and V_{Cu} acceptor defects. The V_{Cu} acceptor plays a fundamental role in intrinsic doping due to the high-efficiency devices being poor in Cu [63–66]. It's seen that even in stoichiometric CZTS, there is a significant bandgap decrease resulting from the CuZn + SnZn and 2CuZn + SnZn defect clusters exhibiting great concentrations damaging to device performance. Thus, high performing devices are suggested to have an arrangement indicating Cu deficient and Zn rich. However, unwanted binary and ternary impurity phases can be formed due to any non-stoichiometry in CZTS [66,67]. In CZTS, the most easily formed accepting defect is Cu_{Zn} and not V_{Cu}, as compared to CIGS. Creation of Cu_2S, SnS, and Cu_2SnS_3 binary and ternary impurity compounds are favoured in CZTS that are Cu and Sn rich, resulting in a decrease in the open circuit voltage of the device due to these impurities being conductive and providing a deviating path in the device. The Zn_S impurity is favoured in Zn rich CZTS which renders the potential shunt path present in the CZTS unreactive, despite it being harmful. Sn leaves in the +IV oxidation sate at its native site in the CZTS lattice, with more multivalent Sn existing in +II or +IV oxidation states. However, Sn can replace Cu and Zn from their lattice sites creating Sn_{Cu} and Sn_{Zn}, which are uninfluential antisite point defects within the bandgap due to their high formation energy. Sn_{Cu} purely occurs as a divalent atom when Sn is at the Cu site creating a shallow single donor level, while Sn at the Zn site can either form a double donor or isoelectronic centre associated with its multivalent nature. A change in the valency of Sn from +IV to +II state creates isoelectronic centres which proceeds as non-radiative recombination centres. When in its +IV valence state, it creates deep donor level a great distance from the conduction band, thus serving as the recombination centre and not as shallow donor [66–68]. The greater valence of Sn(IV) in comparison to Cu(I) and Zn(II), possesses deeper levels for Sn-related defects as a result, with them having a greater formation energy. Around the midgap, the double donor level $\varepsilon(0/2+)$ of Sn_{Zn} can be found [69–71]. N-type doping is difficult due to the easy formation of accepting defects, with Zn_{Cu} substitutions occurring along the 2c site and Cu_{Zn} at the 2d site. Low charge separation also occurs from

the ease of formation of Cu_{Zn} accepting defects, although type-II band alignment of the CZTS/CdS interface could help overcome this drawback. Cu_{Sn} for CZTS and In_{Cu} for CIGS are expected to be the most active recombination centres. The lack of the of defect complex ($2V_{Cu} + In_{Cu}$ for CIGS) is assumed to result in the observed greater defect concentration [49]. High-efficiency CZTS devices are generally always off-stoichiometric, while favoring a Cu-poor (Cu/(Zn+Sn) <1) and Zn-rich (Zn/Sn >1) composition, while maintaining the kesterite structure. This can be realized from the formation of desired defects, especially Cu-on-Zn antisites (CuZn) which have very low formation energies, and are considered to be the principal acceptor-defects in charge of the p-type conductivity of CZTS as seen in figure 2.4.2 [50,72].
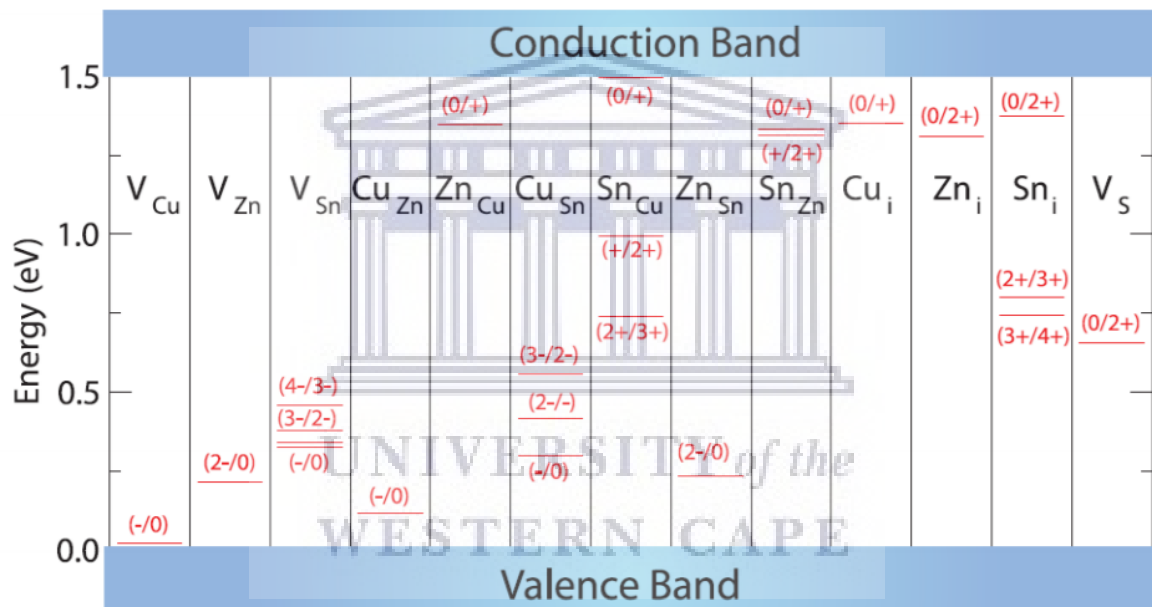
Figure 2.4.2: Calculated defect states in CZTS (Red numbers correspond to charge of defect) [73].

Ito and Nakazawa synthesized the first CZTS solar cell in 1988 [50] and from this point, the CZTS solar cells power conversion efficiency has been constantly improving. Recently, sputtering has produced the champion CZTS devices, and a record efficiency of 9.4% has been obtained by applying a high temperature annealing after CdS deposition. Another fabrication technique is pulsed laser deposition (PLD), which produced an efficiency of 5% [50]. Apart from the mentioned CZTS solar cell fabrication techniques, there are numerous other fabrication techniques that could be employed for example; PVD/ annealing which has showed a steady increase in record efficiency from 1% to 8.5%

between 1998-2012. Electrodeposition/ annealing which shows an increase in the record efficiency from 3.8% to 7.5% between 2009-2011. Colloids in hydrazine/ annealing which were used between 2010-2014 and shows a slight increase in the record efficiency from 9.8% to 10.1%. Nanoparticles came into play around late 2010 with an efficiency of 7.1% [49]. Monograin was used from 2010 with an increase in the record efficiency from 5.9% to 7.1% and Co-evaporation came into use from late 2012 with a record efficiency of 9% [49].

2.4.3 Source and nomenclature

The replacement of CIGS with CZTS is a possibility of producing CZTS solar cells yielding efficiencies up to 12.6% [74]. There are many advantages accompanying the use of CZTS as a bountiful, cheap, non-poisonous thin film PV solar cell absorber such as: p-type semiconductor behaviour resulting from the presence of intrinsic point defects, the presence of a direct bandgap and an absorption coefficient $> 10^4$ cm^{-1}, ideal for PV applications. stoichiometric compositional shifts can occur in the CZTS crystallographic structure [75]. Cu-poor compounds containing both sulfur and selenium generally always offer the best performance. The grain boundaries (GB) of CZTS have identical favorable properties as CIGS, including greatly improved minority carrier collection occurring at the GB [49]. The CIGS scientific community has begun working in $Cu_2ZnSn(S,Se)_4$, (CZTS), which has led to an improvement to the record efficiency of CZTS-based solar cells, from the 6.7% record in 2009 to 10.1% in 2011 [49]. The hydrazine-mediated fabricated selenium-containing CZTSSe has a record efficiency of 12.6%, other solution-processed CZTS devices including both S and Se are performing well, with the best nanoparticle device having an efficiency of 9.0% and the best precursor device having an efficiency of 8.6% [50]. The evaporation fabricated pure selenide CZTSe with a record power conversion efficiency of 11.6% [50]. Precursor films are required to undergo heat treatment at temperatures above 500 °C in order to improve the properties of CZTSSe and to obtain CZTSSe films with a single phase and large crystal size [76–78]. The reason why adding Se improves the efficiency is heavily due to the differences between S and Se for example: The CZTSe has a band gap of 0.95-1.05 eV compared to the 1.45-1.51 eV band gap of CZTS, thus incorporating both S and Se allows for tuning of the band gap tuned according to the solar spectrum. The size of S (1.84 Å) is smaller than Se (1.98 Å), thus a volume expansion occurs when S is replaced by Se in the crystal lattice during annealing,

causing the elimination of voids, leading to the formation of a dense film with fewer GB. Deep sulfur vacancies (V_S) donor defects occur in the sulfide compound as V_S have a significantly lower formation energy than selenium vacancies (V_{Se}). A lower electron trapping of [$2Cu_{Zn}+Sn_{Zn}$] defect clusters exist in CZTSe as well as a lower population of isolated deep defect states in the form of SnZn in CZTSe when compared to CZTS. MoS_2 formation at the back contact during sulfurization, could be damaging the solar cell performance [50].

2.5 Synthetic strategies for kesterite production

2.5.1 One-step or two step processes for thin films

GIS synthesis makes use of "vacuum and non-vacuum techniques" for the deposition process, but for CZTS, these techniques are inaccurate due the fact that cheap deposition does not mean cheap solar modules shown in recent works, therefore, the processes were classified into one-step or two-step processes [79]. The two-step process occurs as follows; an ambient temperature process takes place which incorporates the required elements then an annealing step follows, during this step the precursor becomes infused with the chalcogen. Rapid and cheap techniques for precursor deposition was allowed for use in the processes and until now the best efficiencies (> 10%) was obtained by the two-step processes. For the synthesis of CIGS, one step processes involving the simultaneous incorporation of all the elements often yields better results with an efficiency of 9.15% being the best efficiency. Whereas one step processes aren't always the best for CZTS synthesis. These processes are different, but they achieved good efficiencies (> 9%) [49]. Neither method is intrinsically better as temperature and atmosphere control during each method is the main point [49].

2.5.2 Thin film solar cells fabricated with benign solvents

Benign solutions use water and organic solvents such as; ethanol, thioglycolic acid or ammonium thioglycolate, which possess low molecular weights and low toxicities. Due to water being the most environmentally friendly and cheapest solvent thus, water-based CZTSSe inks have the possibility to be the optimum method for a cheap and green method

of synthesizing high quality CZTSSe films. The last two steps are as follows; firstly, the constituent elements of CZTSSe are transported to the substrate, followed by a heat treatment that transforms the precursor film into the required phase [80]. Through solution-based synthesis, a benign solvent (water/ethanol) is used to dissolve the fundamental CZTs materials according to their solubility. Stability is a crucial aspect of the benign solution for the main synthetic strategy of self-stabilization; this strategy is excellent with aqueous systems due to their incredible durability and availability without the introduction of unwanted carbon chains. There are several coating techniques for the deposition of CZTS films, with electrodeposition outputting the highest quality film despite the complex procedure. Even though the efficiency of benign solution processed CZTS solar cells may not be as high as its non-benign counterpart, the benign solution process is favoured due to it being a high-utilization approach for large-scale synthesis of CZTS thin films that is cheap and green. A competitively variable synthetic method in both the production-cost and film qualities among benign CZTS inks is the self-stabilization route [80].

2.5.3 One pot hydrothermal synthesis

During this synthetic route, water is mixed with copper (II) sulphate ($CuSO_4 \cdot 5H_2O$), zinc nitrate ($Zn(NO_3)_2 \cdot 6H_2O$) and tin (IV) chloride ($SnCl_4 \cdot 5H_2O$, 98%), then thiourea (CH_2SNH_2) and selenium (IV) oxide (SeO_2) are added to the mixture then placed in an autoclave, allowing the hydrothermal reaction carried out for 12 h at 300 °C. After the reaction occurs and is cooled, the precipitate is collected and washed with ethanol then water. The black powder is dried in argon at 110 °C for 1 h as the annealing process is carried out at 550 °C in argon gas (downstream). The newly annealed powder then runs through a tiny amount of sulfur powder placed at 300 °C in a tube furnace for 1 h. A PVD method is used to deposit the CZTSSe films on a clean glass substrate. Some of the synthesised powder is placed on a tungsten boat filament and evacuated the PVD system to a low pressure of $10 - 7$ Torr. Avoiding the possible separation of major compounds due to different melting points, the filament is heated to a temperature above 1200 °C for evaporation. In order to avoid exposure to the atmosphere, the films are stored in a vacuum desiccator. Then the CZTSSe films are annealed in argon at 280 °C for 1.0 h [81].

2.5.4 Polyol-mediated kesterite synthesis

This synthetic route includes the addition of $CuCl_2$, $ZnCl_2$ and $SnCl_2$ to a three-necked flask containing diethyl glycol (DEG). A homogenous mixture is formed by mixing these powder precursors together under continuous stirring, this solution is then heated to 80 °C. Na_2S dissolved in DEG is injected into the heated solution forming a second solution. Immediately after the injection, the temperature is increased to 190 °C. Once solution 2 was heated at this temperature for 30 mins it was cooled and the deep black suspension was diluted with isopropanol. The synthesised CZTS nanoparticles are collected via centrifugation [82].

2.5.5 Facile solvothermal synthesis

For a general synthetic procedure for the production kesterite particle via a facile solvothermal method, magnetic stirring is used to dissolve copper (II) chloride dihydrate, zinc (II) chloride, tin (IV) chloride tetrahydrate, thiourea and PVP in ethylene glycol. Once mixed the solution is placed into a Teflon lined stainless steel autoclave and kept at 230 °C for 24 h then cooled to room temperature. The resulting precipitate is then cleaned with deionized water and ethanol. Once cleaned the product is vacuum-dried at 60 °C [83].

2.5.6 Formation of CZTS thin-films by SILAR method

One cycle of SILAR film formation involves the sequential addition of the cationic precursors; $SnCl_2 \cdot 2H_2O$, $Fe(NO_3)_3 \cdot 9H_2O$, and $CuSO_4 \cdot 5H_2O$ in ethanol, allowing sufficient time for the solute to dissolve. The addition of $Fe(NO_3)_3$ transforms the transparent $SnCl_2$ solution into a golden-yellow colour, thus maintaining its homogeneity. The solution then becomes greenish-yellow in colour with slight turbidity after the addition of the copper precursor. The anionic precursor is $Na_2S \cdot xH_2O$ in ethanol. For the fabrication of the CFTS thin-films, the substrates are drenched in a bath containing the cationic precursors, after some time allowing for their adsorption, the substrates are then rinsed in ethanol then airdried, followed by an immersion in the anionic precursor then rinsed with ethanol and dried. This cycle is repeated in order to obtain films of increased thickness, which is optimized to achieve a most favourable η [84].

2.5.7 Solution synthesis of Kesterite particles

This synthetic route involves the incorporation of copper acetate ($Cu(CH_3COO)_2$), zinc acetate dihydrate ($Zn(CH_3COO)_2.2H_2O$), tin chloride pentahydrate ($SnCl_{4.5}H_2O$), and thiourea (CH_4N_2S) being mixed in deionized water. The solution is transferred to a Teflon lined mixer to form a clear solution from continuous stirring, then kept at 180°C for 6 h. after heating the solution is cooled and the precipitates are filtered then cleaned using distilled water and absolute ethanol. A vacuum is used to dry the final products at 60 °C for 3 h. A similar experiment may be carried out by changing the solvent in order to analyse the effect of solvent on the characteristics of the CZTS nanoparticles, but there is no true significant variation in the yield of the products with different solvents [85].

2.5.8 Formation of CZTS thin-films by sputtering

For the general synthetic procedure, detergent, methanol, ethanol, acetone, and deionized water is used to wash and sequentially clean soda lime glass (SLG) substrates (3×3 cm^2) in an ultrasonic bath for 10 min each, followed by a rinsing in deionized water then dried. A radiofrequency (RF) magnetron sputtering system is used for the deposition of the quaternary kesterites, operating at 80 W for 2 h. The composition, 2:1:1:4 C:Zn:Sn:S, is the target used in this synthetic method, with a purity of 99.99%. The substrate is then coated with the target material by applying a voltage across the cathode (target material) and the anode (substrate). Gas production results from the ionization of the target materials surface electrons, leading to the formation of a plasma. The background gasses are prevented from reacting with the film or sputter target by reducing the chamber pressure. The growth of a thin film on the substrate through sputtering can be carefully monitored by controlling the partial pressures of the reactive gases. The distance between the target and the substrate is set at 7 cm. Deposition of the precursors onto the SLG inside a sputter coater is performed at a working pressure of 4.5 mTorr with an Ar flow of 5 SCCM, when the base pressure reaches 6.3×10^{-6} Torr. Maximum film uniformity and target utilization is achieved by rotating the substrate holder at 20 rpm, while the deposition temperature is kept at 200 °C. The two temperatures used for post annealing are 470 °C and 560 °C, while under an N_2 atmosphere in a tube furnace. The selected temperature at four different base pressures (150 Torr, 250 Torr, 350 Torr, or 450 Torr) are used to maintain the samples for 30 min before cooling while remaining in the annealing chamber [86].

2.6   Kesterites and chalcopyrites

Kesterites with their high "power conversion efficiencies (PCEs)" and direct and tuneable "band gap energies (E_g)", along with the fact that for their fabrication, less material is required in comparison to conventional Si-based solar cells, thin film solar cells are becoming increasingly important. Copper indium selenide (CIS), copper indium gallium selenide (CIGS), and cadmium telluride (CdTe) have PCEs around 22% in comparison to amorphous silicon (a-Si) thin films which have a PCE of around 13.6%. There is a p-type chalcogenide semiconductor Cu_2ZnSnS_4 (CZTS) which is called a kesterite. This kesterite material is another likely solar absorber material acquired from the CIGS chalcopyrite structure by replacing In and Ga with Zn and Sn or similar elements that are less expensive and more earth-abundant [86–90]. Chalcopyrite solar cells have progressively become high-efficiency, thin-film laboratory devices. Incredibly slow leaching kinetics has been used to characterize chalcopyrites, and has been strongly linked to the formation of a passive film on its surface. Fe_2O_3 or its hydrated form $Fe_2O_3.xH_2O$ and $Fe(OH)_3$ have been reported to be the surface products of chalcopyrite oxidation [91]. Chalcopyrite-type materials are seen to be a very promising material for thin-film solar cells, due to their direct band gaps being a good match for the solar spectrum along with their favourable electronic properties resulting in solar cell efficiencies surpassing 20% [92–95]. The mineral $CuFeS_2$ has lent its name to the chalcopyrite crystal structure family, due to $CuFeS_2$ being one of the most important copper (Cu) ores. Chalcopyrite-type materials consist of compounds formed from many groups including the groups I, III, and VI (I-III-VI2) or from group II, IV, and V (II-IV-V2) elements of the periodic table [96]. Gigawatt (GW) range manufacturing volumes are expected in the years to come resulting from a combination of moderately high efficiency and potentially low processing costs. Increased manufacturing volumes have brought forward concerns about the worlds limit of indium will inhibit the quantity of chalcopyrite PV that can be produced at the low cost. It has been suggested that $Cu_2ZnSn(S,Se)_4$, kesterites, can replace conventional CIGS solar cells, in order to alleviate possible future effects of indium scarcity. The idea follows that Zn (group II) and Sn (group IV) atoms replace every two group III (In or Ga) atoms in chalcopyrite structure, therefore keeping the octet rule intact. Something to be taken into consideration is the PCE for CZTS related thin film materials is only around 12.6% and in order to be competitive against the CIGSe solar cells, CZTS-based solar cells must be cost

effective and have a PCE of over 15% [97–100]. Polycrystalline solar cells have improved efficiencies resulting from the increased grain size and the deep defect for absorber material, although the CZTSe possess a narrower single-phase composition range compared to CIGS. The phase stability of the CZTSe quaternary compound is influenced by some factors such as the formation of unacceptable ternary and binary phases as well as the formation of unfavourable defects in their crystal structure [57,101]. There are significant similarities and differences between the chalcopyrites and kesterites. The similarities in theory are similar band edge energies, p-type doping, formation of benign defect complexes, and miscibility of alloys. Although the differences between them involve aspects such as a smaller single-phase composition space and a different dominant intrinsic defect. The "density functional theory (DFT)" can be used to study the structural, electronic and defect properties of both kesterites and chalcopyrites [102]. Selenide and sulfide chalcopyrites along with kesterites all have different "band gaps" (E_g), "valence band edges" (E_v) and "conduction band edges" (E_e) (relative to vacuum). The CISe (chalcopyrite) possesses the following electrochemical properties; a E_g of 1.04 eV, a E_v of -5.64 eV and a E_e of -4.60 eV. The CZTe (kesterite) possesses the following electrochemical properties; a E_g of 1.00 eV, a E_v of -5.56 eV and a E_e of -4.56 eV. The CIS (chalcopyrite) possesses the following electrochemical properties; a E_g of 1.53 eV, a E_v of -5.92 eV and a E_e of -4.39 eV. The CZTS (kesterite) possesses the following electrochemical properties; a E_g of 1.50 eV, a E_v of -5.71 eV and a E_e of -4.21 eV [102]. The positions of the CB and the VB edges are presented parallel to vacuum, where DFT was used to calculate the relative band offsets, and the electron affinity value for CISe is 4.6 eV which is experimental. The band gap of the kesterite is very close to the corresponding chalcopyrite band gaps for the selenides and sulfides. The success of the "CdS/i-ZnO/ZnO:Al buffer" is due to the individual material maintaining a sensible sequence with the CdS conduction band at -4.3 eV [102]. When looking at the stability of single-phase stoichiometric material of chalcopyrites and kesterites, for the CuInSe$_2$, single-phase material can occur for Cu chemical potentials between -0.4 < μCu < 0 eV, and can occur for the corresponding In chemical potentials between -0.4 < μCu < -1.8 eV. While for CZTS, single-phase material occurs at a significantly lesser chemical potential space around (μCu = -0.20 eV, μZn = -1.23 eV, and μSn = -0.50 eV) [102].

2.7   Cerium and Iron oxyselenide analysis

2.7.1   Cerium and Iron oxyselenides crystallographic analysis

Transition metal ion-based materials have gained massive amounts of interest due to their novel electronic, magnetic, and structural properties, exploring materials that constitutes these transitions has procured many incredible discoveries such as high temperature superconductivity as well as superconductivity in $LaFeAsO_{1-x}F_x$ [103]. Research in the magnetism of multiple combined anion systems has been pushed due to the discovery of iron-based superconductivity of these materials associated to their superconducting behaviour, resulting in many fascinating properties of mixed anion systems being highlighted. When looking at the iron-based superconductors, the 1111 family is derived from LnFeAsO (Ln = trivalent lanthanide) and adopts the ZrCuSiAs-structure. The LnFeOAs materials contain layers of fluorite-like edge-shared OIn_4 tetrahedra, alternating with antifluorite-like edge-shared $FeAs_4$ tetrahedra, causing them to possess the ZrCuSiAs like structure. It is possible to chemically dope the fluorite-like $[Ln_2O_2]^{2+}$ layers, causing induced superconductivity in the $[Fe_2As_2]^{2-}$ layers. B-FeSe, containing isostructural 2D layers of edge sharing $FeSe_4$ tetrahedra has shown to possess superconductivity up to 37 K [104,105]. A consequential role for converting superconducting Tc in the doped materials is attributed to the Ln^{3+} cation. This cation is equally important for interpreting the magnetism of the parent non-superconducting materials such as the spinreorientations in NdFeAsO and PrFeAsO, despite the superconductivity arising within the iron arsenide layers resulting in intense research around mixed-anion systems involving the interaction between transition metal and lanthanide magnetic sublattices. $La_2O_2Fe_2OSe_2$ is the identified member of the M_2O'' (M = transition metal) oxyselenide family with fluorite like $[La_2O_2]^{2+}$ slabs assuming a layered structure, similar to those in 1111 iron oxyarsenides, separated by Se^{2-} anions from $[Fe_2O]^{2+}$ sheets. Within the anti-CuO_2 sheets, the Fe^{2+} cations are coordinated by two O ions, while being coordinated by four Se^{2-} ions above and below the sheets, leading to the creation of a network of face-shared FeO_2Se_4 trans octahedra. $La_2O_2Fe_2OSe_2$ orders antiferromagnetically (AFM) below $\sim$ 90 K. In a means to understand and interpret the exchange interactions and magnetic ordering present in these $[Fe_2O]^{2+}$ sheets much research has been done [105–108]. Oxyselenides have caught the eyes of researchers for many decades due to their semiconducting properties and the capacity to tune these properties. The initial interest of oxyselenides was in

photoconductivity which resulted in the discovery of LaCuOS and related materials. Despite this, the major of the focus in oxyselenides are on thermoelectrics due to their tuneable semiconducting properties [103]. Considering and understanding the structural chemistry of oxyselenides as well as their common structural units is highly beneficial. Anion-ordering often results from the size and characteristic differences between the 1st row oxide O^{2-} and 3rd row selenide Se^{2-} anions. The hard cations such as Ln^{3+} ions, as in $Ln_{10}OSe_{14}$ phases tend to coordinate the softer but still relatively hard polarising O^{2-} anions, and it is beneficial to take into consideration the structural areas with regards to oxide-centred tetrahedra. The more covalent Se^{2-} ions tend to coordinate the softer transition metals. These layered structures resulting from this anion-ordering possess relatively contrasting properties correlating to increased ionic oxide and increased covalent selenide layers. These properties can be electronically separated from each other. The properties of the whole material can genuinely be understood from this anisotropy [103,109]. Oxychalcogenide materials have had incredible amounts of interest and research resulting from their paramount electronic and magnetic properties. Of these oxychalcogenide materials an important family with a general composition "$Ln_2O_2Mse_2$ (Ln = La, Ce; M = Mn, Fe, Zn, Cd)", and a jointly associated composition such as $La_2O_2Cu_{2-4x}Cd_{2x}Se_2$. These semiconductor materials which possess a varying bandgap from ~0.3 eV to ~ 3.3 eV. The layered $La_2O_2CdSe_2$ was reported as a wide-gap (3.3 eV) semiconductor which was studied as an optoelectronic device constituent. The $Ln_2O_2Mse_2$ composition has three basic types of structures, most of which acquire a layered structure (α-phase). This type of layered structure can be regulated either in a commensurate or incommensurate manner within individual layers which harbour different transition metal arrangements. The second two types of structures are non-layered structures, orthorhombic β-phase and monoclinic $Pb_2HgCl_2O_2$-type γ-phase [110]. Lately there has been a number of $La_2O_2Fe_2Ose_2$ related materials, with all materials precisely containing the same ~2.8 Å square array of Fe sites, as well as extra oxygen for every two Fe atoms. The Fe-Fe distances are ~6% larger compared to FeSe/FeTe, due to this additional oxygen ion, and ~1% larger than in LaOFeAs [111]. Different "$A_2O_2M_2OSe_2$ Materials, with M = Co, Fe, Mn" has several different lattice parameters for example [111]. Ln-O-Se phases without a transition metal can lead to the structural role of the two anions of individual characters. A crystal structure that constitutes luorite-like $[Ln_4O_4]^{4+}$ oxide sheets is adopted by the "$Ln_4O_4Se_3$ (Ln = La–Nd, Eu–Er, Yb and Y)" family, and these sheets are constructed from

edge-linked Ln_4O tetrahedra and segregated by layers consisting of both Se^{2-} and diselenide Se_2^{2-} anions. The positioning of Se^{2-} and Se_2^{2-} anions in the interlayers differs with Ln^{3+} ionic radii, while the $[Ln_4O_4]^{4+}$ sheets are only slightly altered with Ln. For the "Ln = Gd, Tb and Dy" phases long-range range antiferromagnetic order occurs although has not been detected down to 1.8 K for other analogues. This family of materials consists of four compositions including "$A_{10}OSe_{14}$ (A = La–Nd), A_2OSe_2 (A = Pr, Gd), $A_4O_4Se_3$ (A = La–Nd, Sm) and A_2O_2Se (A = La, Pr, Nd, Sm, Gd, Er, Ho, Yb)" [103,112]. The discovery of β-$La_2O_2MSe_2$, a new structural family was discovered during the initial preparations of the ZrCuSiAs-related $La_2O_2MSe_2$ (M = Mn, Fe) phases. The "luorite-like $[Ln_2O_2]^{2+}$" layers are separated into ribbons and positioned in a herringbonelike fashion, in this β-structure, separating MSe_2 layers. The M(1) ions are coordinated by both O^{2-} and Se^{2-} anions in pseudo-octahedral coordination, while the M(2) site is approximately tetrahedral ($M(2)Se_4$) as a result of this β-structure. β-$La_2O_2MSe_2$ and $Ln_4O_4TiSe_4$ are very closely related with Ti^{4+} cations inhabiting only the M(1) sites in the $Ln_4O_4TiSe_4$ structure. The polymorphism and the tunability of the iron coordination environment with synthesis temperature of the "$Ln_2O_2FeSe_2$ (Ln = La, Ce)" systems has been shown by Nitsche [113]. Stripe-ordered ZrCuSiAs-related phases with tetrahedrally-coordinated Fe^{2+} ions are created at high temperatures. Intermediate temperatures give rise to β-phases consisting of both tetragonal and pseudo-octahedral Fe^{2+} coordination. A completely new phase which constitutes only pseudo-octahedral coordination of Fe^{2+} is formed at low temperatures [103]. Extensive studies in mixed anion materials have undertaken from the revelation of superconductivity at ~26 K in F-doped LaOFeAs. Lately structurally associated oxychalcogenides such as "$Bi_4O_4S_3$ (Tc up to 8.6 K), $LnO_{1-x}F_xBiS_2$ (Ln = La, Ce, Pr, Nd, Yb; Tc 1.9−4.5 K), and $LaO_{0.5}F_{0.5}BiSe_2$ (Tc 2.6 K)" have been reported to possess superconductivity. Apart from superconductivity, these oxychalcogenides possess other fascinating electronic, magnetic, and optical properties such as, LaCuOS being a wide band gap p-type semiconductor possessing an optical band gap of 3.1 eV which can be acceptor-doped to provide room-temperature conductivity up to 2.6×10^{-1} S cm^{-1}. The tetragonal ZrCuSiAs structure with space group P4/nmm, built using alternating layers of fluorite-like $[Ln_2O_2]^{2+}$ and anti-fluorite-like $[Cu_2Ch_2]^{2-}$ sheets, is adopted by both LaCuOS and analogous "LnOCuCh (Ln = La−Nd, Bi; Ch = S, Se, Te)" materials. Compounds affiliated with LnOCuCh possessing divalent transition metal ions have gained a lot of traction, as the divalency results in the half occupancy of the transition metal sites giving

$[MSe_2]^{2-}$ layers, which can possess an elaborate ordering. $Ce_2O_2MnSe_2$, the foremost of these materials, consists of an arbitrary 50% statistical occupancy of Mn on each site, retaining the tetragonal space group P4/nmm of LnOCuCh-type compounds. The $[FeSe_2]^{2-}$ layers in $Ce_2O_2FeSe_2$ contains one-dimensional chains of exclusively edgesharing (E, stripe-like) $FeSe_4$ tetrahedra, compared to $La_2O_2CdSe_2$ which has $[CdSe_2]^{2-}$ layers consisting of purely corner-sharing (C, checkerboard-like) $CdSe_4$ tetrahedra. $La_2O_2ZnSe_2$ can be regarded as a transitional structure between $Ce_2O_2FeSe_2$ and $La_2O_2CdSe_2$ as it contains $[ZnSe_2]^{2-}$ layers containing sections of both stripe-like edgesharing $ZnSe_4$ tetrahedra and checkerboard-like corner-sharing $ZnSe_4$ tetrahedra [114,115].

2.7.2 Synthetic strategies for cerium and iron oxyselenide production

The main synthetic strategy for the production of cerium and iron oxyselenides is by solid state reaction which involves; grounding stoichiometric mixture of reagents together then pressing them into pellets and placed together with an oxygen getter into a quartz tube. The tube is then sealed and heated to 1000 °C then kept for 12 h, once heated a bucket of iced water is used to quench the tube [105].

2.8 Doped kesterites

Doping is the act of changing properties such as electrical, charge transport or interface without manipulating the crystal structure and influencing the optical properties of the host material. Alloying is the act of isoelectronic cation substitution which introduces a mismatch of ionic sizes, which for absorber band engineering, is of significant interest. Using both, doping and alloying synthetic strategies is vital as both these strategies have been crucial for CIGS cells in order to reach their high efficiencies by utilizing alkali natured elements for doping and alloying with Ga for band grading. There are two groups of extrinsic dopants, isoelectronic dopants which are elements possessing oxidation states corresponding to the replaced matrix element; and non-isoelectronic dopants which are Group III elements, matching to the replaced matrix element and non-isoelectronic ones (e.g., Group III elements). The comparison of ionic radii of the matrix and doping elements makes use of Shannon's tables [116] to obtain the crystal (ionic) radii for the tetrahedral coordination [58,117]. Despite the kesterite materials having major potential for use in photovoltaics, their negative aspects such as their point defects and secondary phases impose major limitations on the material for photovoltaic applications. For procuring high-

efficiency devices, an off-stoichiometric composition is essential and the material should be copper-poor and zinc-rich. The general kesterite structure can achieve copper-poor and copper rich compositions, without influencing the structure, besides when it comes to cation distribution [64,65,118,119]. When a kesterite material is doped, its crystallinity and microstructure of the thin film may be tuned, especially the Cu poor and Zn rich films which are regarded to be the most efficient devices which possess reduced cation disorder during phase formation. An efficient method to obtain an adequate microstructure and optimum band gap is by altering the anionic ratio (S/Se). Factors that are limiting their practical usage are the difficulties in regulating the S/Se ratio during thermal annealing process. A method for improving the optoelectronic properties as well as controlling the stoichiometry to attain a suitable crystal phase is through cation substitution [120]. The idea of doping kesterite material is mainly due to the secondary phases that occur during the synthesis of kesterite materials, and the general champion efficiency of CZTSSe solar cells is still 12.6%, resulting from the large "V_{OC} deficit (E_g/q-V_{OC})" [61,98,121]. Some important approaches to minimize the high V_{OC}-deficit of kesterite absorber layer is by either post-deposition or doping of alkali and other associated metals such as Na, K, Cs, Rb, Li, etc, which can improve PCE by aiding in crystallization and decrease elemental disorder. Na doped kesterites have shown to have an enhanced V_{OC} and fill factor due to increased hole density and shifting the acceptor level near to conduction. The electronic properties of Na containing CZTSSe absorbers have been significantly modified with a probability of tuning the doping levels and gradients in order to amplify the collection of photogenerated carriers in thin film CZTSSe solar cells. The thermal activation energy is also lowered while the Fermi level is pulled towards the valance band causing a potential build up (V_{OC}) within the structure due to Na doping. The carrier concentration and grain size are also enhanced by Na doping [122–127]. Inspecting the structural, electronic and optical properties of Na doped CZTS, using the "generalized gradient approximated (GGA)" density functional as well as the "Hubbard U potential (GGA+U)", it's found that the occupancy of interstitial sites is favourable. Doping the kesterite material with both Na and Sb increases the power conversion efficiency up to 5.7% as well as reducing the disorder present in specific lattice positions by influencing the Cu and Sn sites [120,128,129]. When a kesterite superstrate solar cell is doped with lithium, its effective bandgap is altered, comparing this to the "TNR_CZTS device (Li 0 without CdS)", a recognizable variation in their spectral profiles can be seen and this is effect is due to the

integration of Cd into kesterite and the spontaneous formation of $Cu_2Zn_xCd_{1-x}SnS_4$ upon unnealing. There is also a positive effect on the CZTS absorber quality and the associated device performance due to Cd alloying [130,131]. Doping the kesterite material with Cd through an appropriate Zn/Cd ratio will increase the power conversion efficiency from 5.30% to 9.24%. Similarly, the magnetic ions can be doped in order to acquire a larger Seebeck coefficient, with a reduced thermal and improved electrical conductivity. Thus, doping the CZTS/Se with cations can enhance the crystallinity and efficiency [120,132,133]. It's a challenge to produce a $Cu_2ZnSn(S,Se)_4$ single phase, as it's a true quaternary crystal therefore various secondary phases exist. In the phase diagrams of sulphide and selenide kesterites, its predicted that within 1–2% (absolute) deviation in the composition, only a tiny existence region of single phase kesterite occurs, at growth temperatures around 550 °C. In order to minimize the cationic disorder in CZTSSe, essentially the Cu-Zn anti-site defects, isoelectronic cation substitution with larger or smaller ionic radius have been suggested [121,134]. A useful technique for enhancing the properties of kesterite thin films and solar cells is via cation substitution, where extrinsic ions can be used to substitute the Cu^+, Zn^{2+}, and Sn^{4+} ions in Cu_2ZnSnS_4. Doping the kesterite with Ag, leads to Ag occupying the Cu site in the Cu_2ZnSnS_4 lattice reducing, Cu_{Zn} anti-site and V_{Cu} defects which cause damage as a result of the formation energy of the Ag_{Zn} defect being greater than the formation energy of the Cu_{Zn} defect. Ag doping is also used to manipulate the band gap of kesterites. The kesterite absorption can also be increased through the complete or partial substitution of Zn by Cd, Fe, Mn, Mg, or Co, while reducing the "Cu_{Zn} anti-site defect and ZnS secondary phase", and enhancing the crystallinity and conversion efficiency of the Cu_2ZnSnS_4 thin-film solar cell [132,135–143]. Although for chalcopyrites, a Cu deficiency of 4% absolute at the growth temperature is allowed when looking at their phase diagrams. The determination of the stability region can be compared for chalcopyrites and kesterites based on total energy calculations. Under Cu-rich conditions in the chemical potential mSn–mZn diagram, the stability region of Cu_2ZnSnS_4 is about 1 eV long and 0.1 eV wide, while the stability region of $CuInSe_2$ is about 1 eV long but 0.5 eV wide. From this data its shown that the existence region of single phase kesterite compared to the chalcopyrites is much smaller [144]. As it's been shown that chalcogenides possess a greater percentage of single phases than kesterites, it is hypothesized that doping the kesterite material with the chalcopyrite;

cerium and iron oxyselenide, could potentially overcome the issue of secondary phases and potentially tackle the issue of the point defects in the kesterite material.

References:

[1]   K. Vozel, Solar Cells, in: Semin. -1st Year, 2nd Cycle Sol. Cells, Ljubljana, 2011: p. 15. https://www.yumpu.com/s/OIddAW4rZ0w3j4nP.

[2]   J. Nelson, The physics of solar cells, Energy. 21 (2003). doi:10.1142/p276.

[3]   X. Zhang, Y.S. Ang, Z. Ye, S. Su, J. Chen, L.K. Ang, Three-terminal heterojunction bipolar transistor solar cells with non-ideal effects: Efficiency limit and parametric optimum selection, Energy Convers. Manag. 188 (2019) 112–119. doi:10.1016/j.enconman.2019.03.034.

[4]   J.R.L. Mariano, Y.C. Lin, M. Liao, H. Ay, Analysis of power generation for solar photovoltaic module with various internal cell spacing, Sustain. 13 (2021). doi:10.3390/su13116364.

[5]   W. Shockley, H.J. Queisser, Detailed balance limit of efficiency of p-n junction solar cells, J. Appl. Phys. 32 (1961) 510–519. doi:10.1063/1.1736034.

[6]   L. Burton, Phase Stability and Composition of Tin Sulfide for Thin-Film Solar Cells, University of Bath, 2014. http://opus.bath.ac.uk/43937/1/Transfer.pdf.

[7]   A. Mohammad Bagher, Types of Solar Cells and Application, Am. J. Opt. Photonics. 3 (2015) 94. doi:10.11648/j.ajop.20150305.17.

[8]   A. Zekry, A. Shaker, M. Salem, Solar Cells and Arrays: Principles, Analysis, and Design, in: Adv. Renew. Energies Power Technol., 2018: pp. 3–56. doi:10.1016/B978-0-12-812959-3.00001-0.

[9]   J.L. Gray, The Physics of the Solar Cell, Handb. Photovolt. Sci. Eng. (2011) 82–129. doi:10.1002/9780470974704.ch3.

[10]   D. Dexter, R. Knox, M. Stavola, Electron-hole pair excitation in semiconductors via energy transfer from an external sensitizer, Phys. Rev. B. 31 (1985) 2277–2289. doi:10.1017/CBO9781107415324.004.

[11]   A. Goetzberger, V.U. Hoffmann, Photovoltaic Solar Energy Generation. Series: Springer Series in Optical Sciences, 2005.

[12]   N. Guerra, M. Guevara, C. Palacios, F. Crupi, Operation and physics of photovoltaic solar cells: an overview, I+D Tecnológico. 14 (2018) 84–95. doi:10.33412/idt.v14.2.2077.

[13]   S.S. Garcia N., Damask A., Semiconductor Devices, Phys. Comput. Sci. Students. (1998). doi:doi.org/10.1007/978-1-4612-1616-2_26.

[14]   H. Gerischer, Effects of Electronic Excitation on Reaction Rates at the Solid-Electrolyte Interface, Isr. J. Chem. 14 (1975) 138–153. doi:10.1002/ijch.197500054.

[15]   T.M. Razykov, C.S. Ferekides, D. Morel, E. Stefanakos, H.S. Ullal, H.M. Upadhyaya, Solar photovoltaic electricity: Current status and future prospects, Sol. Energy. 85 (2011) 1580–1608. doi:10.1016/j.solener.2010.12.002.

[16]   S.B. Adejuyigbe, B.O. Bolaji, M.U. Olanipekun, M.R. Adu, Development of a solar photovoltaic power system to generate electricity for office appliances, Eng. J. 17 (2013) 29–39. doi:10.4186/ej.2013.17.1.29.

[17]   Joshua M. Pearce, Photovoltaics – a Path to Sustainable Futures, Sci. Technol. Soc. Progr. 34 (2002) 1–2. doi:10.1016/S0016-3287(02)00008-3.

[18]   N. Shankarappa, M. Ahmed, N. Shashikiran, H. Naganagouda, Solar Photovoltaic Systems – Applications & Configurations, Int. Res. J. Eng. Technol. 4 (2017) 1851–1855. https://irjet.net/archives/V4/i8/IRJET-V4I8327.pdf.

[19]   G. Ofualagba, Photovoltaic technology, applications and market, IEEE Power Energy Soc. 2008 Gen. Meet. Convers. Deliv. Electr. Energy 21st Century, PES. (2008). doi:10.1109/PES.2008.4596218.

[20]   M.T. Kibria, A. Ahammed, S.M. Sony, F. Hossain, A Review: Comparative studies on different generation solar cells technology, in: Int. Conf. Environ. Asp. Bangladesh, 2014: pp. 51–53.

[21]   M.A. Green, Recent developments in photovoltaics, Sol. Energy. 76 (2004) 3–8. doi:10.1016/S0038-092X(03)00065-3.

[22]   T. Dey, Role of earth-abundant selenium in different types of solar cells, J. Electr. Eng. 72 (2021) 132–139. doi:10.2478/jee-2021-0019.

[23]   F. Akarslan, Photovoltaic Systems and Applications, in: D.A. Şencan (Ed.), Model. Optim.   Renew.   Energy   Syst.,   InTech,   2012. https://cdn.intechopen.com/pdfs/36830/InTech-Photovoltaic_systems_and_applications.pdf.

[24]   O.A. Abdulrazzaq, V. Saini, S. Bourdo, E. Dervishi, A.S. Biris, Organic solar cells: A review of materials, limitations, and possibilities for improvement, Part. Sci. Technol. 31 (2013) 427–442. doi:10.1080/02726351.2013.769470.

[25]   Y.J. Lee, B.S. Kim, S.M. Ifitiquar, C. Park, J. Yi, Silicon solar cells: Past, present and the future, J. Korean Phys. Soc. 65 (2014) 355–361. doi:10.3938/jkps.65.355.

[26]   R.A. Deshpande, Advances in Solar Cell Technology: An Overview, J. Sci. Res. 65 (2021) 72–75. doi:10.37398/jsr.2021.650214.

[27]   Y. Tang, Copper Indium Gallium Selenide Thin Film Solar Cells, Nanostructured Sol. Cells. (2017). doi:10.5772/65291.

[28]   J. Ramanujam, U.P. Singh, Copper indium gallium selenide based solar cells - A review, Energy Environ. Sci. 10 (2017) 1306–1319. doi:10.1039/c7ee00826k.

[29]   Mahfouz Saeed, Electrochemical fabrication of thin film photovoltaic devices (CIGS   &   CIGSS),   Case   Western   Reserve   University,   2014. https://etd.ohiolink.edu/apexprod/rws_etd/send_file/send?accession=case1396265882&disposition=inline.

[30]   S.K. Wallace, D.B. Mitzi, A. Walsh, The Steady Rise of Kesterite Solar Cells, ACS Energy Lett. 2 (2017) 776–779. doi:10.1021/acsenergylett.7b00131.

[31]   K. Ranabhat, L. Patrikeev, A.A. evna Revina, K. Andrianov, V. Lapshinsky, E. Sofronova, An introduction to solar cell technology, J. Appl. Eng. Sci. 14 (2016) 481–491. doi:10.5937/jaes14-10879.

[32]   P. Jackson, New world record efficiency for $Cu(In,Ga)Se_2$ thin-film solar cells beyond 20%, Prog. PHOTOVOLTAICS Res. Appl. (2011) 894–897. doi:10.1002/pip.1078.

[33]   F. Jellinek, Transition metal chalcogenides. relationship between chemical composition, crystal structure and physical properties, React. Solids. 5 (1988) 323–339. doi:10.1016/0168-7336(88)80031-7.

[34]   V.K. Prokudina, Chalcogenides, Concise Encycl. Self-Propagating High-Temperature Synth. (2017) 61–64. doi:10.1016/b978-0-12-804173-4.00026-0.

[35]   M.L. Tejaswini, K.P. Lakshmi, Study of Chalcogenides –Properties and its Applications, in: 2015: pp. 477–483. doi:10.3850/978-981-09-6200-5_d-49.

[36]   M.N. Tahir, J.K. Sahoo, F. Hoshyargar, W. Tremel, Growth Mechanism and Surface Functionalization of Metal Chalcogenides Nanostructures, 2014. doi:10.1002/9781119008934.ch5.

[37]   A.K. Dasadia, Chapter 1 Introduction and Existing Information about Transition Metal Chalcogenides, in: 2013: pp. 1–21.

[38]   S. Schorr, The crystal structure of kesterite type compounds: A neutron and X-ray diffraction study, Sol. Energy Mater. Sol. Cells. 95 (2011) 1482–1488. doi:10.1016/j.solmat.2011.01.002.

[39]   E.A. Lund, M.A. Scarpulla, Modeling Cu_2ZnSnS_4 (CZTS) solar cells with kesterite and stannite phase variation, Physics, Simulation, Photonic Eng. Photovolt. Devices II. 8620 (2013) 862015. doi:10.1117/12.2012401.

[40]   H. Du, F. Yan, M. Young, B. To, C.S. Jiang, P. Dippo, D. Kuciauskas, Z. Chi, E.A. Lund, C. Hancock, W.M. Hlaing Oo, M.A. Scarpulla, G. Teeter, Investigation of combinatorial coevaporated thin film Cu_2ZnSnS_4. I. Temperature effect, crystalline phases, morphology, and photoluminescence, J. Appl. Phys. 115 (2014). doi:10.1063/1.4871664.

[41]   S. Chen, A. Walsh, X.G. Gong, S.H. Wei, Classification of lattice defects in the kesterite Cu_2ZnSnS_4 and $Cu_2ZnSnSe_4$ earth-abundant solar cell absorbers, Adv. Mater. 25 (2013) 1522–1539. doi:10.1002/adma.201203146.

[42]   D.O. Oseguera-galindo, The Path to Improve Kesterite Solar Cell Efficiency Minireview The Path to Improve Kesterite Solar Cell Efficiency, (2018). doi:10.21127/yaoyigc20180015.

[43]   S. Schorr, G. Gurieva, M. Guc, M. Dimitrievska, A. Pérez-Rodríguez, V. Izquierdo-Roca, C.S. Schnohr, J. Kim, W. Jo, J.M. Merino, Point defects, compositional fluctuations, and secondary phases in non-stoichiometric kesterites, J. Phys. Energy. 2 (2019) 012002. doi:10.1088/2515-7655/ab4a25.

[44]   G. Gurieva, M. Dimitrievska, S. Zander, A. Pérez-Rodríguez, V. Izquierdo-Roca, S. Schorr, Structural characterisation of $Cu_{2.04}Zn_{0.91}Sn_{1.05}S_{2.08}Se_{1.92}$, Phys. Status Solidi Curr. Top. Solid State Phys. 12 (2015) 588–591. doi:10.1002/pssc.201400307.

[45]   R. Gunder, J.A. Márquez-Prieto, G. Gurieva, T. Unold, S. Schorr, Structural characterization of off-stoichiometric kesterite-type $Cu_2ZnGeSe_4$ compound semiconductors: From cation distribution to intrinsic point defect density, CrystEngComm. 20 (2018) 1491–1498. doi:10.1039/c7ce02090b.

[46]   S. Giraldo, Z. Jehl, M. Placidi, V. Izquierdo-Roca, A. Pérez-Rodríguez, E. Saucedo, Progress and Perspectives of Thin Film Kesterite Photovoltaic Technology: A Critical Review, Adv. Mater. 31 (2019). doi:10.1002/adma.201806692.

[47]   V. Bermudez, A. Perez-Rodriguez, Understanding the cell-to-module efficiency gap in $Cu(In,Ga)(S,Se)_2$ photovoltaics scale-up, Nat. Energy. 3 (2018) 466–475. doi:10.1038/s41560-018-0177-1.

[48]   S. Hall, Kesterite, $Cu_2(Zn,Fe)SnS_4$, and stannite, $Cu_2(Fe,Zn)SnS_4$, structurally similar but distinct minerals, Can. Mineral. 16 (1978) 131–137. http://canmin.geoscienceworld.org/content/16/2/131.short.

[49]   S. Delbos, Kësterite thin films for photovoltaics: a review, EPJ Photovoltaics. 3 (2012) 35004. doi:10.1051/epjpv/2012008.

[50]   S. Josefin, Y. Ming, Cu_2ZnSnS_4 Nanoparticle Absorber Layers for Thin-Film Solar Cells, Technical University of Denmark, 2016. https://orbit.dtu.dk/en/publications/cu2znsns4-nanoparticle-absorber-layers-for-thin-film-solar-cells.

[51]   N. Kattan, B. Hou, D.J. Fermín, D. Cherns, Crystal structure and defects visualization of Cu_2ZnSnS_4 nanoparticles employing transmission electron microscopy and electron diffraction, Appl. Mater. Today. 1 (2015) 52–59. doi:10.1016/j.apmt.2015.08.004.

[52]   M. Dimitrievska, F. Boero, A.P. Litvinchuk, S. Delsante, G. Borzone, A. Perez-Rodriguez, V. Izquierdo-Roca, Structural Polymorphism in "Kesterite" Cu_2ZnSnS_4: Raman Spectroscopy and First-Principles Calculations Analysis, Inorg. Chem. 56 (2017) 3467–3474. doi:10.1021/acs.inorgchem.6b03008.

[53]   S.P. Ramkumar, Y. Gillet, A. Miglio, M.J. Van Setten, X. Gonze, G.M. Rignanese, First-principles investigation of the structural, dynamical, and dielectric properties of kesterite, stannite, and PMCA phases of Cu_2ZnSnS_4, Phys. Rev. B. 94 (2016) 1–10. doi:10.1103/PhysRevB.94.224302.

[54]   S. Chen, X.G. Gong, A. Walsh, S.H. Wei, Defect physics of the kesterite thin-film solar cell absorber Cu_2ZnSnS_4, Appl. Phys. Lett. 96 (2010) 8–10. doi:10.1063/1.3275796.

[55]   J. Kim, L. Larina, S.Y. Chung, D. Shin, B. Shin, Atomistic consideration of earth-abundant chalcogenide materials for photovoltaics: Kesterite and beyond, J. Mater. Res. 33 (2018) 3986–3998. doi:10.1557/jmr.2018.350.

[56]   P. Xu, S. Chen, B. Huang, H.J. Xiang, X.G. Gong, S.H. Wei, Stability and electronic structure of Cu_2ZnSnS_4 surfaces: First-principles study, Phys. Rev. B - Condens. Matter Mater. Phys. 88 (2013) 1–8. doi:10.1103/PhysRevB.88.045427.

[57]   M. Kumar, A. Dubey, N. Adhikari, S. Venkatesan, Q. Qiao, Strategic review of secondary phases, defects and defect-complexes in kesterite CZTS-Se solar cells, Energy Environ. Sci. 8 (2015) 3134–3159. doi:10.1039/c5ee02153g.

[58]   Y.E. Romanyuk, S.G. Haass, S. Giraldo, M. Placidi, D. Tiwari, D.J. Fermin, X. Hao, H. Xin, T. Schnabel, M. Kauk-Kuusik, P. Pistor, S. Lie, L.H. Wong, Doping and alloying of kesterites, J. Phys. Energy. 1 (2019) 044004. doi:10.1088/2515-7655/ab23bc.

[59]   S. Giraldo, M. Neuschitzer, T. Thersleff, S. Lõpez-Marino, Y. Sánchez, H. Xie, M. Colina, M. Placidi, P. Pistor, V. Izquierdo-Roca, K. Leifer, A. Pérez-Rodríguez, E. Saucedo, Large Efficiency Improvement in $Cu_2ZnSnSe_4$ Solar Cells by Introducing a Superficial Ge Nanolayer, Adv. Energy Mater. 5 (2015) 1–6. doi:10.1002/aenm.201501070.

[60]   M. Ritzer, S. Schönherr, P. Schöppe, W. Wisniewski, S. Giraldo, G. Gurieva, A. Johannes, C.T. Plass, K. Ritter, G. Martínez-Criado, S. Schorr, E. Saucedo, C. Ronning, C.S. Schnohr, On the Germanium Incorporation in $Cu_2ZnSnSe_4$ Kesterite Solar Cells Boosting Their Efficiency, ACS Appl. Energy Mater. 3 (2020) 558–564. doi:10.1021/acsaem.9b01784.

[61]   J. Li, D. Wang, X. Li, Y. Zeng, Y. Zhang, Cation Substitution in Earth-Abundant Kesterite Photovoltaic Materials, Adv. Sci. 5 (2018). doi:10.1002/advs.201700744.

[62]   M. Salvador, S.M. Vorpahl, H. Xin, W. Williamson, G. Shao, D.U. Karatay, H.W. Hillhouse, D.S. Ginger, Nanoscale surface potential variation correlates with local S/Se ratio in solution-processed CZTSSe solar cells, Nano Lett. 14 (2014) 6926–6930. doi:10.1021/nl503068h.

[63]   S. Bourdais, C. Choné, B. Delatouche, A. Jacob, G. Larramona, C. Moisan, A. Lafond, F. Donatini, G. Rey, S. Siebentritt, A. Walsh, G. Dennler, Is the Cu/Zn Disorder the Main Culprit for the Voltage Deficit in Kesterite Solar Cells?, Adv. Energy Mater. 6 (2016) 1–21. doi:10.1002/aenm.201502276.

[64]   V. Trifiletti, Kesterite Solar Cells, Mod. Concepts Mater. Sci. 1 (2019) 3–6. doi:https://irispublishers.com/mcms/pdf/MCMS.MS.ID.000524.pdf.

[65]   K. Ito, Copper Zinc Tin Sulfide-Based Thin-Film Solar Cells, 1st ed., 2015 John Wiley & Sons, Ltd Registered, 2015. doi:10.1002/9781118437865.

[66]   G.K. Gupta, V.R. Reddy, A. Dixit, Impact of excess and disordered Sn sites on Cu_2ZnSnS_4 absorber material and device performance: A 119 Sn Mössbauer study, Mater. Chem. Phys. 225 (2019) 410–416. doi:10.1016/j.matchemphys.2018.12.078.

[67]   S. Chen, L.W. Wang, A. Walsh, X.G. Gong, S.H. Wei, Abundance of CuZn+ SnZn and 2CuZn +Sn Zn defect clusters in kesterite solar cells, Appl. Phys. Lett. 101 (2012) 1–5. doi:10.1063/1.4768215.

[68]   K. Biswas, S. Lany, A. Zunger, The electronic consequences of multivalent elements in inorganic solar absorbers: Multivalency of Sn in Cu_2ZnSnS_4, Appl. Phys. Lett. 96 (2010) 2012–2015. doi:10.1063/1.3427433.

[69]   S. Kim, J.S. Park, A. Walsh, Identification of Killer Defects in Kesterite Thin-Film Solar Cells, ACS Energy Lett. 3 (2018) 496–500. doi:10.1021/acsenergylett.7b01313.

[70]   K. Biswas, S. Lany, A. Zunger, The electronic consequences of multivalent elements in inorganic solar absorbers: Multivalency of Sn in Cu_2ZnSnS_4, Appl. Phys. Lett. 96 (2010) 2–5. doi:10.1063/1.3427433.

[71]   D. Han, Y.Y. Sun, J. Bang, Y.Y. Zhang, H.B. Sun, X. Bin Li, S.B. Zhang, Deep electron traps and origin of p-type conductivity in the earth-abundant solar-cell material Cu_2ZnSnS_4, Phys. Rev. B - Condens. Matter Mater. Phys. 87 (2013) 2–7. doi:10.1103/PhysRevB.87.155206.

[72]   S. Chen, J.H. Yang, X.G. Gong, A. Walsh, S.H. Wei, Intrinsic point defects and complexes in the quaternary kesterite semiconductor Cu_2ZnSnS_4, Phys. Rev. B - Condens. Matter Mater. Phys. 81 (2010). doi:10.1103/PhysRevB.81.245204.

[73]   A. Walsh, S. Chen, S.H. Wei, X.G. Gong, Kesterite thin-film solar cells: Advances in materials modelling of Cu_2ZnSnS_4, Adv. Energy Mater. 2 (2012) 400–409. doi:10.1002/aenm.201100630.

[74]   L. Choubrac, Stability domain of the selenide kesterite photovoltaic materials and NMR investigation of Cu/Zn disorder in $Cu_2ZnSnSe_4$ (CZTSe), Phys. Chem. Chem. Phys. 17 (2015). doi:10.1039/C5CP01709B.

[75]   H. Katagiri, K. Jimbo, M. Tahara, H. Araki, K. Oishi, The influence of the composition ratio on CZTS-based thin film solar cells Hironori Katagiri, Kazuo Jimbo, Masami Tahara, Hideaki Araki and Koichiro Oishi Nagaoka National College of Technology, 888 Nishikatakai, Nagaoka, Niigata 940-8532, Japan, Mater. Res. Soc. Symp. Proc. Vol. 1165. 1165 (2009) 1165-M04-01. doi:10.1016/j.solmat.2011.05.050.

[76]   D. Jiang, Y. Zhang, Y. Sui, W. He, Z. Wang, L. Yang, F. Wang, B. Yao, Investigation on the selenization treatment of kesterite $Cu_2Mg_{0.2}Zn_{0.8}Sn(S,Se)_4$ films for solar cell, Nanomaterials. 9 (2019). doi:10.3390/nano9070946.

[77]   Z.Y. Xiao, B. Yao, Y.F. Li, Z.H. Ding, Z.M. Gao, H.F. Zhao, L.G. Zhang, Z.Z. Zhang, Y.R. Sui, G. Wang, Influencing Mechanism of the Selenization Temperature and Time on the Power Conversion Efficiency of $Cu_2ZnSn(S,Se)_4$-Based Solar Cells, ACS Appl. Mater. Interfaces. 8 (2016) 17334–17342. doi:10.1021/acsami.6b05201.

[78]   J.J. Scragg, T. Ericson, T. Kubart, M. Edo, C. Platzer-bj, Chemical Insights into the Instability of Cu_2ZnSnS_4 Films during.pdf, (2011) 4625–4633.

[79]   T. Ratz, G. Brammertz, R. Caballero, M. León, S. Canulescu, J. Schou, L. Gütay, D. Pareek, T. Taskesen, D.-H. Kim, J.-K. Kang, C. Malerba, A. Redinger, E. Saucedo, B. Shin, H. Tampo, K. Timmo, N.D. Nguyen, B. Vermang, Physical routes for the synthesis of kesterite, J. Phys. Energy. 1 (2019) 042003. doi:10.1088/2515-7655/ab281c.

[80]   C. Zhang, J. Zhong, J. Tang, $Cu_2ZnSn(S,Se)_4$ thin film solar cells fabricated with benign solvents, Front. Optoelectron. 8 (2015) 252–268. doi:10.1007/s12200-015-0539-2.

[81]   Z. Shi, A.H. Jayatissa, One-pot hydrothermal synthesis and fabrication of kesterite $Cu_2ZnSn(S,Se)_4$ thin films, Prog. Nat. Sci. Mater. Int. 27 (2017) 550–555. doi:10.1016/j.pnsc.2017.09.006.

[82]   H. Dong, T. Schnabel, E. Ahlswede, C. Feldmann, Polyol-mediated synthesis of $Cu_2ZnSn(S,Se)_4$ kesterite nanoparticles and their use in thin-film solar cells, Solid State Sci. 29 (2014) 52–57. doi:10.1016/j.solidstatesciences.2014.01.006.

[83]   Y.L. Zhou, W.H. Zhou, Y.F. Du, M. Li, S.X. Wu, Sphere-like kesterite Cu_2ZnSnS_4 nanoparticles synthesized by a facile solvothermal method, Mater. Lett. 65 (2011) 1535–1537. doi:10.1016/j.matlet.2011.03.013.

[84]   S. Chatterjee, A.J. Pal, A solution approach to p-type Cu_2FeSnS_4 thin-films and pn-junction solar cells: Role of electron selective materials on their performance, Sol. Energy Mater. Sol. Cells. 160 (2017) 233–240. doi:10.1016/j.solmat.2016.10.037.

[85]   A.G. Kannan, T.E. Manjulavalli, J. Chandrasekaran, Influence of Solvent on the Properties of CZTS Nanoparticles, Procedia Eng. 141 (2016) 15–22. doi:10.1016/j.proeng.2015.08.1112.

[86]   A. Sharmin, M.S. Bashar, M. Sultana, S.M.M. Al Mamun, Sputtered single-phase kesterite Cu_2ZnSnS_4 (CZTS) thin film for photovoltaic applications: Post annealing parameter optimization and property analysis, AIP Adv. 10 (2020). doi:10.1063/1.5129202.

[87]   H. Sai, T. Matsui, T. Koida, K. Matsubara, M. Kondo, S. Sugiyama, H. Katayama, Y. Takeuchi, I. Yoshida, Triple-junction thin-film silicon solar cell fabricated on periodically textured substrate with a stabilized efficiency of 13.6%, Appl. Phys. Lett. 106 (2015) 30–34. doi:10.1063/1.4921794.

[88]   M.A. Green, Y. Hishikawa, W. Warta, E.D. Dunlop, D.H. Levi, J. Hohl-Ebinger, A.W.H. Ho-Baillie, Solar cell efficiency tables (version 50), Prog. Photovoltaics Res. Appl. 25 (2017) 668–676. doi:10.1002/pip.2909.

[89]   A. Haddout, A. Raidou, M. Fahoume, A review on the numerical modelling of CdS/CZTS-based solar cells, Appl. Phys. A Mater. Sci. Process. 125 (2019) 1–16. doi:10.1007/s00339-019-2413-3.

[90]   A. Kowsar, M. Rahaman, M.S. Islam, A.Y. Imam, S.C. Debnath, M. Sultana, M.A. Hoque, A. Sharmin, Z.H. Mahmood, S.F.U. Farhad, Progress in major thin-film solar cells: Growth technologies, layer materials and efficiencies, Int. J. Renew. Energy Res. 9 (2019) 579–597.

[91]   T. Moyo, J. Petersen, Study of the dissolution of chalcopyrite in solutions of different ammonium salts, J. South. African Inst. Min. Metall. 116 (2016) 509–516. doi:10.17159/2411-9717/2016/v116n6a4.

[92]   R. Klenk, Chalcopyrite solar cells and modules, Springer Ser. Mater. Sci. 104 (2008) 415–437. doi:10.1007/978-3-540-73612-7_9.

[93]   J. Reichardt, M. Bär, A. Grimm, I. Kötschau, I. Lauermann, S. Sokoll, M.C. Lux-Steiner, C.H. Fischer, C. Heske, L. Weinhardt, O. Fuchs, C. Jung, W. Gudat, T.P. Niesen, F. Karg, Inducing and monitoring photoelectrochemical reactions at surfaces and buried interfaces in $Cu(In,Ga)(S,Se)_2$ thin-film solar cells, Appl. Phys. Lett. 86 (2005) 1–3. doi:10.1063/1.1906309.

[94]   S. Ishizuka, $CuGaSe_2$ Thin Film Solar Cells: Challenges for Developing Highly Efficient Wide-Gap Chalcopyrite Photovoltaics, Phys. Status Solidi Appl. Mater. Sci. 216 (2019) 1–9. doi:10.1002/pssa.201800873.

[95]   K. Takuya, $Cu(In,Ga)(Se,S)_2$ solar cell research in Solar Frontier : Progress and current status temperatures, Jpn. J. Appl. Phys. 56 (2017) 1. http://stacks.iop.org/1347-4065/56/i=4S/a=04CA02.

[96]   T. Unold, C.A. Kaufmann, Chalcopyrite thin-film materials and solar cells, 1st ed., Elsevier Ltd., Berlin, 2012. doi:10.1016/B978-0-08-087872-0.00121-9.

[97]   K.J. Yang, J.H. Sim, D.H. Son, D.H. Jeon, D.K. Hwang, D. Nam, H. Cheong, S.Y. Kim, J.H. Kim, D.H. Kim, J.K. Kang, Comparison of chalcopyrite and kesterite thin-film solar cells, J. Ind. Eng. Chem. 45 (2017) 78–84. doi:10.1016/j.jiec.2016.09.005.

[98]   W. Wang, M.T. Winkler, O. Gunawan, T. Gokmen, T.K. Todorov, Y. Zhu, D.B. Mitzi, Device characteristics of CZTSSe thin-film solar cells with 12.6% efficiency, Adv. Energy Mater. 4 (2014) 1–5. doi:10.1002/aenm.201301465.

[99]   C. Wadia, A.P. Alivisatos, D.M. Kammen, Materials availability expands the opportunity for large-scale photovoltaics deployment, Environ. Sci. Technol. 43 (2009) 2072–2077. doi:10.1021/es8019534.

[100] D.B. Mitzi, O. Gunawan, T.K. Todorov, A.R.D. Barkhouse, Prospects and performance limitations for Cu-Zn-Sn-S-Se photovoltaic Technology, Philos. Trans. R. Soc. A Math. Phys. Eng. Sci. 371 (2013). doi:10.1098/rsta.2011.0432.

[101] O.K. Simya, B. Geetha Priyadarshini, K. Balachander, A.M. Ashok, Formation of a phase pure kesterite CZTSe thin films using multisource hybrid physical vapour deposition, Mater. Res. Express. 7 (2020). doi:10.1088/2053-1591/ab64ee.

[102] I. Repins, N. Vora, C. Beall, S.H. Wei, F. Yan, M. Romero, G. Teeter, H. Du, B. To, M. Young, R. Noufi, Kesterites and chalcopyrites: A comparison of close cousins, Mater. Res. Soc. Symp. Proc. 1324 (2012) 97–108. doi:10.1557/opl.2011.844.

[103] C. Stock, E.E. McCabe, The magnetic and electronic properties of oxyselenides - Influence of transition metal ions and lanthanides, J. Phys. Condens. Matter. 28 (2016) 1–35. doi:10.1088/0953-8984/28/45/453001.

[104] E.E. McCabe, D.G. Free, J.S.O. Evans, A new iron oxyselenide $Ce_2O_2FeSe_2$: Synthesis and characterisation, Chem. Commun. 47 (2011) 1261–1263. doi:10.1039/c0cc03477k.

[105] E.E. McCabe, A.S. Wills, L. Chapon, P. Manuel, J.S.O. Evans, Structural and magnetic characterisation of iron oxyselenides $Ce_2O_2Fe_2OSe_2$ and $Nd_2O_2Fe_2OSe_2$, Phys. Rev. (2014). http://arxiv.org/abs/1410.4990.

[106] A. Marcinkova, T.C. Hansen, J.W.G. Bos, Iron spin-reorientation transition in NdFeAsO, J. Phys. Condens. Matter. 24 (2012) 3–7. doi:10.1088/0953-8984/24/25/256007.

[107] J. Zhang, Q. Tan, W. Li, H. Kim, Magnetic structures and interplay between rare earth Ce and Fe magnetism in single-crystal CeFeAsO, (2013) 1–11.

[108] O. V. Gornostaeva, K. V. Lamonova, S.M. Orel, Y.G. Pashkevich, Magnetic properties of Ce3+ ion in iron-containing oxypnictide CeFeAsO, Low Temp. Phys. 39 (2013) 343–350. doi:10.1063/1.4801990.

[109]   S. V. Krivovichev, O. Mentré, O.I. Siidra, M. Colmont, S.K. Filatov, Anion-centered tetrahedra in inorganic compounds, Chem. Rev. 113 (2013) 6459–6535. doi:10.1021/cr3004696.

[110]   C.H. Wang, C.M. Ainsworth, S.D. Champion, G.A. Stewart, M.C. Worsdale, T. Lancaster, S.J. Blundell, H.E.A. Brand, J.S.O. Evans, Crystal structure and magnetic modulation in β-$Ce_2O_2FeSe_2$, Phys. Rev. Mater. 1 (2017). doi:10.1103/PhysRevMaterials.1.034403.

[111]   D.G. Free, N.D. Withers, P.J. Hickey, J.S.O. Evans, Synthesis, structure and properties of several new oxychalcogenide materials with the general formula $A_2O_2M_2OSe_2$ (A = La-Sm, M = Fe, Mn), Chem. Mater. 23 (2011) 1625–1635. doi:10.1021/cm1035453.

[112]   A.J. Tuxworth, C.H. Wang, J.S.O. Evans, Synthesis, characterisation and properties of rare earth oxyselenides $A_4O_4Se_3$ (A = Eu, Gd, Tb, Dy, Ho, Er, Yb and Y), Dalt. Trans. 44 (2015) 3009–3019. doi:10.1039/c4dt03336a.

[113]   F. Nitsche, R. Niklaus, D. Johrendt, New Polymorphs of RE $_2FeSe_2O_2$ (RE = La, Ce), Zeitschrift Fur Anorg. Und Allg. Chemie. 640 (2014) 2897–2902. doi:10.1002/zaac.201400371.

[114]   C.M. Ainsworth, C.H. Wang, M.G. Tucker, J.S.O. Evans, Synthesis, structural characterization, and physical properties of the new transition metal oxyselenide $Ce_2O_2ZnSe_2$, Inorg. Chem. 54 (2015) 1563–1571. doi:10.1021/ic502551n.

[115]   A. Krzton-Maziopa, Z. Guguchia, E. Pomjakushina, V. Pomjakushin, R. Khasanov, H. Luetkens, P.K. Biswas, A. Amato, H. Keller, K. Conder, Superconductivity in a new layered bismuth oxyselenide: $LaO_{0.5}F_{0.5}BiSe_2$, J. Phys. Condens. Matter. 26 (2014) 1–6. doi:10.1088/0953-8984/26/21/215702.

[116]   R.D. Shannon, Revised Effective Ionic Radii and Systematic Studies of Interatomie Distances in Halides and Chalcogenides, Acta Crystallogr. 32 (1976) 751–767. doi:10.1107/s0567739476001551.

[117]   T. Feurer, P. Reinhard, E. Avancini, B. Bissig, J. Löckinger, P. Fuchs, R. Carron, T.P. Weiss, J. Perrenoud, S. Stutterheim, S. Buecheler, A.N. Tiwari, Progress in thin film CIGS photovoltaics – Research and development, manufacturing, and applications, Prog. Photovoltaics Res. Appl. 25 (2017) 645–667. doi:10.1002/pip.2811.

[118]   H. Katagiri, N. Sasaguchi, S. Hando, S. Hoshino, J. Ohashi, T. Yokota, Preparation and evaluation of Cu_2ZnSnS_4 thin films by sulfurization of E-B evaporated precursors, Sol. Energy Mater. Sol. Cells. 49 (1997) 407–414. doi:10.1016/S0927-0248(97)00119-0.

[119]   L.E. Valle Rios, K. Neldner, G. Gurieva, S. Schorr, Existence of off-stoichiometric single phase kesterite, J. Alloys Compd. 657 (2016) 408–413. doi:10.1016/j.jallcom.2015.09.198.

[120]   M. V. Jyothirmai, H. Saini, N. Park, R. Thapa, Screening of suitable cationic dopants for solar absorber material CZTS/Se: A first principles study, Sci. Rep. 9 (2019) 1–12. doi:10.1038/s41598-019-52410-3.

[121]   X. Li, Z. Hou, S. Gao, Y. Zeng, J. Ao, Z. Zhou, B. Da, W. Liu, Y. Sun, Y. Zhang, Efficient Optimization of the Performance of Mn2+-Doped Kesterite Solar Cell: Machine Learning Aided Synthesis of High Efficient $Cu_2(Mn,Zn)Sn(S,Se)_4$ Solar Cells, Sol. RRL. 2 (2018) 1–8. doi:10.1002/solr.201800198.

[122]   D.S. Dhawale, A. Ali, A.C. Lokhande, Impact of various dopant elements on the properties of kesterite compounds for solar cell applications: A status review, Sustain. Energy Fuels. 3 (2019) 1365–1383. doi:10.1039/c9se00040b.

[123]   G. Rey, F. Babbe, T.P. Weiss, H. Elanzeery, M. Melchiorre, N. Valle, B. El Adib, S. Siebentritt, Post-deposition treatment of $Cu_2ZnSnSe_4$ with alkalis, Thin Solid Films. 633 (2017) 162–165. doi:10.1016/j.tsf.2016.11.021.

[124]   Y.T. Hsieh, Q. Han, C. Jiang, T. Bin Song, H. Chen, L. Meng, H. Zhou, Y. Yang, Efficiency Enhancement of $Cu_2ZnSn(S,Se)_4$ Solar Cells via Alkali Metals Doping, Adv. Energy Mater. 6 (2016) 1–6. doi:10.1002/aenm.201502386.

[125] S.G. Haass, C. Andres, R. Figi, C. Schreiner, M. Bürki, A.N. Tiwari, Y.E. Romanyuk, Effects of potassium on kesterite solar cells: Similarities, differences and synergies with sodium, AIP Adv. 8 (2018). doi:10.1063/1.5013114.

[126] U. Saha, M.K. Alam, Boosting the efficiency of single junction kesterite solar cell using Ag mixed Cu_2ZnSnS_4 active layer†, RSC Adv. 8 (2018) 4905–4913. doi:10.1039/c7ra12352c.

[127] R. Caballero, S.G. Haass, C. Andres, L. Arques, F. Oliva, V. Izquierdo-Roca, Y.E. Romanyuk, Effect of magnesium incorporation on solution-processed kesterite solar cells, Front. Chem. 6 (2018) 1–9. doi:10.3389/fchem.2018.00005.

[128] Z.Y. Zhao, X. Zhao, First-principles study on doping effects of sodium in kesterite Cu_2ZnSnS_4, Inorg. Chem. 53 (2014) 9235–9241. doi:10.1021/ic5013268.

[129] D. Tiwari, T. Koehler, X. Lin, R. Harniman, I. Griffiths, L. Wang, D. Cherns, R. Klenk, D.J. Fermin, Cu_2ZnSnS_4 Thin Films Generated from a Single Solution Based Precursor: The Effect of Na and Sb Doping, Chem. Mater. 28 (2016) 4991–4997. doi:10.1021/acs.chemmater.6b01499.

[130] Z. Wang, N. Brodusch, R. Gauvin, G.P. Demopoulos, Lithium-doped Cu_2ZnSnS_4 superstrate solar cells with 5% efficiency – An alternative to thin film kesterite photovoltaics, Nano Energy. 53 (2018) 130–134. doi:10.1016/j.nanoen.2018.08.049.

[131] C. Yan, K. Sun, J. Huang, S. Johnston, F. Liu, B.P. Veettil, K. Sun, A. Pu, F. Zhou, J.A. Stride, M.A. Green, X. Hao, Beyond 11% Efficient Sulfide Kesterite $Cu_2Zn_xCd_{1-x}SnS_4$ Solar Cell: Effects of Cadmium Alloying, ACS Energy Lett. 2 (2017) 930–936. doi:10.1021/acsenergylett.7b00129.

[132] Z. Su, J.M.R. Tan, X. Li, X. Zeng, S.K. Batabyal, L.H. Wong, Cation Substitution of Solution-Processed Cu_2ZnSnS_4 Thin Film Solar Cell with over 9% Efficiency, Adv. Energy Mater. 5 (2015) 2–8. doi:10.1002/aenm.201500682.

[133] C. Xiao, K. Li, J. Zhang, W. Tong, Y. Liu, Z. Li, P. Huang, B. Pan, H. Su, Y. Xie, Magnetic ions in wide band gap semiconductor nanocrystals for optimized thermoelectric properties, Mater. Horizons. 1 (2014) 81–86. doi:10.1039/c3mh00091e.

[134] D. Shin, B. Saparov, D.B. Mitzi, Defect Engineering in Multinary Earth-Abundant Chalcogenide Photovoltaic Materials, Adv. Energy Mater. 7 (2017). doi:10.1002/aenm.201602366.

[135] L. Qiu, J. Xu, Fabrication of Ag and Mn Co-Doped Cu_2ZnSnS_4 Thin Film, Nanomaterials. 9 (2019) 1520. doi:10.3390/nano9111520.

[136] W. Li, X. Liu, H. Cui, S. Huang, X. Hao, The role of Ag in $(Ag,Cu)_2ZnSnS_4$ thin film for solar cell application, J. Alloys Compd. 625 (2015) 277–283. doi:10.1016/j.jallcom.2014.11.136.

[137] A. Guchhait, Z. Su, Y.F. Tay, S. Shukla, W. Li, S.W. Leow, J.M.R. Tan, S. Lie, O. Gunawan, L.H. Wong, Enhancement of Open-Circuit Voltage of Solution-Processed Cu_2ZnSnS_4 Solar Cells with 7.2% Efficiency by Incorporation of Silver, ACS Energy Lett. 1 (2016) 1256–1261. doi:10.1021/acsenergylett.6b00509.

[138] J. Henry, K. Mohanraj, G. Sivakumar, Vacuum evaporated $FTO/(Cu, Ag)_2ZnSnSe_4$ thin films and its electrochemical analysis, Vacuum. 160 (2019) 347–354. doi:10.1016/j.vacuum.2018.11.055.

[139] T.H. Nguyen, T. Kawaguchi, J. Chantana, T. Minemoto, T. Harada, S. Nakanishi, S. Ikeda, Structural and Solar Cell Properties of a Ag-Containing Cu_2ZnSnS_4 Thin Film Derived from Spray Pyrolysis, ACS Appl. Mater. Interfaces. 10 (2018) 5455–5463. doi:10.1021/acsami.7b14929.

[140] J. Kumar, S. Ingole, Structural and optical properties of $(Ag_xCu_{1-x})_2ZnSnS_4$ thin films synthesised via solution route, J. Alloys Compd. 727 (2017) 1089–1094. doi:10.1016/j.jallcom.2017.08.222.

[141] M.S. Kumar, S.P. Madhusudanan, S.K. Batabyal, Substitution of Zn in Earth-Abundant $Cu_2ZnSn(S,Se)_4$ based thin film solar cells – A status review, Sol. Energy Mater. Sol. Cells. 185 (2018) 287–299. doi:10.1016/j.solmat.2018.05.003.

[142] B. Ananthoju, J. Mohapatra, M.K. Jangid, D. Bahadur, N. V. Medhekar, M. Aslam, Cation/Anion Substitution in Cu_2ZnSnS_4 for Improved Photovoltaic Performance, Sci. Rep. 6 (2016) 1–11. doi:10.1038/srep35369.

[143] K.L. Huang, C.H. Huang, W.T. Lin, Y.S. Fu, T.F. Guo, Solvothermal synthesis and tunable bandgap of $Cu_2(Zn_{1-x}Co_x)SnS_4$ and $Cu_2(Fe_{1-x}Co_x)SnS_4$ nanocrystals, J. Alloys Compd. 646 (2015) 1015–1022. doi:10.1016/j.jallcom.2015.05.176.

[144] S. Schorr, H. Berlin, M. Tovar, H. Berlin, A. Weber, A. Gmbh, E. Synchrotron, R. Facility, N.L. Camera, Kesterite – an alternative absorber material for thin-film solar cells, (2008). doi:10.1002/pip.2156.

CHAPTER 3

EXPERIMENTAL METHODOLOGY

Chapter Overview

This chapter discusses the chemicals used in the design and synthetic process of the $Ce_2O_2Fe_2OSe_2$, kesterite and doped kesterite nanoparticle production, followed by the fabrication of pristine kesterite and doped kesterite solar cells. It further discusses a description of the experimental techniques used for the characterisation of the synthesized $Ce_2O_2Fe_2OSe_2$, kesterite and doped kesterite nanoparticles as well as the pristine and doped kesterite solar cells.

3.1   Introduction

The synthesis of the cerium and iron oxyselenide dopant is prepared under air and heated in a furnace. The synthesis of the kesterite and doped kesterite nanoparticles is carried out with the use of argon inert gas protection. All the analytical characterization was performed in normal air conditions.

3.1.1   Materials

Cerium (IV) oxide (CeO_2, 99.95%), carbonyl iron (Fe, ≥97%), selenium (Se, ≥99.5%), aluminium (Al, 99.9%), copper (II) chloride ($CuCl_2$, anhydrous, >98%), zinc chloride ($ZnCl_2$, 97%), diethylene glycol (DEG, 99%) and tin (II) chloride ($SnCl_2$, anhydrous, >98%) was obtained from Merck South Africa (Germiston, Johannesburg, South Africa).

3.1.2   Cerium and Iron Oxyselenide synthetic methodology

For $Ce_2O_2Fe_2OSe_2$, a stoichiometric mixture of 2.88 g (16.72×10^{-3} mol) of CeO_2, 0.93 g (16.72×10^{-3} mol) of Fe and 1.32 g (16.72×10^{-3} mol) of Se is pulverized together into a powder which was placed in a ceramic crucible with an oxygen-getter (Al powder in 10%

excess). The crucible was then sealed, and slowly heated to 1000 °C. Once at the desired temperature the crucible was kept at this temperature for 12 h. The crucible was then quenched into a bucket of iced water [1]. This procedure was performed a second time without the use of the oxygen getter.

3.1.3 Kesterite and doped Kesterite synthetic methodology

For the synthesis of the kesterite nanoparticles, 226 mg of $CuCl_2$, 150 mg of $ZnCl_2$, 190 mg of $SnCl_2$ is added to a flask containing 60 ml of DEG. A small magnetized rod was placed into the flask containing the mixture in order to allow continuous stirring which dissolved and mixed these powder precursors, forming a homogeneous brownish-yellow solution. The flask containing the solution was then placed into an oil bath and heated to 80 °C, once at this temperature 254.10 mg of Na_2Se dissolved in 4 ml of DEG was injected into the solution, thus forming solution 2. Solution 2 was then heated to 190 °C and kept for 30 min, then cooled to room temperature naturally. The final deep black suspension was diluted with isopropanol and centrifuged in order to collect the kesterite nanoparticle which were washed 3 times by repeated centrifugation in isopropanol [2]. This process is repeated with the addition of 657.64 mg of $Ce_2O_2Fe_2OSe_2$, in order to produce the doped kesterite nanoparticles. The synthetic process of the kesterite and doped kesterite nanoparticles are highlighted in figure 3.1.3.
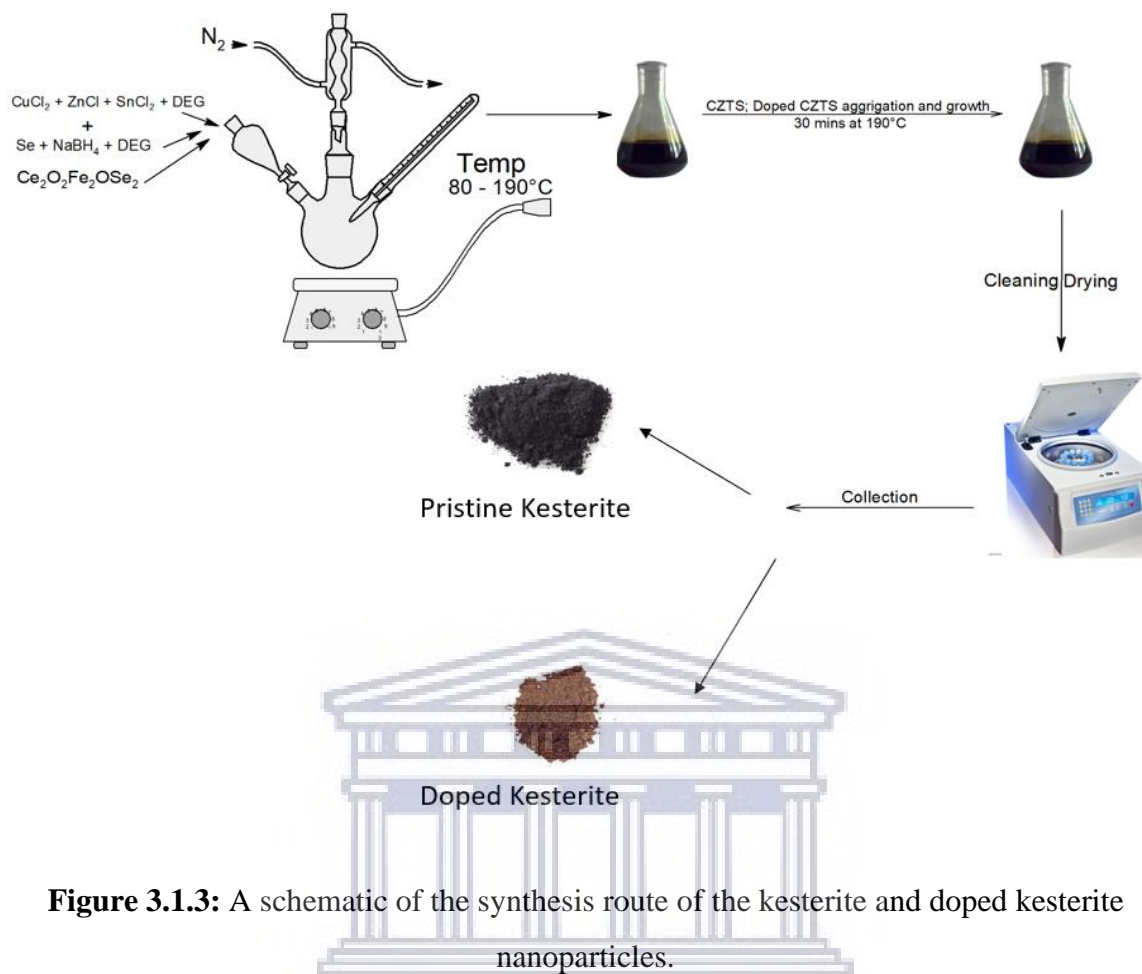
Figure 3.1.3: A schematic of the synthesis route of the kesterite and doped kesterite nanoparticles.

3.2 Fabrication of pristine kesterite and doped kesterite solar cells

3.2.1 Materials

The following materials were used for the fabrication process of the kesterite solar cell and all the reagents were of analytical grade: Hellmanex III, isopropanol, Al-doped ZnO, ZnO, cadmium nitrate tetrahydrate, thiourea and ITO coated glass was obtained from Merck South Africa (Germiston, Johannesburg, South Africa).

3.2.2 Device fabrication layers

There are several different methods for the fabrication of kesterite based solar cells. A lot of these involve deposition techniques which makes use of both "vacuum and non-vacuum" deposition techniques. When analysing the "vacuum and non-vacuum" methods that are used for the deposition as well as the fabrication of CZTS photovoltaics, the vacuum routes involve the use of some techniques such as atomic beam sputtering, RF

magnetron sputtering, thermal evaporation etc. These methods suffer major drawbacks such as high input capita, low output and difficulties during deposition into large area-based devices. All these limitations and shortcomings are hindering the ultimate goal of maximal PCE of low cost, environmentally sustainable CZTS photovoltaics. As a result, non-vacuum deposition techniques involving electrochemical deposition, spray pyrolysis, SILAR method and sol gel method etc, are superior methods for fabrication of CZTS photovoltaics [3–7]. This study made use of the non-vacuum deposition technique, including an ink deposition method. This deposition process involved dissolving the different layers in a suitable solvent and spin coating them over an ITO glass plate following layer by layer process and subsequently heating the glass to evaporate the solvent leaving behind the different layer on the glass used [8,9]. The fabrication of the kesterite and doped kesterite solar cell followed this architecture.

3.2.2.1 ITO-coated glass preparation

The process involved in the cleaning of the ITO-coated glass before deposition is as follows; The glass was sonicated for 5 min in a hot Hellmanex III solution, after five minutes, the glass was removed and rinsed twice in hot de-ionized water. Subsequently the glass was sonicated for another 5 min in isopropanol after which it was rinsed thoroughly twice in hot de-ionized water. Finally, the glass was dried using N_2 gas gun and kept for deposition.

3.2.2.2 Kesterite absorber layer preparation

The synthesized kesterite and doped kesterite nanoparticles were prepared into an ink for use in the deposition process. The following procedure was observed in the preparation of the kesterite absorber ink; 150 mg of the synthesized kesterite and doped kesterite nanoparticles were weighed on a weighing balance and poured into glass vials and properly labelled correctly. 1 ml of ethanol was added to each of the nanoparticles and was sonicated for 35 min to allow for a homogenous dispersion of the nanoparticles in the solvent. The final dark ink obtained was kept ready for deposition on the ITO-coated glass.

3.2.2.3 Cadmium sulfide buffer layer preparation

The procedure used for the preparation of the cadmium buffer layer is as follows; 0.1 M of Cadmium nitrate tetrahydrate and 0.1 M thiourea was dissolved in methanol. The solution

was stabilized with the addition of 1 ml of deionized water. The solution was stirred at room temperature for 15 min until a clear transparent and homogeneous mixtures was procured. The solution was kept and used for deposition of the layer.

3.2.2.4 Zinc oxide resistive layer preparation

The following procedure of the zinc oxide resistive layer preparation was observed in the preparation of the kesterite absorber ink; 150 mg of the zinc oxide was dissolved 1 ml of Isopropanol and then kept for deposition.

3.2.2.5 Aluminium doped zinc oxide window layer preparation

The window layer of Al: ZnO was prepared by sol-gel method which involved dissolving 6% aluminium dopant-ZnO nanoparticles in isopropanol. The sol-gel solution formed was then kept for deposition.

3.3   Device layer deposition

During the deposition of the synthesised layers, all the layers of the device were spin coated and dried on a hot plate to evaporate the solvents. Firstly, the Kesterite and doped kesterite nanoparticles where dispersed and suspended in solution forming an ink, due to nanoparticles not being very soluble. This ink was then deposited onto the cleaned ITO-coated glass via spin coating at a speed of 1500 rpm for 30 secs, then dried on a hot plat for 5 mins at 200 ˚C. In order to obtain an adequate thickness for the absorber layer, this was repeated a total of five times. Finally, the absorber layer was annealed for 1.5 h at 400 ˚C in an inert condition. Once cooled the cadmium sulfide solution was spin coated onto the absorber layer at 1000 rpm for 30 secs then annealed for 5 mins at 200 ˚C. This was repeated 5 times to obtain a desirable thickness of the film. The Al- doped ZnO window layer was spin-coated at 1000 rpm for 30 secs then dried at 250 ˚C for 5 mins in air using a hot plate. Lastly the Ag cathode layer was deposited on the window layer of the device via drawing it on [8,10] The final architecture of the prepared kesterite and doped kesterite devices are shown in figure 3.3 below:
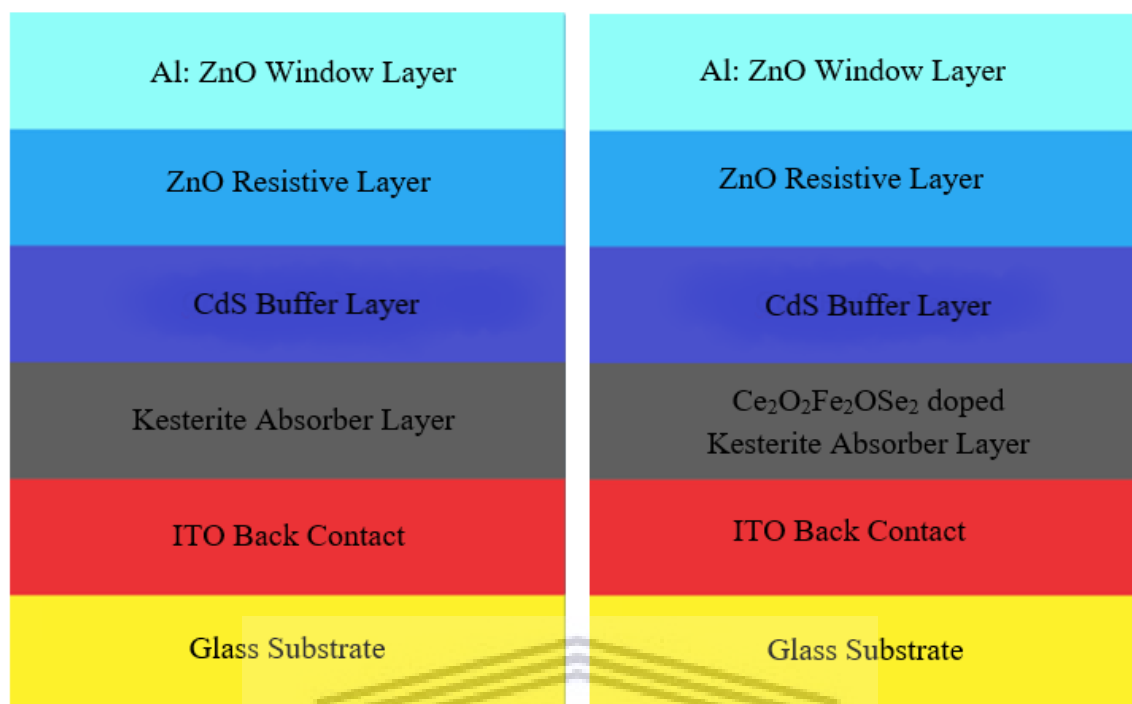
Figure 3.3: Device architecture of the prepared kesterite and doped kesterite PV cells.

3.4 Material characterisation techniques and instrumentation

3.4.1 Morphological and structural characterization

3.4.1.1 Fourier-Transform Infra-Red Spectroscopy (FTIR)

"FTIR spectroscopy" was used in this research, to confirm the functional groups that are present in the $Ce_2O_2FeOSe_2$, pristine and doped kesterite nanoparticles. This characterization technique is a versatile analytical technique for non-destructive, chemical characterization of various types of samples [11]. Each of the materials were mixed with KBr to form a pellet in order to be analysed. 100mg of $Ce_2O_2FeOSe_2$ was mixed and crushed with 10 mg of KBr, 100 mg of pristine kesterite was mixed and crushed with 50 mg of KBr due to the pristine kesterite being very dark and moisture absorbent, lastly 100 mg of the doped kesterite was mixed and crushed with 20 mg of KBr. Once formed, the pellets were used to obtain the FTIR spectra. FTIR spectra were obtained using a "Perkin Elmer Spectrum 100 series Attenuated Total Reflection (ATR) FTIR spectrometer (Perkin-Elmer, Boston, MA, USA)".

3.4.1.2 X-ray Diffraction (XRD) Spectroscopy

XRD was used in this research, in order to obtain the "crystalline pattern, phase purity, crystallite size and lattice parameters" of the $Ce_2O_2FeOSe_2$, pristine and doped kesterite nanoparticles. The x-rays used to analyse the samples are created by the use of monochromatic radiation, collimated to concentrate, and directed toward the sample. This monochromatic radiation was produced by a cathode ray tube [12]. 5 mg of each sample was dried as much as possible then used in the XRD analysis. A "D8 Advanced Multipurpose X-Ray Diffractometer (BRUKER AXS, Berlin, Germany)" using an "X-ray tube with copper K-alpha radiation operated at 40 kV and 40 mA and a position sensitive detector Vantec_1 which enables fast data acquisition" was used to acquire the XRD measurements. "Measurements were taken in the 2-theta range of 0.5^{o}- 130° with a step size of 0.034^{o}".

3.4.1.3 Structural modelling of the nanoparticle samples

The XRD data provided the information required in order to model the structural data of the $Ce_2O_2FeOSe_2$, pristine and doped kesterite nanoparticles. When modelling the XRD data to provide a structure, the following process was used: in Diamond 4, the crystal structures cell parameters and space group information (from XRD data) was typed in, followed by the different elements in each material as well as their atomic parameters were typed in and then the structure was created for each sample. Diamond 4 (crystal-impact software, http://www.crystalimpact.com/diamond/Default.htm) was used to simulate the crystal structure of the synthesized nanoparticles from XRD data.

3.4.1.4 High-Resolution Scanning Electron Microscopy (HRSEM)

"High-Resolution Scanning Electron Microscopy" (HRSEM) was used in this study to analyse the surface morphology and the elemental composition/ X-ray maps of the $Ce_2O_2FeOSe_2$, pristine and doped kesterite nanoparticles. HRSEM produces an image resulting from the acquisition of signals generated from the electron beam and specimen interactions. A real-time observation is provided by the electron beam scanning coils, signal detection, and processing system as well as image recording of the specimen surface [13]. 50 mg of each sample was taken and analysed. Each sample was held on a carbon grid supported by alumina. The samples became conductive due to sputter coating with a gold-palladium alloy for 30 min. "The ZEISS ULTRA Scanning Electron Microscope

fitted with an Energy Dispersive X-ray Spectrometer (EDS) from Carl Zeiss Microscopy GmbH (Jena, Germany)" was used to obtain these SEM images.

3.4.1.5 High-Resolution Transmission Electron Microscopy (HRTEM)

In this study, HRTEM was used to obtain the morphological aspects of the materials such as the internal ultra-structure, crystallinity (lattice fringes) and the elemental composition of the synthesized nanoparticles. In HRTEM, field-emission sources have provided an increase in image resolution while promoting the development of computational techniques that further extend image resolution and image interpretability [14]. HRTEM analysis was performed by dispersing 40 mg the synthesized material in isopropanol and placed on a on a copper-nickel grid for analysis, this was done for each sample. Analysis was performed using a Field Electron and Ion Company (FEI) Tecnai G2 F2O X-Twin MAT 200 kV Field Emission Transmission Electron Microscope (Eindhoven, The Netherlands) equipped with both EDS and selected area diffraction (SAED) capabilities.

3.4.1.6 Small Angle X-ray Scattering (SAXS) Spectroscopy

SAXS was performed in this study in order to determine and analyse the structural characterization of the nanomaterials. The SAXS technique is based on elastic scattering of high energy photons by electrons of an irradiated sample. This technique is able to deliver structural information of macromolecules between 5 and 25 nm, of repeat distances in partially ordered systems of up to 150 nm [15,16]. The SAXS analysis was performed on 100 mg of solid samples coated between stick tap and measured with SAXspace P/N 100100 (Anton Paar GmbH, Graz, Austria), which was repeated for each of the $Ce_2O_2FeOSe_2$, pristine and doped kesterite nanoparticles.

3.4.2 Optical characterization

3.4.2.1 Ultraviolet-Visible Spectroscopy (UV-Vis)

UV-Vis was performed to ascertain the optical properties of the $Ce_2O_2FeOSe_2$, pristine kesterite and doped kesterite nanoparticles such as the absorbance and optical band gap. This absorption is often referred to as electronic spectroscopy, as the transition from low electronic energy levels to higher electronic energy levels within the molecule result from the absorption of ultraviolet or visible radiation by the molecule. Valuable structural proposals can be obtained from combining the spectroscopy data with the IR spectral data

[17]. UV-Vis analysis was performed by dispersing 100 mg of each material in dichloromethane, ethanol and deionized water, respectively then placed in the chamber of the "Varian Cary 300 UV-Vis-NIR Spectrometer (Agilent, Santa Clara, CA, USA)" at a wavelength of 300 to 1100 nm at room temperature.

3.4.3 Electrochemical characterization

3.4.3.1 Cyclic Voltammetry (CV)

In this research, CV experiments were carried out using a "CH Instrument Electrochemical Analyzer Model CHI 760E (CH Instrument, Houston, Texas, USA)". CV is an accurate application of potential functions and measurement of the resultant current can be obtained from the use the three electrodes (working, auxiliary and reference) along with the potentiostat instrument. All the voltammetric techniques are described as some function of E, i, and t [18]. 2 mg of the sample was dissolved in in 1 mL of "N-methyl-z-pyrrolidine". Then 1.5 μL of this mixture was drop coated onto the electrode. A traditional 10 mL electrochemical cell constituting a three-electrode arrangement was used. The working electrode was a glassy carbon electrode, the counter electrode was a platinum wire while the reference electrode consisted of an Ag/AgCl electrode that was stored in 3 M NaCl, with a phosphate-buffered saline (BPS) electrolyte.

3.4.3.2 Electrochemical Impedance Spectroscopy (EIS)

EIS was especially useful in this research in order to identify and study the electron transfer kinetics/dynamics, while establishing the diffusive processes occurring at the electrode/electrolyte interfaces of the $Ce_2O_2FeOSe_2$, pristine kesterite and doped kesterite nanoparticles. In EIS, information about the interface, its structure and reactions are found during the analysis of the systems response, resulting from an electrical perturbation applied to an electrical circuit. The potential-current dependencies of electrochemical systems in general are non-linear [19,20]. 2 mg of the sample was dissolved in in 1 mL of "N-methyl-z-pyrrolidine". Then 1.5 μL of this mixture was drop coated onto the electrode. A traditional 10 mL electrochemical cell constituting a three-electrode arrangement was used. The working electrode was a glassy carbon electrode, the counter electrode was a platinum wire while the reference electrode consisted of an Ag/AgCl electrode that was stored in 3 M NaCl, with a phosphate-buffered saline (BPS) electrolyte. EIS experiments

were carried out using a "CH Instrument Electrochemical Analyzer Model CHI 760E (CH Instrument, Houston, Texas, USA)".

3.4.3.3 Current-Voltage Curve (I-V curve)

In this study, IV-curves were utilized to determine electrochemical efficiencies of the $Ce_2O_2Fe_2OSe_2$, pristine kesterite and doped kesterite nanoparticles. Then the IV-curves were utilized to determine electrochemical efficiencies of the fabricated pristine kesterite and doped kesterite solar cells. For the IV-curve analysis of the materials 2 mg of the sample was dissolved in 1 mL of "N-methyl-z-pyrrolidine". Then 1.5 μL of this mixture was drop coated onto the electrode. A traditional 10 mL electrochemical cell constituting a three-electrode arrangement was used. The working electrode was a glassy carbon electrode, the counter electrode was a platinum wire while the reference electrode consisted of an Ag/AgCl electrode that was stored in 3 M NaCl, with a phosphate-buffered saline (BPS) electrolyte. IV-curve experiments were carried out using a "CH Instrument Electrochemical Analyzer Model CHI 760E (CH Instrument, Houston, Texas, USA)". For the IV-curve measurements of the fabricated solar cells, each cell was fabricated using the method stated in 3.3 then left to settle overnight. The solar cells were then attached to the Sciencetech SS1.0kW-UV 1000W UV Solar Simulator (Sciencetech, Inc., London, ON, Canada) and analysed using the Ossila Solar Cell IV 1.0.40 software.

References

[1]   E.E. McCabe, A.S. Wills, L. Chapon, P. Manuel, J.S.O. Evans, Structural and magnetic characterisation of iron oxyselenides $Ce_2O_2Fe_2OSe_2$ and $Nd_2O_2Fe_2OSe_2$, Phys. Rev. (2014). http://arxiv.org/abs/1410.4990.

[2]   H. Dong, T. Schnabel, E. Ahlswede, C. Feldmann, Polyol-mediated synthesis of $Cu_2ZnSn(S,Se)_4$ kesterite nanoparticles and their use in thin-film solar cells, Solid State Sci. 29 (2014) 52–57. doi:10.1016/j.solidstatesciences.2014.01.006.

[3]   S. Das, K. Sa, P.C. Mahakul, J. Raiguru, I. Alam, B. Subramanyam, P. Mahanandia, Synthesis of quaternary chalcogenide CZTS nanoparticles by a hydrothermal route, IOP Conf. Ser. Mater. Sci. Eng. 338 (2018). doi:10.1088/1757-899X/338/1/012062.

[4]   S. Das, I. Alam, J. Raiguru, B.V.R.S. Subramanyam, P. Mahanandia, A facile method to synthesize CZTS quantum dots for solar cell applications, Phys. E Low-Dimensional Syst. Nanostructures. 105 (2019) 19–24. doi:10.1016/j.physe.2018.08.020.

[5]   T. Ratz, G. Brammertz, R. Caballero, M. León, S. Canulescu, J. Schou, L. Gütay, D. Pareek, T. Taskesen, D.-H. Kim, J.-K. Kang, C. Malerba, A. Redinger, E. Saucedo, B. Shin, H. Tampo, K. Timmo, N.D. Nguyen, B. Vermang, Physical routes for the synthesis of kesterite, J. Phys. Energy. 1 (2019) 042003. doi:10.1088/2515-7655/ab281c.

[6]   S. Abdelhaleem, A.E. Hassanien, R. Ahmad, M. Schuster, A.H. Ashour, M. Distaso, W. Peukert, P.J. Wellmann, Tuning the Properties of CZTS Films by Controlling the Process Parameters in Cost-Effective Non-vacuum Technique, J. Electron. Mater. 47 (2018) 7085–7092. doi:10.1007/s11664-018-6636-4.

[7]   Y.Y. Prawira, E.C. Prima, G. Refantero, H.S. Nugroho, C. Harito, R.A. Wibowo, Nugraha, C. Panatarani, B. Yuliarto, All-solution-non-vacuum fabrication process of CZTS solar cell using zto as non-toxic buffer layer, Int. J. Nanoelectron. Mater. 13 (2020) 307–314.

[8]   K. Tanaka, M. Oonuki, N. Moritake, H. Uchiki, Cu_2ZnSnS_4 thin film solar cells prepared by non-vacuum processing, Sol. Energy Mater. Sol. Cells. 93 (2009) 583–587. doi:10.1016/j.solmat.2008.12.009.

[9]   E.P. Subramaniam, G. Rajesh, N. Muthukumarasamy, M. Thambidurai, V. Asokan, D. Velauthapillai, Solar cells of Cu_2ZnSnS_4 thin films prepared by chemical bath deposition method, Indian J. Pure Appl. Phys. 52 (2014) 620–624.

[10]   J.J. Chaudhari, U.S. Joshi, Fabrication of high-quality kesterite Cu_2ZnSnS_4 thin films deposited by an optimized sol–gel sulphurization technique for solar cells, J. Mater. Sci. Mater. Electron. 31 (2020) 14411–14420. doi:10.1007/s10854-020-04000-7.

[11]   Y. Chen, C. Zou, M. Mastalerz, S. Hu, C. Gasaway, X. Tao, Applications of micro-fourier transform infrared spectroscopy (FTIR) in the geological sciences—A Review, Int. J. Mol. Sci. 16 (2015) 30223–30250. doi:10.3390/ijms161226227.

[12]   A.A. Bunaciu, E. gabriela Udriştioiu, H.Y. Aboul-Enein, X-Ray Diffraction: Instrumentation and Applications, Crit. Rev. Anal. Chem. 45 (2015) 289–299. doi:10.1080/10408347.2014.949616.

[13]   W. Zhou, R. Apkarian, Z.L. Wang, D. Joy, Fundamentals of scanning electron microscopy (SEM), Scanning Microsc. Nanotechnol. Tech. Appl. (2007) 1–40. doi:10.1007/978-0-387-39620-0_1.

[14]   A. I. Kirkland, N. Young, Advances in high-resolution transmission electron microscopy for materials science, Microsc. Anal. 25 (2012) 19–23. https://pdfs.semanticscholar.org/42cb/e97a100809873b4bf748c31f1ee2b98dcab6.pdf%0A http://wiley.mypreviewurl.co.uk/sites/default/files/magazine_pdfs/mag 2012_September_Kirkland.pdf.

[15]   J. Li, A. Jiao, S. Chen, Z. Wu, E. Xu, Z. Jin, Application of the small-angle X-ray scattering technique for structural analysis studies: A review, J. Mol. Struct. 1165 (2018) 391–400. doi:10.1016/j.molstruc.2017.12.031.

[16]   T.W. Gräwert, D.I. Svergun, Structural Modeling Using Solution Small-Angle X-ray Scattering (SAXS), J. Mol. Biol. 432 (2020) 3078–3092. doi:10.1016/j.jmb.2020.01.030.

[17]   C. De Caro, UV/VIS Spectrophotometry - Fundamentals and Applications, in: Mettler-Toledo Int., Mettler-Toledo Publication No. ME-30256131, 2015: pp. 4–14.

[18]   L. Leonat, G. Sbârcea, I.V. Branzoi, Cyclic voltammetry for energy levels estimation of organic materials, UPB Sci. Bull. Ser. B Chem. Mater. Sci. 75 (2013) 111–118.

[19]   S. Sarker, A.J.S. Ahammad, H.W. Seo, D.M. Kim, Electrochemical impedance spectra of dye-sensitized solar cells: Fundamentals and spreadsheet calculation, Int. J. Photoenergy. 2014 (2014). doi:10.1155/2014/851705.

[20]   H. Cesiulis, N. Tsyntsaru, A. Ramanavicius, G. Ragoisha, The Study of Thin Films by Electrochemical Impedance Spectroscopy, Springer International Publishing, 2016. doi:10.1007/978-3-319-30198-3.

CHAPTER 4
RESULTS AND DISCUSSION

Chapter overview

This chapter examines and describes the characterisation of cerium and iron oxyselenide $[Ce_2O_2Fe_2OSe_2]$, kesterite $[Cu_2ZnSnSe_4]$ and doped kesterite $[(Cu,Ce)_2(Zn,Fe)SnSe_4]$ nanoparticles by "microscopic (HRSEM and HRTEM), and spectroscopic (FTIR, XRD, UV-Vis Spectroscopy and TGA) techniques". The various characterizations help determine the various properties exhibited by these synthesized nanoparticles.

4.1 Structural Characterization

4.1.1 FTIR

The nature of bonds and functional groups present in the synthesized nanoparticles was analysed through Fourier transform infra-red spectroscopy (FTIR). A Perkin-Elmer spectrometer was used to record the FTIR spectra of $Ce_2O_2Fe_2OSe_2$ with and without an oxygen getter in the range of 4000 to 400 cm^{-1} as shown in figure 4.1.1.1.
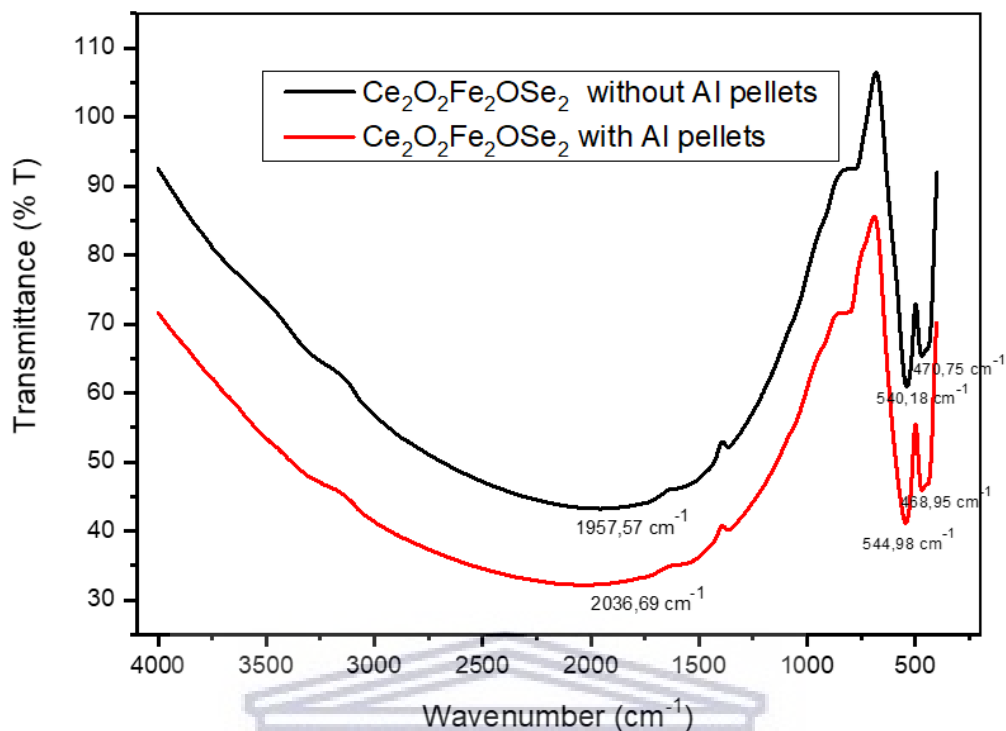
Figure 4.1.1.1: FTIR of the $Ce_2O_2Fe_2OSe_2$ nanoparticles with and without an oxygen getter.

When looking at the $Ce_2O_2Fe_2OSe_2$ without an oxygen getter, the broad stretch at 1957.57 cm^{-1} is a result of the stretching vibration of Se-O. The vibrational band at 540.18 cm^{-1} is ascribed to the Ce-O stretching mode of vibration. The vibrational band at 470.75 cm^{-1} is a result of the Fe-O stretching mode of vibration. When looking at the $Ce_2O_2Fe_2OSe_2$ with an oxygen getter, the broad stretch at 2036.69 cm^{-1} is a result of the stretching vibration of Se-O. The vibrational band at 544.98 cm^{-1} is ascribed to the Ce-O stretching mode of vibration. The vibrational band at 469.95 cm^{-1} is a result of the Fe-O stretching mode of vibration. Thus, its seen that the oxygen getter makes very little difference in the FTIR results of the $Ce_2O_2Fe_2OSe_2$, therefore when comparing the $Ce_2O_2Fe_2OSe_2$ nanoparticles to the kesterite and doped kesterite nanoparticles, the $Ce_2O_2Fe_2OSe_2$ without an oxygen getter result can be used [1].
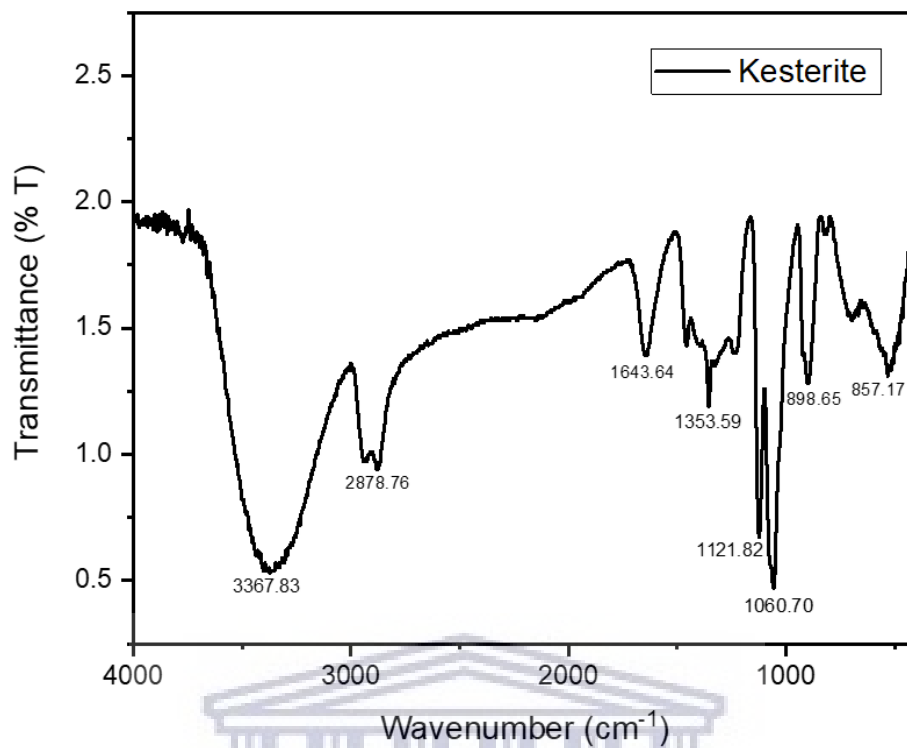
Figure 4.1.1.2: FTIR of the kesterite nanoparticles.
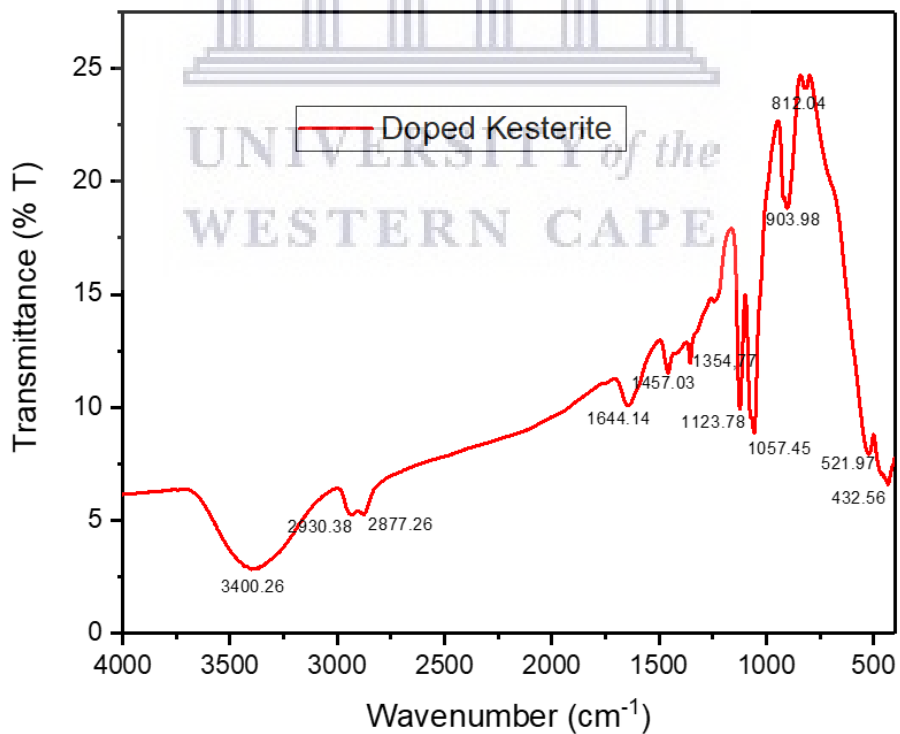
Figure 4.1.1.3: FTIR of the doped kesterite nanoparticles.

A Perkin-Elmer spectrometer was used to record the FTIR spectra of the kesterite [$Cu_2ZnSnSe_4$] and doped kesterite [$(Cu,Ce)_2(Zn,Fe)SnSe_4$] material in the range of 400 – 4000 cm^{-1} as shown in Fig 4.1.1.2 and Fig 4.1.1.3. The FTIR of the kesterite in Fig 4.1.1.2, shows several different characteristic vibrational bands, including v(O-H) (3367.83 cm^{-1}), v(C-H) (2878.76 cm^{-1}), v(C-H2) (1643.64 – 1353.59 cm^{-1}), v(C-O) (1121.82 – 1060.70 cm^{-1}), and bands (898.65 – 857.17 cm^{-1}) are due to the resonance interaction between vibrational modes of selenide ions in the crystal. The FTIR of the doped kesterite in Fig 4.1.1.3, shows several different characteristic vibrational bands, including v(O-H) (3400.26 cm^{-1}), v(C-H) (2930.38 – 2877.26 cm^{-1}), v(C-H2) (1644.14 – 1354.77 cm^{-1}), v(C-O) (1123.78 – 1057.45 cm^{-1}), and bands (903.98 – 812.04 cm^{-1}) are due to the resonance interaction between vibrational modes of selenide ions in the crystal. The peak at 524.97 cm^{-1} is ascribed to the Ce-O stretching mode of vibration. The peak at 432.56 cm^{-1} is a result of the Fe-O stretching mode of vibration [2–4].

4.1.2 XRD

The phase composition of the kesterite nanoparticles was authenticated by XRD Fig. 4.1.2.1. These XRD patterns displays broad Bragg peaks ascribed to the small particle size. The results of the XRD were obtained at room temperature, using Cu-Kα radiation (λKα1=1.5406Å) with a LynxEye (Position sensitive detector).
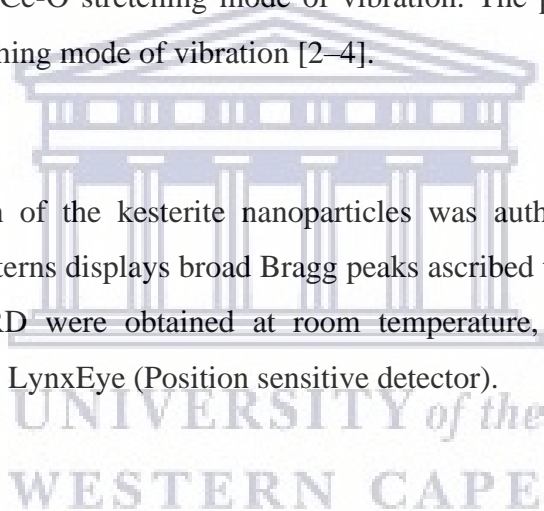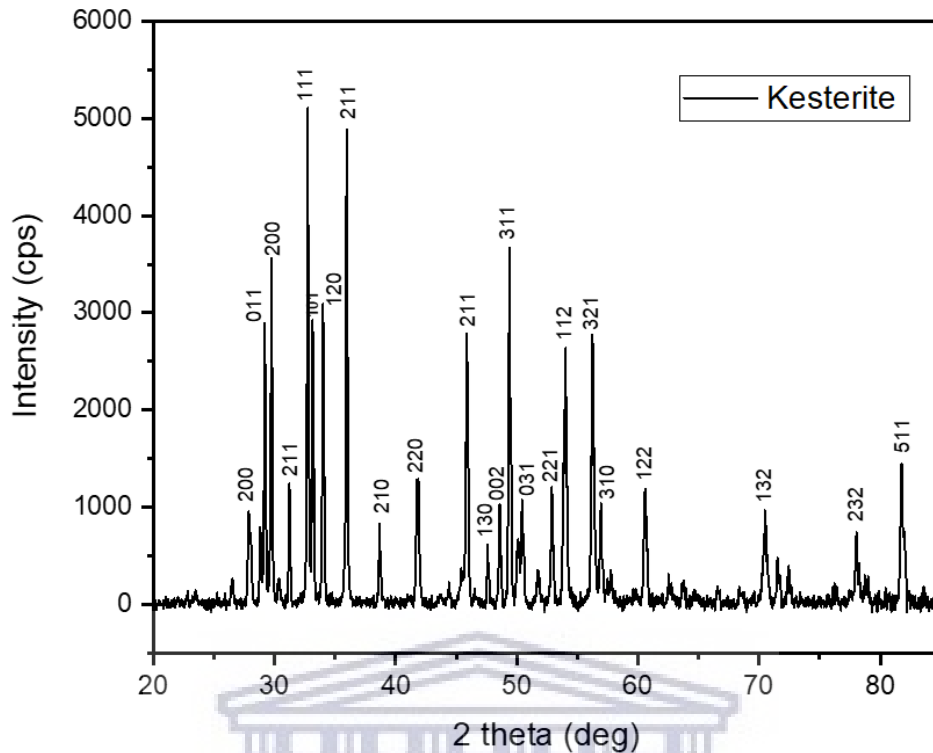
Figure 4.1.2.1: XRD patterns of the kesterite nanoparticles.

From the XRD patterns in Fig 4.1.2.1; the kesterite has peaks (200) which are broad Bragg thus assumed to belong to a second phase. This peak at (200) could also suggest a possible structural fault in the kesterite sample. The peaks sharpen and increase dramatically indicating an increase in the crystallization. A further increase in peak sharpness can be seen at (111). The peaks observed at (011), (200) and (211) are peaks in the secondary phase of Cu_2Se suggesting the kesterite was prepared with a high Cu/(Zn+Se) ratio. The most intense peak of the kesterite is at (111). There are some small extra peaks observed that are compatible with that of kesterite reflections [5–8]. The phase composition and appearance of the tetragonal kesterite phase is evident. The diffraction peaks for the kesterite observed at 2θ = 27.77, 29.18, 32.72, 33.13, 33.93 and 35.94 correspond to (011), (200), (211), (111), (120) and (211) crystal planes respectfully, confirming the kesterite phase in the CZTSe sample.
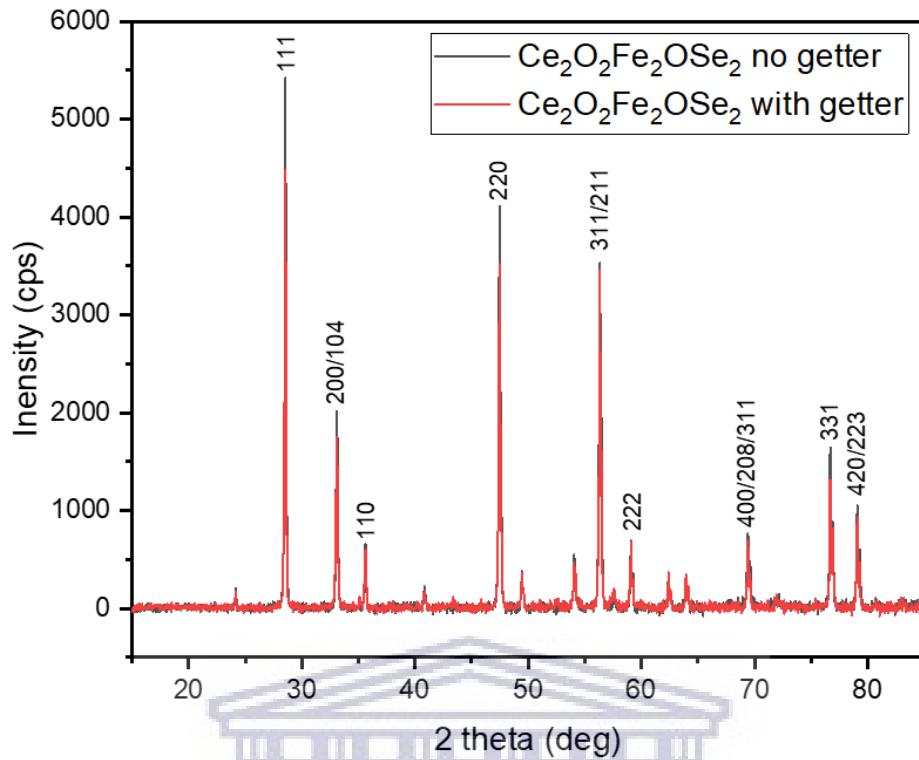
Figure 4.1.2.2: XRD patterns of the $Ce_2O_2Fe_2OSe_2$ nanoparticles.
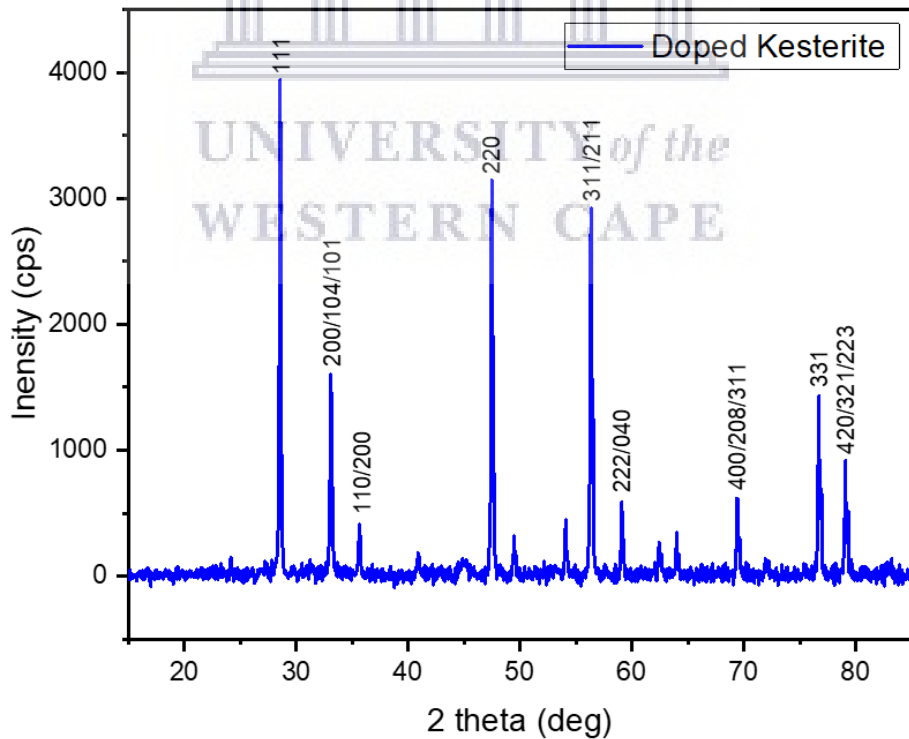
Figure 4.1.2.3: XRD patterns of the doped kesterite nanoparticles.

The phase composition of the cerium and iron oxyselenide and doped kesterite nanoparticles was validated by XRD (Fig. 4.1.2.2 and Fig. 4.1.2.3). The results of the XRD were obtained at room temperature, using Cu-Kα radiation (λKα1=1.5406Å) with a LynxEye (Position sensitive detector). From the XRD patterns in Fig. 4.1.2.2; the cerium and iron oxyselenides had peaks (111), (200), (220), (311), (331) and (420) which are due to the cerium oxide (CeO_2) formation, with the tallest peak being (111). The peaks (104), (211) and (223) are due to the hematite (Fe_2O_3) formation, while the peaks (101) and (321) are due to the formation of tin oxide (SnO_2). The peaks sharpen, increase steadily then decrease indicating stability in the crystallization. The most intense peak of the cerium and iron oxyselenides is at (111). The doped kesterite seems to be heavily influenced by the cerium and iron oxyselenide dopant as the doped kesterite follows the general trend of the cerium and iron oxyselenide dopants, suggesting the doped kesterite was prepared with a high Ce/(Zn,Fe+Se) ratio [9,10]. The phase composition and occurrence of the tetragonal doped kesterite phase was observed as it also followed the trends of the kesterite. The diffraction peaks for the doped kesterite observed at 2θ = 28.56, 33.15, 47.48, 56.15, 76.70 and 78.71 correspond to (111), (104), (220), (211), (331) and (321) crystal planes respectfully, confirming the kesterite phase in the doped CZTS sample.

4.2   Composition analysis
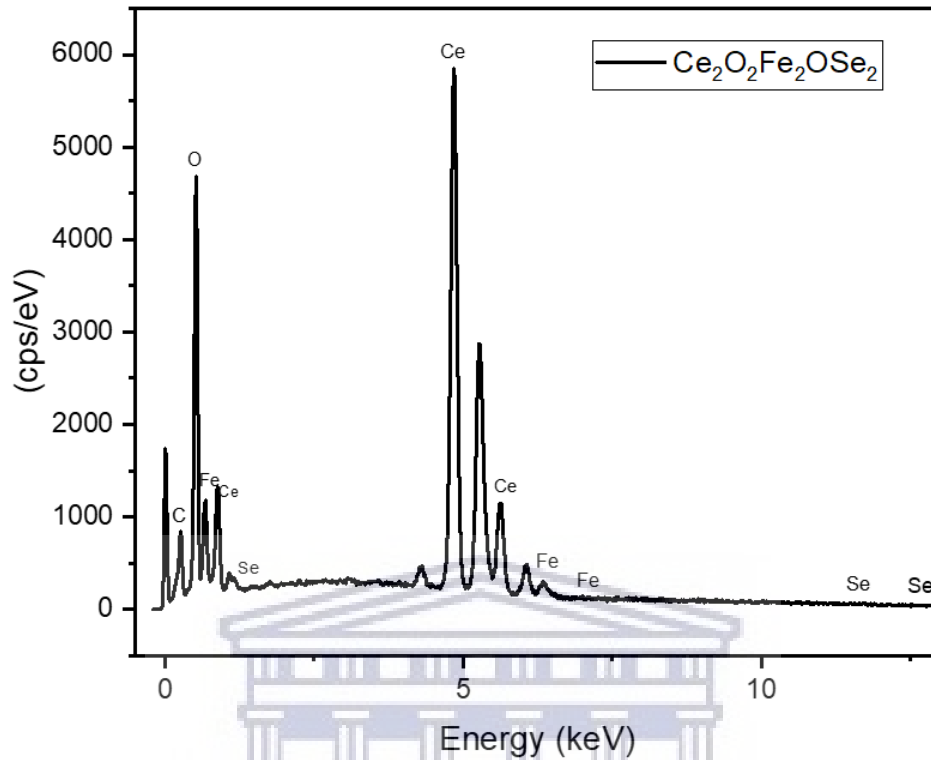
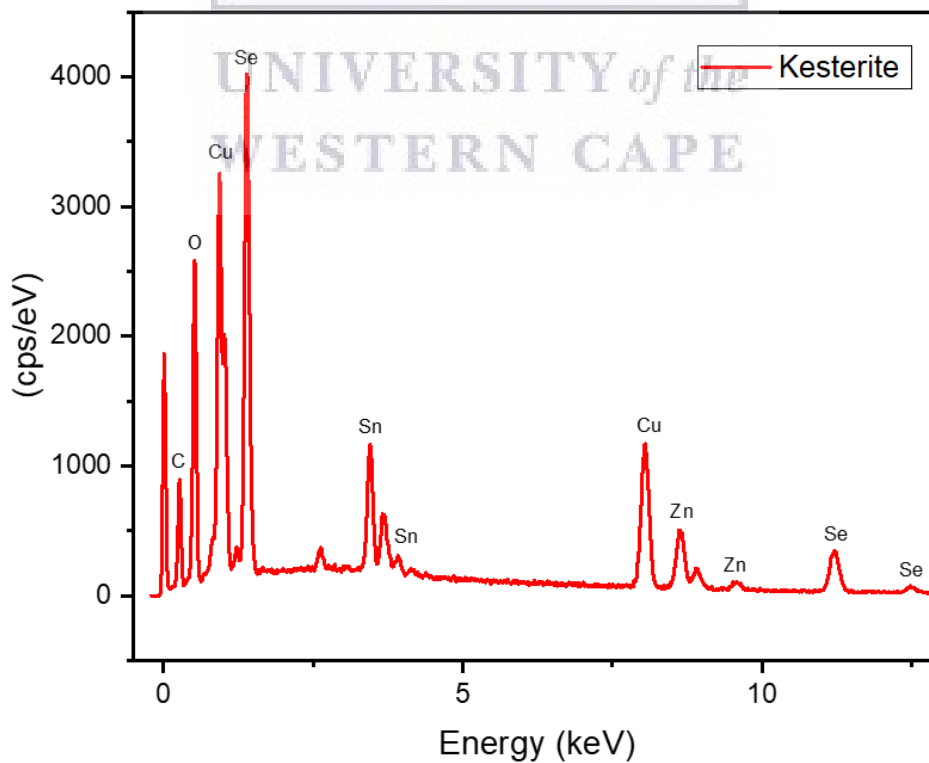**Figure 4.2.1:** EDS spectrum of $Ce_2O_2Fe_2OSe_2$ nanoparticles.

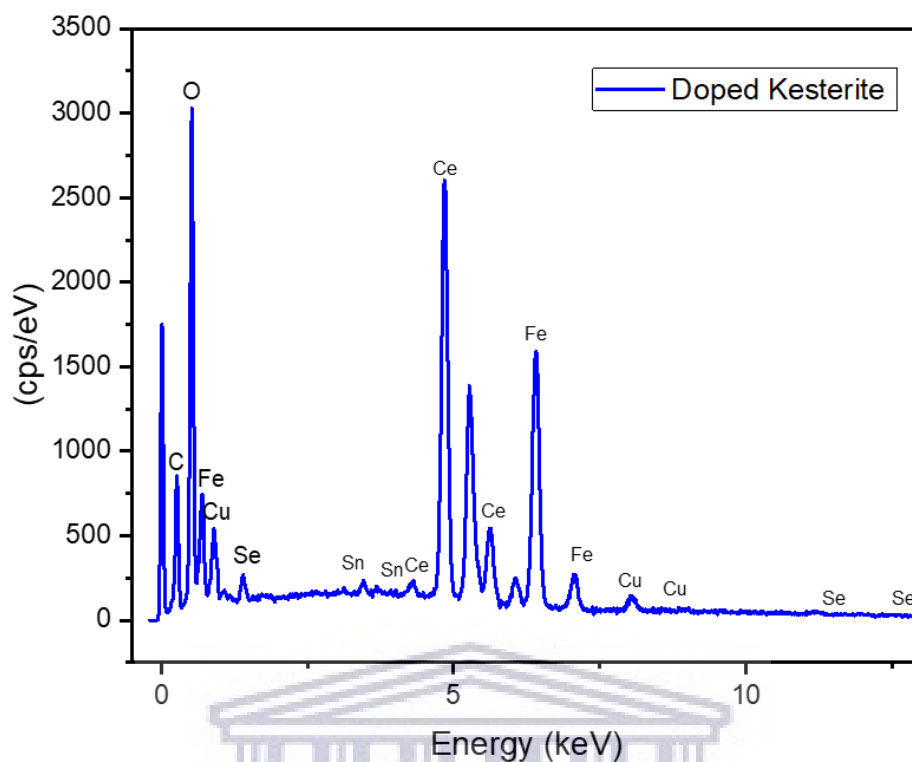**Figure 4.2.2:** EDS spectrum of kesterite nanoparticles.

Figure 4.2.3: EDS spectrum of doped kesterite nanoparticles.

Table 4.2.1: Elemental composition of kesterite and doped kesterite nanoparticles with respect to weight percentage.

	Cu Conc. In solution (mM)	Zn Conc. In solution (mM)	Sn Conc. In solution (mM)	Dopant Conc. In solution (mM)
Kesterite	0.84	0.55	0.50	-
Doped Kesterite	0.84	0.55	0.50	0.55

Table 4.2.2: Elemental ratio of kesterite and doped kesterite nanoparticles with copper and dopant concentration.

	Ratio Sn/Cu	Ratio Zn/Cu	Ratio Zn/Sn	Cu/ (Zn+Sn)	Ratio Sn/ $Ce_2O_2Fe_2OSe_2$	Ratio Zn/ $Ce_2O_2Fe_2OSe_2$	$Ce_2O_2Fe_2OSe_2$/ (Zn+Sn)
Kesterite	0.60	0.65	1.10	0.80	-	-	-
Doped Kesterite	0.60	0.65	1.10	0.80	0.91	1.00	0.52

4.3   Morphology Characterization

4.3.1   High Resolution Scanning Electron Microscopy

The surface morphology of the cerium and iron oxyselenide, kesterite and doped kesterite nanoparticles were shown by the HRSEM images in Fig. 4.3.1. The instrument used for this analysis is "ZEISS ULTRA scanning electron microscope" with acceleration voltage of 5.0 kV.
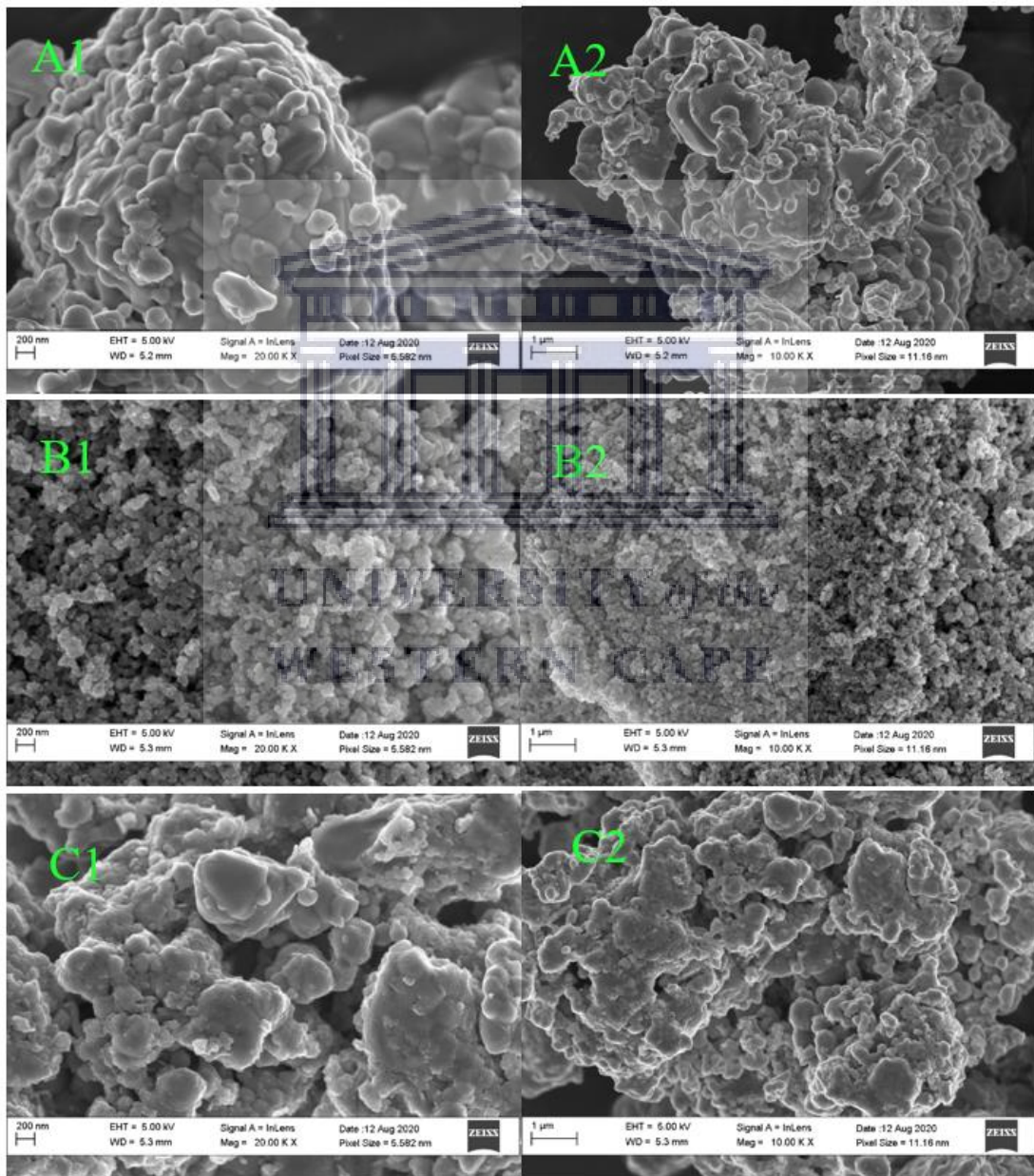
Figure 4.3.1: HRSEM images of $Ce_2O_2Fe_2OSe_2$ (A1, A2), kesterite (B1, B2) and doped kesterite (C1, C2) nanocrystals.

Looking at the cerium and iron oxyselenide nanoparticles (A1, A2) the SEM images shows grain growth structures which do not possess uniform surface features over the entire area. These grain boundaries are irregular and possess intense aggregation delineating an inhomogeneous composition. The particles are quite agglomerated with some extended aggregation and the film is shown to be non-porous with no gaps in consideration to the particle size. The kesterite nanoparticles (B1, B2) SEM images shows grain growth structures which possess uniform surface features over the entire area. These grain boundaries are regular and possess minimal aggregation delineating a homogeneous composition. The average shape of the kesterite particles is a general rod shape, suggesting nanostructured morphology. The particles show mild agglomeration with no extended aggregation and the film is shown to be porous with small to average sized gaps in consideration to the particle size. The doped kesterite nanoparticles (C1, C2) SEM images shows grain growth structures which possess a mix of both uniform and non-uniform surface features over the entire area. These grain boundaries are irregular and possess general aggregation delineating an inhomogeneous composition. The average shape of the doped kesterite particles is a general rod shape, suggesting nanostructured morphology. The particles show intense agglomeration with some extended aggregation and the film is shown to be porous with large gaps in consideration to the particle size [11–14].

4.3.2 High Resolution Transmission Electron Microscopy

The "High-resolution TEM" images of the interface region of the cerium and iron oxyselenide, kesterite and doped kesterite nanoparticles were shown in Fig. 4.3.2 at the back contact provides increased details about microstructure evolution and interfacial reactions. The TEM instrument used for this analysis is the "TECNAI G2 F2O X-TWIN MAT 200 kV field emission".
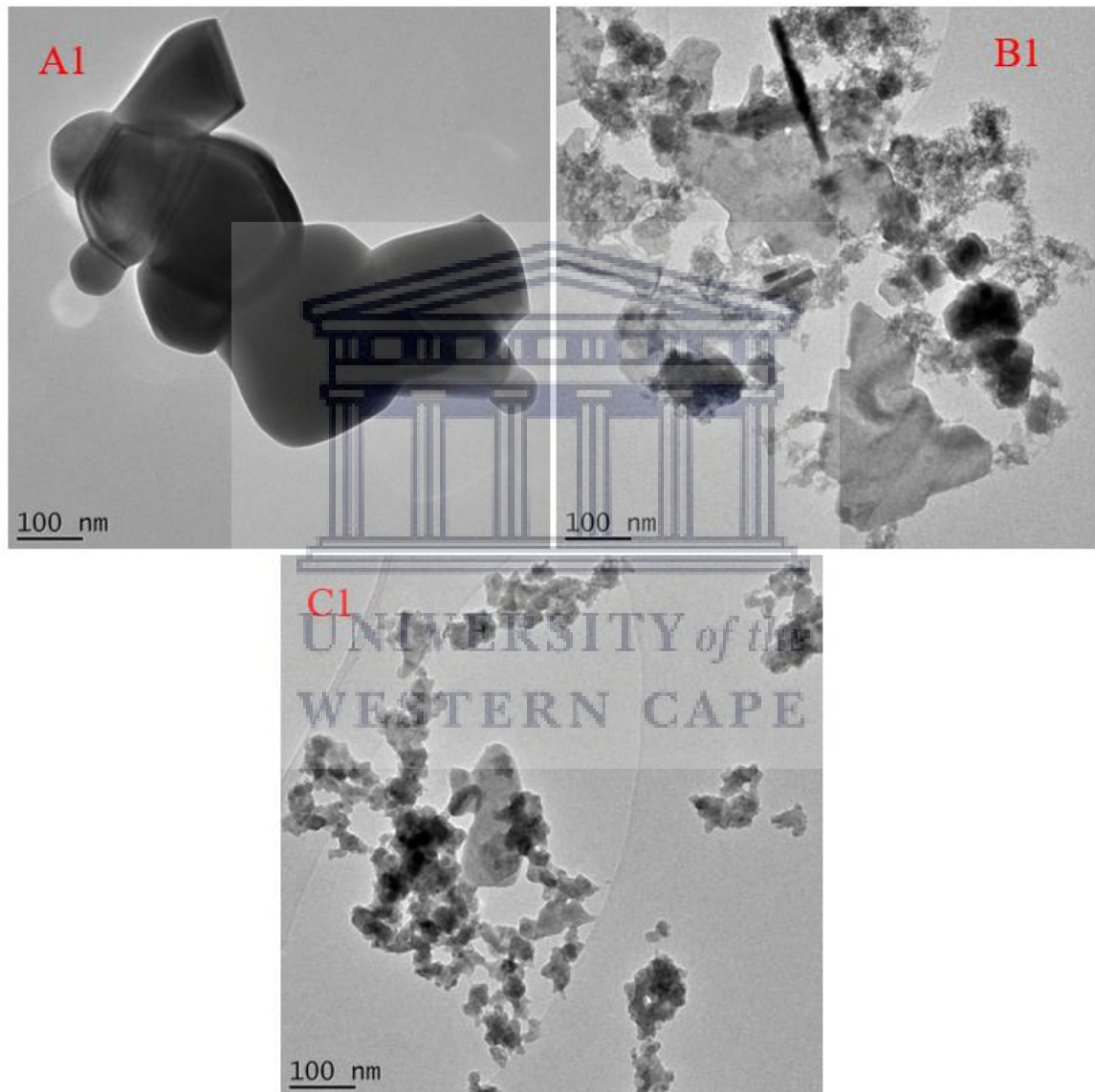

Figure 4.3.2.1: HRTEM images of the $Ce_2O_2Fe_2OSe_2$ (A1), kesterite (B1) and doped kesterite (C1) nanocrystals.
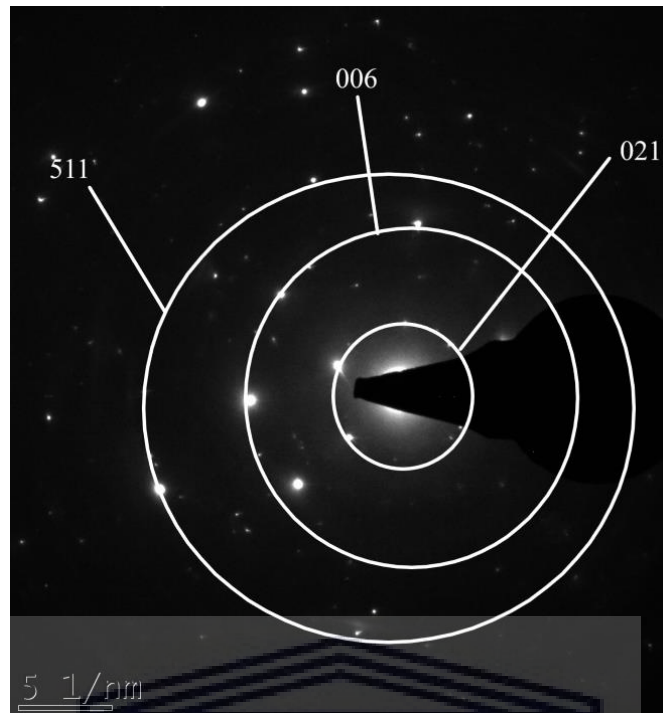
Figure 4.3.2.2: SAED micrograph of the $Ce_2O_2Fe_2OSe_2$ nanoparticles confirming the hkl miller index (planes) found in XRD.
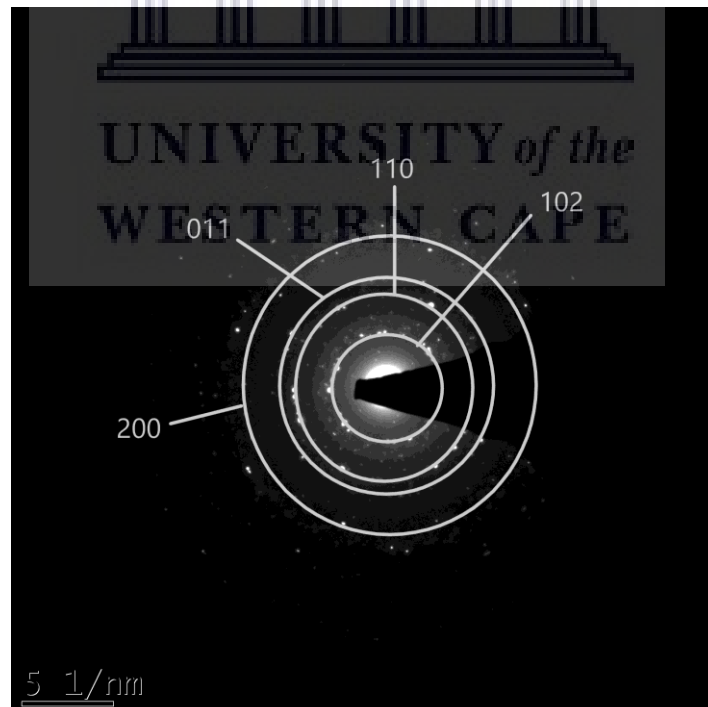
Figure 4.3.2.3: SAED micrograph of the kesterite nanoparticles confirming the hkl miller index (planes) found in XRD.
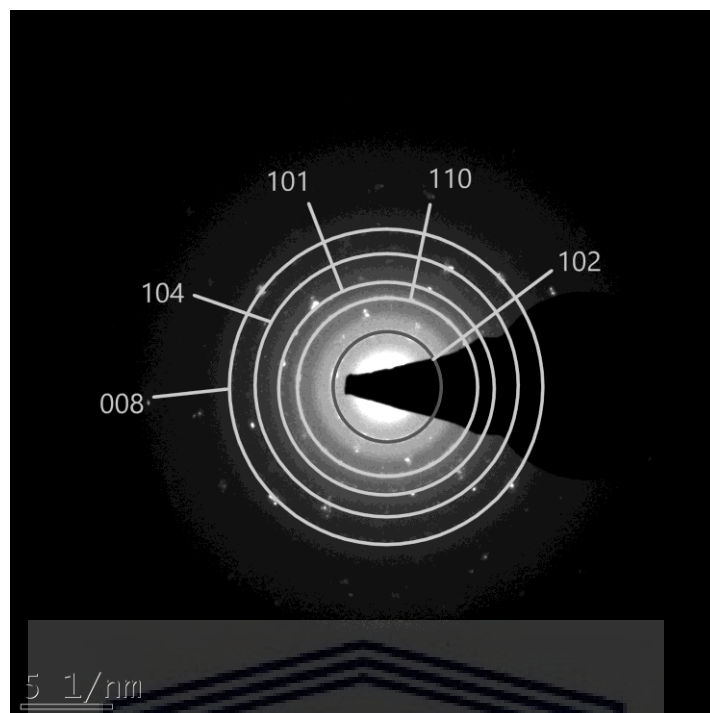
Figure 4.3.2.4: SAED micrograph of the doped kesterite nanoparticles confirming the hkl miller index (planes) found in XRD.

When looking at the cerium and iron oxyselenide nanoparticles (A1) the TEM images shows the individual $Ce_2O_2Fe_2OSe_2$ nanoparticles having an irregular, highly agglomerated spheres forming an L like shape and the selected area electron diffraction (SAED) image (Fig. 4.3.2.2) shows Debye rings indicating the polycrystalline nature of the compound. From these Debye rings, some d-spacing values are found which corresponds to (111), (200) and (220) planes of CeO_2 or (104), (211) and (223) planes of Fe_2O_3 or (101) and (321) planes of SnO_2. Some of these phases have been detected from the XRD pattern of the $Ce_2O_2Fe_2OSe_2$ nanoparticles [15]. When looking at the kesterite nanoparticles (B1) the TEM images shows the individual kesterite nanoparticles have more of an irregular rod and spherical shape with some level of agglomeration, these nanocrystal agglomerates possess an irregular shape. The SAED image (Fig. 4.3.2.3) shows Debye rings indicating the polycrystalline nature of the compound. From these Debye rings, some d-spacing values; 27.77, 29.18, 32.72, 33.13, 33.93 and 35.94 are found which corresponds to (011), (200), (211), (111), (120) and (211) crystal planes respectfully. Some of these phases have been detected from the XRD pattern of the kesterite nanoparticles [16,17]. When looking at the doped kesterite nanoparticles (C1) the TEM images shows the individual doped kesterite nanoparticles having a spherical shape with a high level of agglomeration, these

nanocrystal agglomerates possess an irregular shape. The SAED image (Fig. 4.3.2.4) shows Debye rings indicating the polycrystalline nature of the compound. From these Debye rings, some d-spacing values; 28.56, 33.15, 47.48, 56.15, 76.70 and 78.71 are found which corresponds to (111), (104), (220), (211), (331) and (321) crystal planes respectfully. Some of these phases have been detected from the XRD pattern of the doped kesterite nanoparticles [16–20].

The lattice fringe images obtained for the synthesized nanoparticles further confirms that the nanoparticles were crystalline and the d-spacing value of the lattice fringes were evaluated and assigned with the corresponding plane (miller index) as can be seen in the tables bellow;

Table 4.3.2.1: The radii, d-spacing and miller indices of the $Ce_2O_2Fe_2OSe_2$ nanoparticles.

S.No	$1/2r$ (nm^{-1})	$1/r$ (nm^{-1})	r (nm)	d-spacing Å	(hkl)
1	7.467	3.7335	0.267845185	2.678451855	(012)
2	16.655	8.3275	0.120084059	1.200840588	(006)
3	26.658	13.329	0.075024383	0.750243829	(511)

Table 4.3.2.2: The radii, d-spacing and miller indices of the kesterite nanoparticles.

S.No	$1/2r$ (nm^{-1})	$1/r$ (nm^{-1})	r (nm)	d-spacing Å	(hkl)
1	6.299	3.1495	0.317510716	3.17510716	(102)
2	10.144	5.072	0.197160883	1.971608833	(110)
3	12.167	6.0835	0.164379058	1.643790581	(011)
4	15.484	7.742	0.12916559	1.291655903	(200)

Table 4.3.2.3: The radii, d-spacing and miller indices of the doped kesterite nanoparticles.

S.No	$1/2r$ (nm^{-1})	$1/r$ (nm^{-1})	r (nm)	d-spacing Å	(hkl)
1	5.92	2.96	0.337837838	3.378378378	(102)
2	9.769	4.8845	0.204729246	2.047292456	(110)
3	11.521	5.7605	0.173596042	1.73596042	(101)
4	14.115	7.0575	0.141693234	1.416932341	(104)
5	17.245	8.6225	0.115975645	1.159756451	(008)

The d-spacing was determined and calculated using Brags Law with the following equation;

$$n\lambda = 2d\sin\theta$$

"Where n is the diffraction order, λ is the wavelength of light, d is the integer spacing and θ is the incident angle of light". The correct miller indices were obtained by comparing the d-spacing to the radius of the individual crystal rings [21–25]. Therefore, these TEM results agree with the XRD results.
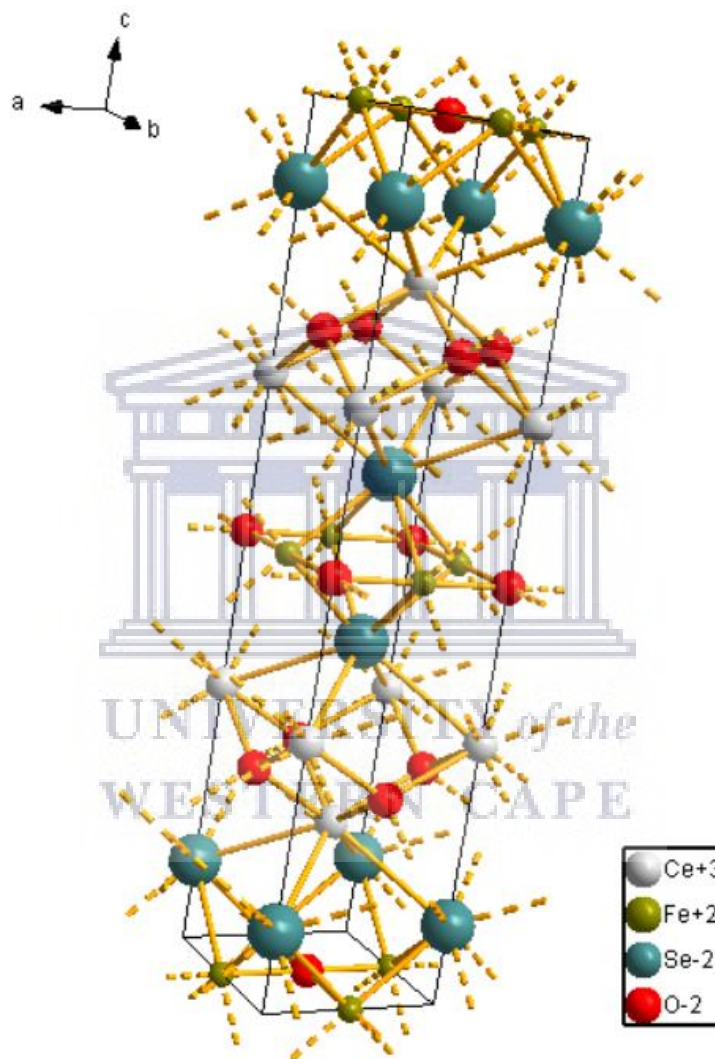
4.3.3 Modelled nanoparticle structure

Figure 4.3.3.1: Diamond simulation of the XRD data of the synthesized $Ce_2O_2Fe_2OSe_2$ nanoparticles showing their tetragonal crystal structure.
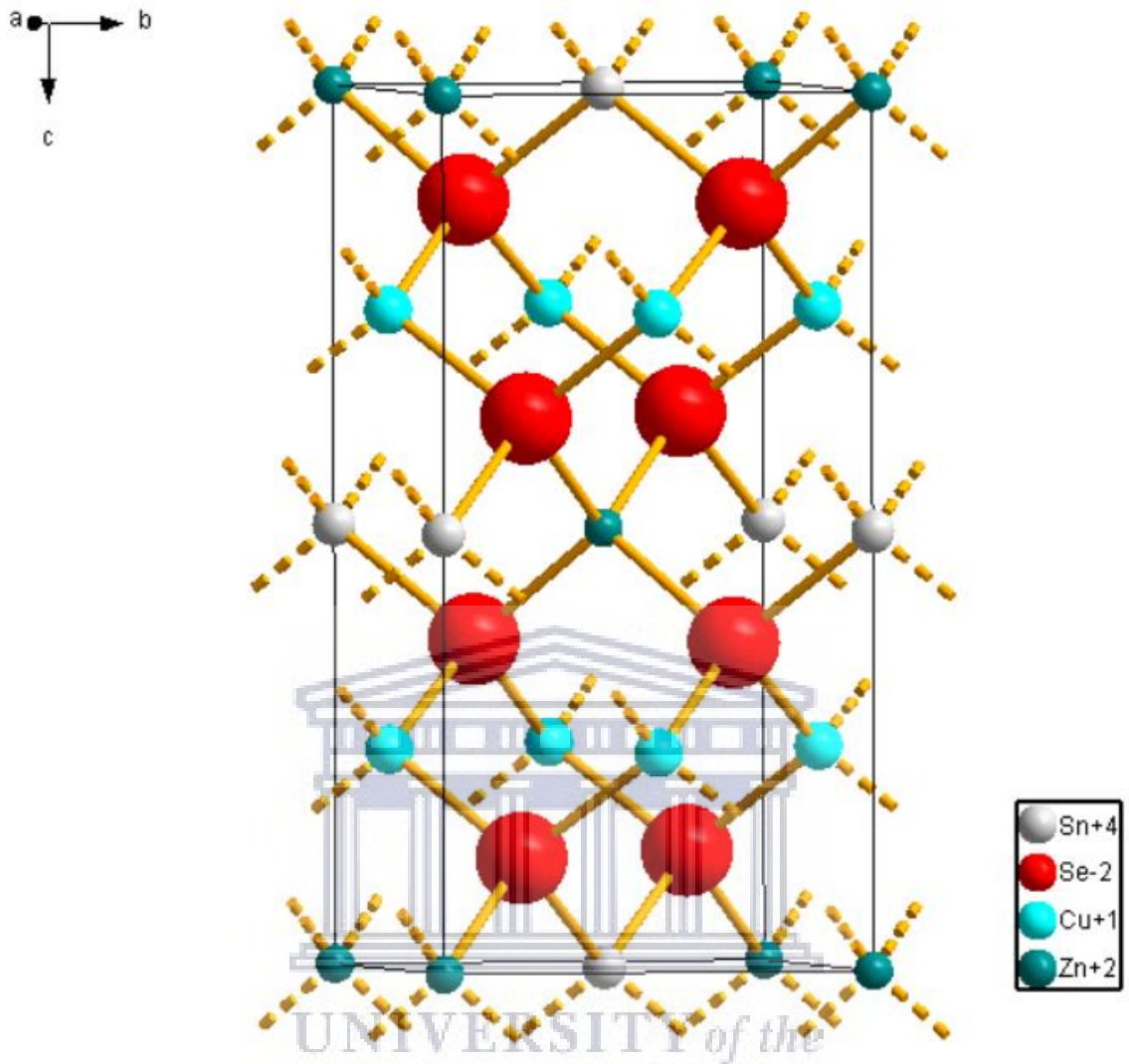
Figure 4.3.3.2: Diamond simulation of the XRD data of the synthesized kesterite nanoparticles showing their tetragonal crystal structure.
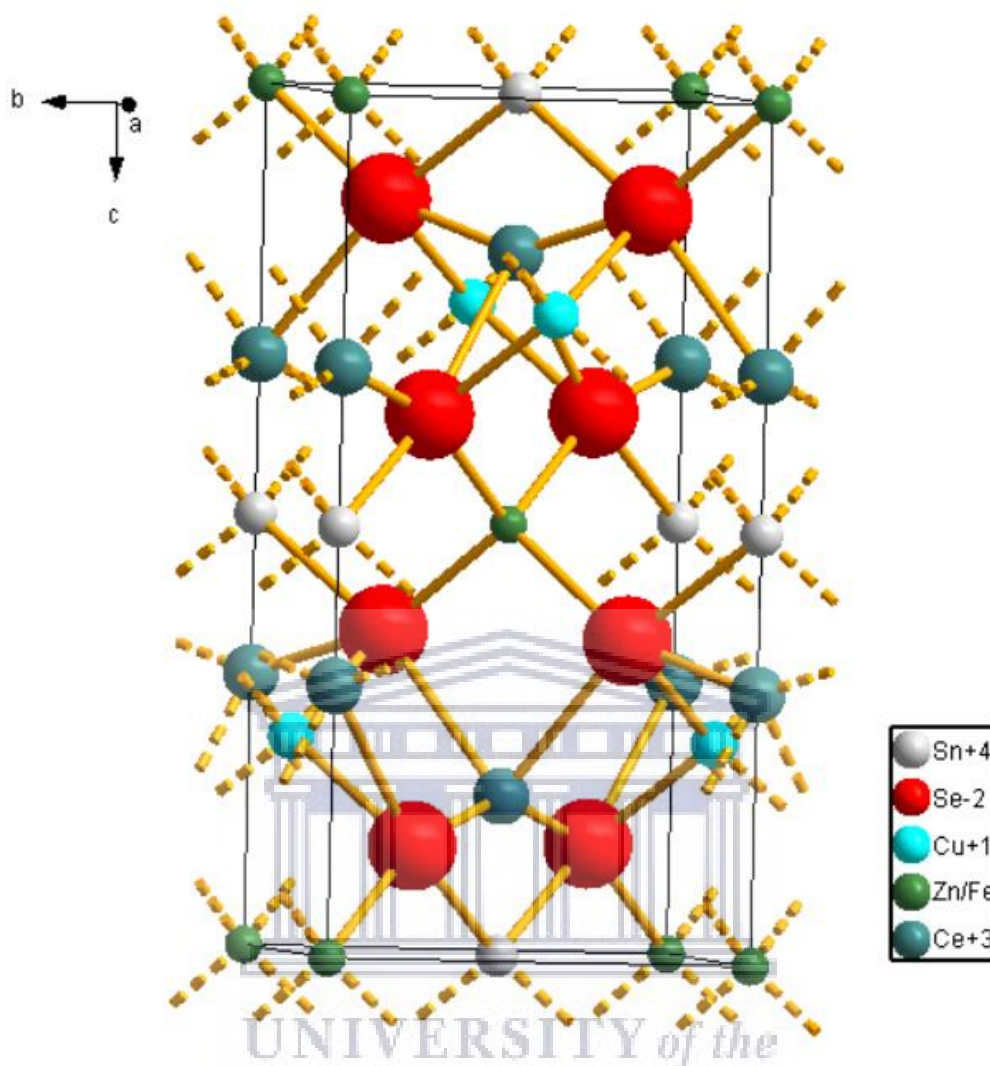
Figure 4.3.3.3: Diamond simulation of the XRD data of the synthesized doped kesterite nanoparticles showing their tetragonal crystal structure.

The simulations of the crystal structure of the synthesized nanoparticles from XRD data was achieved using the Diamond, crystal-impact software. The simulation obtained agreed with the conventional tetragonal structure of the $Ce_2O_2Fe_2OSe_2$, kesterite and doped kesterite phase. The parameters used in simulating the crystal structure for each of the synthesized nanoparticles are shown in the following tables:

Table 4.3.3.1: Phase data of the synthesized $Ce_2O_2Fe_2OSe_2$ nanoparticles.

Phase data	
Space-group	I 4/m m m (139) - tetragonal
Cell	a = 4.0311 Å c = 18.1500 Å
	c/a = 4.5025
	V = 294.93 Å^3

Table 4.3.3.2: Atomic parameters of the synthesized $Ce_2O_2Fe_2OSe_2$ nanoparticles.

Atomic parameters						
Atom	**Ox.**	**Wyck.**	**Site**	**x/a**	**y/b**	**z/c**
Ce1	3	4e	4 m m	1/2	1/2	0.18471
Fe1	2	4c	m m m.	1/2	0	0
Se1	-2	4e	4 m m	0	0	0.09755
O1	-2	4d	-4 m2	1/2	0	1/4
O2	-2	2b	4 /m m m	1/2	1/2	0

Table 4.3.3.3 Phase data of the synthesized kesterite nanoparticles.

Phase data	
Space-group	I -4 2 m (121) - tetragonal
Cell	a = 5.4464 Å c = 10.8000 Å
	c/a = 1.9830
	V = 320.36 Å^3

Table 4.3.3.4 Atomic parameters of the synthesized kesterite nanoparticles.

Atomic parameters						
Atom	**Ox.**	**Wyck.**	**Site**	**x/a**	**y/b**	**z/c**
Sn1	4	2b	-42 m	0	0	1/2
Se1	-2	8i	..m	0.2587	0.2587	0.3714
Cu1	1	4d	-4..	0	1/2	1/4
Zn1	2	2a	-42 m	0	0	0

Table 4.3.3.5 Phase data of the synthesized doped kesterite nanoparticles.

Phase data	
Space-group	I -4 (82) - tetragonal
Cell	a = 5.4270 Å c = 10.8710 Å
	c/a = 2.0031
	V = 320.18 Å^3

Table 4.3.3.6 Atomic parameters of the synthesized doped kesterite nanoparticles.

Atomic parameters						
Atom	Ox.	Wyck.	Site	x/a	y/b	z/c
Sn1	4	2b	-4..	0	0	1/2
Se1	-2	8g	1	0.25870	0.25870	0.37140
Cu1	1	2c	-4..	0	1/2	1/4
Zn1	2	2a	-4..	0	0	0
Fe1	2	2a	-4..	0	0	0
Ce1	3	4e	2..	1/2	1/2	0.18471

The $Ce_2O_2Fe_2OSe_2$ nanoparticles have a I 4/m m m (139) – tetragonal structure with respect to the following parameters; a = 4.0311 Å, c = 18.1500 Å, c/a = 4.5025 and V=294.93 Å3. Some of these bond stretches are due to Ce-O and Fe-O fibrational bands while the stronger bonds are due to the Se-O vibrational bands. While refining the $Ce_2O_2Fe_2OSe_2$ structure, the Ln = Ce phases are in consensus with the nuclear structure. The site occupancy refinement yielded occupancies near the stoichiometric $(Ce_2O_{1.99}Fe_{2.00}O_{0.99}Se_{2.0})$. The predicted decrease in unit cell parameters of the Ln = Ce phases, with decreasing Ln^{3+} ionic radii is observed, followed by a sharp decline in the amount of c unit cell parameter is observed below TN, similarly to that of $La_2O_2Fe_2OSe_2$. Additional Bragg reflections were seen for $Ce_2O_2Fe_2OSe_2$ below TN [26–29]. The kesterite structure consists of alternating cation layers of CuSn, CuZn, CuSn and CuZn at z¼0, 1/4, 1/2 and 3/4, respectively indicating that a Sigle copper ion occupies the 2a (0,1/2,1/4) position with zinc and the remaining copper ordered at 2c (0/0/0) and 2d (0,0,0) resulting in the space group I4-42m (121), with respects to the following parameters; a = 5.4464 Å, c = 10.8000 Å, c/a = 1.9830 and V = 320.36 Å3. These bond interactions can be greatly attributed to different types of bonding, C-H, C-H2, O-H and C-O which are due to the interactions of Cu-Sn, Cu-Se, Sn-Zn and Se-Zn and similar bonding interactions. The anion lies on the (110) mirror plane at8g (x,y,z) for the kesterite structure, tetragonal structural modifications of the kesterite type structure may be considered, belonging to the space groups P4⁻2c, P4⁻21c and P2. Cyrillization in the kesterite structure describes an ordered distribution of the cations. A disordered distribution of the cations may result in vacancies and anti-site defects (point defects) influencing the electronic properties of the material [30–34]. The doped kesterite structure is similar to the kesterite structure but the Cu sites are shared with Ce and the Zn sites are shared with Fe thus, consists of alternating cation layers of CuSn, CuZn, CuFe, CeSn, CeZn and CeFe. The doped kesterite

nanoparticles possesses a I -4 (82) – tetragonal structure with respects to the following parameters; a = 5.4270 Å, c = 10.8710 Å, c/a = 2.0031 and V = 320.18 Å3. A lot of the bonding is similar to that of the kesterites but it has major influences from the vibrational bonding that takes place in the $Ce_2O_2Fe_2OSe_2$ nanoparticles which result in new structural bonds such as Ce-Cu, Zn-Fe, Ce-Sn, Fe-Cu.

4.3.4 SAXS prediction of internal structure and shape

The HRTEM technique could not fully describe the nanoparticle internal structure, thus another characterization technique was performed known as "Small Angle X-ray Scattering (SAXS)" in order to observe and better understand the nanoparticle internal structure. The SAXS analysis was performed using SAXS Space by Anton Paar.
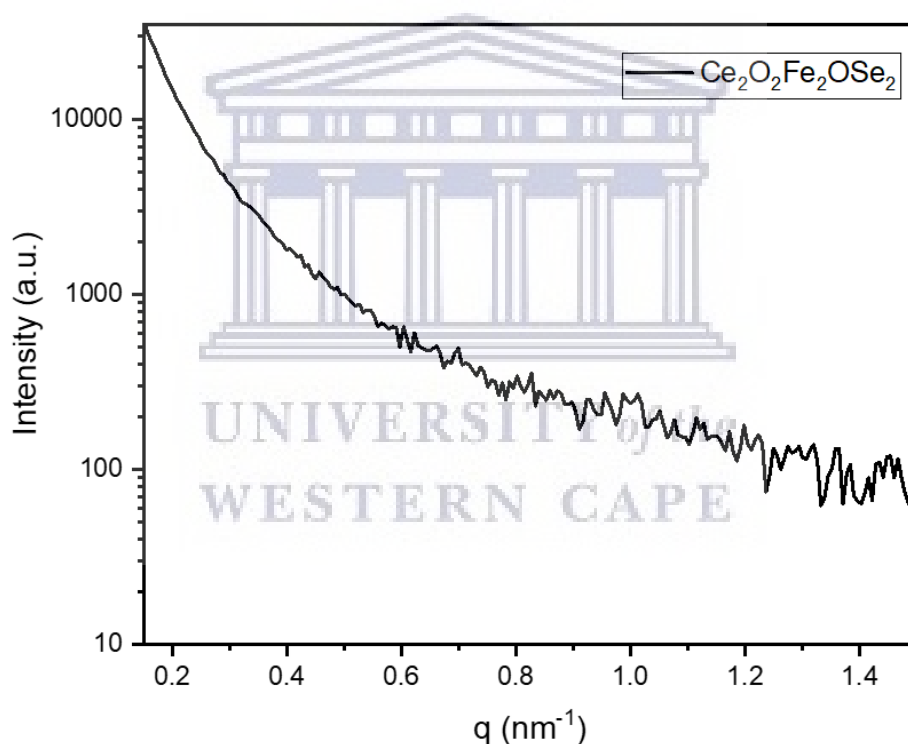
Figure 4.3.4.1: SAXS scattering spectra vs q of the $Ce_2O_2Fe_2OSe_2$ nanoparticles.
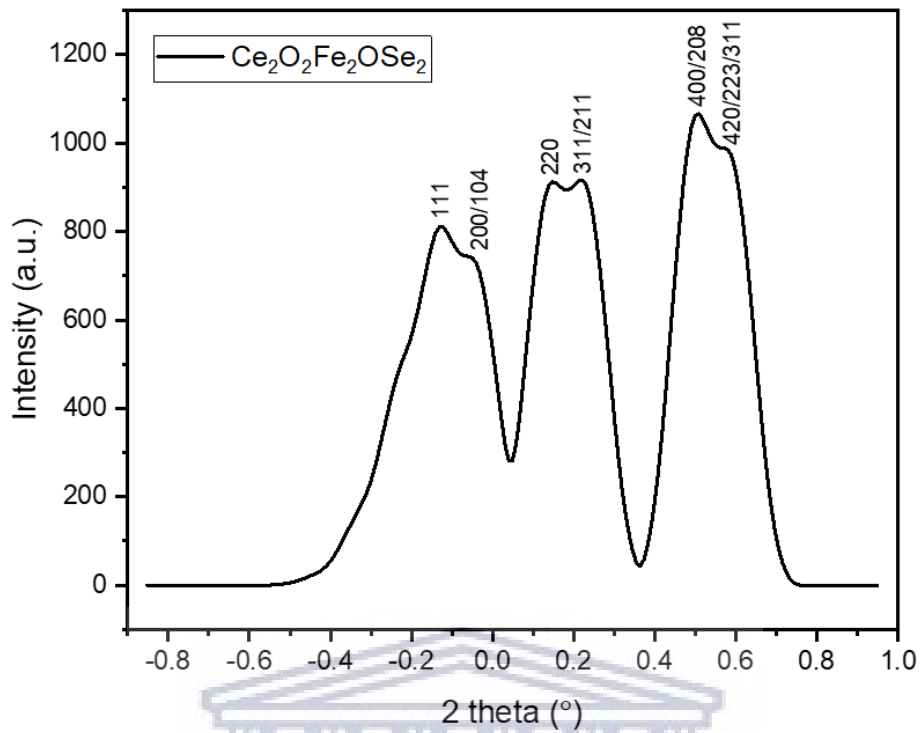
Figure 4.3.4.2: SAXS scattering spectra vs 2 theta of the $Ce_2O_2Fe_2OSe_2$ nanoparticles.
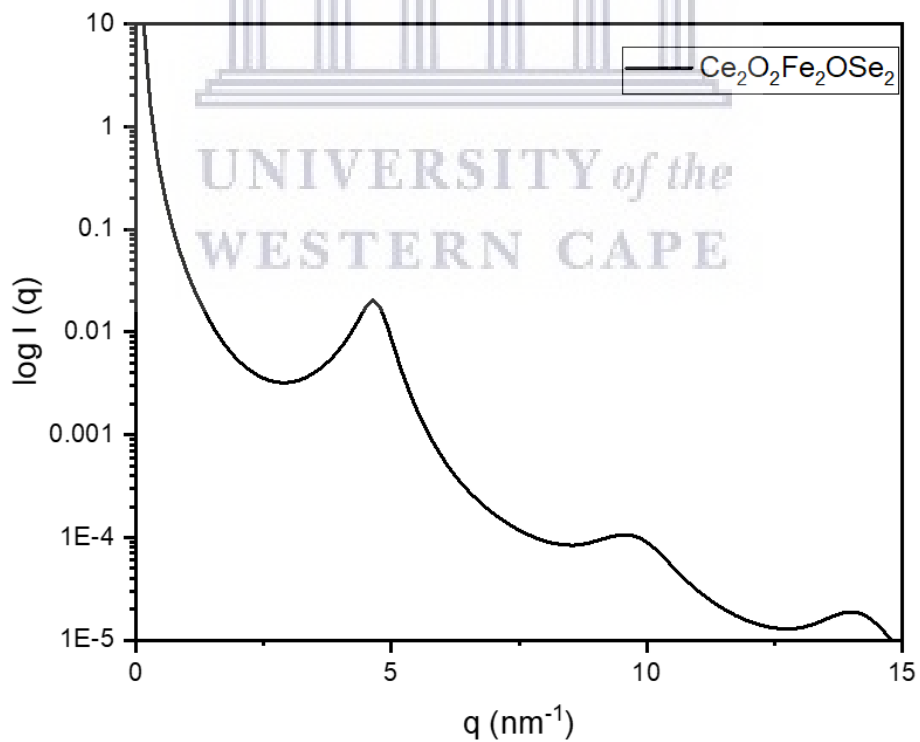
Figure 4.3.4.3: SAXS plot of the form factor of the $Ce_2O_2Fe_2OSe_2$ nanoparticles.
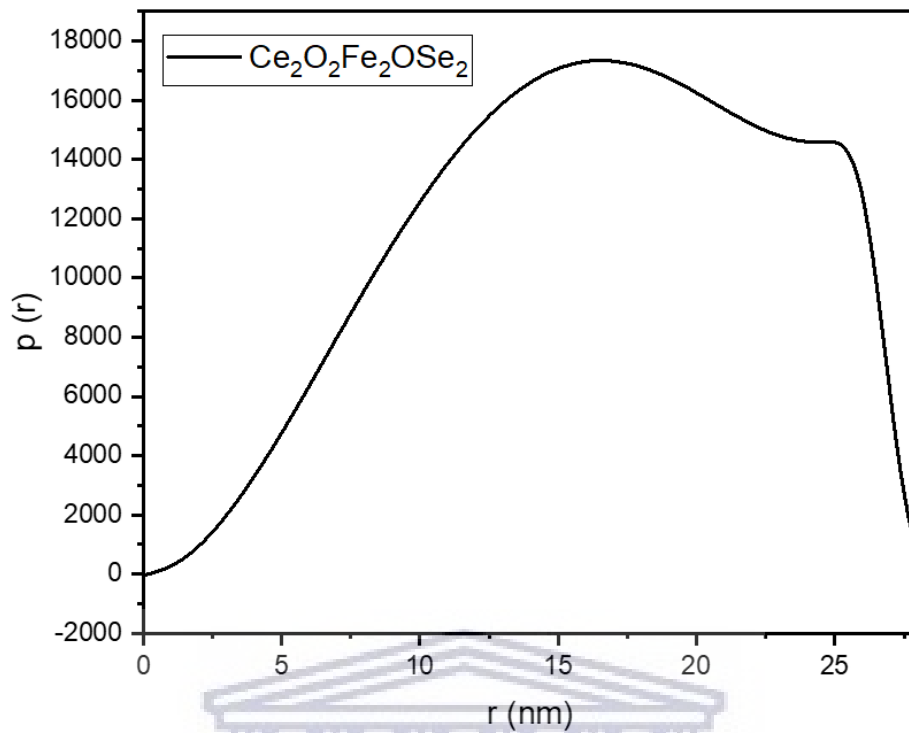
Figure 4.3.4.4: SAXS plot of the internal structure of the $Ce_2O_2Fe_2OSe_2$ nanoparticles.
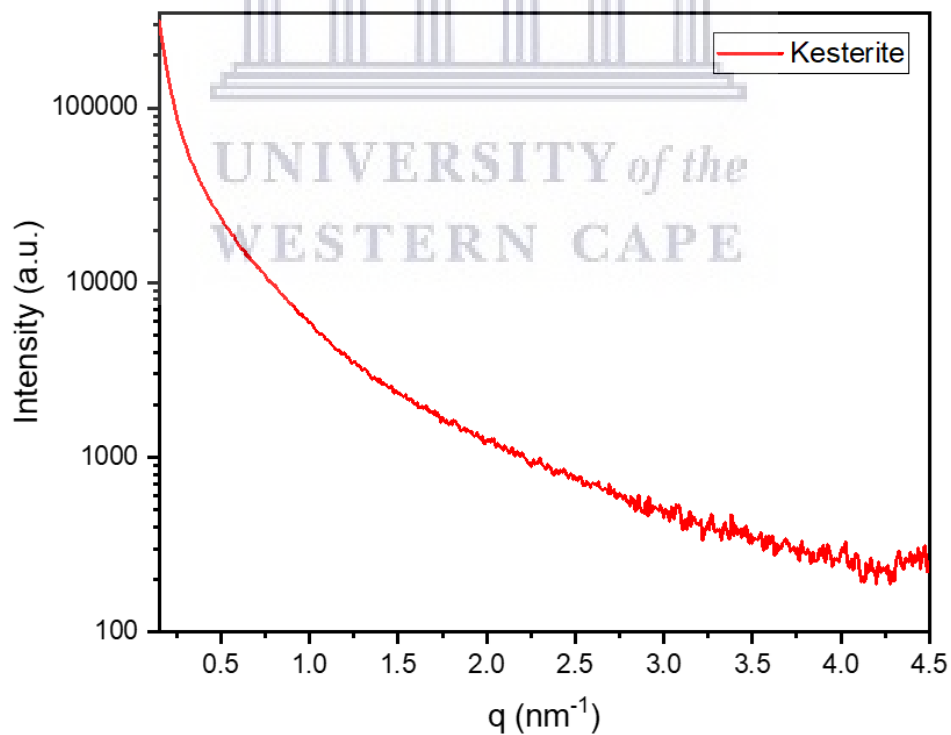
Figure 4.3.4.5: SAXS scattering spectra vs q of the kesterite nanoparticles.
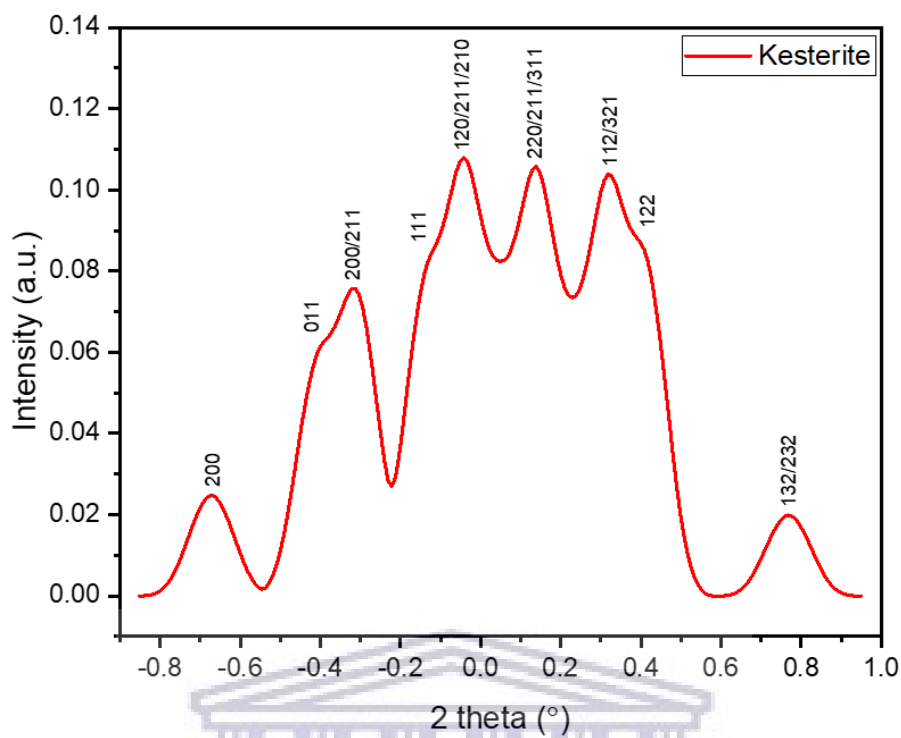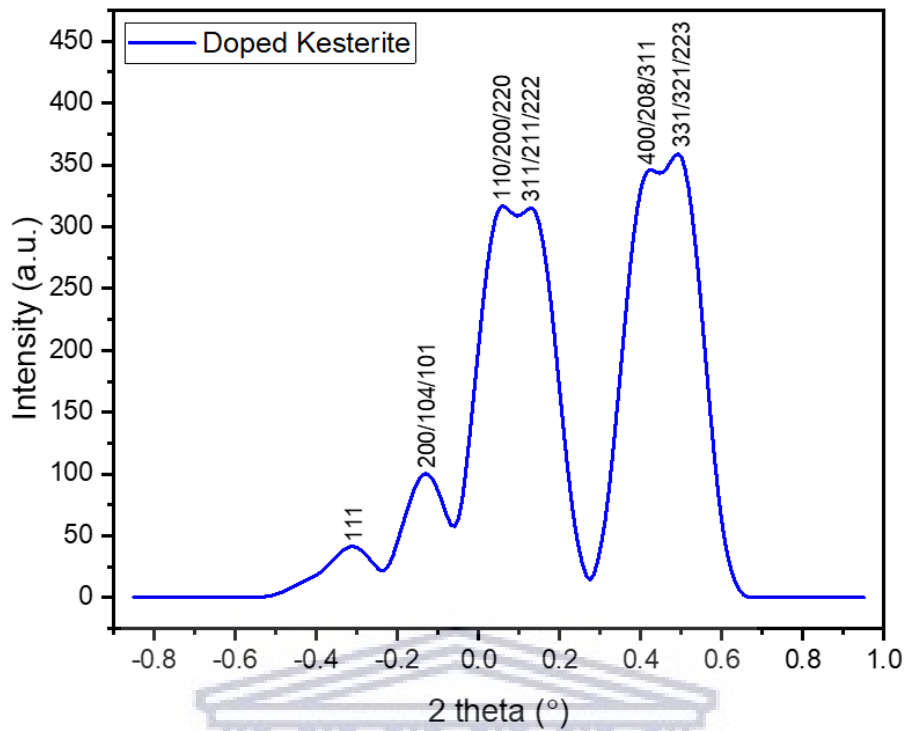
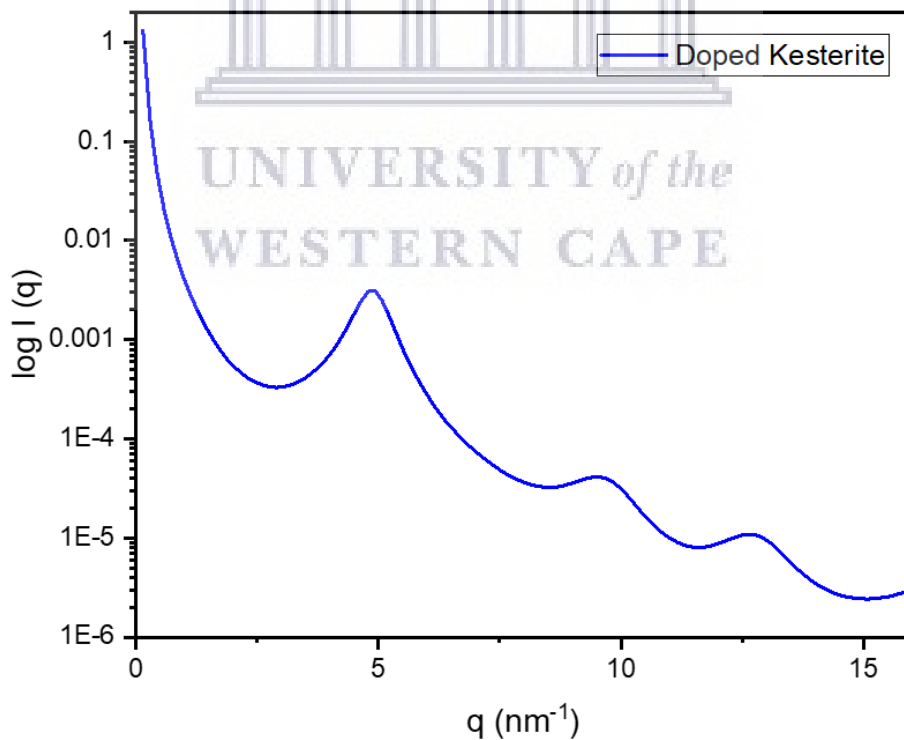**Figure 4.3.4.6:** SAXS scattering spectra vs 2 theta of the kesterite nanoparticles.
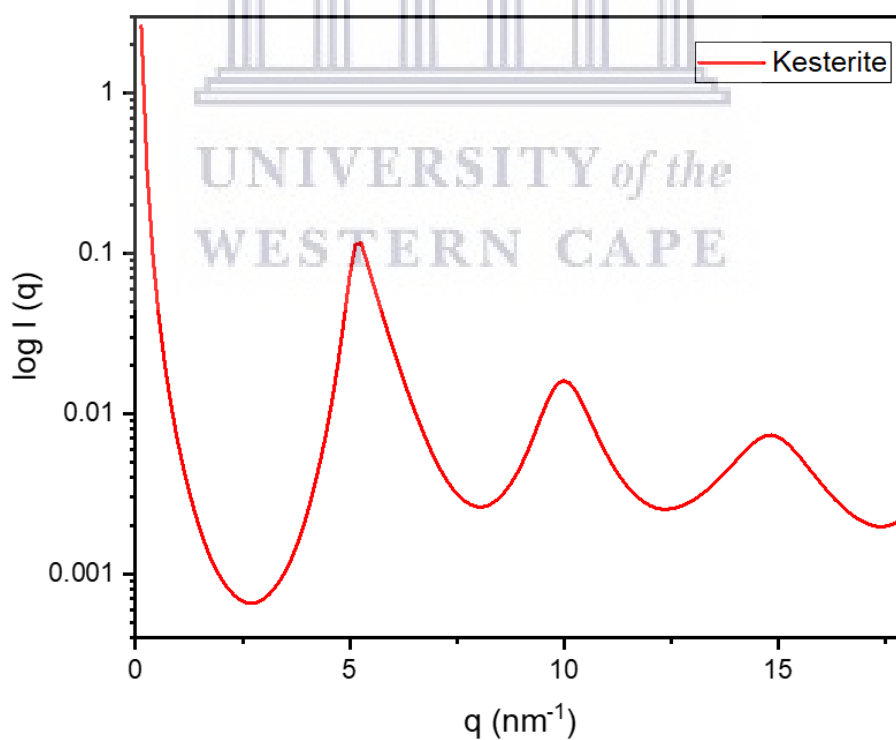
Figure 4.3.4.7: SAXS plot of the form factor of the kesterite nanoparticles.
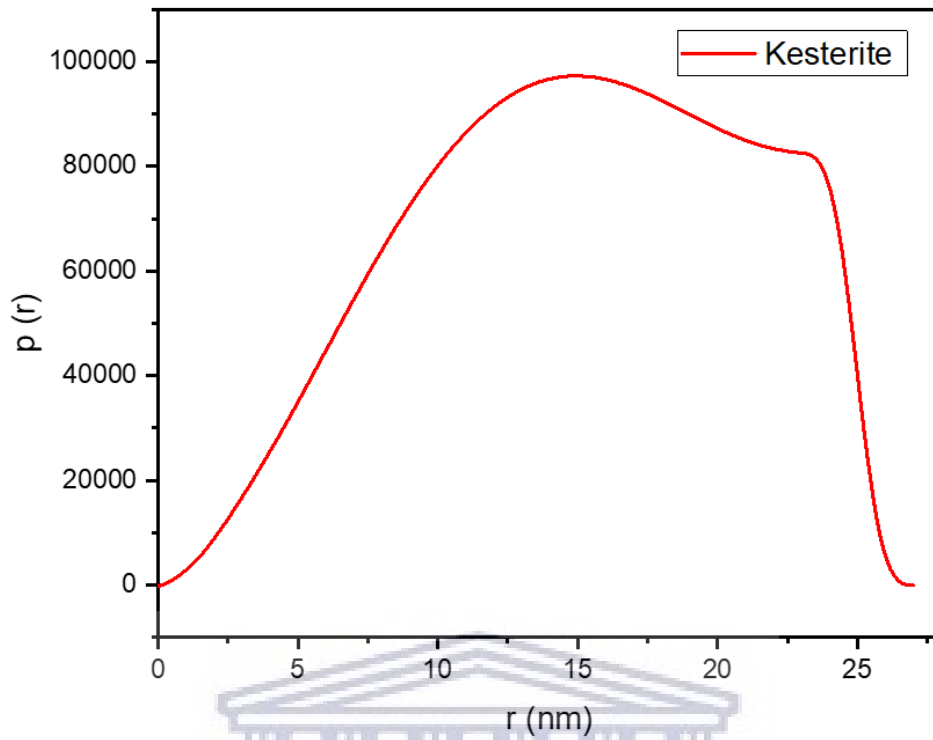
Figure 4.3.4.8: SAXS plot of the internal structure of the kesterite nanoparticles.
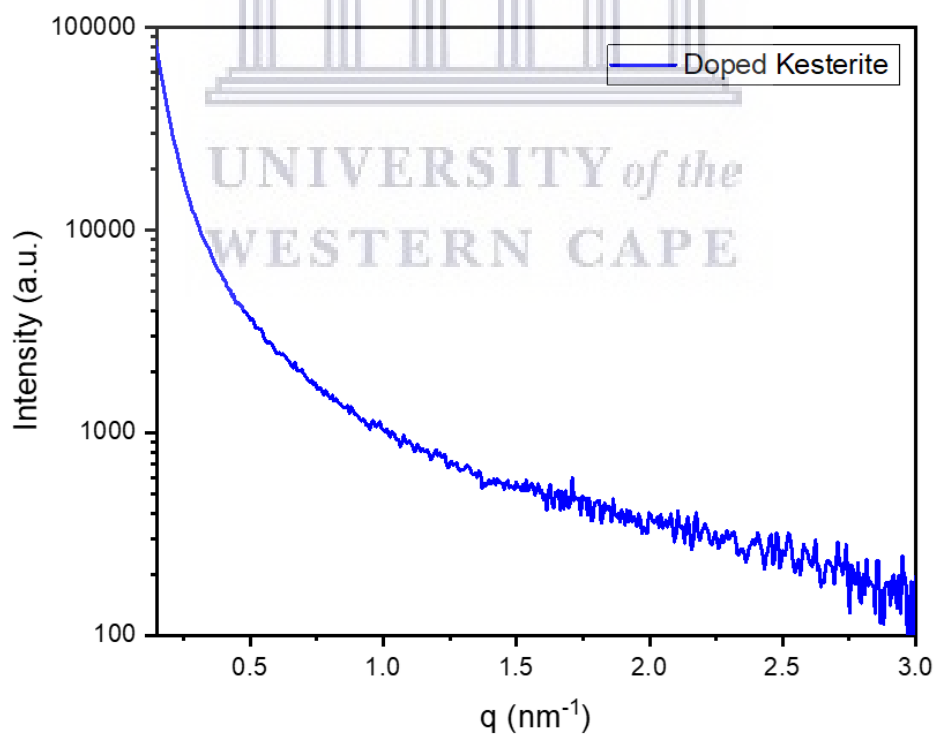
Figure 4.3.4.9: SAXS scattering spectra vs q of the doped kesterite nanoparticles.

91

Figure 4.3.4.10: SAXS scattering spectra vs 2 theta of the doped kesterite nanoparticles.

Figure 4.3.4.11: SAXS plot of the form factor of the doped kesterite nanoparticles.
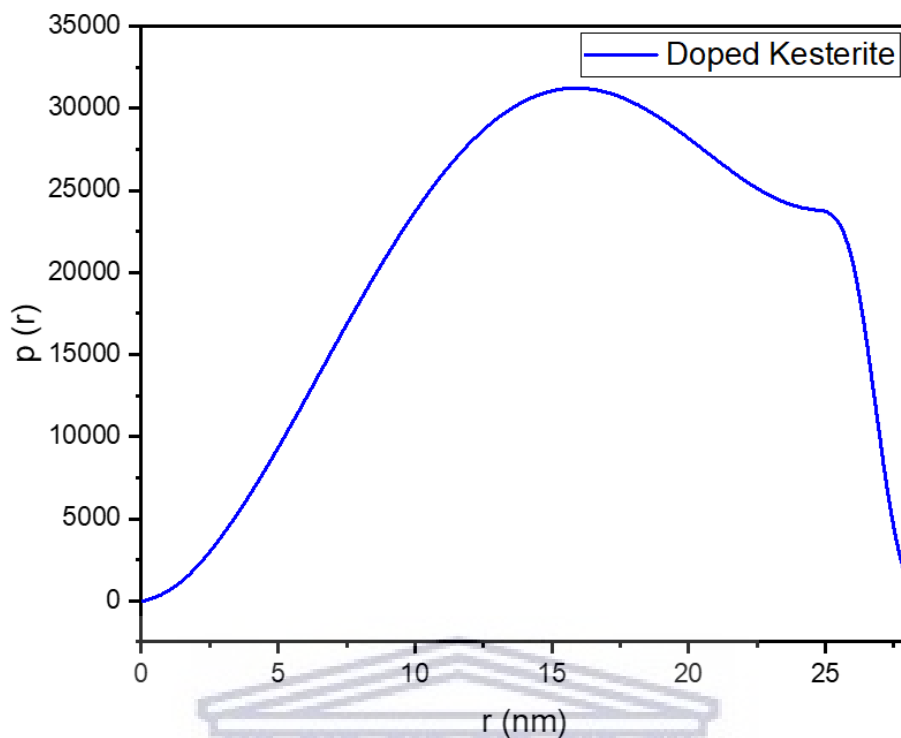
Figure 4.3.4.12: SAXS plot of the internal structure of the doped kesterite nanoparticles.
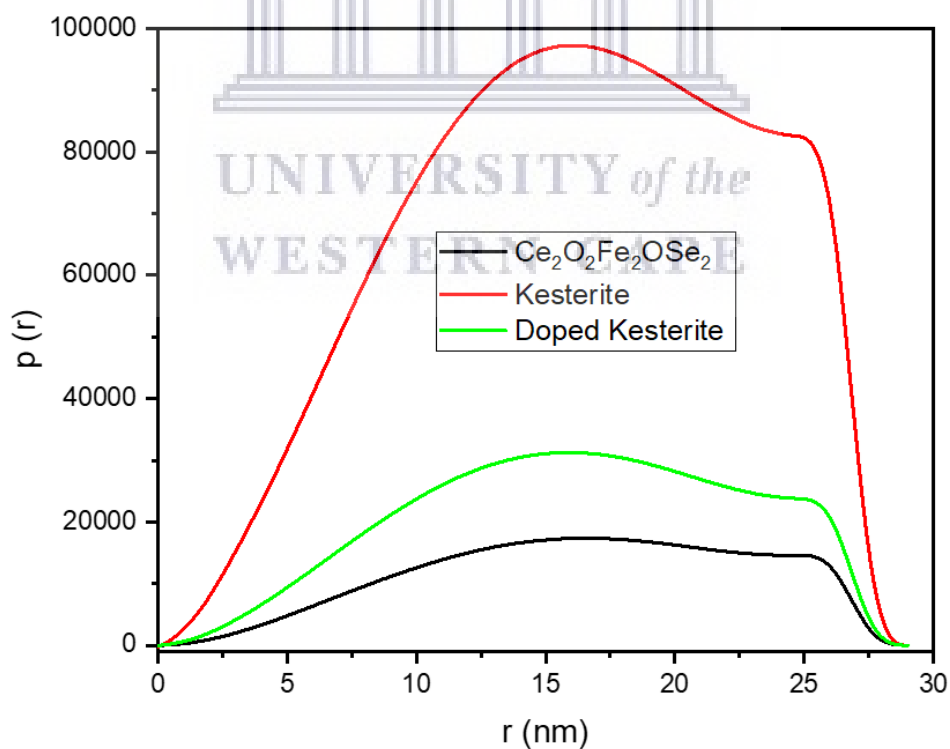
Figure 4.3.4.13: SAXS plot of the internal structure of the $Ce_2O_2Fe_2OSe_2$, kesterite and doped kesterite nanoparticles.

Fig. 4.3.4.1, 4.3.4.5 and 4.3.4.9 provide the SAX scattering (intensity vs q) plots of the $Ce_2O_2Fe_2OSe_2$, kesterite and doped kesterite nanoparticles respectively. These plots of the materials show that the samples all had different shapes along with their general overall shape and different sizes which results from the different levels of particle agglomeration in each sample as well as the occurrences of excess DEG in the kesterite and doped kesterite sample. Fig. 4.3.4.2, 4.3.4.6 and 4.3.4.10 show the SAX scattering (intensity vs 2 theta) plots of the $Ce_2O_2Fe_2OSe_2$, kesterite and doped kesterite nanoparticles respectively. These plots relate the SAXS spectra to the XRD spectra of the materials, although the SAXS intensity vs 2 theta plots contain overlapping intensity peaks due to the occurrence of agglomeration amongst the nanoparticles, this occurs due to the fact that SAXS is a small-angle scattering characterization technique while XRD is a wide-angle diffraction technique. The shape analysis plots Fig. 4.3.4.1 – 4.3.4.9 reveals that the nanoparticles were agglomerated and that synthesised nanoparticles had a core and a shell, with the core being the nanoparticles themselves and the shell being attributed to the DEG solvent. The $Ce_2O_2Fe_2OSe_2$, kesterite and doped kesterite nanoparticles all possess a mixed hollow sphere and flat disk shape, with the $Ce_2O_2Fe_2OSe_2$ nanoparticles being non uniform and highly agglomerated, this agglomeration is seen and further supported by the shoulder seen in the SAXs plot of the $Ce_2O_2Fe_2OSe_2$ nanoparticles. Both the kesterite and doped kesterite nanoparticles posses' spherical and rod like shapes with the shoulders in the SAXs plots of the nanoparticles indicating high levels of agglomeration. The mix spherical like and rod/ flat disk like shapes obtained for the nanoparticles agrees with the morphology earlier reported from the HRSEM and HRTEM results [35–38].
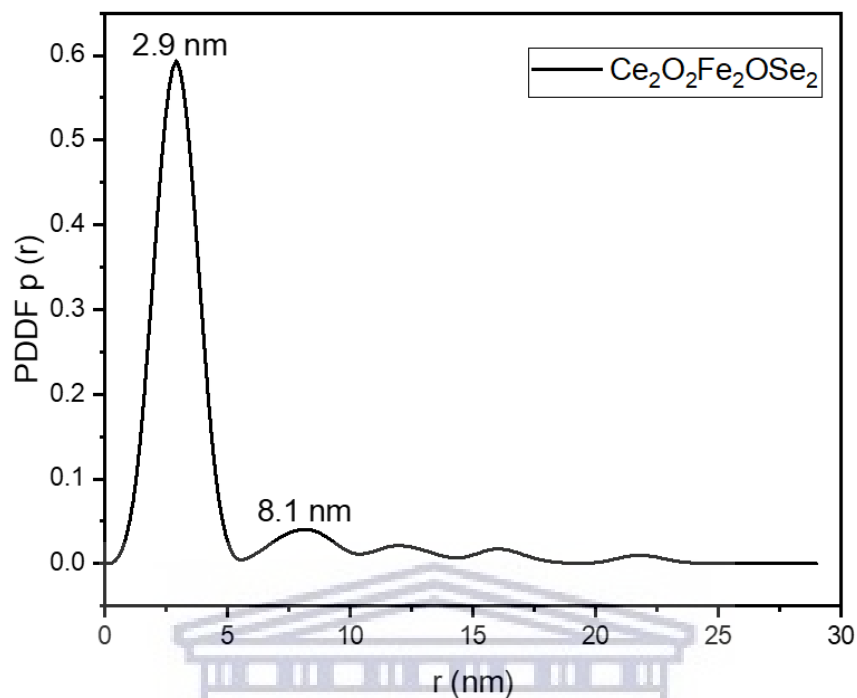
4.3.5 Size Distribution

Figure 4.3.5.1: SAXS plot of the size distribution by number of the $Ce_2O_2Fe_2OSe_2$ nanoparticles.

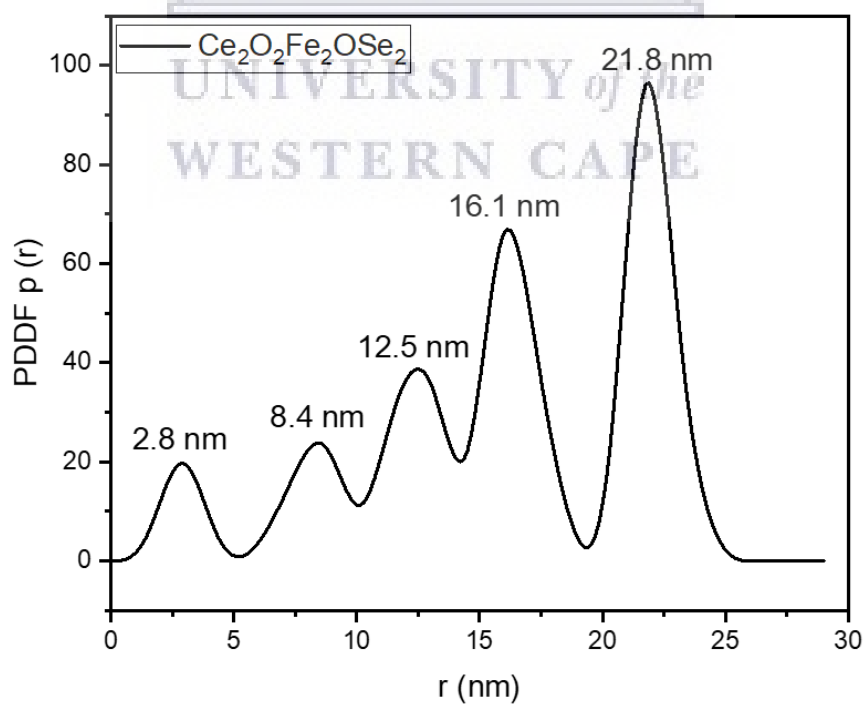**Figure 4.3.5.2:** SAXS plot of the size distribution by volume of the $Ce_2O_2Fe_2OSe_2$ nanoparticles.
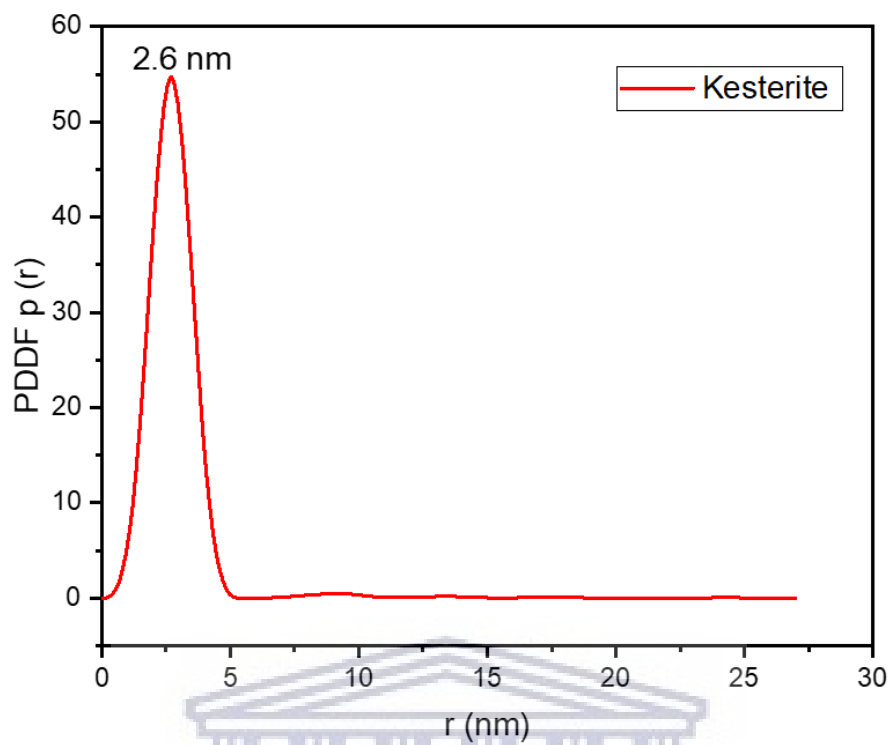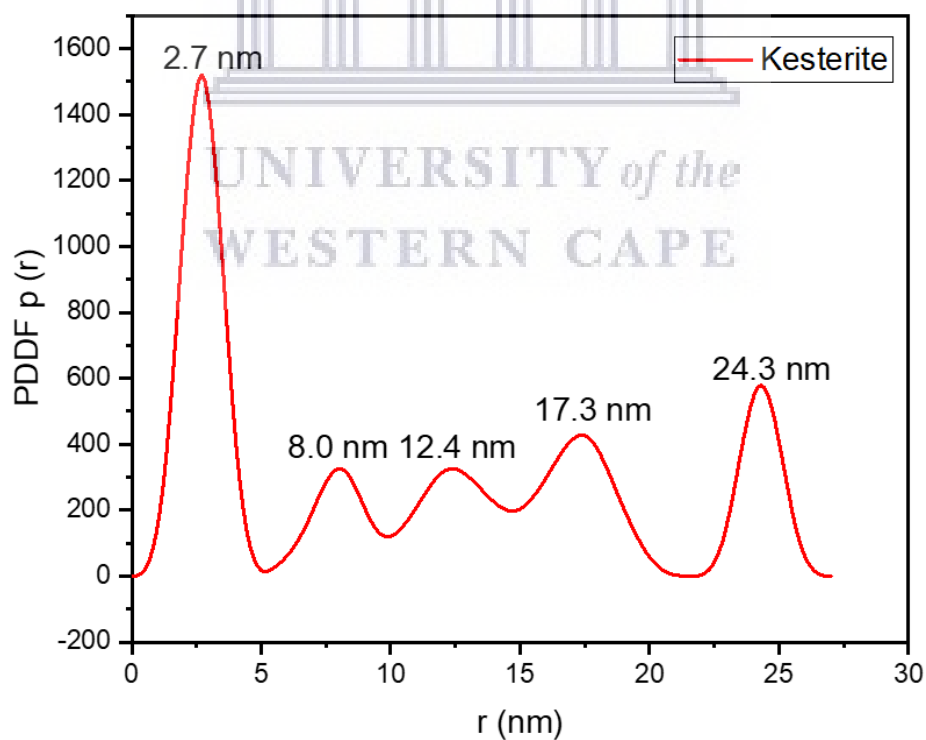
Figure 4.3.5.3: SAXS plot of the size distribution by number of the kesterite nanoparticles.

Figure 4.3.5.4: SAXS plot of the size distribution by volume of the kesterite nanoparticles.
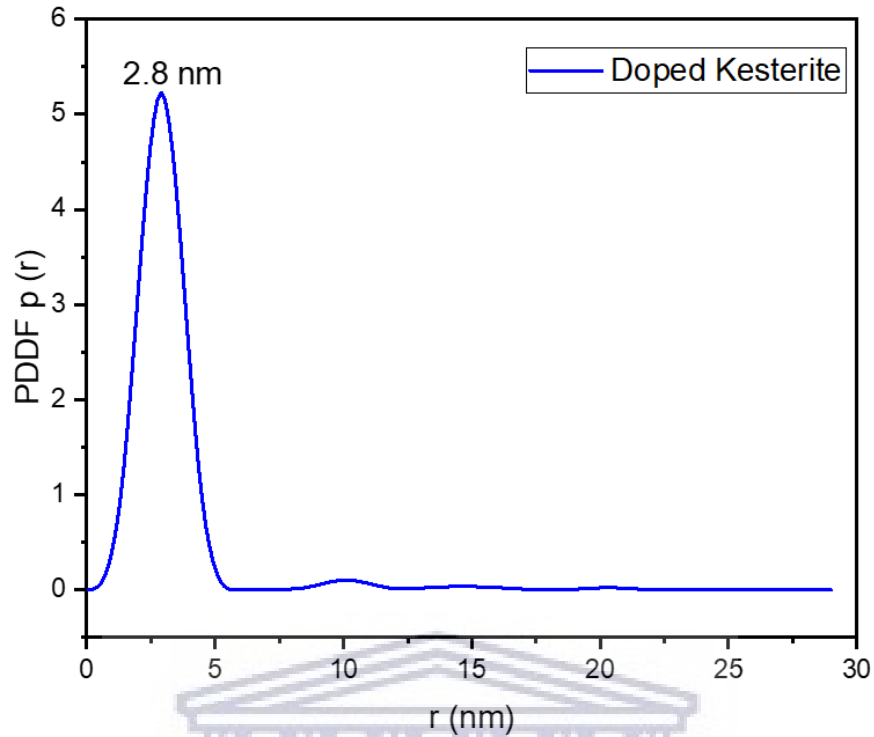
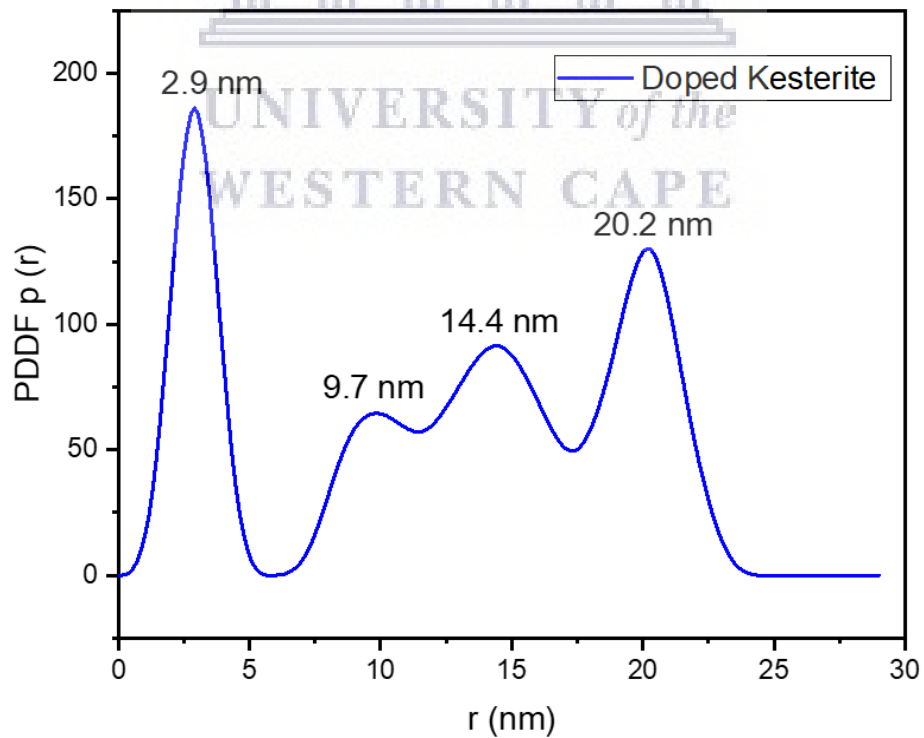**Figure 4.3.5.5:** SAXS plot of the size distribution by number of the doped kesterite nanoparticles.

Figure 4.3.5.6: SAXS plot of the size distribution by volume of the doped kesterite nanoparticles.

The size distribution of the nanoparticles was analysed using SAXs for the particle size and XRD for the crystal size. Fig. 4.3.5.1 and Fig. 4.3.5.2 shows the size distribution by number and volume of the $Ce_2O_2Fe_2OSe_2$ nanoparticles respectively, which shows a mean particle size of 2,8/ 2,9 nm, as well as a massive particle size of 21,8 nm, shown in the distribution by volume plot. This is due to intense agglomeration of the nanoparticles. Further looking at the distribution by volume plot, the peaks at 8,4 nm, 12,5 nm and 16,1 nm are due to the presence of CeO, FeO and SeO which did not attach strongly to the $Ce_2O_2Fe_2OSe_2$ nanoparticles. Fig. 4.3.5.3 and Fig. 4.3.5.4 shows the size distribution by number and volume of the Kesterite nanoparticles respectively, which shows a mean particle size of 2,6/ 2,7 nm, the particle size of 21,8 nm, shown in the distribution by volume plot is due to agglomeration of the nanoparticles. Further looking at the distribution by volume plot, the peaks at 8,0 nm, 12,4 nm and 17,3 nm are due to the presence of the DEG solvent and loosely attached Cu, Sn and Se. Fig. 4.3.5.5 and Fig. 4.3.5.6 shows the size distribution by number and volume of the Doped Kesterite nanoparticles respectively, which shows a mean particle size of 2,8/ 2,9 nm, the big particle size of 20.2 nm, shown in the distribution by volume plot is due to agglomeration of the nanoparticles. Further looking at the distribution by volume plot, the peaks at 9,7 nm and 14.4 nm are due to the presence of the DEG solvent and loosely attached Cu/ Ce and Se [39–41].

Together with SAXS analysis, XRD is also a very useful tool for size analysis. The XRD pattern was used in order to determine the crystal size of nanoparticles (D), through the use of the Scherrer equation:

$$D = \frac{0.9\lambda}{\beta\cos\theta}$$ (4.1)

"Where λ is the wavelength which has a value of 1.5406 nm, β is the full width at half maximum (FWHM) and θ is the Bragg angle, k is Scherrer constant which can take values from 0.9 to 1, where 0.9 was chosen". The FWHM value is converted to radians. The plane calculated was the (112) which had the most intense peak [7,42–47].
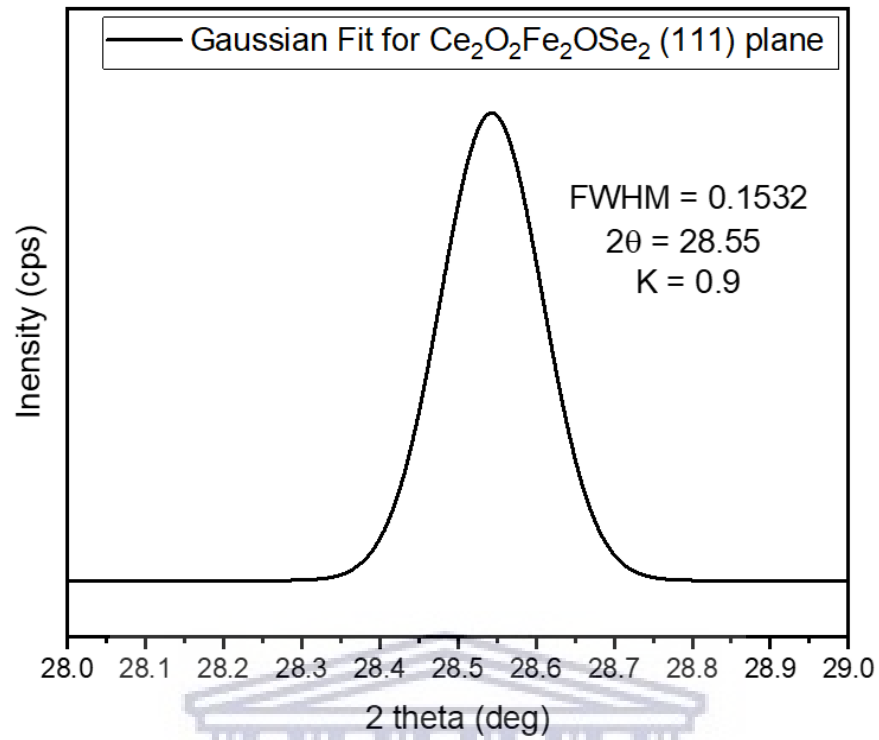
Figure 4.3.5.7: Gaussian fit of the Ce$_2$O$_2$Fe$_2$OSe$_2$ nanoparticles (111) plane.
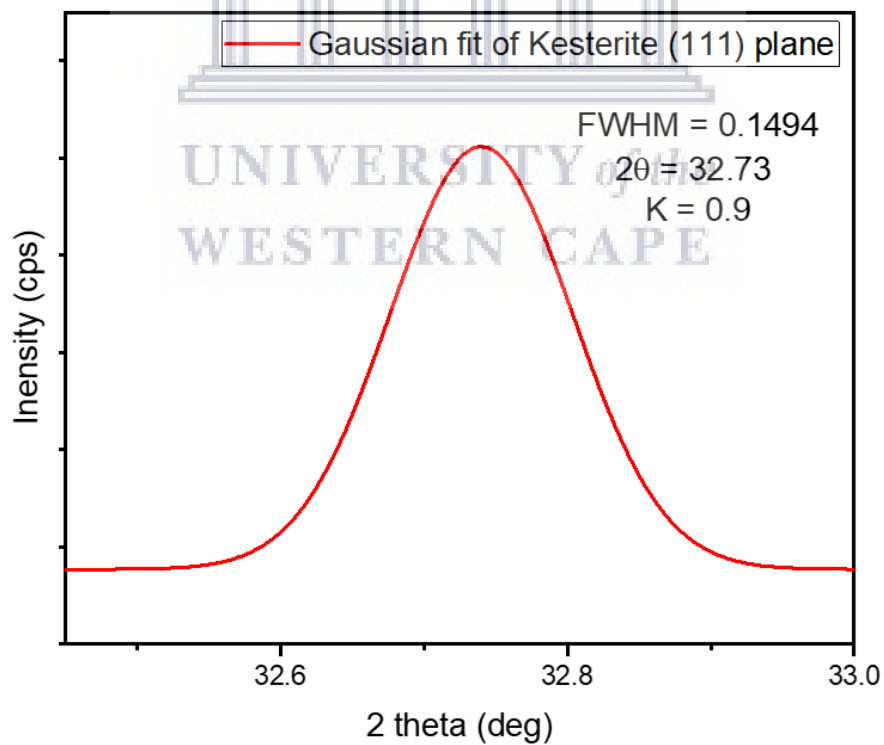

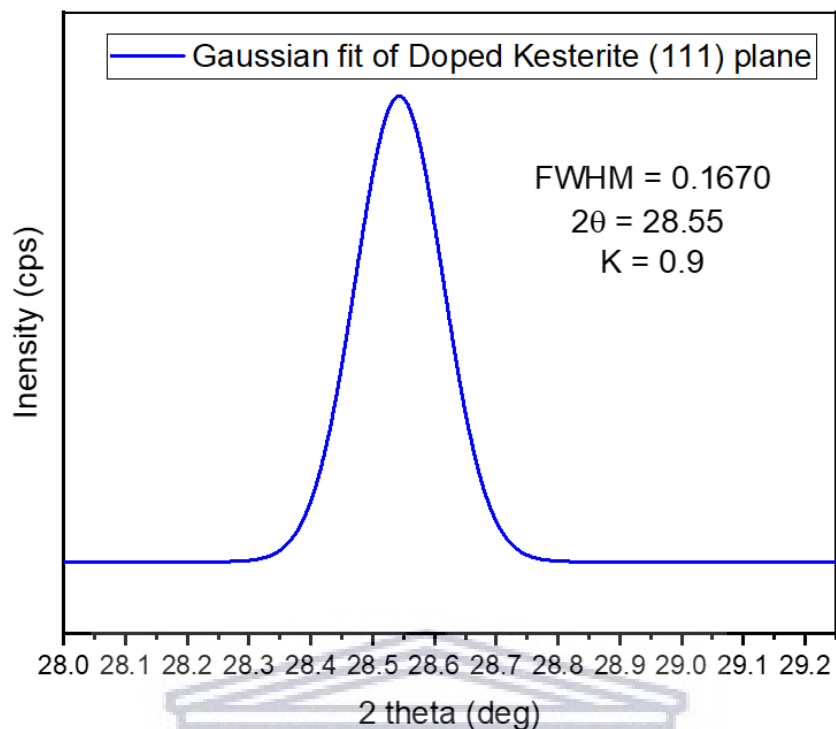**Figure 4.3.5.8:** Gaussian fit of the kesterite nanoparticles (111) plane.

Figure 4.3.5.9: Gaussian fit of the doped kesterite nanoparticles (111) plane.

Table 4.3.5: Parameters for the Gaussian plots of the nanoparticles.

	2θ (°)	Θ (RAD)	FWHM (°)	FWHM (RAD)	K	λ (nm)	Crystal size (nm)
$Ce_2O_2Fe_2OSe_2$	28.55	0.4983	0.1532	0.0026	0.9	1.5406	9.34
Kesterite	32.73	0.5712	0.1494	0.0026	0.9	1.5406	9.67
Doped kesterite	28.55	0.4983	0.1670	0.0029	0.9	1.5406	8.57

The sizes of the cerium and iron oxyselenide, kesterite and doped kesterite nanoparticles are 9.34 nm, 9.67 nm and 8.57 nm respectively. The SAXs shows an individual particle size of 2.8 nm, 2.7 nm and 2.9 nm for the cerium and iron oxyselenide, kesterite and doped kesterite nanoparticles respectively while showing sizes between 8.5 to 12.4 nm for the $Ce_2O_2Fe_2OSe_2$, 8 to 12.4 nm for the kesterite and 9.7 to 14.4 nm for the doped kesterite. These sizes are due to use of small angle scattering rays across the nanoparticles in order to obtain the sizes while the sizes of the nanoparticles obtained from XRD are in the range of

8 to 10 nm which are obtained using wide angle rays, thus the SAXs and XRD data present different particle sizes [48,49].

4.4 Thermogravimetric analysis

The "thermal stability" of the synthesized nanoparticles was analysed by "thermogravimetry analysis". The instrument used for the analysis is a PerkinElmer Pyriss simultaneous TGA/DTA Analyzer (TG-4000). The temperature range used for the analysis is from 30 ˚C to 650 ˚C under nitrogen gas atmosphere at a heating rate of 10 ˚C min^{-1}.
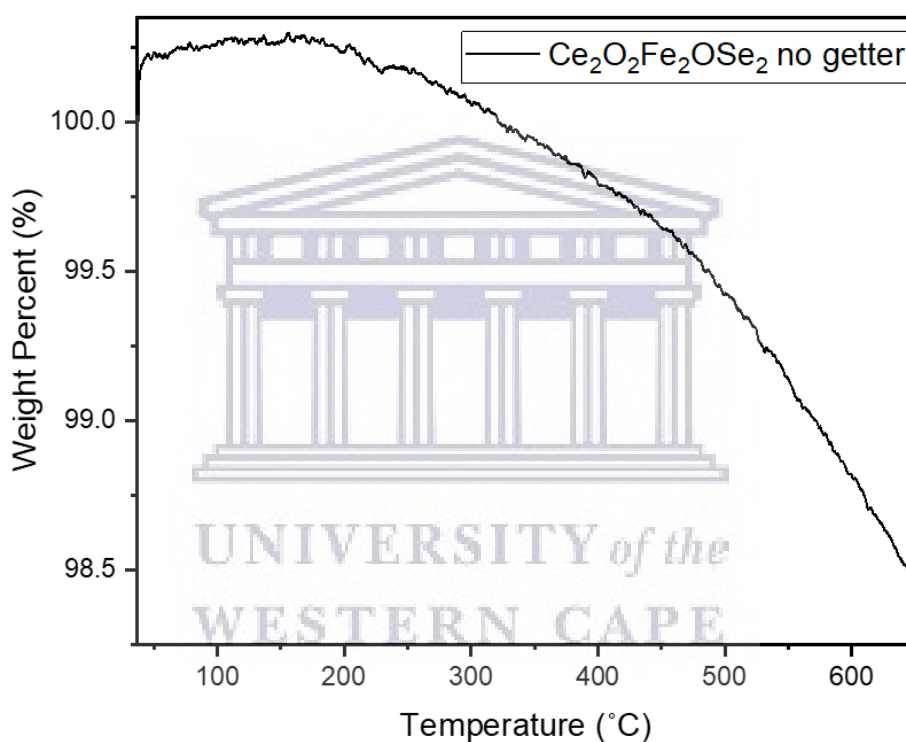

Figure 4.4.1: TGA curve of the $Ce_2O_2Fe_2OSe_2$ nanoparticles without an oxygen getter.

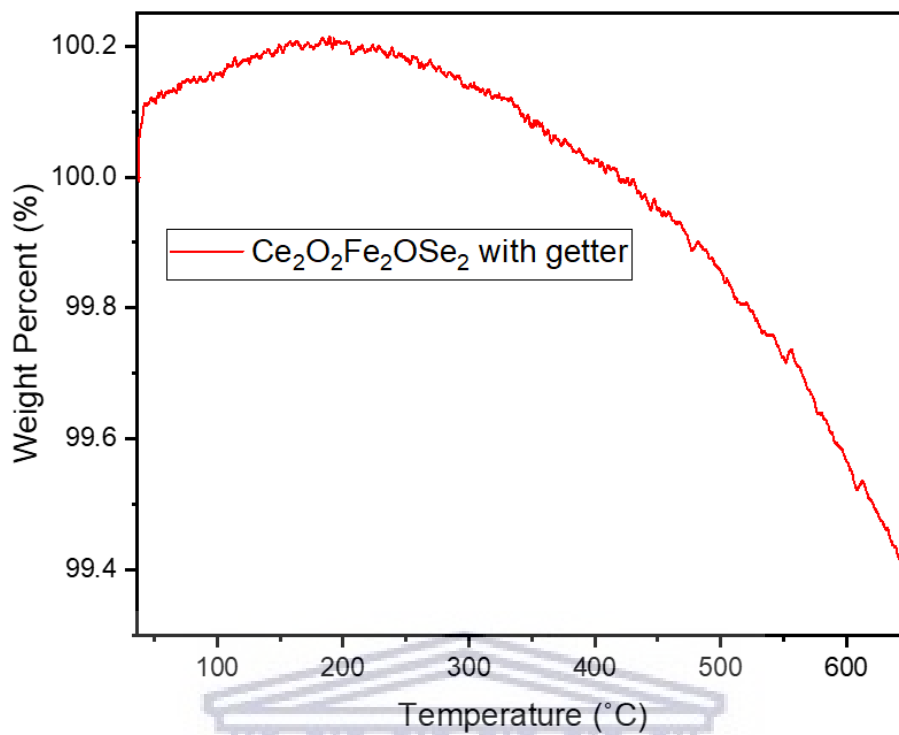**Figure 4.4.2:** TGA curve of the $Ce_2O_2Fe_2OSe_2$ nanoparticles with an oxygen getter.
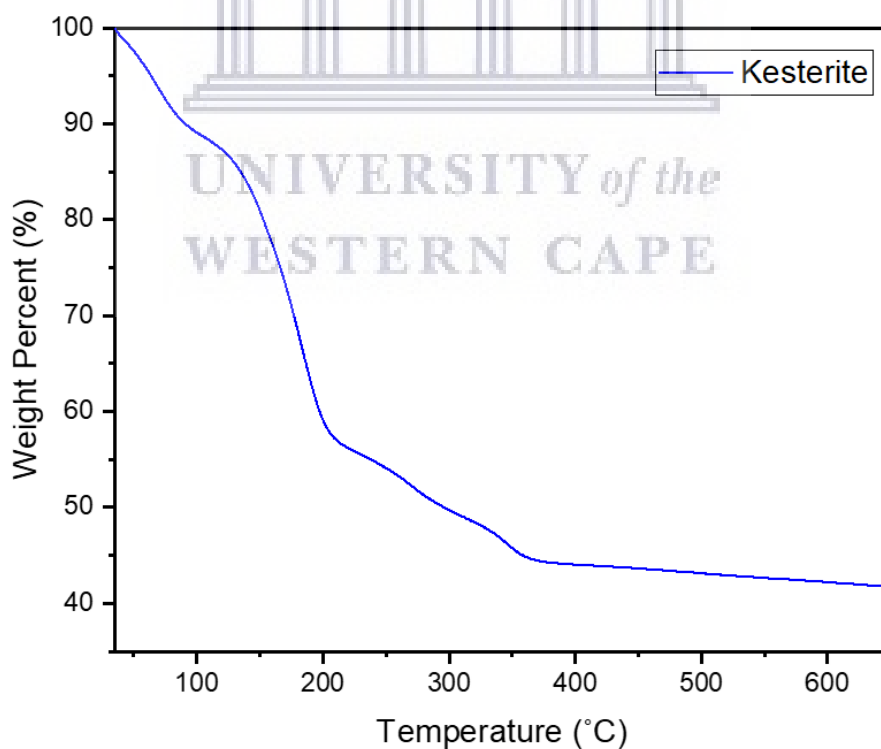

Figure 4.4.3: TGA curve of the kesterite nanoparticles.

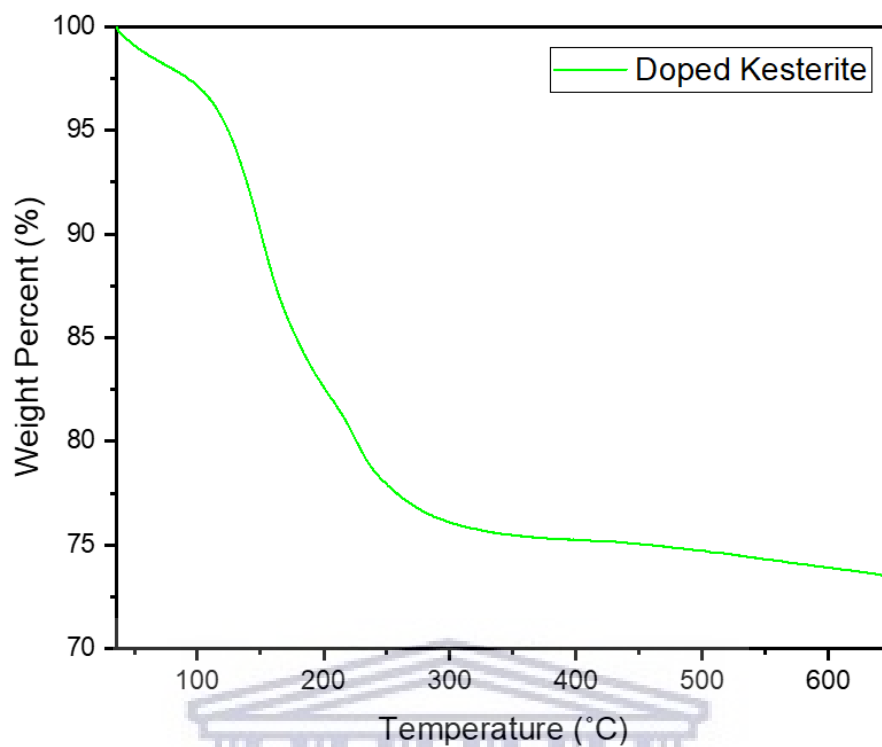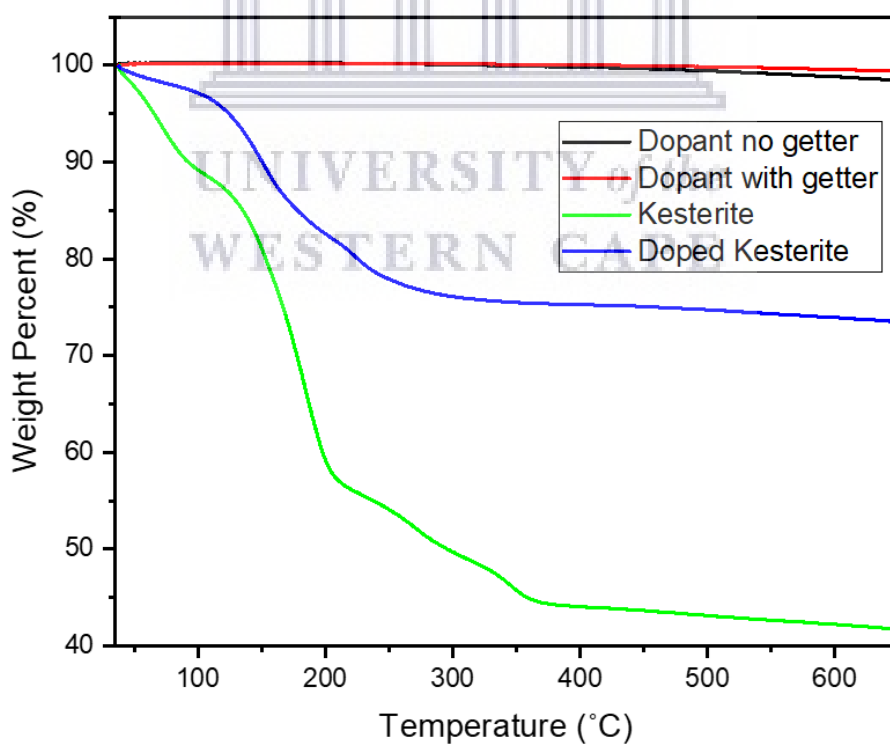**Figure 4.4.4:** TGA curve of the doped kesterite nanoparticles.

Figure 4.4.5: TGA curve of the $Ce_2O_2Fe_2OSe_2$ nanoparticles with and without an oxygen getter, kesterite nanoparticles and doped kesterite nanoparticles.

Fig. 4.4.1 shows the TGA curve for the $Ce_2O_2Fe_2OSe_2$ nanoparticles without an oxygen getter, and the initial 0.025% increase in the weight percent between 30 – 280 °C is due to the fact that this material was basically synthesized via calcination at high temperatures so the increase in temperature seems to have produced more of the sample, which was not expected at all. The loss of 0.5% between 281 – 465 °C is caused by the loss of any moisture still contained within the sample. The further loss of 1% between 466 – 650 °C is due to any impurities being burnt away from the sample. Therefore, there is a total of 1.5% that is lost from the $Ce_2O_2Fe_2OSe_2$ nanoparticles without an oxygen getter. Fig. 4.4.2 shows the TGA curve for the $Ce_2O_2Fe_2OSe_2$ nanoparticles with an oxygen getter. This getter seems to make a difference during the heating of the sample. Similar to the sample without a getter, there is an initial 0.025% increase in the weight percent, but this time between 30 – 360 °C, this is because the getter makes the synthesis of the sample more efficient. The loss of 0.5% between 361 – 650 °C is caused by the loss of any moisture still contained within the sample. And there is no further loss of weight percent as there is minimal impurities in this sample due to the better synthesis efficiency resulting from the getter. Fig. 4.4.3 shows the TGA curve for the kesterite nanoparticles, the initial loss of 10% at 100 °C is caused by the evaporation of water. The drastic loss of 32% from 100 – 200 °C is attributed to the loss of Isopropanol or DEG from the nanoparticles. The loss of 10% from 200 – 360 °C results from the loss of chalcogens that where not actually incorporated into the lattice of the nanoparticles. The further loss of 2% between 360 – 650 °C is due to the loss of Sn through the sublimation of SnSe. Fig. 4.6.4 shows the TGA curve for the doped kesterite nanoparticles, the initial loss of 4% at 100 °C is caused by the evaporation of water. The drastic loss of 23% from 100 – 200 °C is attributed to the loss of Isopropanol or DEG from the nanoparticles. The loss of 11% from 200 – 300 °C results from the loss of chalcogens that where not actually incorporated into the lattice of the nanoparticles. The further loss of 1% between 300 – 650 °C is due to the loss of Sn through the sublimation of SnSe. Thus, the doped kesterite follows the same trend as the kesterite but to a much lesser extent, this is due to the cerium and iron oxyselenide in the doped kesterite which drastically improves the thermal stability of the kesterite nanoparticles [50–53].

4.5 Optical Characterization

4.5.1 UV-Vis Spectroscopy

The optical properties of the $Ce_2O_2Fe_2OSe_2$, kesterite and doped kesterite nanoparticles were determined by UV-Vis spectroscopy (Fig. 4.5.1.1 – 4.5.1.15). The UV-Vis experiment was performed three times using different solvents which were dichloromethane, ethanol, and deionized water respectfully.
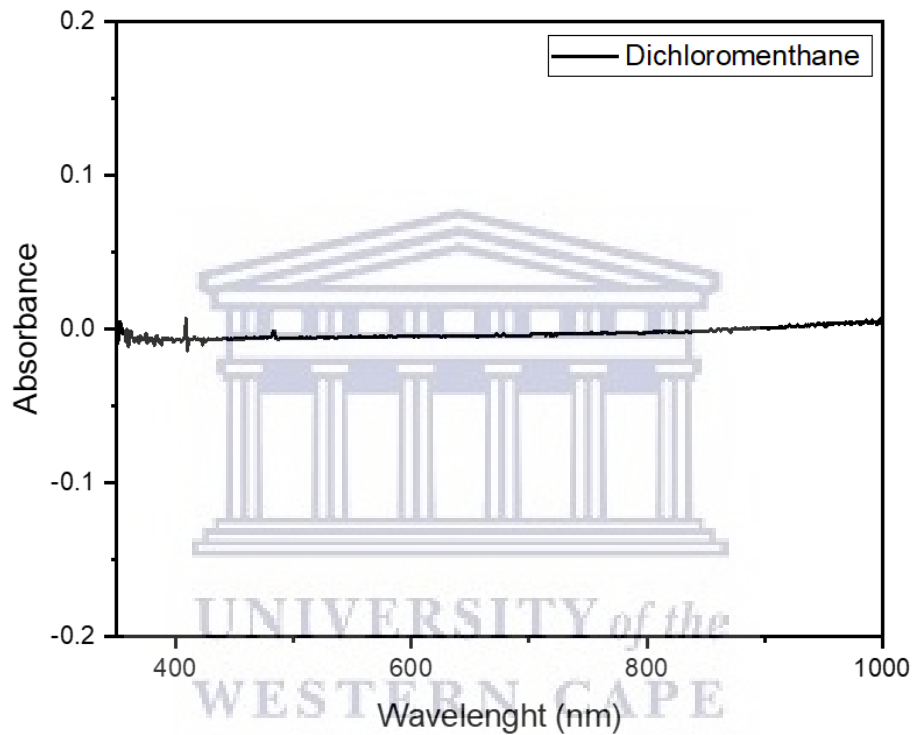

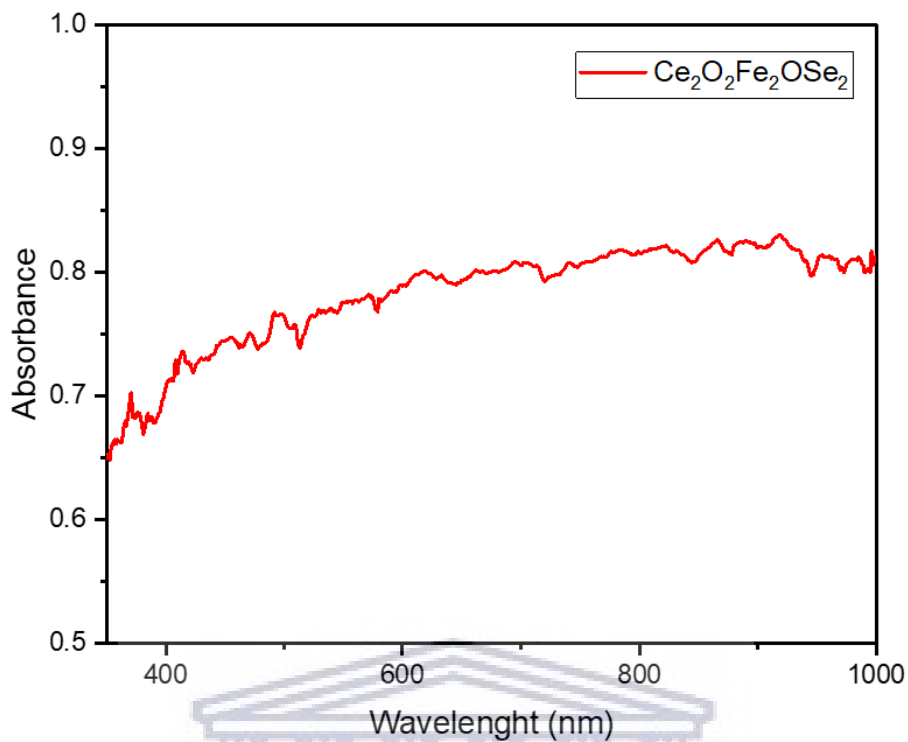**Figure 4.5.1.1:** UV-Vis spectrum of dichloromethane.

Figure 4.5.1.2: UV-Vis spectrum of the $Ce_2O_2Fe_2OSe_2$ nanoparticles in dichloromethane.

Figure 4.5.1.3: UV-Vis spectrum of the kesterite nanoparticles in dichloromethane.

Figure 4.5.1.4: UV-Vis spectrum of the doped kesterite nanoparticles in dichloromethane.

Figure 4.5.1.5: UV-Vis spectrum of the $Ce_2O_2Fe_2OSe_2$, kesterite and doped kesterite nanoparticles in dichloromethane.
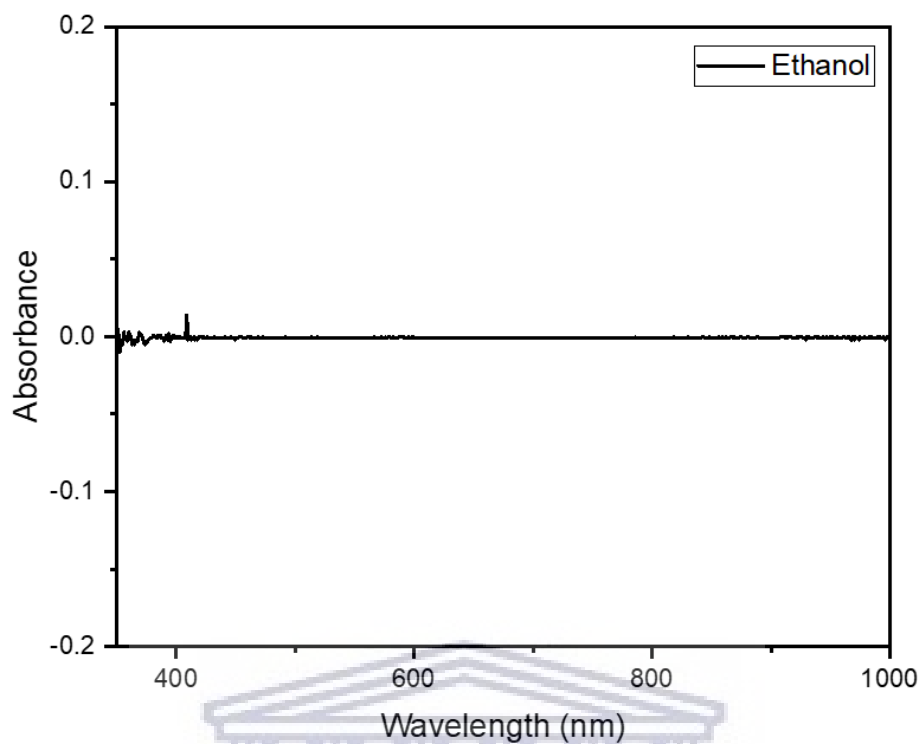
Figure 4.5.1.6: UV-Vis spectrum of ethanol.
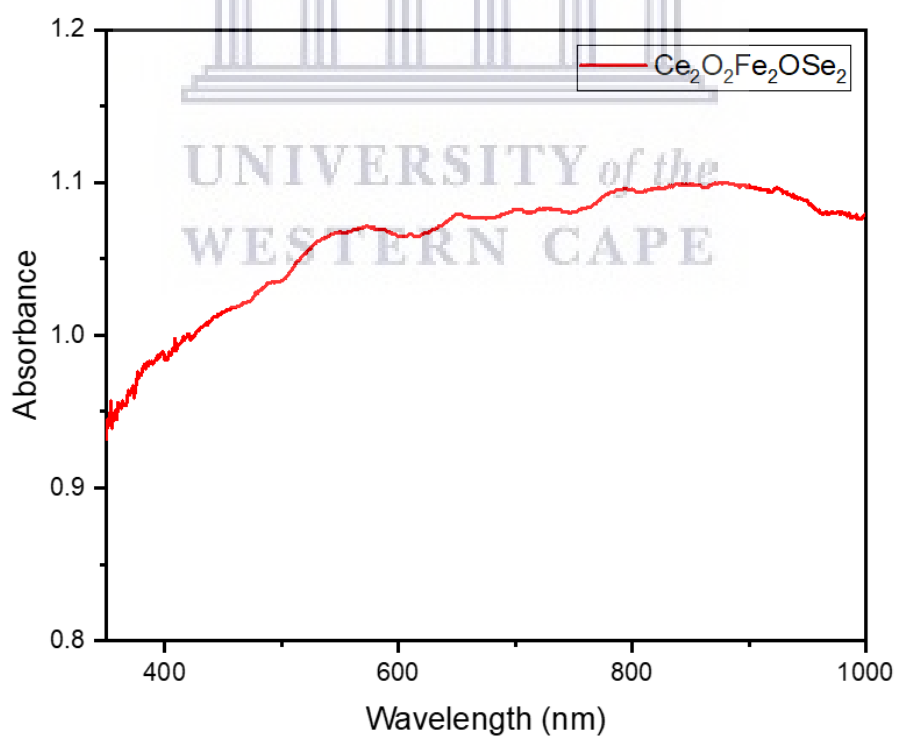
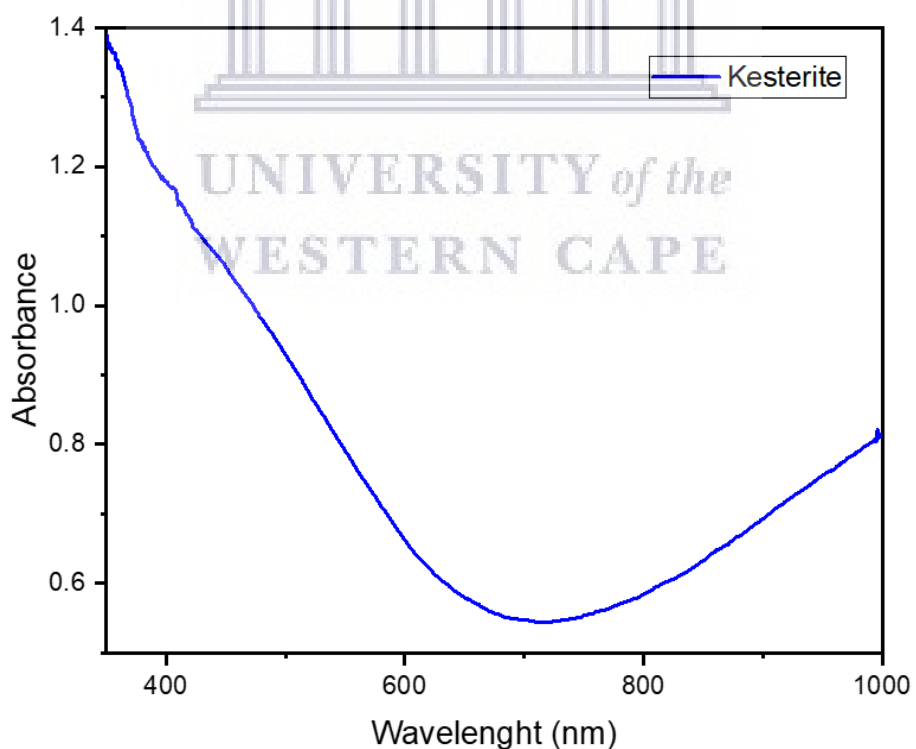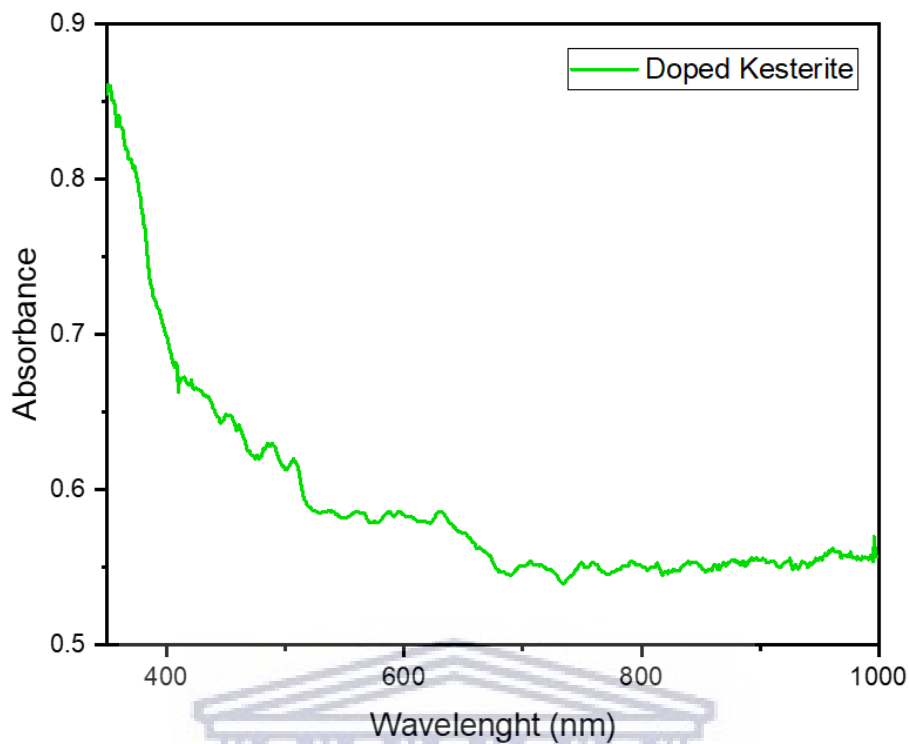**Figure 4.5.1.7:** UV-Vis spectrum of the $Ce_2O_2Fe_2OSe_2$ nanoparticles in ethanol.
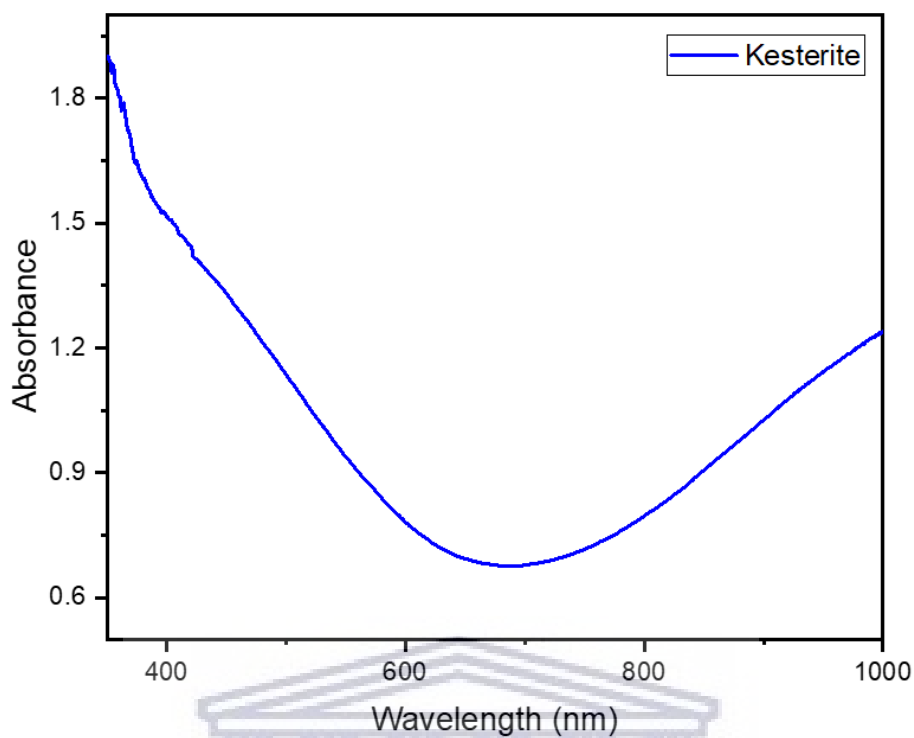
Figure 4.5.1.8: UV-Vis spectrum of the kesterite nanoparticles in ethanol.
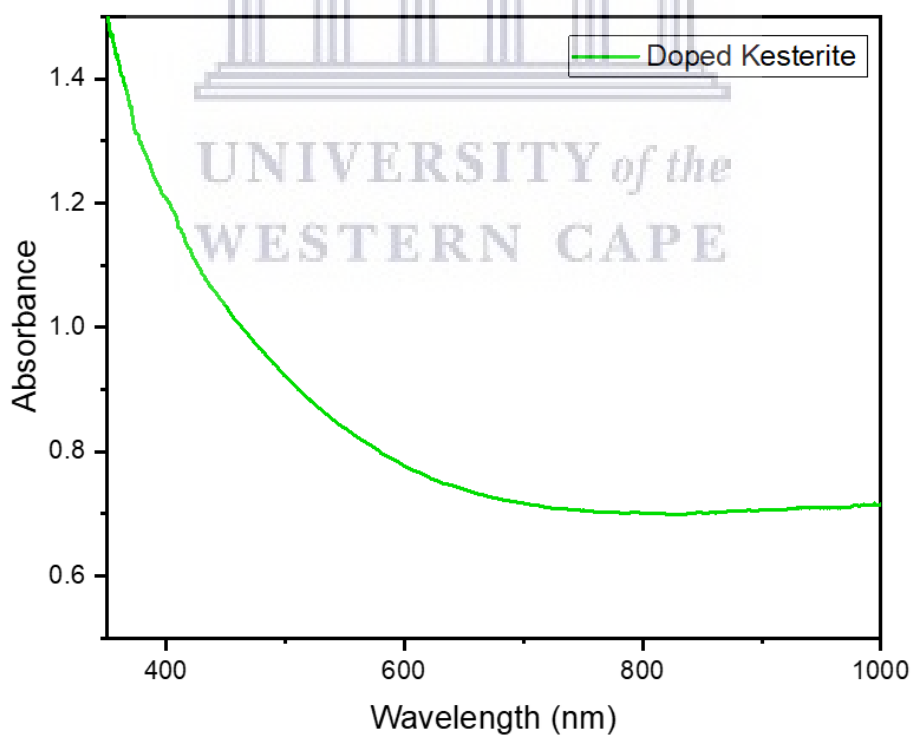
Figure 4.5.1.9: UV-Vis spectrum of the doped kesterite nanoparticles in ethanol.
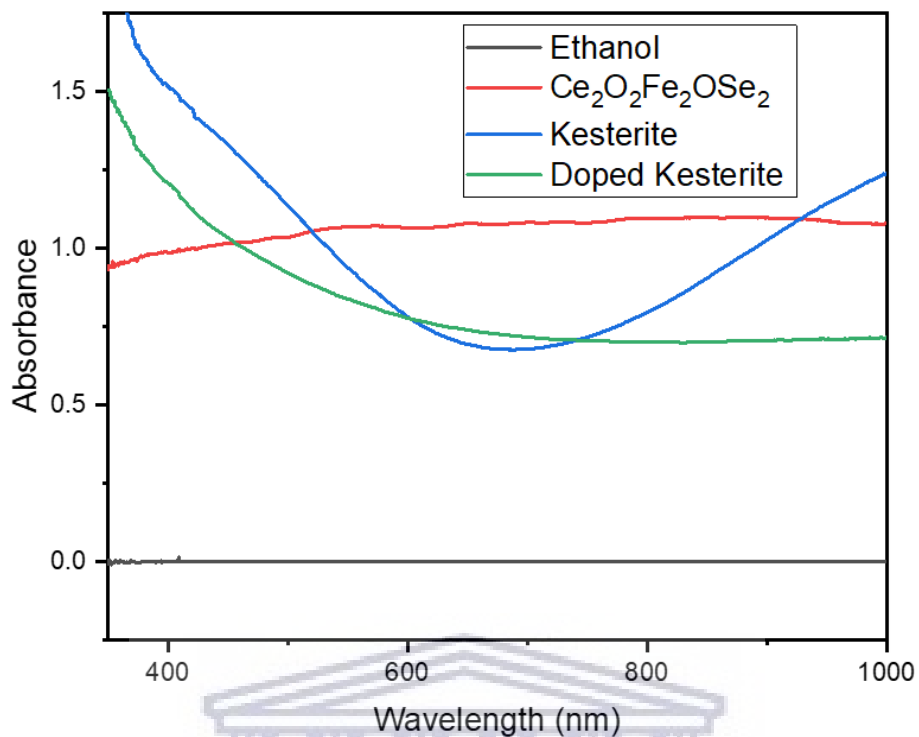
Figure 4.5.1.10: UV-Vis spectrum of the $Ce_2O_2Fe_2OSe_2$, kesterite and doped kesterite nanoparticles in ethanol.
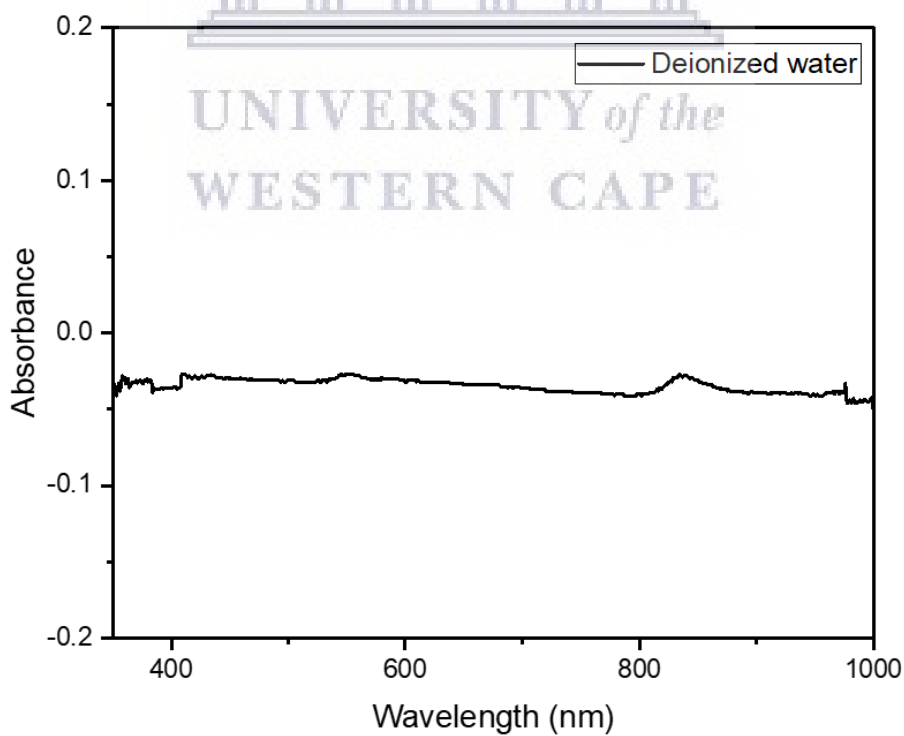
Figure 4.5.1.11: UV-Vis spectrum of deionized water.
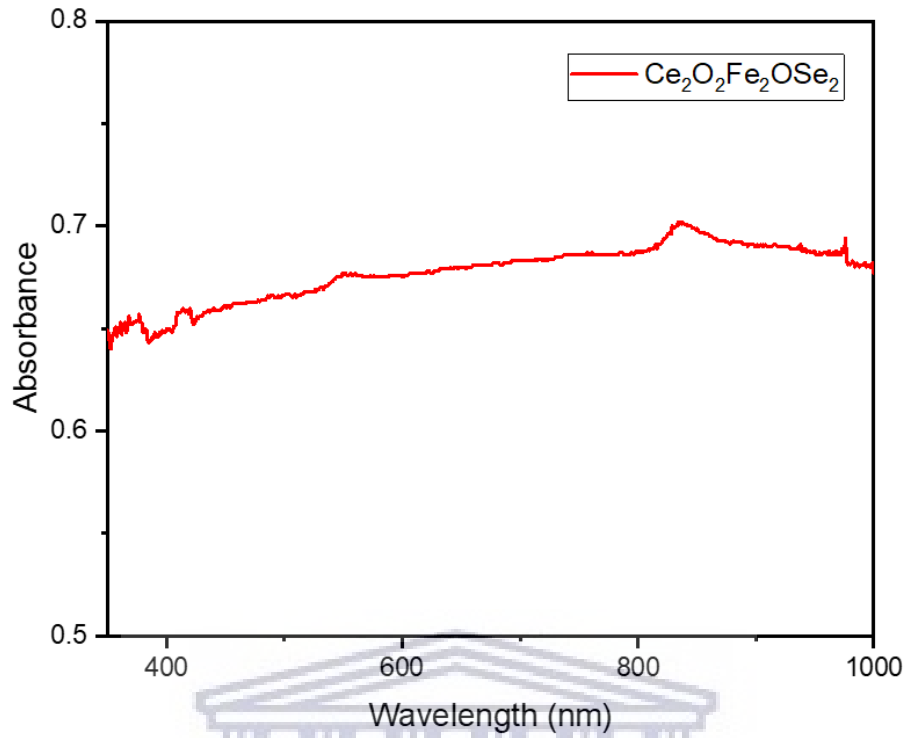
Figure 4.5.1.12: UV-Vis spectrum of the $Ce_2O_2Fe_2OSe_2$ nanoparticles in deionized water.

Figure 4.5.1.13: UV-Vis spectrum of the kesterite nanoparticles in deionized water.

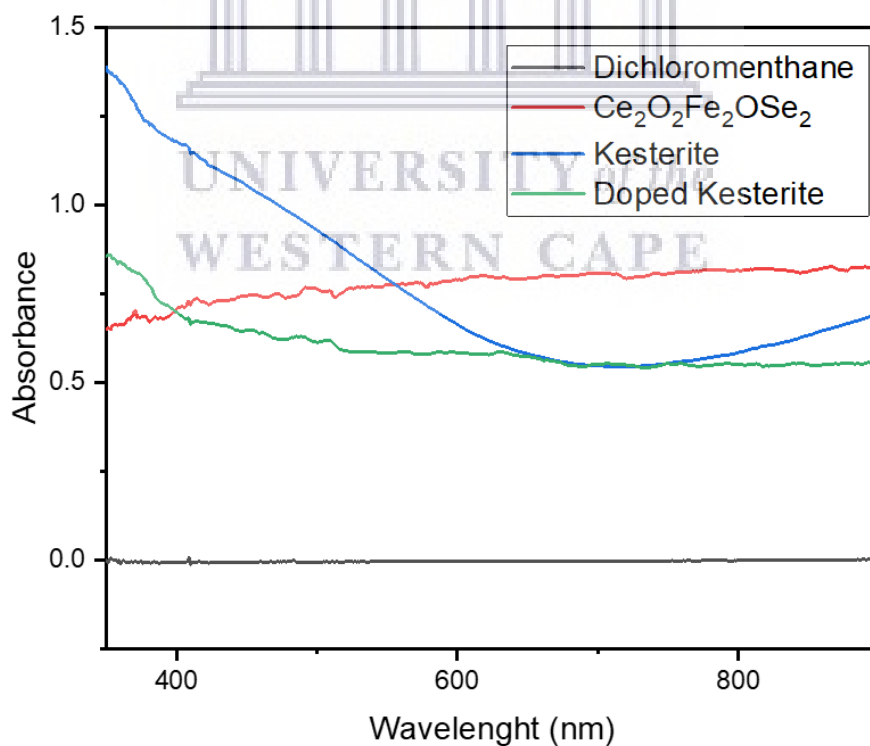**Figure 4.5.1.14:** UV-Vis spectrum of the doped kesterite nanoparticles in deionized water.

Figure 4.5.1.15: UV-Vis spectrum of the $Ce_2O_2Fe_2OSe_2$, kesterite and doped kesterite nanoparticles in deionized water.

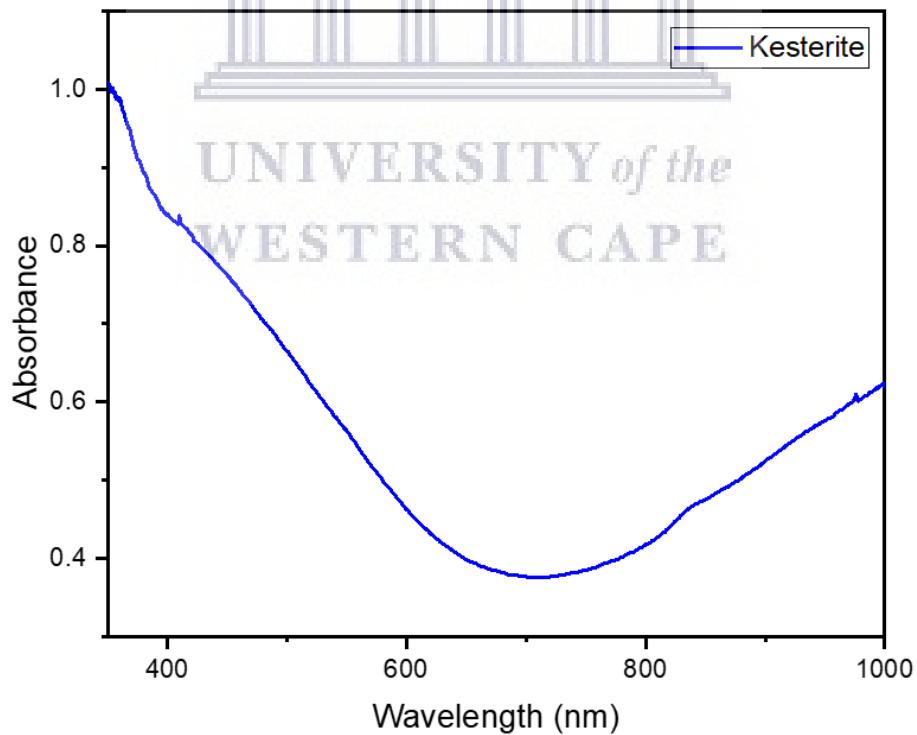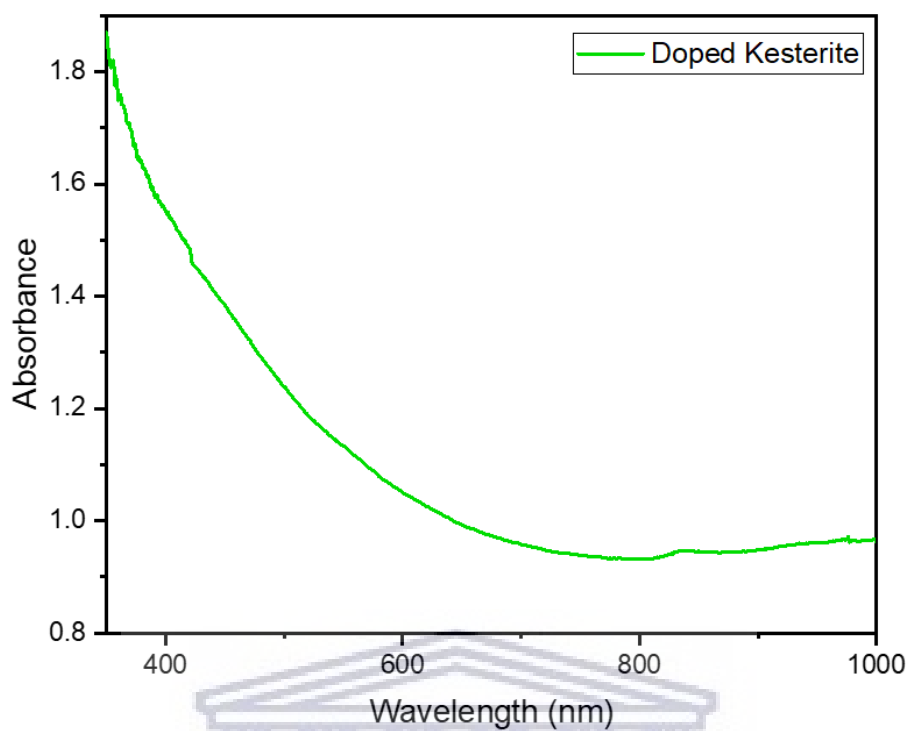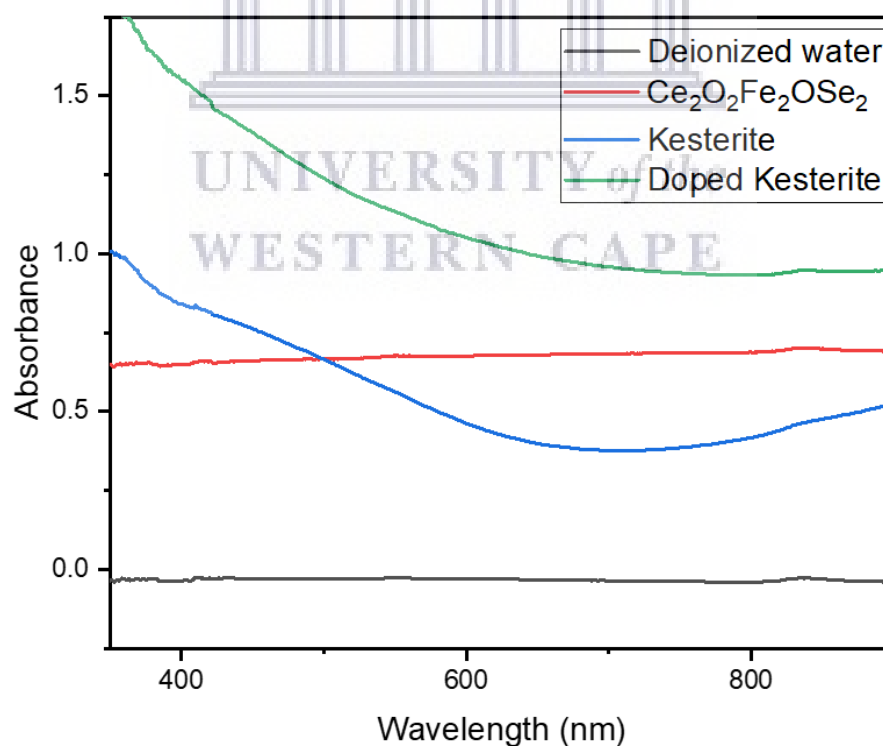Looking at Fig. 4.5.1.1 – Fig. 4.5.1.5, with the dichloromethane solvent, when comparing the wavelengths of light absorbance, it shows the absorption wavelength of the cerium and iron oxyselenide dopant increase steadily from 400 nm to 900 nm in Fig. 4.5.1.2 and the absorption wavelength of the kesterite stabilizes around 650 nm then starts increasing from 750 nm in Fig. 4.5.1.3. This could result from things such as the occurrence of multiple phases and morphology of the films, which is in accordance to previous findings which states that the onset for light absorption of the material gradually shifts to longer wavelengths as the duration of the absorption increases [54]. Overall Fig. 4.5.1.3, shows that the kesterite sample has a slightly greater absorbance than that of the doped kesterite sample (Fig. 4.5.1.4), whereas the doped kesterite sample has the broadest and widest absorption indicating is superiority for use in photovoltaics. Fig. 4.5.1.6 – Fig. 4.5.1.10, with the ethanol solvent closely follows the same trend as the samples in the dichloromethane solvent except with ethanol, the samples have far greater absorbances. Overall, the doped kesterite nanoparticles in ethanol (Fig. 4.5.1.9), has a similar trend to the doped kesterite sample in dichloromethane (Fig. 4.5.1.4). Looking at Fig. 4.5.1.11 – Fig 4.5.1.15, with the deionized water solvent, the plots in this graph follow the same trends and patterns of those with the first two solvents, except for the doped kesterite which was the weakest absorber while using the first two solvents, now it's the strongest absorber while using deionized water as a solvent. Fig. 4.5.1.14, shows that the doped kesterite sample has a greater absorbance. This indicates that the solvent makes a difference as the samples dissolved best in ethanol, dissolved well in dichloromethane and dissolved poorly in deionized water. Overall, from these UV-Vis graphs its seen that the doped kesterite would be better suited for photovoltaic applications, due to it having the broadest and widest absorption [2,11,54–56]. A perfect semiconductor would possess a square root like behaviour of the density of states near the valence band maximum and the conduction band minimum with energy. A direct semiconductor translates this directly into a square root like behaviour of the "absorption coefficient α as a function of energy E". Therefore, the bandgap E_g, as the abscissa intercept, is obtained from a Tauc plot of $\alpha^2 E^2$ vs. E. This produces the bandgap of extended states [57].
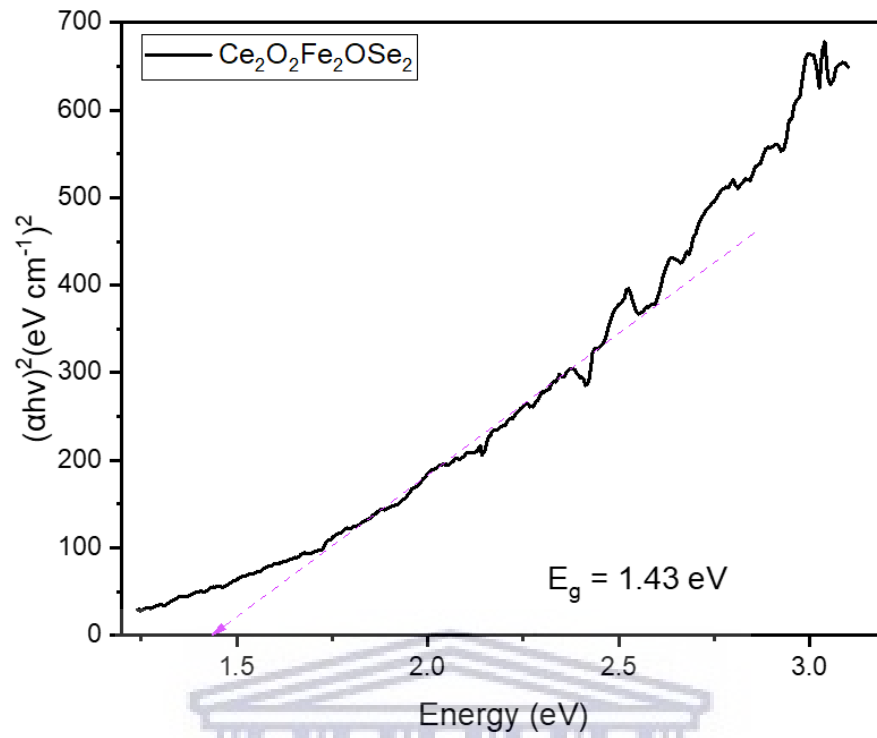
Figure 4.5.1.16: Tauc plot of the $Ce_2O_2Fe_2OSe_2$ nanoparticles in dichloromethane.

Figure 4.5.1.17: Tauc plot of the kesterite nanoparticles in dichloromethane.
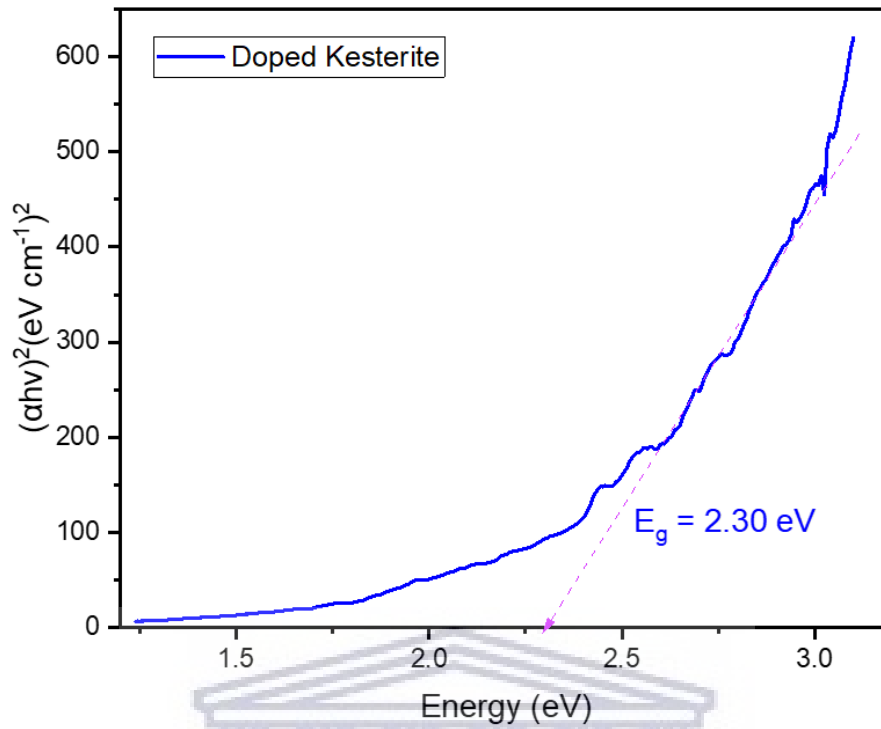
Figure 4.5.1.18: Tauc plot of the doped kesterite nanoparticles in dichloromethane.
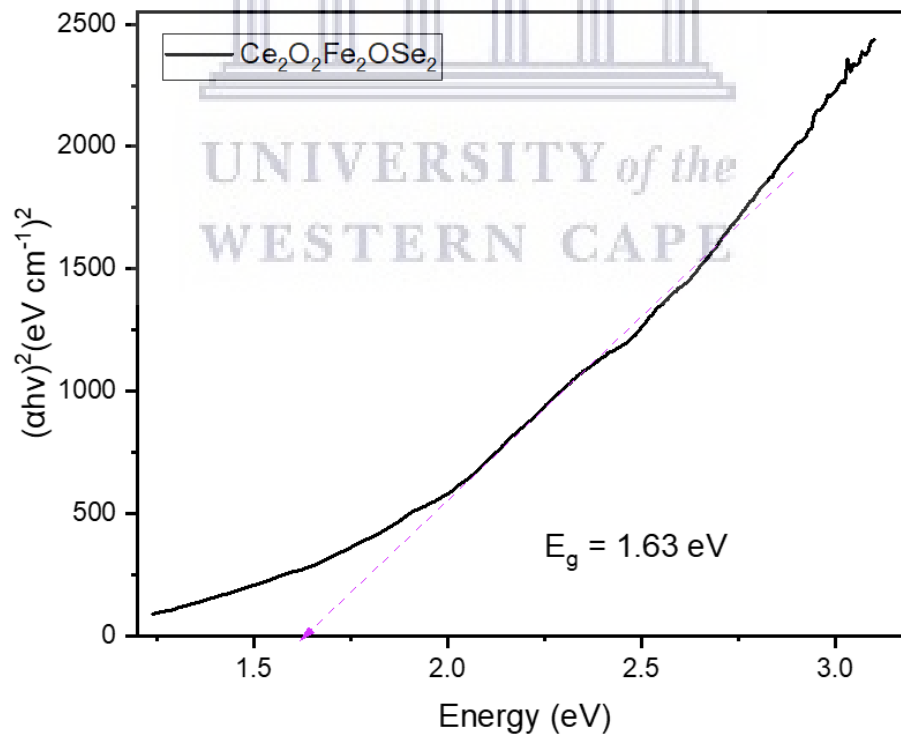
Figure 4.5.1.19: Tauc plot of the $Ce_2O_2Fe_2OSe_2$ nanoparticles in ethanol.
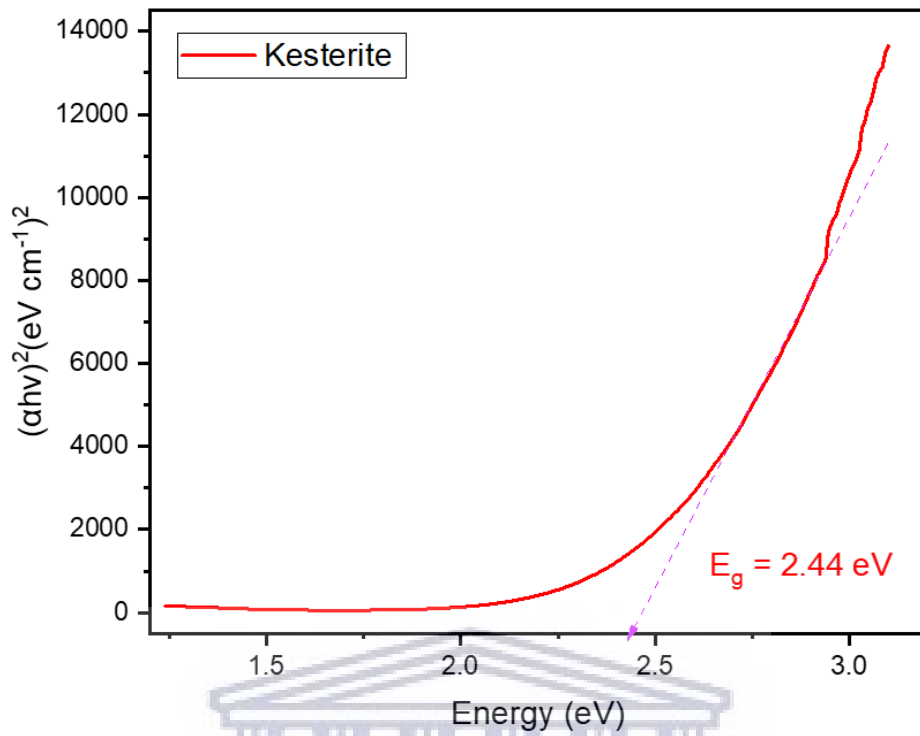
Figure 4.5.1.20: Tauc plot of the kesterite nanoparticles in ethanol.
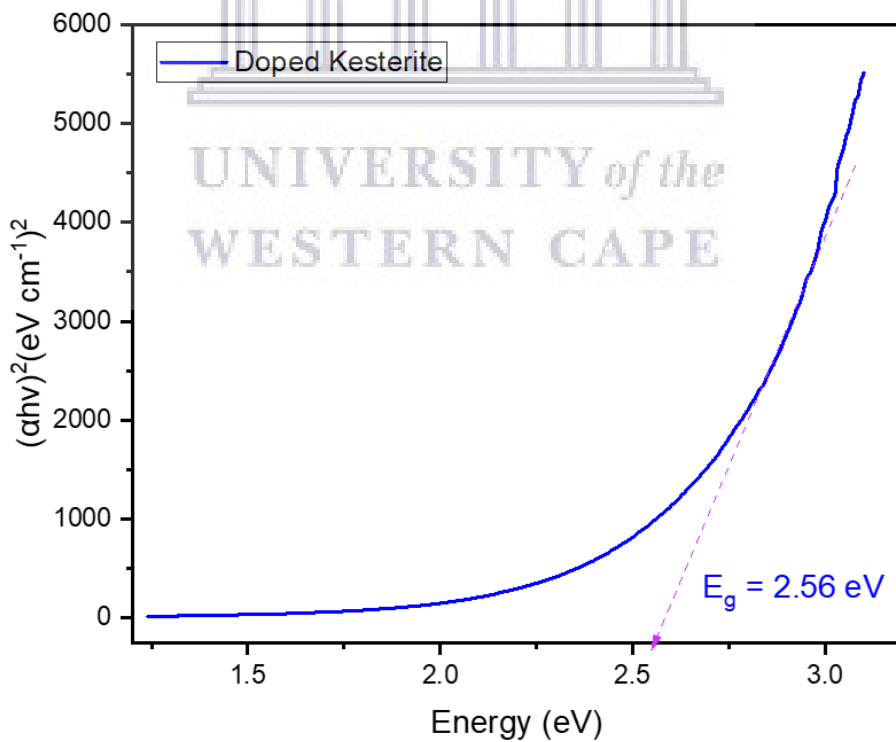
Figure 4.5.1.21: Tauc plot of the doped kesterite nanoparticles in ethanol.
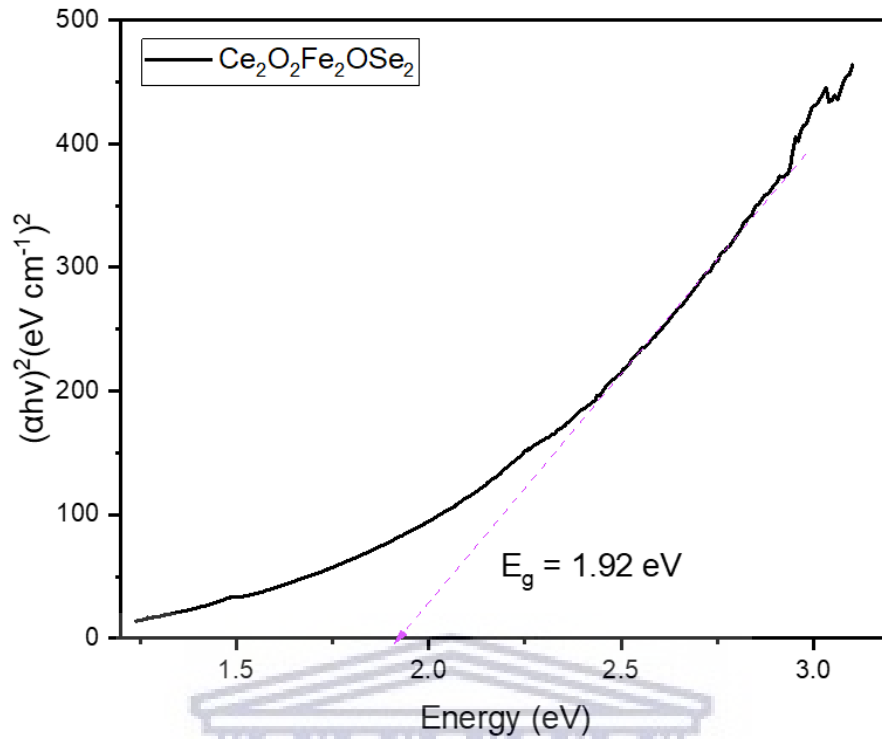
Figure 4.5.1.22: Tauc plot of the $Ce_2O_2Fe_2OSe_2$ nanoparticles in deionized water.
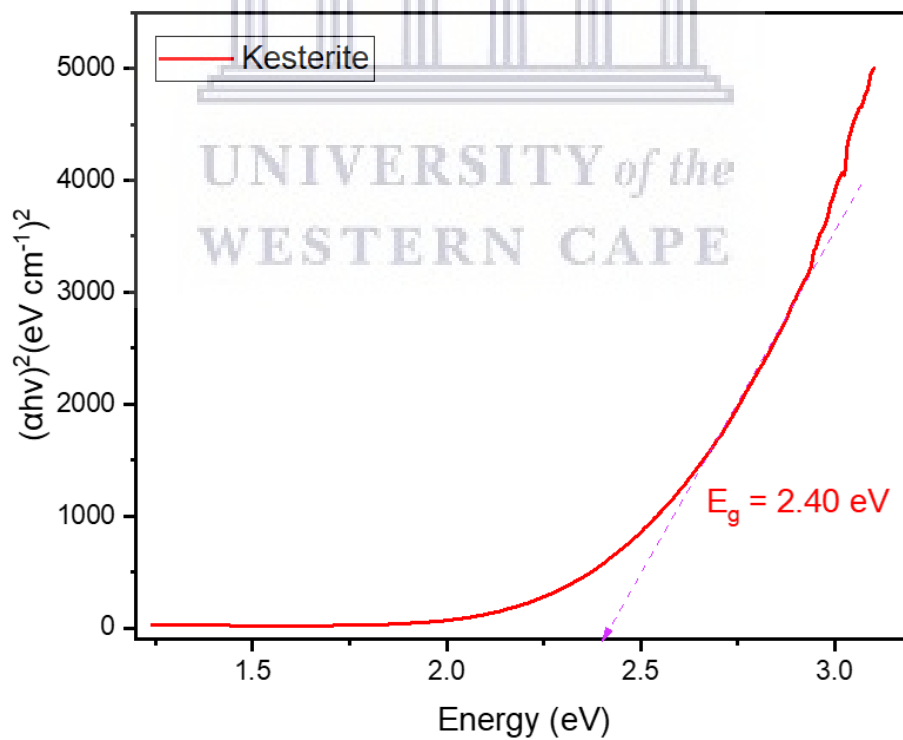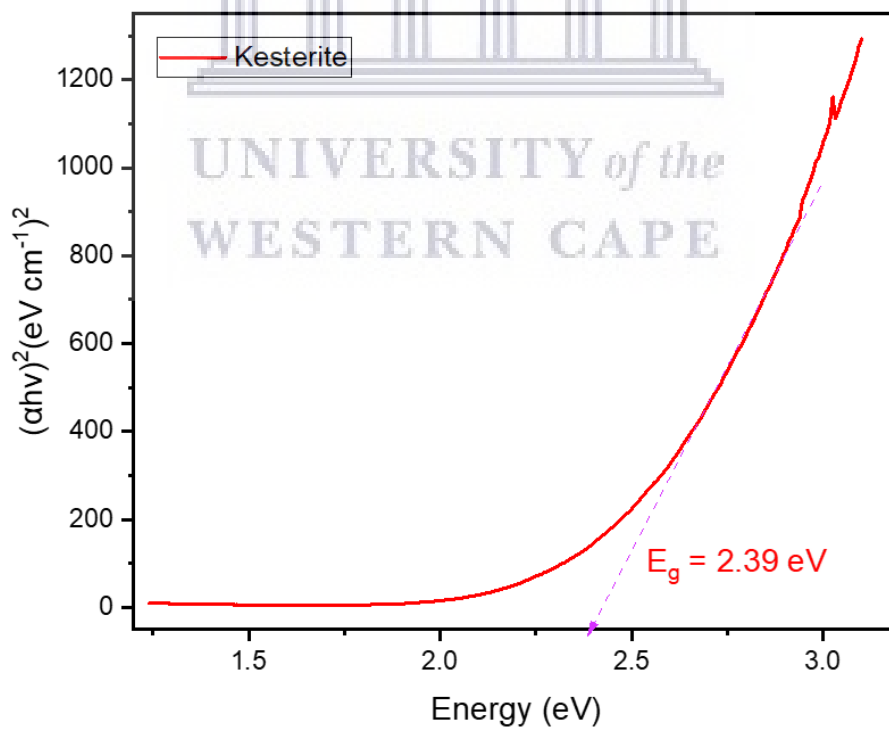

Figure 4.5.1.23: Tauc plot of the kesterite nanoparticles in deionized water.
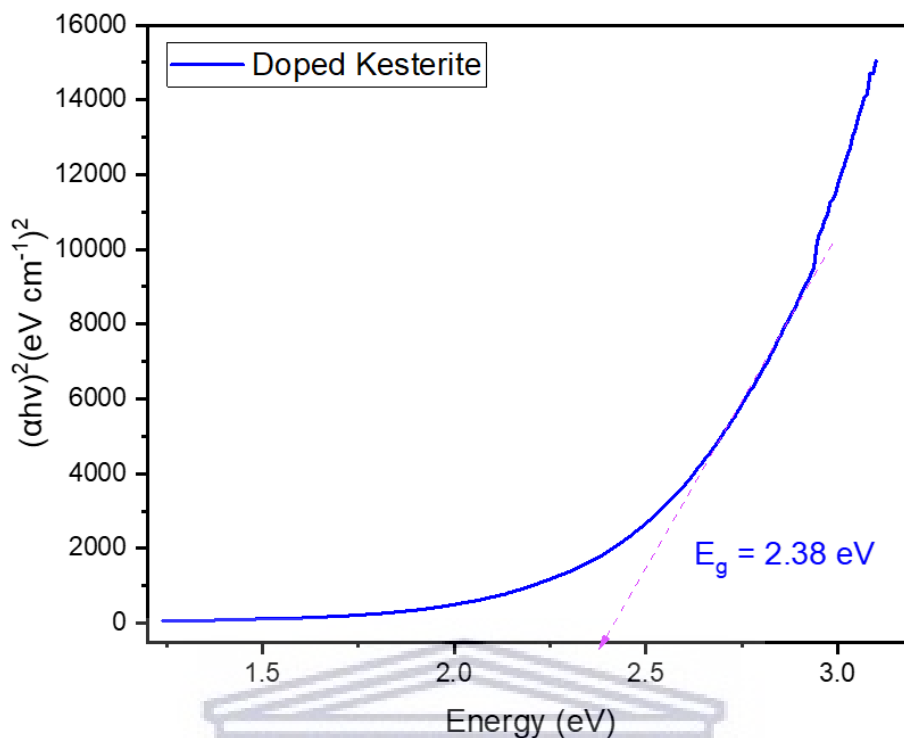
Figure 4.5.1.24: Tauc plot of the doped kesterite nanoparticles in deionized water.

Fig. 4.5.1.16 – 4.5.1.24 shows the tauc plots for all samples in the following solvents: dichloromethane, ethanol, and deionized water respectively. Fig. 4.5.1.16 and Fig. 4.5.1.18, the Tauc plots of the $Ce_2O_2Fe_2OSe_2$ and doped kesterite nanoparticles in dichloromethane, shows optical band gaps of 1.43 eV and 2.30 eV for the $Ce_2O_2Fe_2OSe_2$ and doped kesterite nanoparticles respectively. Fig 4.5.1.17, the Tauc plot of the kesterite nanoparticles in dichloromethane, shows an optical band gap of 2.40 eV. The band gap was obtained via extrapolation of the straight line to zero absorption for the synthesized nanoparticles. Fig. 4.5.1.19 and Fig. 4.5.1.21, the Tauc plots of the $Ce_2O_2Fe_2OSe_2$ and doped kesterite nanoparticles in ethanol, shows optical band gaps of 1.63 eV and 2.56 eV for the $Ce_2O_2Fe_2OSe_2$ and doped kesterite nanoparticles respectively. Fig 4.5.1.20, the Tauc plot of the kesterite nanoparticles in ethanol, shows an optical band gap of 2.44 eV. The band gap was obtained via extrapolation of the straight line to zero absorption for the synthesized nanoparticles. Fig. 4.5.1.22 and Fig. 4.5.1.23, the Tauc plots of the $Ce_2O_2Fe_2OSe_2$ and kesterite nanoparticles in deionized water, shows optical band gaps of 1.92 eV and 2.39 eV for the $Ce_2O_2Fe_2OSe_2$ and kesterite nanoparticles respectively. Fig 4.5.1.24, the Tauc plot of the doped kesterite nanoparticles in deionized water, shows an optical band gap of 2.38 eV. The band gap was obtained via extrapolation of the straight

line to zero absorption for the synthesized nanoparticles. From these Tauc plots, despite the samples having slightly different optical band gaps based on the solvent used, its seen that doping the kesterite with cerium and iron oxyselenides reduces the optical band gap in some cases but the band gap in general is not really influenced. The obtained optical bandgaps for the samples are in correlation with previous findings, although the kesterite nanoparticles have an E_g that greatly exceeds that of literature as reported by Xiao et al [58]. This could possibly be due to the Zn/Cu ratio, which is 0.65 for the kesterite nanoparticles. From the Tauc plots its seen that the kesterite nanoparticles and the doped kesterite nanoparticles have a similar optical band gap, and the changes to this bandgap is due to the presence of the cerium and iron oxyselenide dopant. The $Ce_2O_2Fe_2OSe_2$ dopant results in the manipulation of the bandgap as it only has a $Ce_2O_2Fe_2OSe_2$/ (Zn+Sn) ratio of only 0.50 and the kesterite nanoparticles not having a $Ce_2O_2Fe_2OSe_2$/ (Zn+Sn) ratio. It has also been found that a high amount of Sulphur content in kesterite increases the band-gap value which can affect the PCE of the solar cell [58–63]. The values of the bandgap obtained from the Tauc plot are verging on the optimum value of semiconductor band gap necessary for highly efficient solar cell.

Table 4.5.1: The optical band gap values of the as-prepared nanoparticles.

	Solvent	Band gap value (eV)	Average band gap value (eV)
Cerium and iron oxyselenide	Dichloromethane	1.43	1.66
	Ethanol	1.63	
	Deionized water	1.92	
Kesterite	Dichloromethane	2.40	2.41
	Ethanol	2.44	
	Deionized water	2.39	
Doped Kesterite	Dichloromethane	2.30	2.41
	Ethanol	2.56	
	Deionized water	2.38	

4.5.2 Solid State UV-Vis Spectroscopy
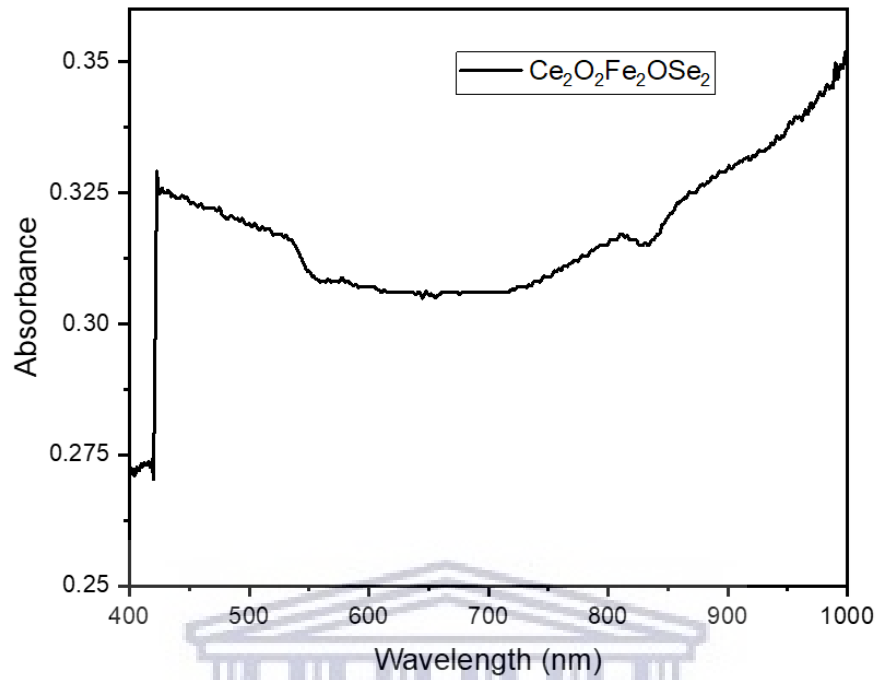
Figure 4.5.2.1: Solid State UV-Vis spectrum of the $Ce_2O_2Fe_2OSe_2$ nanoparticles on ITO glass.
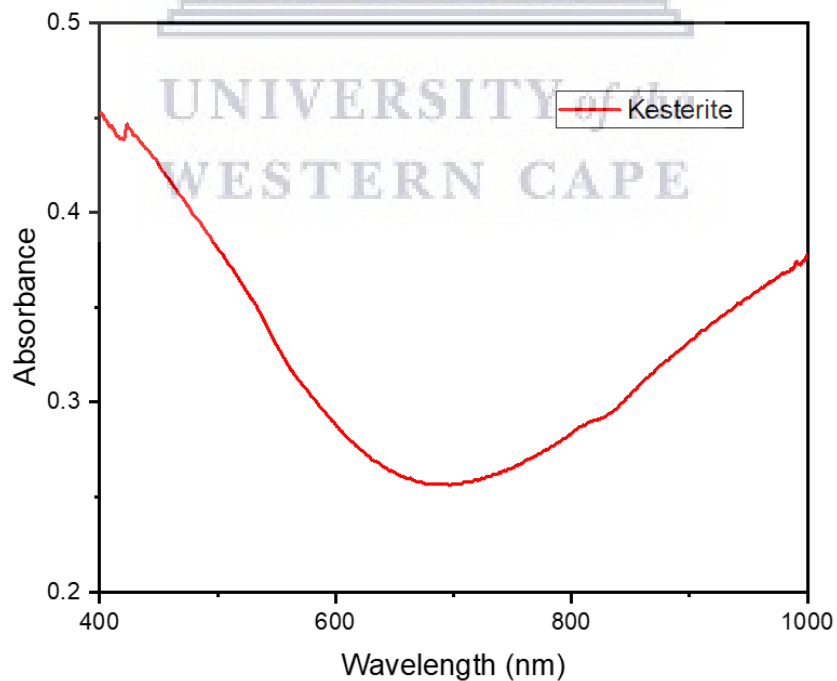
Figure 4.5.2.2: Solid State UV-Vis spectrum of the kesterite nanoparticles on ITO glass.
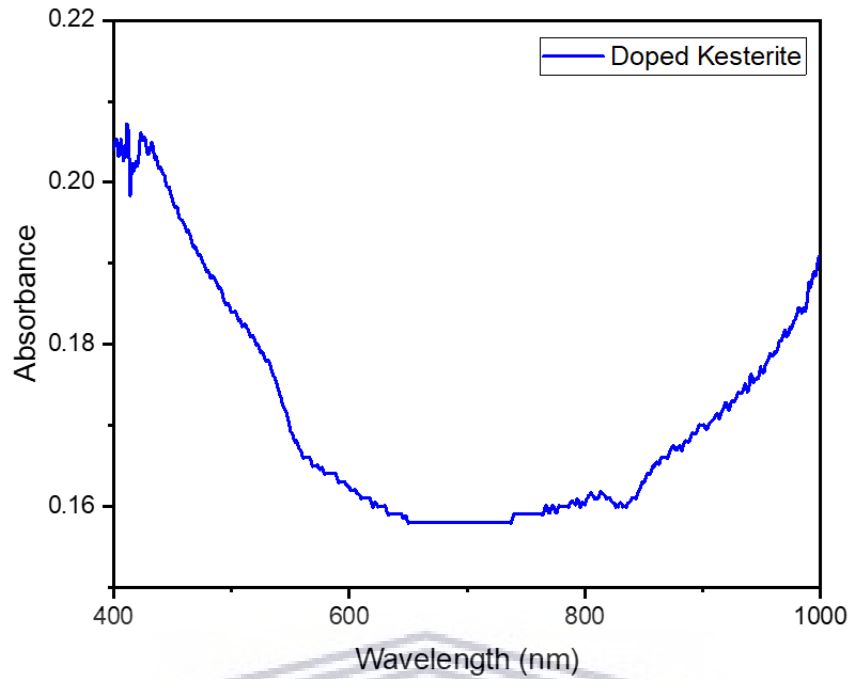
Figure 4.5.2.3: Solid State UV-Vis spectrum of the doped kesterite nanoparticles on ITO glass.
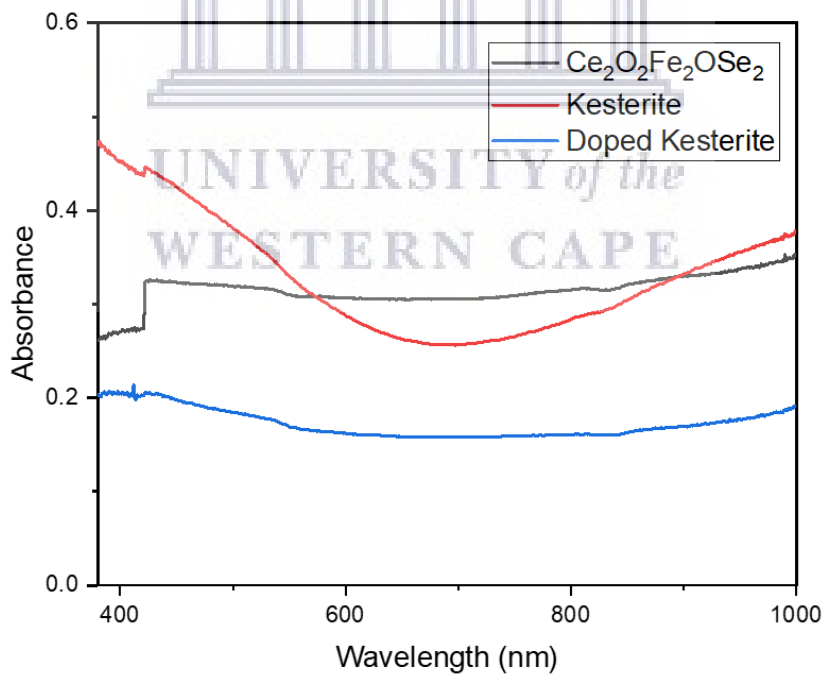
Figure 4.5.2.4: Solid State UV-Vis spectrum of the $Ce_2O_2Fe_2OSe_2$, kesterite and doped kesterite nanoparticles on ITO glass.

The optical properties of the $Ce_2O_2Fe_2OSe_2$, kesterite and doped kesterite nanoparticles were further analysed by Solid State UV-Vis spectroscopy. Looking at Fig. 4.5.2.4, when comparing the maximum wavelength of the cerium and iron oxyselenide dopant, $\lambda(max) = 1000$ nm, the kesterite, $\lambda(max) = 380$ nm, and the doped kesterite, $\lambda(max) = 380$ nm, as well as the overall broadness of the curves, its seen that the kesterite would be better suited for photovoltaic applications, due to it having the greatest and broadest absorption. When comparing the curves of the liquid state UV-Vis and solid-state UV-Vis, its seen that the samples possess greater absorbances when in a liquid form compared to a solid form, and both liquid and solid-state UV-Vis suggests that the doped kesterite nanoparticles are best suited for photovoltaic applications [54–56].
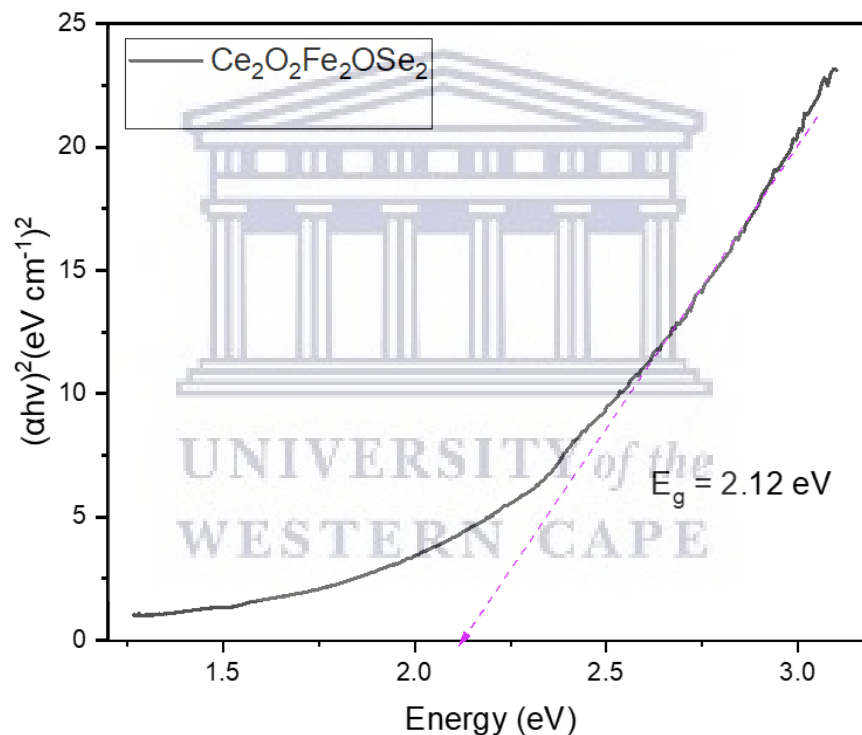
Figure 4.5.2.5: Tauc plot of the $Ce_2O_2Fe_2OSe_2$ nanoparticles on ITO glass.
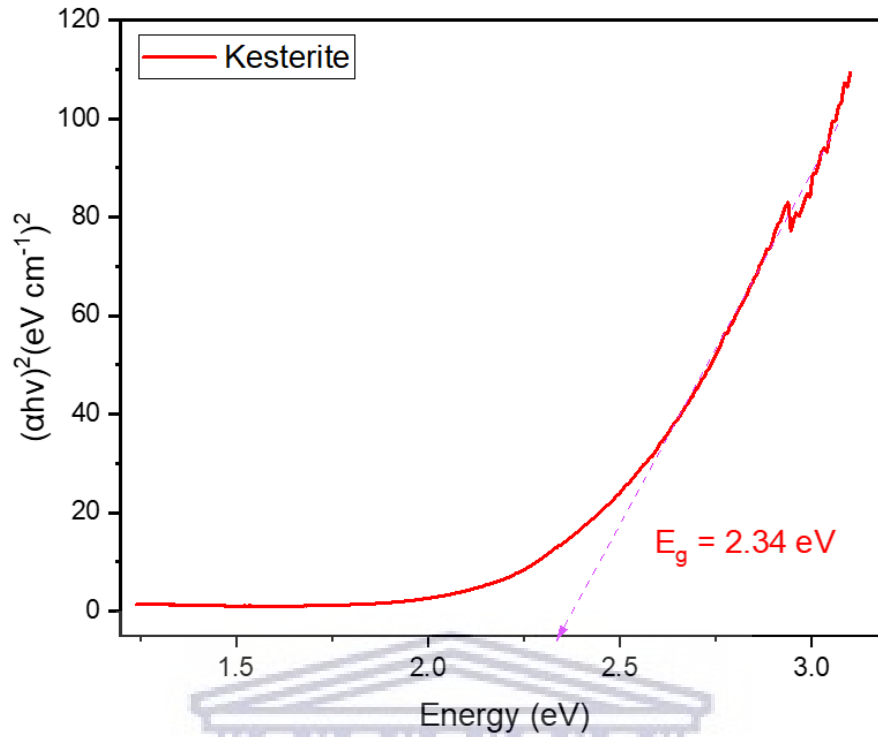
Figure 4.5.2.6: Tauc plot of the kesterite nanoparticles on ITO glass.
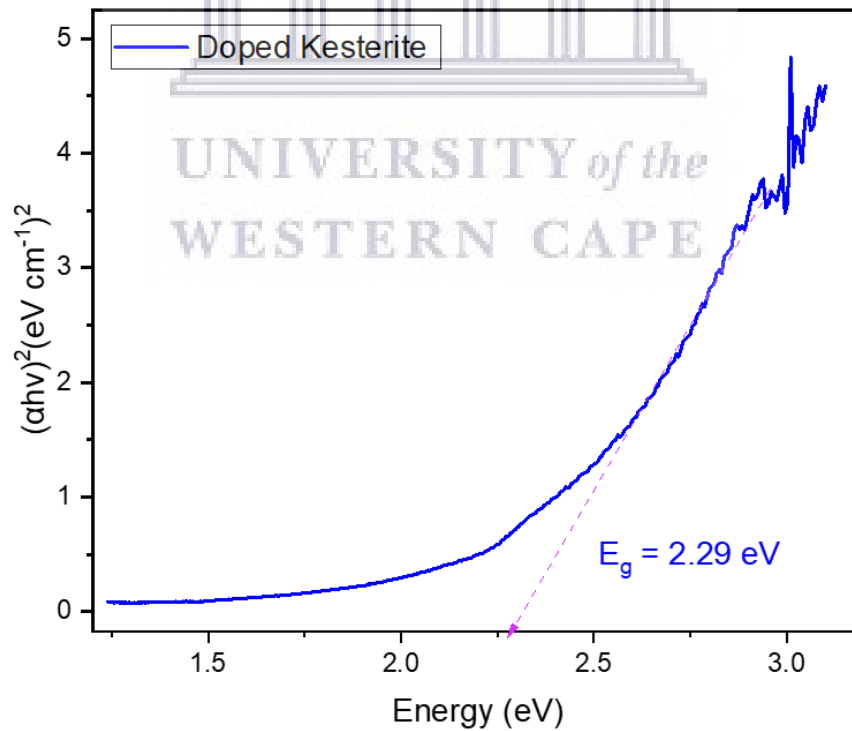
Figure 4.5.2.7: Tauc plot of the doped kesterite nanoparticles on ITO glass.

Fig. 4.5.2.5 – 4.5.2.7 shows the tauc plots for all samples on ITO glass plates. According to Fig. 4.5.2.5, the $Ce_2O_2Fe_2OSe_2$ nanoparticles have a solid-state optical band gap of 2.12 eV. Fig 4.7.2.6, shows that the kesterite nanoparticles have a solid-state optical band gap of 2.34 eV. Fig 4.5.2.7, shows that the doped kesterite nanoparticles have a solid-state optical band gap of 2.29 eV. From these Tauc plots, its seen that doping the kesterite with cerium and iron oxyselenides reduces the optical band gap, thus making them more efficient for photovoltaic applications, these results are in agreement with the liquid state UV-Vis results [58–63].

4.6 Electrochemical Characterization

4.6.1 Cyclic Voltammetry

In order to estimate the band structure parameters, electrochemical band gap and electron affinity of $Ce_2O_2Fe_2OSe_2$, kesterite and doped kesterite nanoparticles, cyclic voltammetry (CV) measurements were carried out and recorded with a "glassy carbon working electrode (WE)", "platinum counter electrode (CE)" and a "Ag/AgCl reference electrode (RE)" in a bath consisting of Ce_2, Fe and S precursors for the $Ce_2O_2Fe_2OSe_2$ sample and Cu, Zn, Sn and S precursors for the kesterite and doped kesterite sample. The cyclic voltammetry (CV) runs where performed at room temperature (25 °C) in an argon saturated phosphate-buffered saline (PBS) electrolyte.
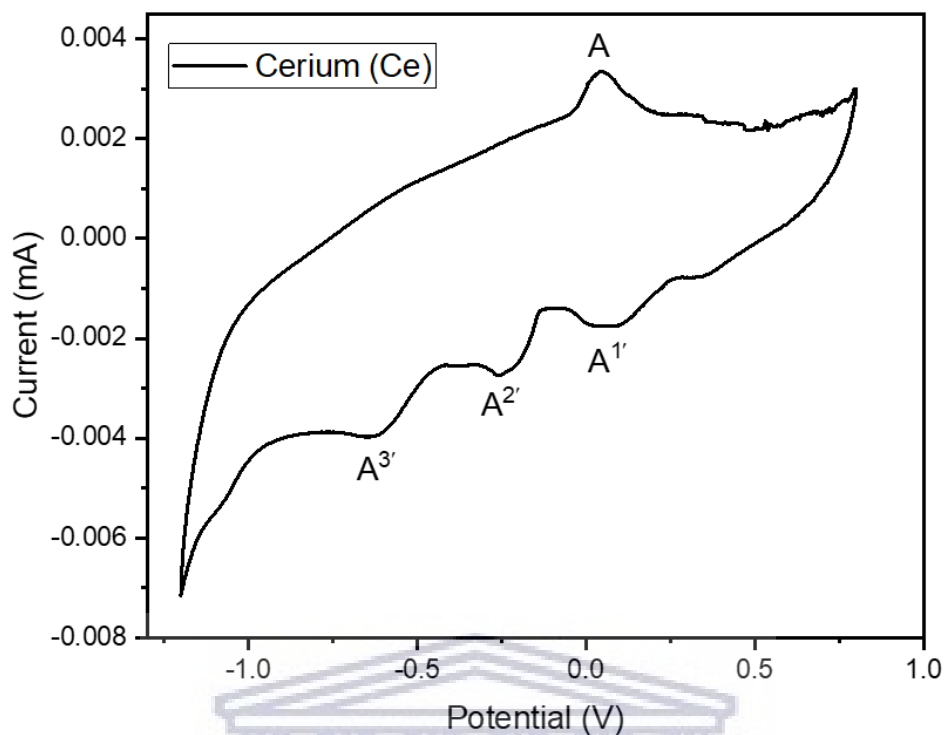
Figure 4.6.1.1: Cyclic voltammogram of cerium (Ce) (20 mV/s).
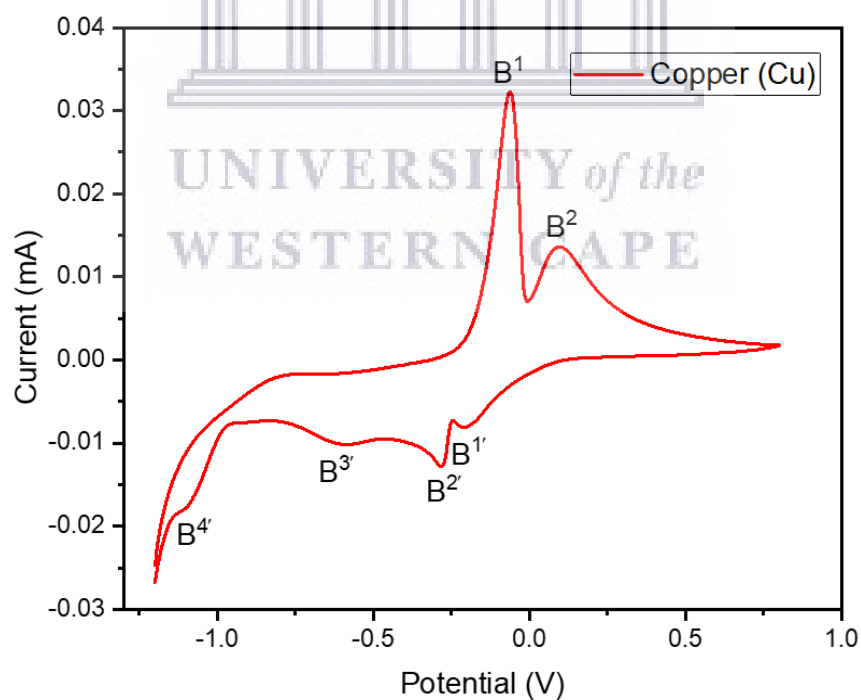
Figure 4.6.1.2: Cyclic voltammogram of copper (Cu) (20 mV/s).
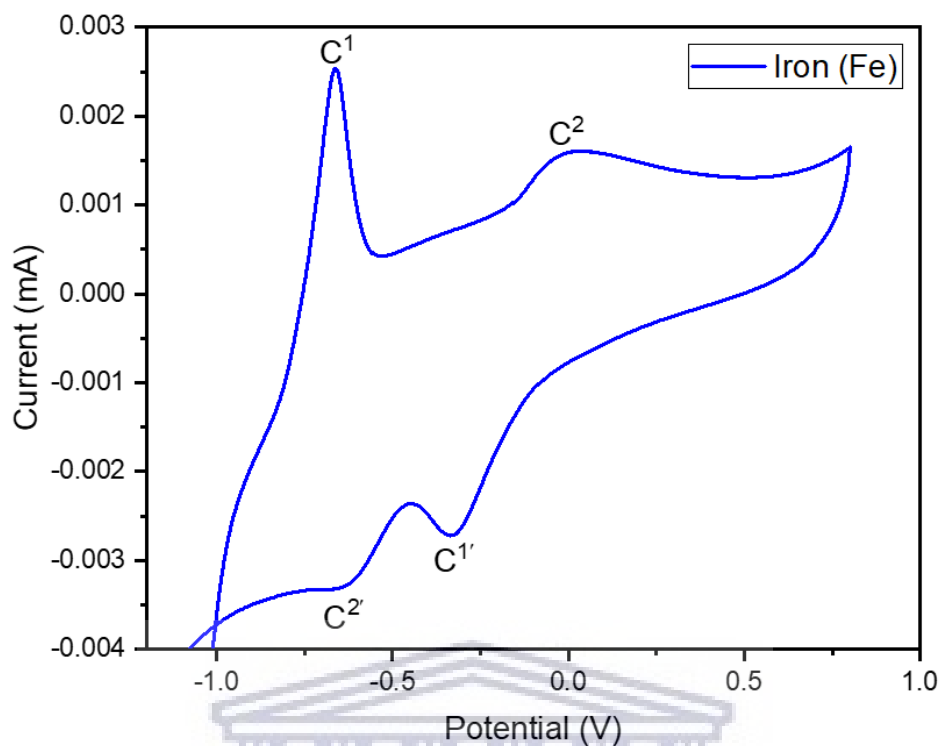
Figure 4.6.1.3: Cyclic voltammogram of iron (Fe) (20 mV/s).
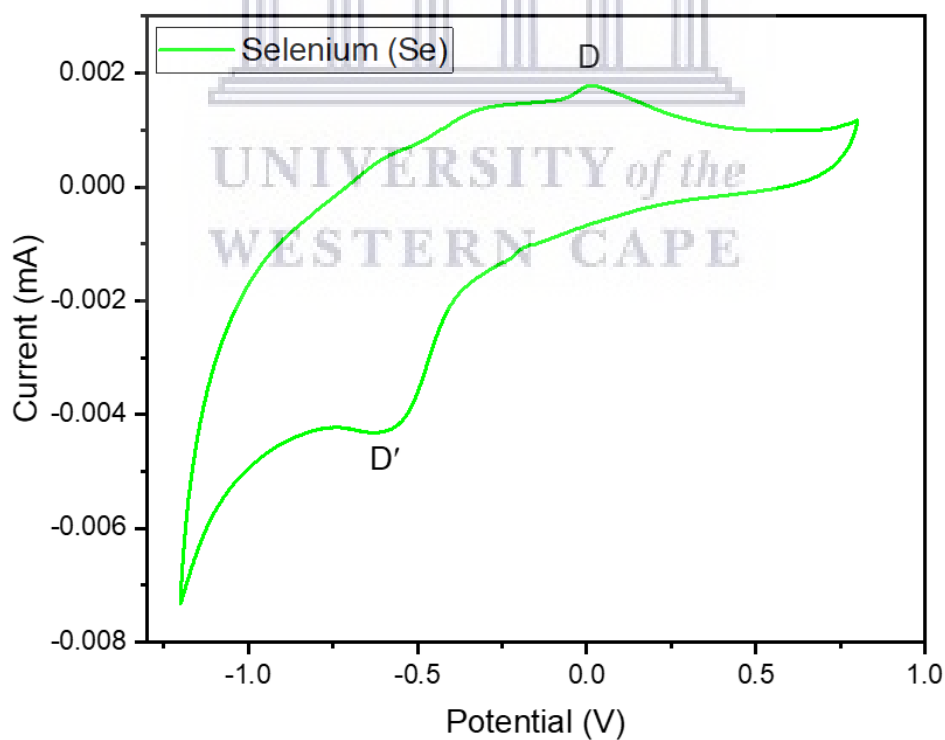
Figure 4.6.1.4: Cyclic voltammogram of selenium (Se) (20 mV/s).
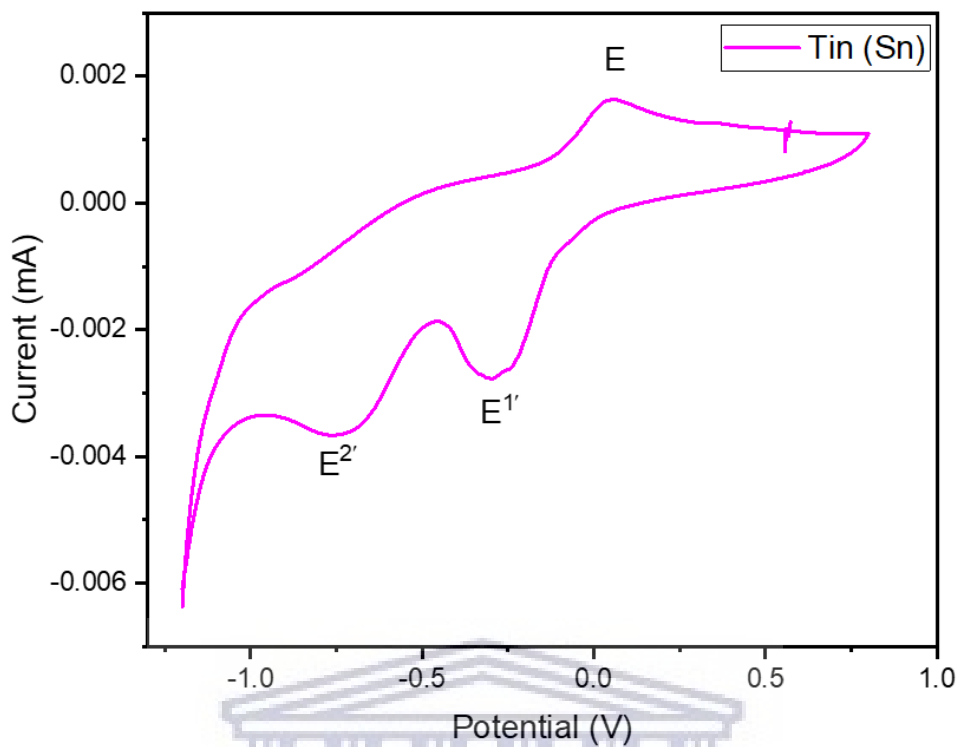
Figure 4.6.1.5: Cyclic voltammogram of tin (Sn) (20 mV/s).
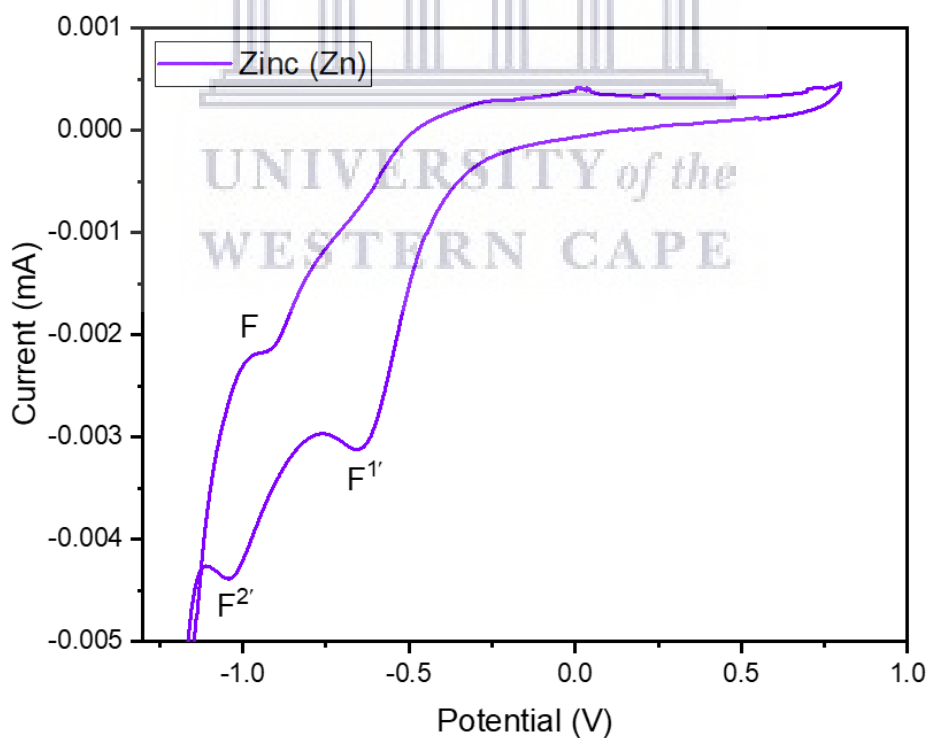
Figure 4.6.1.6: Cyclic voltammogram of zinc (Zn) (20 mV/s).

For all samples, a phosphate-buffered saline (PBS) electrolyte was used. For the forward curve, the potential is scanned negatively and thus is anodic while the reverse curve, potential is scanned positively and thus is cathodic, within a "potential range of -1.2 V to 0.8 V". Looking at Fig. 4.6.1.1; during the forward anodic scan for the cerium, the following redox reactions took place:
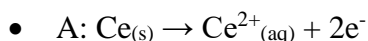
Oxidation:

- A: $Ce_{(s)} \rightarrow Ce^{2+}_{(aq)} + 2e^-$

During the reverse cathodic scan, the following redox reactions took place:

Reduction:

- $A^{1\prime}$: $Ce^{2+}_{(aq)} + 2e^- \rightarrow Ce_{(s)}$

- $A^{2\prime}$: $Ce^{2+}_{(aq)} + 2e^- \rightarrow Ce_{(s)}$
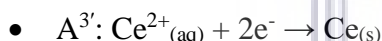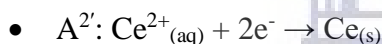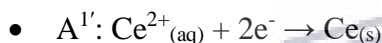
- $A^{3\prime}$: $Ce^{2+}_{(aq)} + 2e^- \rightarrow Ce_{(s)}$

At peak A (0.04V) the current increased as the cerium was oxidized: $Ce_{(s)} \rightarrow Ce^{2+}_{(aq)} + 2e^-$. Peak $A^{1\prime}$ (0.05V), $A^{2\prime}$ (-0.26V), and $A^{3\prime}$ (-0.64V) shows that the current increased, suggesting maximum precursor deposition and reduction of cerium: $Ce^{2+}_{(aq)} + 2e^- \rightarrow Ce_{(s)}$.

Looking at Fig. 4.6.1.2; during the forward anodic scan for the copper, the following redox reactions took place:

Oxidation:

- B^1: $Cu_{(s)} \rightarrow Cu^{2+}_{(aq)} + 2e^-$

- B^2: $Cu_{(s)} \rightarrow Cu^{2+}_{(aq)} + 2e^-$
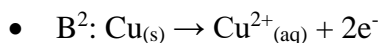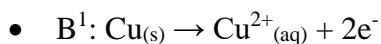
During the reverse cathodic scan, the following redox reactions took place:

Reduction:
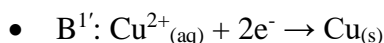
- $B^{1\prime}$: $Cu^{2+}_{(aq)} + 2e^- \rightarrow Cu_{(s)}$

- $B^{2\prime}$: $Cu^{2+}_{(aq)} + 2e^- \rightarrow Cu_{(s)}$

- $B^{3\prime}$: $Cu^{2+}_{(aq)} + 2e^- \rightarrow Cu_{(s)}$

- $B^{4\prime}$: $Cu^{2+}_{(aq)} + 2e^- \rightarrow Cu_{(s)}$

At peak B^1 (-0.07V) the current increased substantially due to the oxidation of copper and peak B^2 (0.09V) is due to the further oxidation of copper: $Cu_{(s)} \rightarrow Cu^{2+}_{(aq)} + 2e^-$. Peak $B^{1\prime}$ (-0.21V), $B^{2\prime}$ (-0.28V), and $B^{3\prime}$ (-0.63V) shows that the current increased, suggesting maximum precursor deposition and reduction of copper, peak $B^{4'}$ (-1.09V) is due to the further reduction of copper: $Cu^{2+}_{(aq)} + 2e^- \rightarrow Cu_{(s)}$.

Looking at Fig. 4.6.1.3; during the forward anodic scan for the iron, the following redox reactions took place:

Oxidation:

- C^1: $Fe_{(s)} \rightarrow Fe^{2+}_{(aq)} + 2e^-$

- C^2: $Fe_{(s)} \rightarrow Fe^{2+}_{(aq)} + 2e^-$

During the reverse cathodic scan, the following redox reactions took place:

Reduction:

- $C^{1\prime}$: $Fe^{2+}_{(aq)} + 2e^- \rightarrow Fe_{(s)}$

- $C^{2\prime}$: $Fe^{2+}_{(aq)} + 2e^- \rightarrow Fe_{(s)}$

At peak C^1 (-0.67V) the current increased substantially due to the oxidation of iron and peak C^2 (0.01V) is due to the further oxidation of copper: $Fe_{(s)} \rightarrow Fe^{2+}_{(aq)} + 2e^-$. Peak $C^{1\prime}$ (-0.33V) and $C^{2\prime}$ (-0.66V) shows that the current increased, suggesting maximum precursor deposition and reduction of copper: $Fe^{2+}_{(aq)} + 2e^- \rightarrow Fe_{(s)}$.
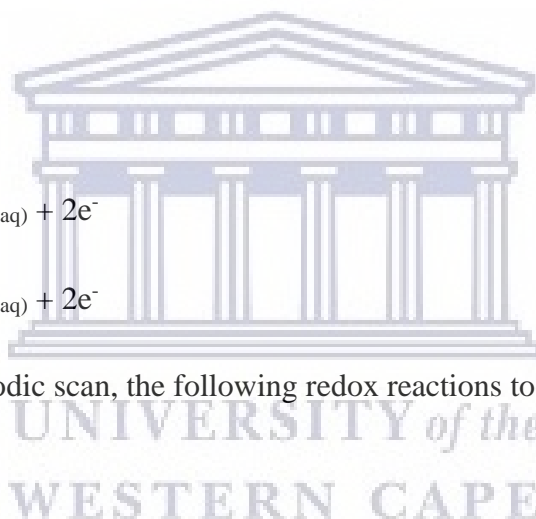
Looking at Fig 4.6.1.4; during the forward anodic scan for the selenium, the following redox reactions took place:

Oxidation:

- D: $Se_{(s)} \rightarrow Se^{2+}_{(aq)} + 2e^-$

During the reverse cathodic scan, the following redox reactions took place:

Reduction:

- D′: $Se^{2+}_{(aq)} + 2e^- \rightarrow Se_{(s)}$

At peak D (0.01V) the current increased substantially due to the oxidation of selenium: $Se_{(s)} \rightarrow Se^{2+}_{(aq)} + 2e^-$. Peak D′ (-0.59V) shows that the current increased, suggesting maximum precursor deposition and reduction of selenium: $Se^{2+}_{(aq)} + 2e^- \rightarrow Se_{(s)}$.

Looking at Fig 4.6.1.5; during the forward anodic scan for the tin, the following redox reactions took place:

Oxidation:

- E: $Sn_{(s)} \rightarrow Sn^{2+}_{(aq)} + 2e^-$

During the reverse cathodic scan, the following redox reactions took place:

Reduction:

- E^{1}′: $Sn^{2+}_{(aq)} + 2e^- \rightarrow Sn_{(s)}$

- E^{2}′: $Sn^{2+}_{(aq)} + 2e^- \rightarrow Sn_{(s)}$

At peak E (0.05V) the current increased as the tin was oxidized: $Sn_{(s)} \rightarrow Sn^{2+}_{(aq)} + 2e^-$. Peak E^{1}′ (-0.29V) and E^{2}′ (-0.75V) shows that the current increased, suggesting maximum precursor deposition and reduction of tin: $Sn^{2+}_{(aq)} + 2e^- \rightarrow Sn_{(s)}$.

Looking at Fig. 4.6.1.6; during the forward anodic scan for the zinc, the following redox reactions took place:

Oxidation:

- F: $Zn_{(s)} \rightarrow Zn^{2+}_{(aq)} + 2e^-$

During the reverse cathodic scan, the following redox reactions took place:

Reduction:

- $F^{1\prime}$: $Zn^{2+}_{(aq)} + 2e^- \rightarrow Zn_{(s)}$

- $F^{2\prime}$: $Zn^{2+}_{(aq)} + 2e^- \rightarrow Zn_{(s)}$

At peak F (-0.97V) the current increased as the zinc was oxidized: $Zn_{(s)} \rightarrow Zn^{2+}_{(aq)} + 2e^-$. Peak $F^{1\prime}$ (-0.65V) and $F^{2\prime}$ (-1.04V) shows that the current increased, suggesting maximum precursor deposition and reduction of zinc: $Zn^{2+}_{(aq)} + 2e^- \rightarrow Zn_{(s)}$.
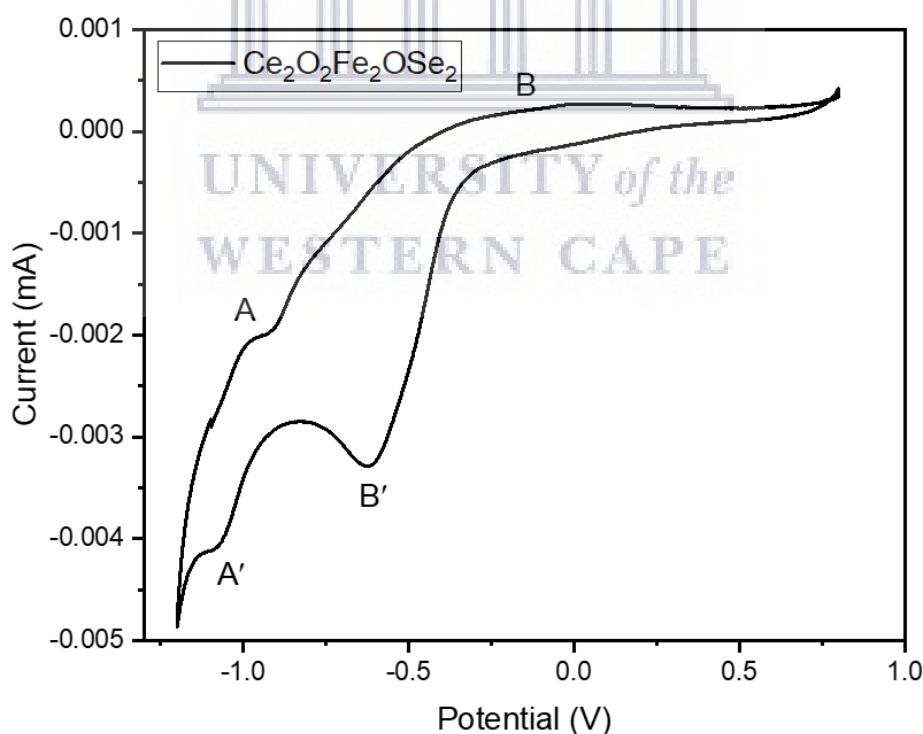
**Figure 4.6.1.7:** Cyclic voltammogram of the $Ce_2O_2Fe_2OSe_2$ nanoparticles (20 mV/s).
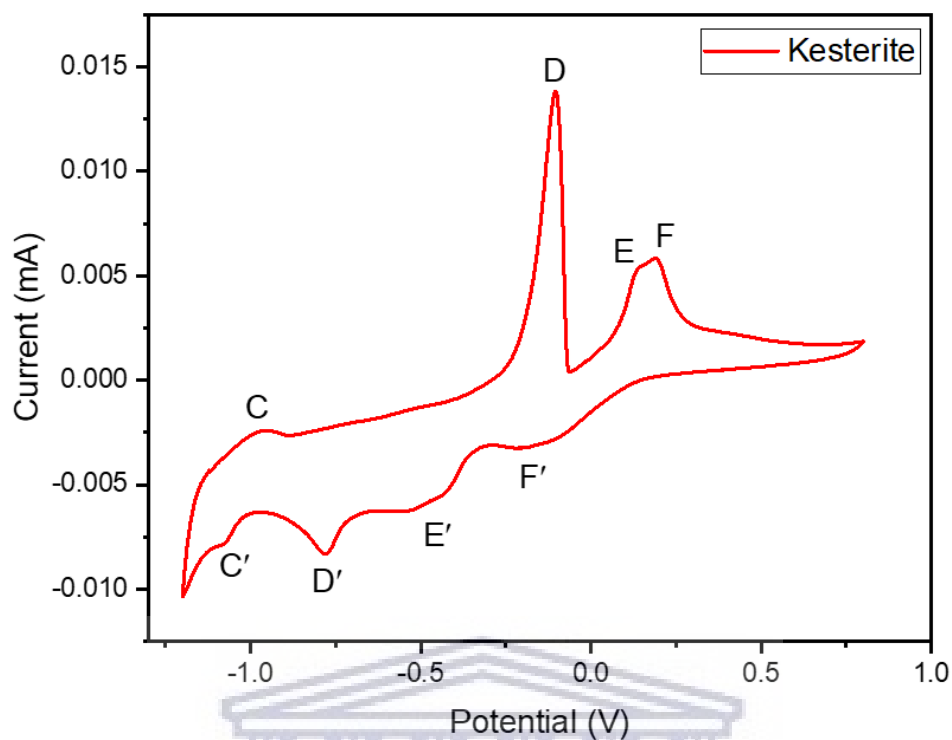
Figure 4.6.1.8: Cyclic voltammogram of the kesterite nanoparticles (20 mV/s).
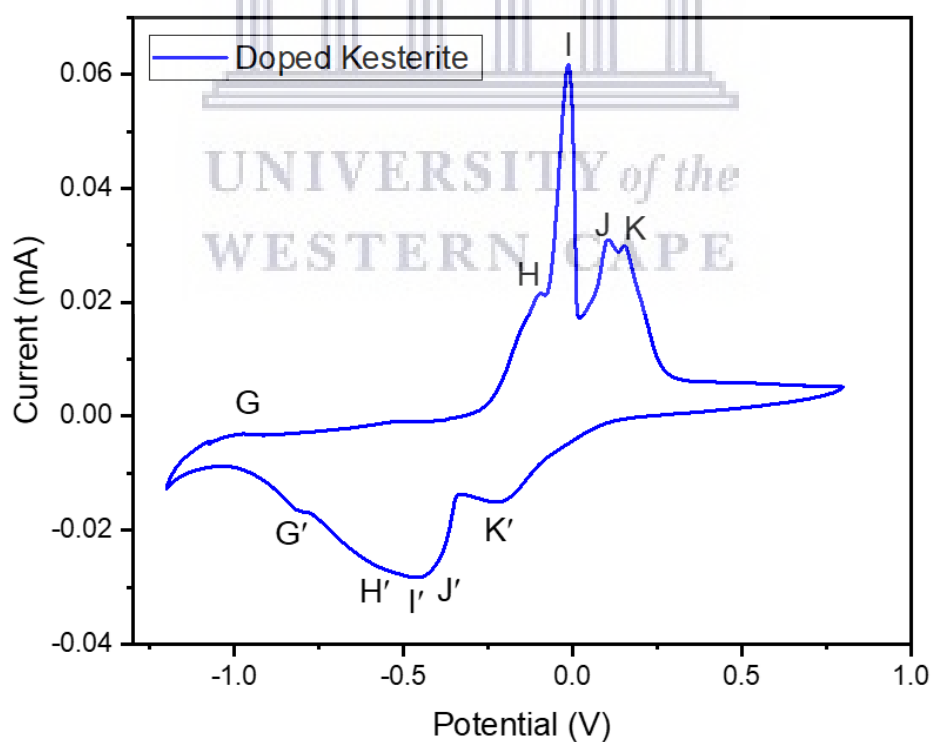
Figure 4.6.1.9: Cyclic voltammogram of the doped kesterite nanoparticles (20 mV/s).
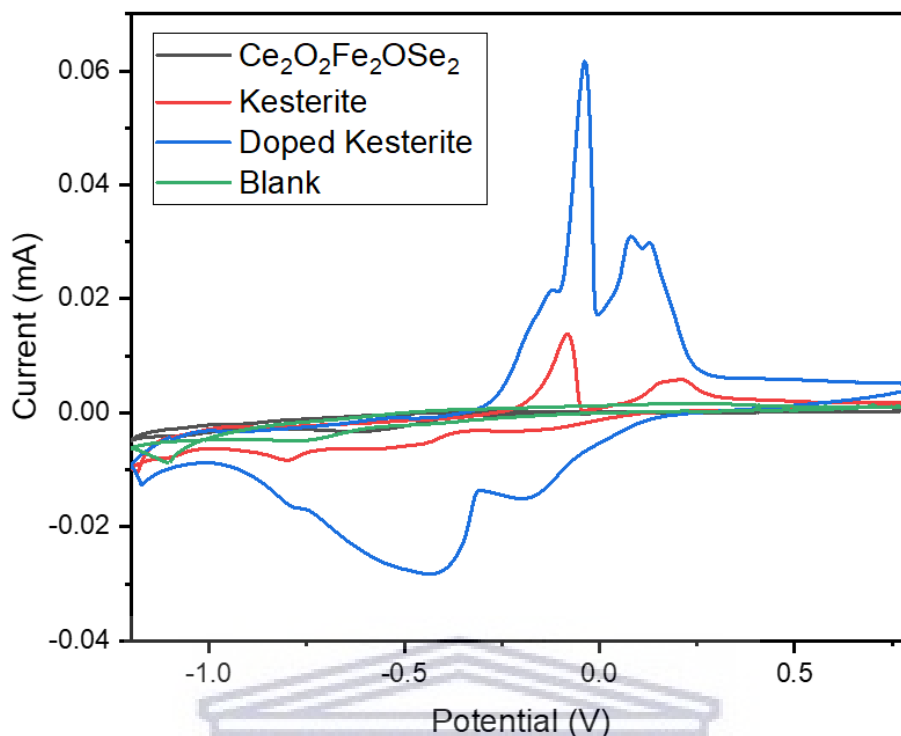
Figure 4.6.1.10: Cyclic voltammogram of all sample nanoparticles (20 mV/s).

For the cerium and iron oxyselenide sample, the electrolyte solution contained Ce^{2+}, Fe^{2+} and Se ions while for the kesterite and doped kesterite samples, the electrolyte solution contained Cu^{2+}, Zn^{2+} and Sn^{4+} ions. Fig. 4.6.1.10 shows the CV for all the sample nanoparticles at a "scan rate of 20 mV/s". The co-deposition of Cu, Zn, Sn and S is difficult as the redox potential of these elements is different [64,65]. Looking at Fig. 4.6.1.7; during the forward anodic scan for the $Ce_2O_2Fe_2OSe_2$ nanoparticles, the following redox reactions took place:

Oxidation:

- A: $Fe_{(s)} \rightarrow Fe^{2+}_{(aq)} + 2e^-$

- B: $Ce_{(s)} \rightarrow Ce^{2+}_{(aq)} + 2e^-$

During the reverse cathodic scan, the following redox reactions took place:

Reduction:

- A′: $Fe^{2+}_{(aq)} + 2e^- \rightarrow Fe_{(s)}$

- B′: $Ce^{2+}_{(aq)} + 2e^- \rightarrow Ce_{(s)}$
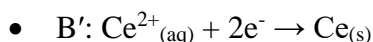
At peak A (- 0.97V) the current slightly increased as a small amount of iron was oxidized: $Fe_{(s)} \rightarrow Fe^{2+}_{(aq)} + 2e^-$. The current then further increased to a maximum of 0.003 mA (-0.14V), which forms peak B, suggesting the oxidation of cerium: $Ce_{(s)} \rightarrow Ce^{2+}_{(aq)} + 2e^-$. Peak B′ (-0.62V) shows that current increased, suggesting maximum precursor deposition ideally due to the reduction and metallic deposition of cerium: $Ce^{2+}_{(aq)} + 2e^- \rightarrow Ce_{(s)}$. at peak A′ (-1.08V) the current slightly increased as iron was reduced and deposited: $Fe^{2+}_{(aq)} + 2e^- \rightarrow Fe_{(s)}$. The electrochemical bandgap was determined using the equations:

- $E_{HOMO} = -e (E_{onset.ox} + 4.5)$ eV

- $E_{LUMO} = -e (E_{onset.red} + 4.5)$ eV

- $E_g = E_{LUMO} - E_{HOMO}$

Where the oxidation peak is: -0.14 V and the reduction peak is -0.62 V, thus:

- $E_{HOMO} = -e (-0.14 + 4.5)$ eV = - 4.34 eV

- $E_{LUMO} = -e (-0.62 + 4.5)$ eV = - 3.86 eV

- E_g = - 3.86 eV + 4.34 eV = 0.48 eV

Therefore, the electrochemical bandgap (E_g) for the cerium and iron oxyselenide nanoparticles is 0.48 eV [66–68].

Looking at Fig. 4.6.1.8; during the forward anodic scan for the kesterite nanoparticles, the following redox reactions took place:

Oxidation:

- C: $Zn_{(s)} \rightarrow Zn^{2+}_{(aq)} + 2e^-$

- D: $Cu_{(s)} \rightarrow Cu^{2+}_{(aq)} + 2e^-$

- E: $Se_{(s)} \rightarrow Se^{2+}_{(aq)} + 2e^-$

- F: $Sn_{(s)} \rightarrow Sn^{2+}_{(aq)} + 2e^-$

During the reverse cathodic scan, the following redox reactions took place:

Reduction:

- C′: $Zn^{2+}_{(aq)} + 2e^- \rightarrow Zn_{(s)}$

- D′: $Cu^{2+}_{(aq)} + 2e^- \rightarrow Cu_{(s)}$

- E′: $Se^{2+}_{(aq)} + 2e^- \rightarrow Se_{(s)}$

- F′: $Sn^{2+}_{(aq)} + 2e^- \rightarrow Sn_{(s)}$

At peak C (- 0.97V) the current slightly increased as a small amount of zinc was oxidized: $Zn_{(s)} \rightarrow Zn^{2+}_{(aq)} + 2e^-$. The current then greatly increased to (-0.11V), which forms peak D, suggesting the oxidation of copper: $Cu_{(s)} \rightarrow Cu^{2+}_{(aq)} + 2e^-$. The current increased further forming peaks E (0.13V) and peaks F (0.19V) which are due to the oxidation of selenium: $Se^{2+}_{(aq)} + 2e^- \rightarrow Se_{(s)}$ and tin: $Sn^{2+}_{(aq)} + 2e^- \rightarrow Sn_{(s)}$, respectively. Peak F′ (-0.18V) is due to an increase in current resulting from the reduction and deposition of tin: $Sn^{2+}_{(aq)} + 2e^- \rightarrow Sn_{(s)}$. Peak E′ (-0.47V) is due to the reduction and deposition of selenium: $Se^{2+}_{(aq)} + 2e^- \rightarrow Se_{(s)}$. Peak D′ (-0.78V) shows that current increased, suggesting maximum precursor deposition ideally due to the reduction and metallic deposition of copper: $Cu^{2+}_{(aq)} + 2e^- \rightarrow Cu_{(s)}$. At peak C′ (-1.07V) the current slightly increased as zinc was reduced and deposited: $Zn^{2+}_{(aq)} + 2e^- \rightarrow Zn_{(s)}$ [64,65]. The electrochemical bandgap was determined using the equations:

- $E_{HOMO} = -e (E_{onset.ox} + 4.5) \, eV$

- $E_{LUMO} = -e (E_{onset.red} + 4.5) \, eV$

- $E_g = E_{LUMO} - E_{HOMO}$

Where the oxidation peak is: -0.11 V and the reduction peak is -0.78 V, thus:

- $E_{HOMO} = -e (-0.11 + 4.5) \, eV = - 4.39 \, eV$

- $E_{LUMO} = -e (-0.78 + 4.5) \, eV = - 3.72 \, eV$

- $E_g = - 3.72 + 4.39 \, eV = 0.67 \, eV$

Therefore, the electrochemical bandgap (E_g) for the kesterite nanoparticles is 0.67 eV [66–68].

Looking at Fig. 4.6.1.9; during the forward anodic scan for the doped kesterite nanoparticles, the following redox reactions took place:

<u>Oxidation:</u>

- G: $Zn_{(s)} \rightarrow Zn^{2+}_{(aq)} + 2e^-$; $Fe_{(s)} \rightarrow Fe^{2+}_{(aq)} + 2e^-$

- H: $Ce_{(s)} \rightarrow Ce^{2+}_{(aq)} + 2e^-$

- I: $Cu_{(s)} \rightarrow Cu^{2+}_{(aq)} + 2e^-$

- J: $Se_{(s)} \rightarrow Se^{2+}_{(aq)} + 2e^-$

- K: $Sn_{(s)} \rightarrow Sn^{2+}_{(aq)} + 2e^-$

During the reverse cathodic scan, the following redox reactions took place:

<u>Reduction:</u>

- G′: $Zn^{2+}_{(aq)} + 2e^- \rightarrow Zn_{(s)}$; $Fe^{2+}_{(aq)} + 2e^- \rightarrow Fe_{(s)}$

- H′: $Ce^{2+}_{(aq)} + 2e^- \rightarrow Ce_{(s)}$

- I′: $Cu^{2+}_{(aq)} + 2e^- \rightarrow Cu_{(s)}$

- J′: $Se^{2+}_{(aq)} + 2e^- \rightarrow Se_{(s)}$

- K′: $Sn^{2+}_{(aq)} + 2e^- \rightarrow Sn_{(s)}$

At peak G (-0.96V) the current increased rapidly as both zinc and iron was oxidized: $Zn_{(s)} \rightarrow Zn^{2+}_{(aq)} + 2e^-$, $Fe_{(s)} \rightarrow Fe^{2+}_{(aq)} + 2e^-$. Peak H (-0.11V) indicates the oxidation of cerium: $Ce_{(s)} \rightarrow Ce^{2+}_{(aq)} + 2e^-$. The current further increased to 0.064 mA(-0.01V), which forms peak I, indicating the oxidation of copper: $Cu_{(s)} \rightarrow Cu^{2+}_{(aq)} + 2e^-$. Peaks J (0.10V) and Peaks K (0.16V) are due to the oxidation of selenium: $Se^{2+}_{(aq)} + 2e^- \rightarrow Se_{(s)}$ and tin: $Sn^{2+}_{(aq)} + 2e^- \rightarrow Sn_{(s)}$, respectively. Peak K′ (-0.23V) is due to the reduction and deposition of tin: $Sn^{2+}_{(aq)} + 2e^- \rightarrow Sn_{(s)}$. Peak J′, I′ and H′ (-0.47V) shows a massive increase in current and is

due to the added combination of the reduction and deposition of selenium: $Se^{2+}_{(aq)} + 2e^- \rightarrow Se_{(s)}$, the maximum precursor deposition ideally due to the reduction and metallic deposition of copper: $Cu^{2+}_{(aq)} + 2e^- \rightarrow Cu_{(s)}$ and cerium: $Ce^{2+}_{(aq)} + 2e^- \rightarrow Ce_{(s).}$ Peak G′ (-0.82V) shows that current increased, indicating the reduction and deposition of both zinc: $Zn^{2+}_{(aq)} + 2e^- \rightarrow Zn_{(s)}$ and iron: $Fe^{2+}_{(aq)} + 2e^- \rightarrow Fe_{(s)}$ [64,65]. The electrochemical bandgap was determined using the equations:

- $E_{HOMO} = -e \, (E_{onset.ox} + 4.5) \, eV$

- $E_{LUMO} = -e \, (E_{onset.red} + 4.5) \, eV$

- $E_g = E_{LUMO} - E_{HOMO}$

Where the oxidation peak is: -0.01 V and the reduction peak is -0.47 V, thus:

- $E_{HOMO} = -e \, (-0.11 + 4.5) \, eV = -4.49 \, eV$

- $E_{LUMO} = -e \, (-0.47 + 4.5) \, eV = -4.03 \, eV$

- $E_g = -4.03 \, eV + 4.49 \, eV = 0.46 \, eV$

Therefore, the electrochemical bandgap (E_g) for the doped kesterite nanoparticles is 0.46 eV [66–68].
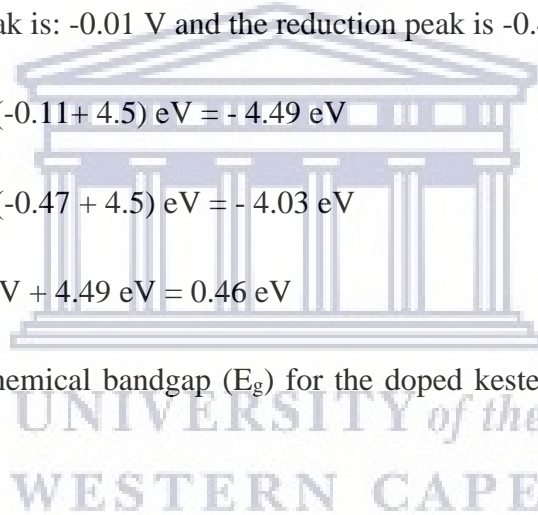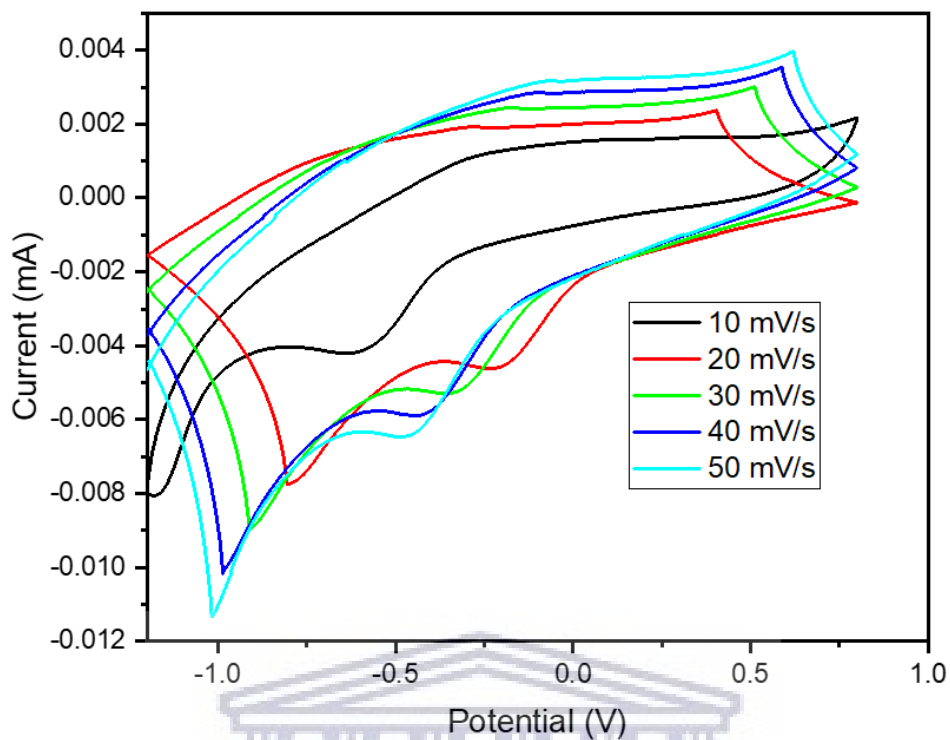
Figure 4.6.1.11: Cyclic voltammogram of the $Ce_2O_2Fe_2OSe_2$ nanoparticles (10 – 50 mV/s).
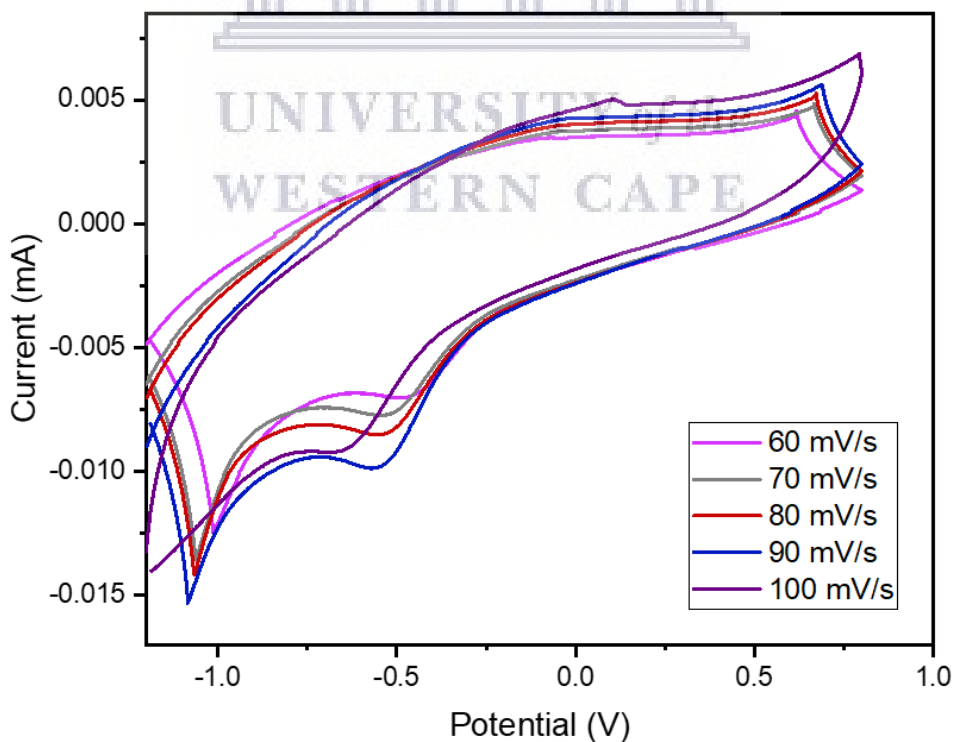
Figure 4.6.1.12: Cyclic voltammogram of the $Ce_2O_2Fe_2OSe_2$ nanoparticles (60 – 100 mV/s).

Table 4.6.1.1: Redox parameters obtained from the cyclic voltammograms of the $Ce_2O_2Fe_2OSe_2$ nanoparticles from 10 – 100 mV/s. (The values were taken from Fig. 4.6.1.11 and Fig. 4.6.1.12).

$Ce_2O_2Fe_2OSe_2$	I_{pa} (mA)	I_{pc} (mA)	E_{pa} (V)	E_{pc} (V)	ΔEp (mV)	E^o (mV)
10	0.0002	-0.0013	-0.3038	-0.6012	14.5	-452.50
20	0.0003	-0.0017	0.4013	-0.8022	14.5	-200.45
30	0.0003	-0.0019	0.5100	-0.9076	14.5	-198.80
40	0.0004	-0.0022	0.5870	-0.9851	14.5	-199.05
50	0.0004	-0.0025	0.6178	-1.0158	14.5	-199.00
60	0.0005	-0.0028	0.6149	-1.0096	14.5	-197.35
70	0.0005	-0.0031	0.6645	-1.0591	14.5	-197.30
80	0.0006	-0.0035	0.6674	-1.0654	14.5	-199.00
90	0.0006	-0.0039	0.6861	-1.0808	14.5	-197.35
100	0.0007	-0.0043	0.0983	-0.6257	14.5	-263.70

Equation		y = a + b*x	
Plot		Ipa/Ipc	C
Intercept		-4.03085E-5 ± 3.87457E-5	
Slope		6.9008E-5 ± 5.22447E-6	-4.29034E-4 ± 3.24413E-
Residual Sum of Squares		9.86478E-9	3.80363E-7
Pearson's r		0.97783	-0.97789
R- Square (COD)		0.95616	0.95626
Adj. R-Square		0.95068	0.95079
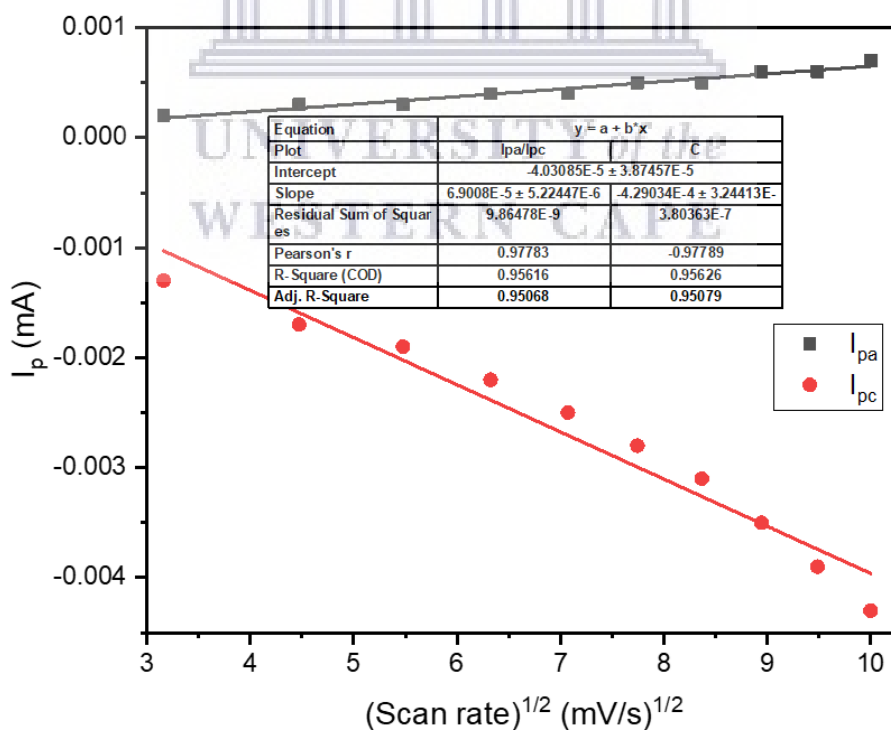
Figure 4.6.1.13: Randles–Ševčík plots of the CVs of $Ce_2O_2Fe_2OSe_2$ nanoparticles. (I_p values were taken from Table 4.6.1.1).
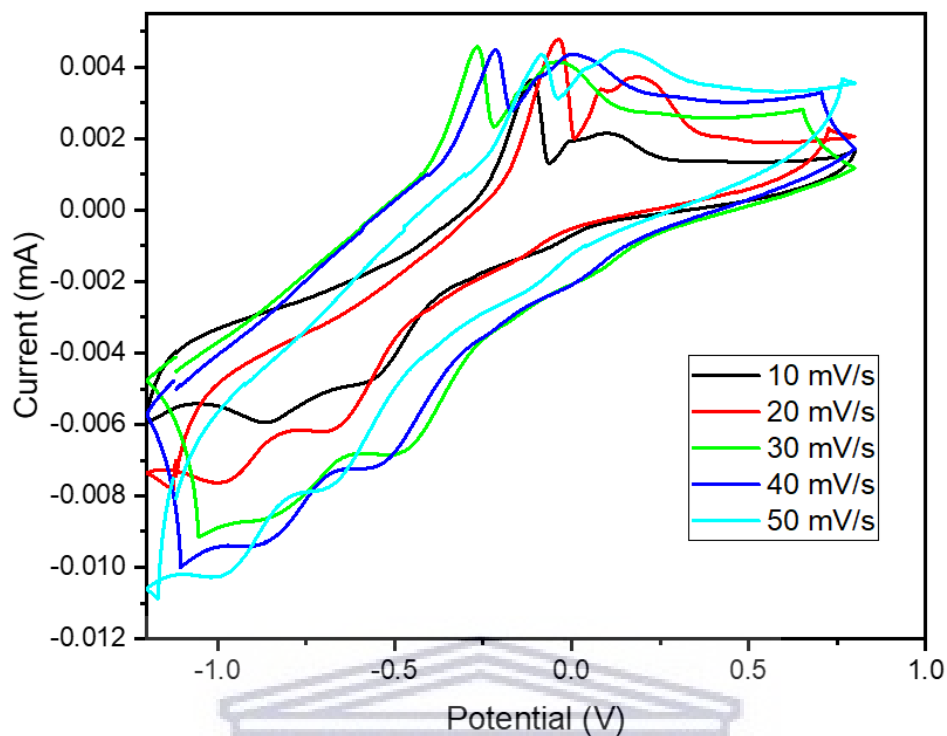
Figure 4.6.1.14: Cyclic voltammogram of the kesterite nanoparticles (10 – 50 mV/s).
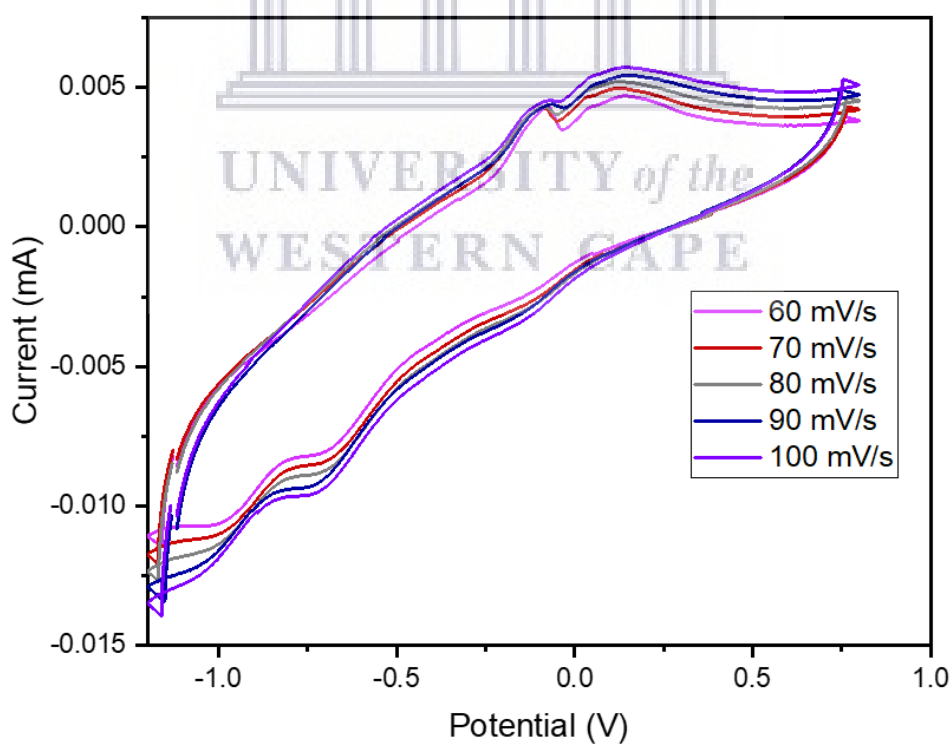
Figure 4.6.1.15: Cyclic voltammogram of the kesterite nanoparticles (60 – 100 mV/s).

Table 4.6.1.2: Redox parameters obtained from the cyclic voltammograms of the kesterite nanoparticles from 10 – 100 mV/s. (The values were taken from Fig. 4.6.1.14 and Fig. 4.6.1.15).

Kesterite	I_{pa} (mA)	I_{pc} (mA)	E_{pa} (V)	E_{pc} (V)	ΔE_p (mV)	E^o (mV)
10	0.0029	-0.0001	-0.1153	-0.8546	7.25	-484.95
20	0.0024	-0.0004	-0.0378	-0.9817	7.25	-509.75
30	0.0023	-0.0005	-0.2668	-0.8239	7.25	-545.35
40	0.0020	-0.0005	-0.2172	-0.8427	7.25	-529.95
50	0.0017	-0.0006	-0.0845	-0.9663	7.25	-525.40
60	0.0015	-0.0006	-0.0783	-0.9817	7.25	-530.00
70	0.0012	-0.0006	-0.0908	-0.9691	7.25	-529.95
80	0.0010	-0.0005	-0.0908	-0.9970	7.25	-543.90
90	0.0008	-0.0005	-0.0748	-1.0249	7.25	-549.85
100	0.0007	-0.0005	-0.0908	-1.0375	7.25	-564.15
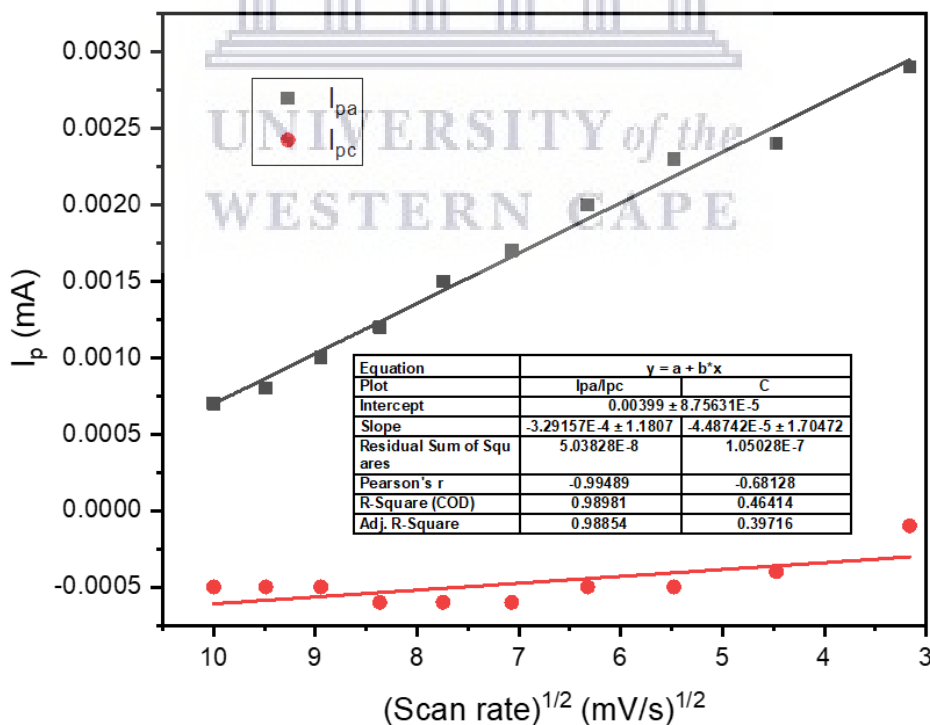
Figure 4.6.1.16: Randles–Ševčík plots of the CVs of kesterite nanoparticles. (I_p values were taken from Table 4.6.1.2).
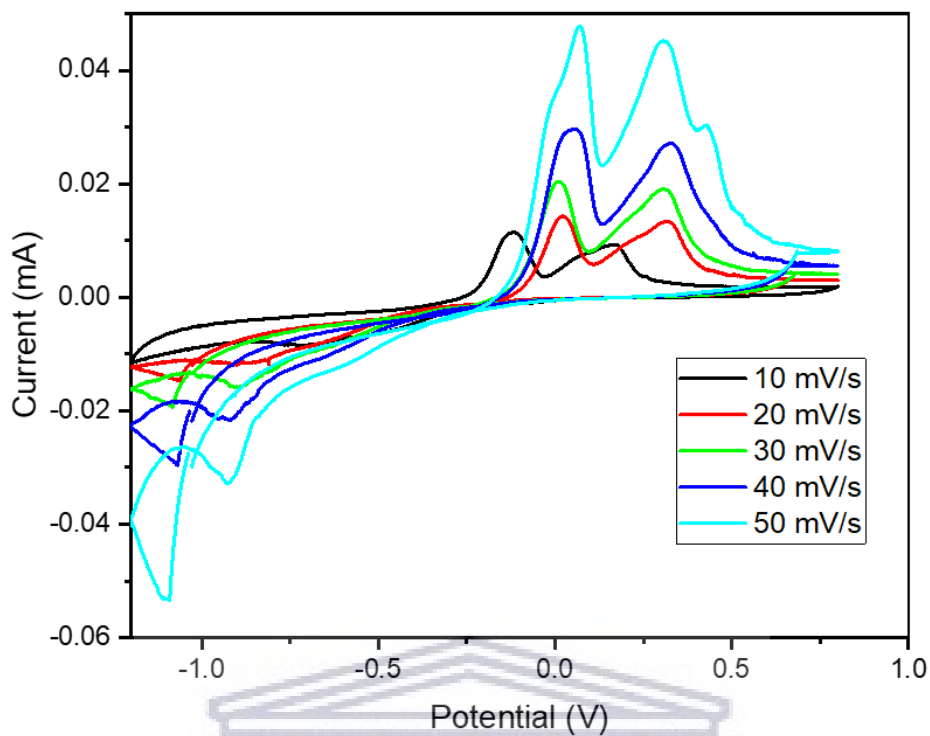
Figure 4.6.1.17: Cyclic voltammogram of the doped kesterite nanoparticles (10 – 50 mV/s).
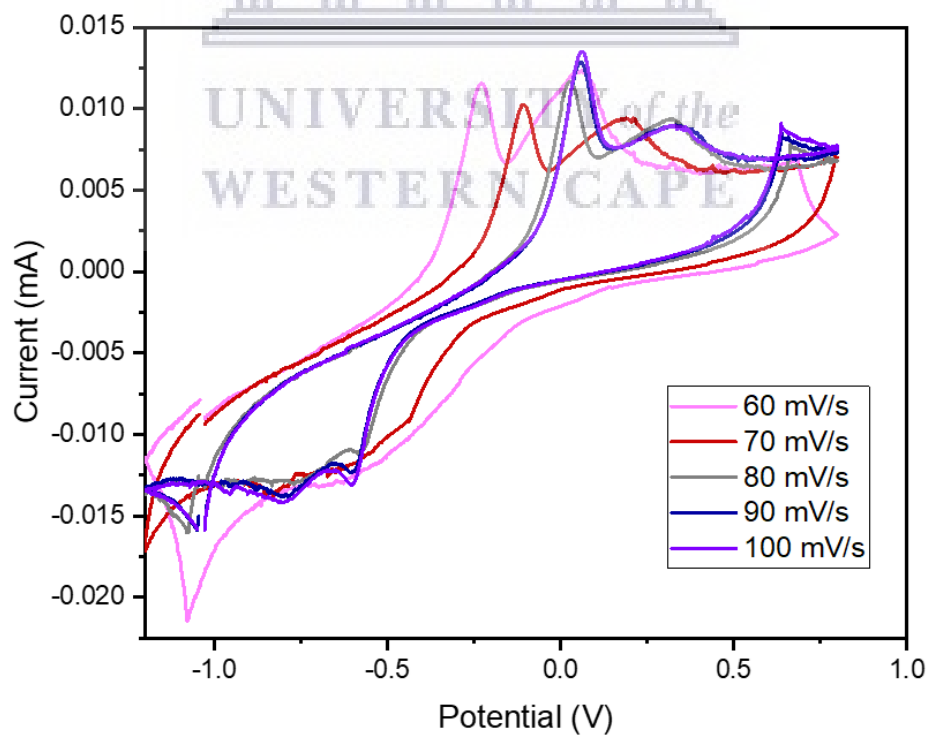
Figure 4.6.1.18: Cyclic voltammogram of the doped kesterite nanoparticles (60 – 100 mV/s).

Table 4.6.1.3: Redox parameters obtained from the cyclic voltammograms of the doped kesterite nanoparticles from 10 – 100 mV/s. (The values were taken from Fig. 4.6.1.17 and Fig. 4.6.1.18).

Doped kesterite	I_{pa} (mA)	I_{pc} (mA)	E_{pa} (V)	E_{pc} (V)	ΔE_p (mV)	E^o (mV)
10	0.0089	-0.0005	-0.1181	-0.7094	4.80	-413.75
20	0.0096	-0.0008	0.0208	-0.8489	4.80	-414.05
30	0.0139	-0.0023	0.0117	-0.8979	4.80	-443.10
40	0.0198	-0.0036	0.0516	-0.9200	4.80	-434.20
50	0.0286	-0.0060	0.0670	-0.9258	4.80	-429.40
60	0.0690	-0.0085	-0.2300	-1.0779	4.80	-653.95
70	0.0560	-0.0130	-0.1090	-0.8267	4.80	-467.85
80	0.0630	-0.0020	0.0271	-0.9817	4.80	-477.30
90	0.0710	-0.0090	0.0579	-0.7897	4.80	-365.90
100	0.0780	-0.0110	0.0613	-0.7994	4.80	-369.05
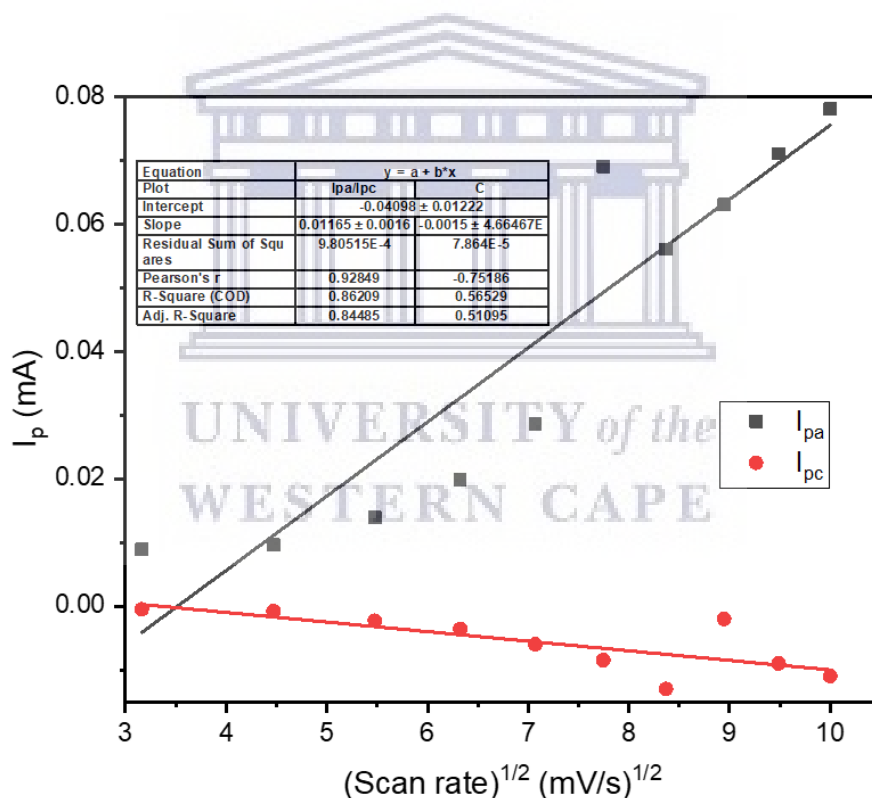
Figure 4.6.1.19: Randles–Ševčík plots of the CVs of doped kesterite nanoparticles. (I_p values were taken from Table 4.6.1.3).

From the tables and graphs above, its seen that the $Ce_2O_2Fe_2OSe_2$ nanoparticles are the most conductive as its anodic and cathodic peak current values are the greatest, along with having the highest ΔE_p (mV) and E^o (mV) values. It's also seen that doping the kesterite nanoparticles with the $Ce_2O_2Fe_2OSe_2$ nanoparticles improves their conductivity as the

anodic and cathodic peak current values are the greater for the doped kesterite nanoparticles than the normal kesterite nanoparticles. It's seen that a "linear relationship with the square root of the scan rate is indicated by the peak current", thus further confirms the fact that the peak current is directly proportional to the concentration of the ions in the majority of the material. Thus, the electrochemical process occurring at the surface of these electrodes is diffusion controlled.

Table 4.6.1.4: Electrochemical and Optical band gap of the cerium and iron oxyselenide, kesterite and doped kesterite nanoparticles.

Sample	Electrochemical band gap (eV)	Optical band gap (eV)
$Ce_2O_2Fe_2OSe_2$	0.48	1.66
Kesterite	0.67	2.41
Doped kesterite	0.46	2.41

Table 4.6.1.2 shows a difference between the electrochemical and optical bandgap for all samples; therefore, the electrochemical and optical bandgaps are not in agreement with each other. From the table, it seen the doped kesterite has the lowest electrochemical band gap and its optical band gap is in line with the kesterites optical band gap. From the results, the doped kesterite nanoparticles are better suited for use in PV applications due to their lower electrochemical band gap, thus, indicating that doping the kesterite nanoparticles with cerium and iron oxyselenide does in fact reduce the kesterite electrochemical band gap.

4.6.2 Electrochemical Impedance Spectroscopy

"Electrochemical impedance spectroscopy (EIS)" is a "measurement of the response of an electrode to a sinusoidal potential modulation at different frequencies", with one of the modules being superimposed either onto an applied anodic, cathodic or an open circuit potential. EIS is also used to study and determine the "resistance of the solution R_s, double layer capacitance C_{dl}, charge transfer resistance R_{ct} and Warburg impedance" which helps in evaluating the Warburg diffusion value. Essentially Warburg is constant phase element with a constant phase shift of 45⁰ and its impedance can be defined by resolving Fick's law. The mathematical approach of electrochemical impedance data is based on Ohm's law, "where the linear interdependency is between potential perturbation and current response or vice versa". Keep in mind, that the potential-current dependencies of

electrochemical systems in general are non-linear [69–73]. Zview software was used to fit the EIS data in order to obtain the resistance values, Warburg diffusion coefficient and double layer capacitance values, from this fitting the equivalent circuit of the EIS spectra can be obtained. EIS was performed on the cerium and iron oxyselenide dopant, kesterite and doped kesterite nanoparticles to see the effect of the dopant on the interface resistance, which yielded two different spectra, Bode plot and Nyquist plot. Nyquist plot shows the relation between the imaginary impedance and real impedance and Bode plot is the plot of total Impedance against frequency both as logarithm values as well as phase angle against frequency where frequency is in logarithm form.
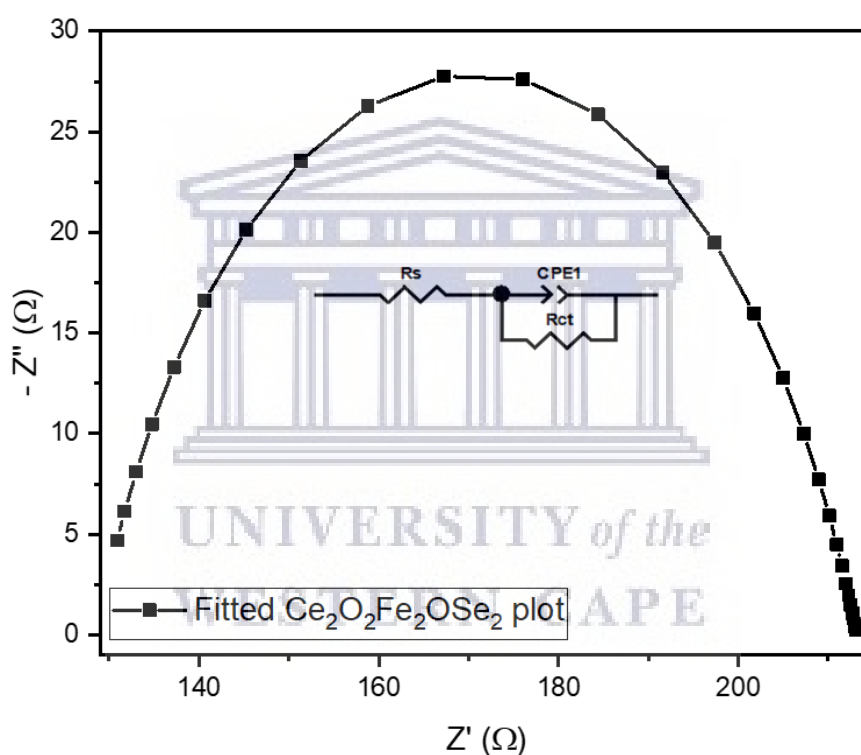
Figure 4.6.2.1: Fitted Nyquist plot of the $Ce_2O_2Fe_2OSe_2$ nanoparticles with inset of the equivalent circuit simulated using ZView.
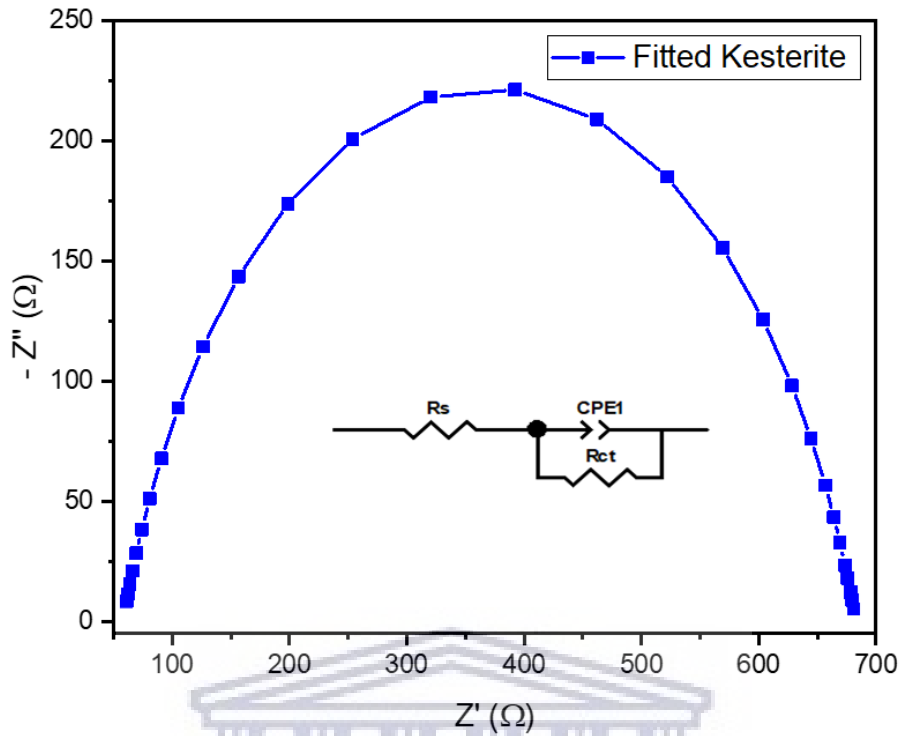
Figure 4.6.2.2: Fitted Nyquist plot of the kesterite nanoparticles with inset of the equivalent circuit simulated using ZView.
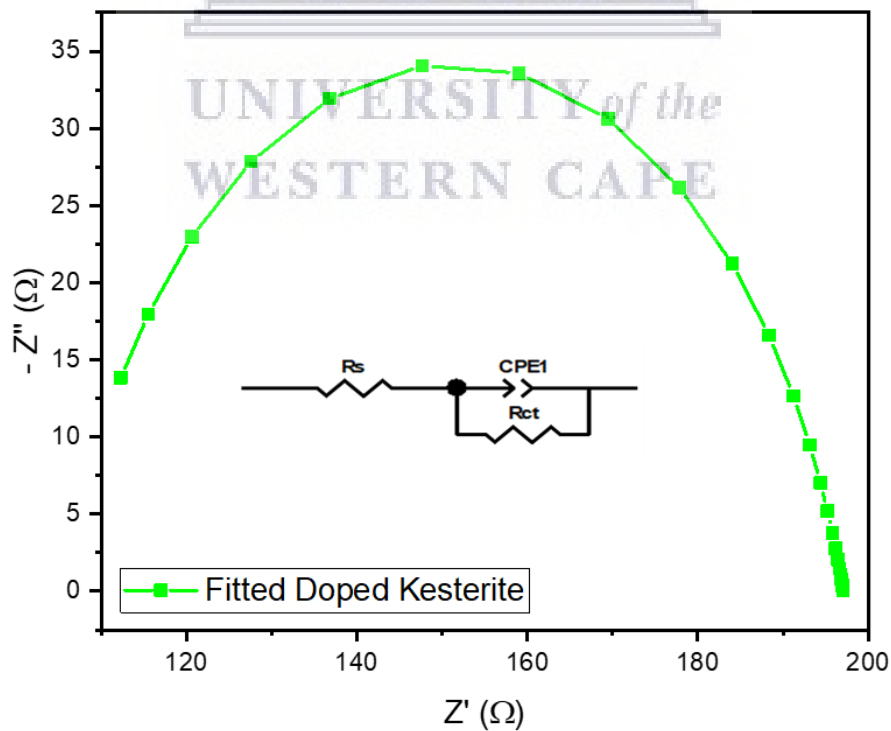
Figure 4.6.2.3: Fitted Nyquist plot of the doped kesterite nanoparticles with inset of the equivalent circuit simulated using ZView.

The fitted equivalent circuit for the $Ce_2O_2Fe_2OSe_2$ nanoparticles:
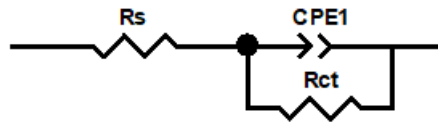
The fitted equivalent circuit for the kesterite nanoparticles:
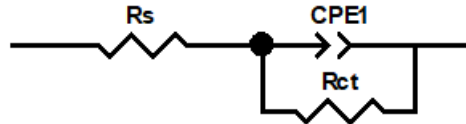
The fitted equivalent circuit for the doped kesterite nanoparticles:
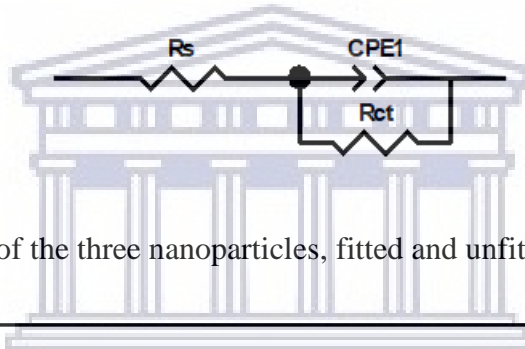
To compare the spectra of the three nanoparticles, fitted and unfitted plots were obtained.
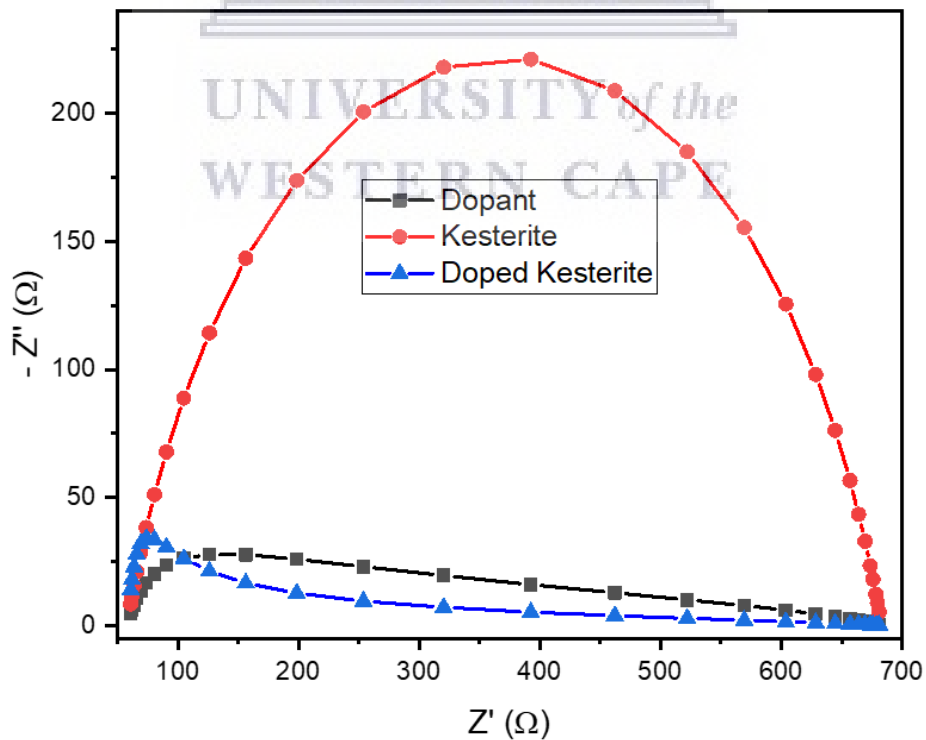
Figure 4.6.2.4: Nyquist plot comparing the $Ce_2O_2Fe_2OSe_2$, kesterite and doped kesterite nanoparticles.

Table 4.6.2: Fitted equivalent circuit values for the as-synthesized nanoparticles.

	Rs (Ω)	**CPE1-P (°)**	**Rct (Ω)**
$Ce_2O_2Fe_2OSe_2$	128.5	0.74215	84.64
Kesterite	57.84	0.78603	625
Doped Kesterite	105.6	0.81771	91.44

Fig. 4.6.2.1 – 4.6.2.3 shows the fitted nyquist plots for the $Ce_2O_2Fe_2OSe_2$, kesterite and doped kesterite nanoparticles respectively along with the inset equivalent circuits, while table 4.6.2 summarizes the equivalent circuit parameters obtained by best fitting the impedance data. R_s, CPE1-P and R_{ct} make up the equivalent circuit elements, with R_s being the ohmic series resistance of the electrode system, contributing to the electrical contact of the electrode-electrolyte and resistivity of electrolyte solution. CPE1-P stands for the chemical capacitance at the electrode-electrolyte inter-face with values ranging from 0 - 1. Where 1 describes ideal capacitive behaviour while 0 describes pure resistive character and R_{ct} represents recombination charge transfer resistance. Looking at table 4.6.2, its seen that the cerium and iron oxyselenide nanoparticles have the lowest R_{ct} = 84.64 Ω, the kesterite nanoparticles have the greatest R_{ct} = 625 Ω while the doped kesterite nanoparticles have the second lowest R_{ct} = 91.44 Ω. The cerium and iron oxyselenide and doped kesterite nanoparticles with the lowest R_{ct} values indicates that they are the most conductive while the kesterite nanoparticles with the greatest R_{ct} value indicates that it is the least conductive. This shows that doping the kesterite nanoparticles with the cerium and iron oxyselenides does greatly reduce the charge transfer resistance making the nanoparticles far more conductive which is ideal for photovoltaic applications. It's also known that doped kesterite nanoparticles with reduced/lower R_{ct} values, show good catalytic activity. The fitted equivalent circuit of all the nanoparticles didn't fit with a Warburg, this is supported by the bode plots where the phase angles of the nanoparticles did not start or end at 45º which is a constant phase parameter for a Warburg diffusion [74–79]. The Bode plot offers several advantages over the Nyquist plot such as; the individual charge transfer processes are resolvable; the frequency is explicit and small impedances in presence of large impedances can be identified easily.
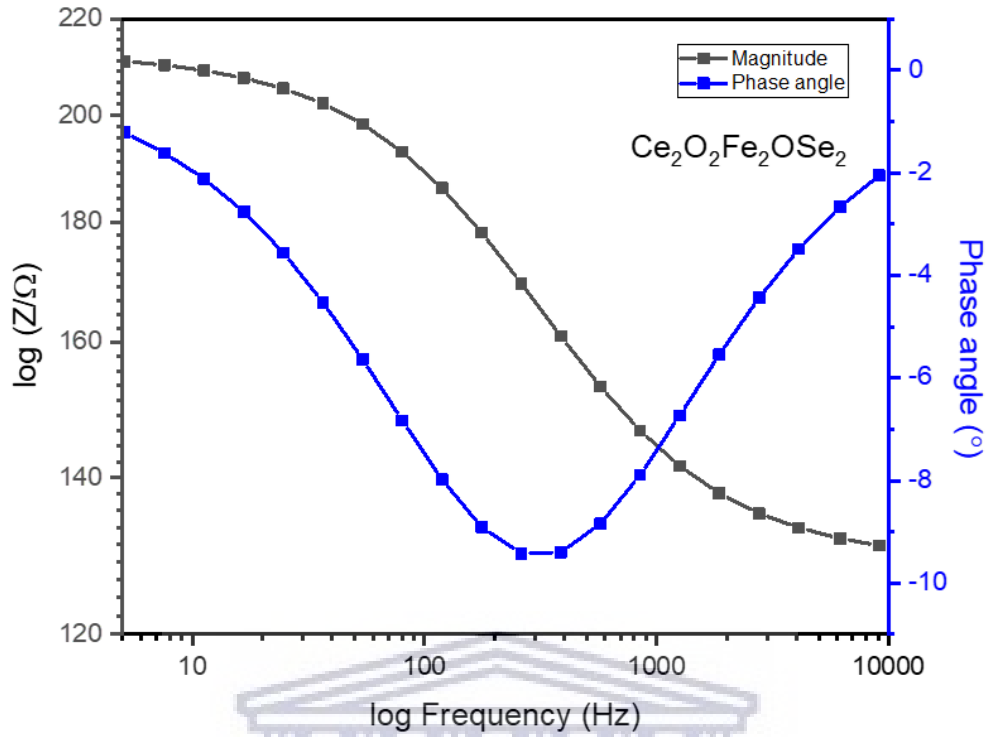
Figure 4.6.2.5: EIS Bode plot of the $Ce_2O_2Fe_2OSe_2$ nanoparticles.
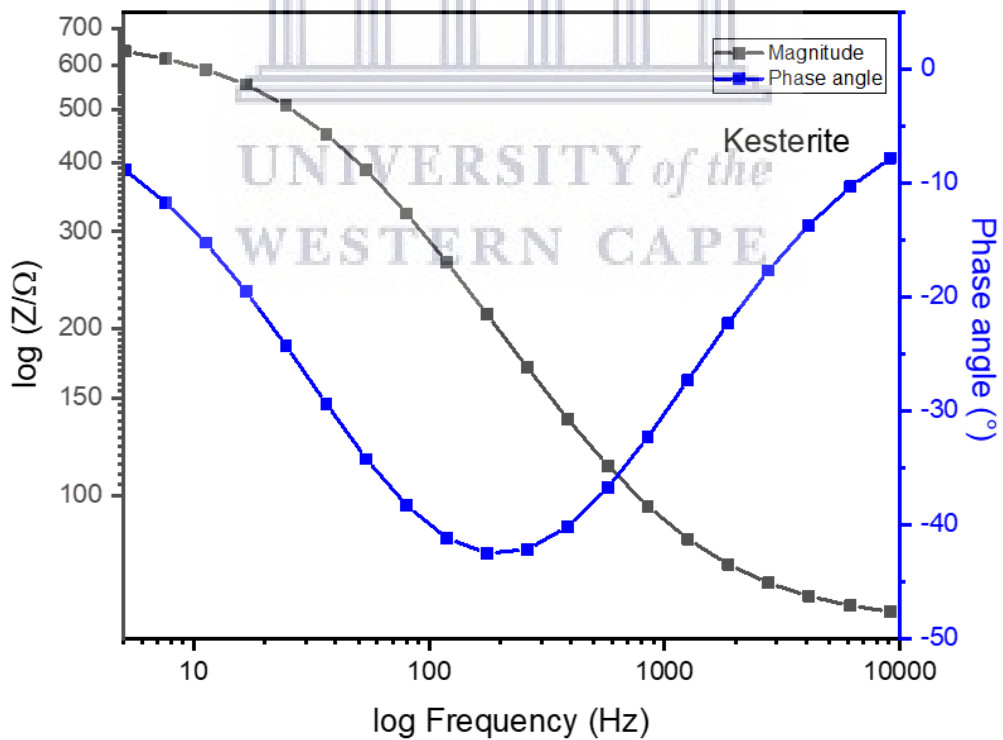
Figure 4.6.2.6: EIS Bode plot of the kesterite nanoparticles.
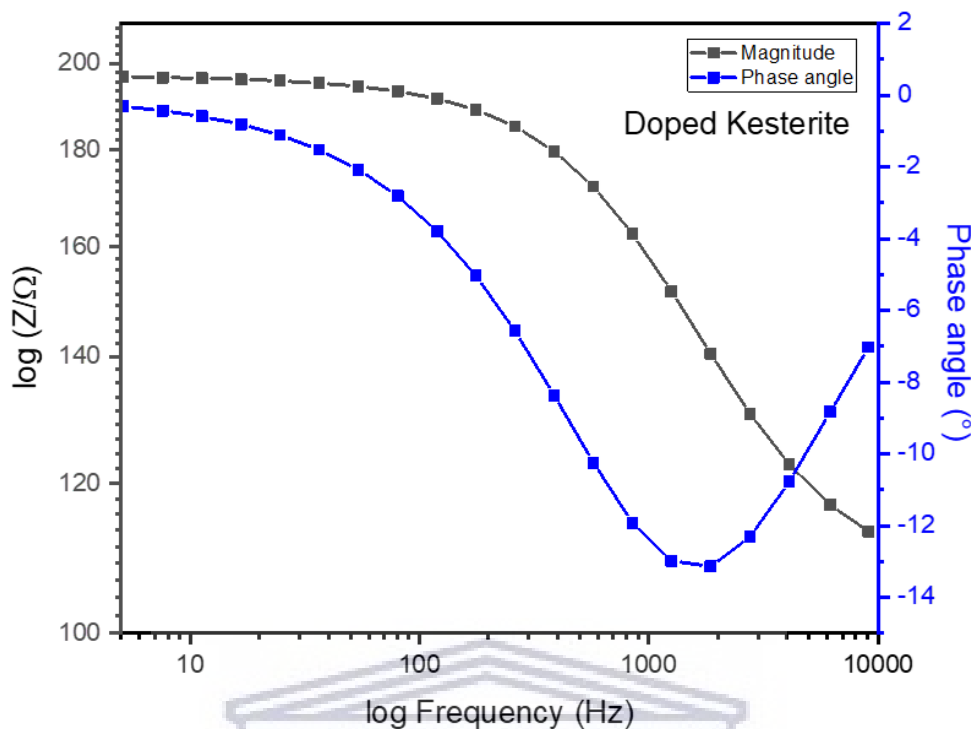
Figure 4.6.2.7: EIS Bode plot of the doped kesterite nanoparticles.

When looking at the bode plots, Fig. 4.6.2.5 shows the Bode plot of the $Ce_2O_2Fe_2OSe_2$ nanoparticles measured with the frequency range 9 kHz to 100 Hz and a potential of -1.9 V. The phase angle starts off low at -1.4° and increases along with a magnitude of 211.21 Ω that decreases slightly at the lower frequency range (0 – 60 Hz), suggesting some electron transfer resistance from CE to electrolyte and thus possesses electrical conductivity due to a low phase shift. From low-frequency range to the mid-frequency range there is a rapid increase in the phase angle while the magnitude decreases rapidly. At the mid-frequency range (100 – 1000 Hz), the phase angle reaches a maximum of -9.5° and begins levelling off then decreases while the magnitude continues to rapidly decrease from 178.07 Ω to 152.83 Ω. As the phase angle decreases from -7° to -2° while the magnitude continues to decrease from 137.85 Ω to 130.94 Ω in the higher frequency range (1050 – 10000 Hz) the electrical conductivity remains constant. The low phase angle and conductivity of the $Ce_2O_2Fe_2OSe_2$ nanoparticles is due to their low electrochemical reactivity [69,70,80,81]. Fig. 4.6.2.6 shows the bode plot of the kesterite nanoparticles measured with the frequency range 9 kHz to 100 Hz and a potential of -1.9 V. The phase angle starts off at 9.7° then rapidly increases along with a magnitude of 633.28 Ω which decreases at the lower frequency range (0 – 60 Hz), suggesting a small electron

transferring resistance from CE to electrolyte resulting in electrical conductivity. From low-frequency range to the mid-frequency range, the trend in the phase angle continues along with a rapid decrease in magnitude. At the mid-frequency range (100 – 1000 Hz), the phase angle reaches a maximum of 43° then starts decreasing while the magnitude continues to decrease from 264.29 Ω to 95.92 Ω. As the phase angle begins rapidly decreasing to 7° while the magnitude starts levelling off to 61.95 Ω in the higher frequency range (1050 – 10000 Hz) the electrical conductivity increases [69,70,80,81]. Fig. 4.6.2.7 shows the bode plot of the doped kesterite nanoparticles measured with the frequency range 9 kHz to 100 Hz and a potential of -1.85 V. The phase angle starts off at 0.3° then slightly increases along with a stable magnitude of 196.24 Ω at the lower frequency range (0 – 60 Hz), suggesting some electron transferring resistance from CE to electrolyte and thus indicating electrical conductivity due to a low phase shift. From low-frequency range to the mid-frequency range there is a slight increase in the phase angle along with a stable magnitude. In the mid-frequency range (100 – 1000 Hz), the phase angle increases rapidly from -2.7° to -12.2° while the magnitude decreases rapidly from 189.05 Ω to 162.45 Ω. At the high-frequency range (1050 – 10000 Hz), the phase angle reaches a maximum of -13° then decreases to -7° while the magnitude decreases slowly from 139.85Ω then levels off to 113.03 Ω suggesting a constant electrical conductivity [69,70,80,81]. Thus, doping the kesterite with $Ce_2O_2Fe_2OSe_2$ nanoparticles increases its conductivity.

4.6.3 Electrochemical Efficiencies

With solar energy being one of the most prominent and sought-after renewable energy sources, extensive investment, research and development has been done in this field in order to maximize efficiency and output power from solar cells (at device-level) and solar farms (at system-level). Kesterite solar cells are of major interest possessing a world record efficiency of 12.6%. In order to characterize the performance and efficiencies of solar cells, certain parameters must be determined. These parameters are; "peak power (P_{max}), short-circuit current density (J_{sc}), open circuit voltage (V_{oc}) and the fill factor (FF)", once these parameters are known the conversion efficiency (η) can be determined. "The current that flows through the external circuit when the electrodes of the solar cell are short circuited is termed the short circuit current (I_{sc}) and depends on the photon flux incident on the solar cell". The I_{sc} depends on the area of the solar cell and to remove this dependence, the short-circuit current density is used to describe the maximum current delivered by a

solar cell. The major performance gap between CZTS and CIGS solar cells is the large open circuit voltage deficit. Thus, the "V_{oc} deficit is the key limiting factor" for highly efficient CZTS solar cells. The open-circuit voltage is the maximum voltage that a solar cell can deliver, and is the voltage at which no current flows through the external circuit. The ratio between the "maximum power ($P_{max} = J_{mpp}V_{mpp}$)" of a solar cell and the product of V_{oc} with J_{sc} is known as the fill factor. The ratio between the maximal generated power and the incident power is calculated to determine the conversion efficiency [82–86].

Table 4.6.3.1: Electrochemical efficiencies of the $Ce_2O_2Fe_2OSe_2$ nanoparticles at different scan rates.

Scan rate (mV/s)	10	20	30	40	50	60	70	80	90	100
I_{sc} (μA)	0.48	0.79	1.35	1.71	1.35	2.748	3.52	3.33	5.275	5.547
E_{oc} (V)	0.45	0.48	0.58	0.56	0.384	0.553	0.58	0.43	0.541	0.433
P_T (μW)	0.22	0.38	0.78	0.96	0.518	1.519	2.03	1.45	2.855	2.405
P_{max} (μW)	4.32	6.22	7.67	9.3	11.33	11.62	13	15	15.39	17.24
FF (%)	20.1	16.4	9.79	9.72	21.86	7.65	6.39	10.3	5.39	7.17
P_s (W/m^2)	100	100	100	100	100	100	100	100	100	100
S (cm^2)	0.02	0.02	0.02	0.02	0.02	0.02	0.02	0.02	0.02	0.02
Ef (%)	2.16	3.11	3.84	4.65	5.66	5.81	6.48	7.45	7.69	8.62

Table 4.6.3.2: Electrochemical efficiencies of the kesterite nanoparticles at different scan rates.

Scan rate (mV/s)	10	20	30	40	50	60	70	80	90	100
I_{sc} (μA)	0.89	0.75	0.54	0.42	0.14	0.12	0.006	0.04	0.34	0.3
E_{oc} (V)	0.25	0.2	0.13	0.11	0.06	0.06	0.035	0.03	0.07	0.03
P_T (μW)	0.22	0.15	0.07	0.05	0.01	0.01	0.0002	0	0.02	0.01
P_{max} (μW)	2.06	2.36	2.19	2.71	3.33	3.75	4.534	5.14	6.32	6.52
FF (%)	9.19	16.2	39	58.2	38.2	0.01	1E-06	45.5	25.7	72.5
P_s (W/m^2)	100	100	100	100	100	100	100	100	100	100
S (cm^2)	0.02	0.02	0.02	0.02	0.02	0.02	0.02	0.02	0.02	0.02
Ef (%)	1.03	1.18	1.4	1.35	1.67	1.87	2.27	2.57	3.16	3.26

Table 4.6.3.3: Electrochemical efficiencies of the doped kesterite nanoparticles at different scan rates.

Scan rate (mV/s)	10	20	30	40	50	60	70	80	90	100
I_{sc} (μA)	0.82	1.12	0.92	1.13	1.39	1.38	1.31	0.97	0.52	1.603
E_{oc} (V)	0.35	0.34	0.19	0.2	0.22	0.19	0.16	0.11	0.08	0.022
P_T (μW)	0.28	0.38	0.18	0.23	0.31	0.27	0.21	0.11	0.04	0.036
P_{max} (μW)	1.52	2.06	2.6	3.08	3.57	4.15	4.83	5.73	7	11.58
FF (%)	5.36	5.49	14.8	13.6	11.6	15.5	22.6	51.8	17.9	32.84
P_s (W/m^2)	100	100	100	100	100	100	100	100	100	100
S (cm^2)	0.02	0.02	0.02	0.02	0.02	0.02	0.02	0.02	0.02	0.02
Ef (%)	0.76	1.03	1.3	1.54	1.78	2.07	2.41	2.87	3.47	5.79
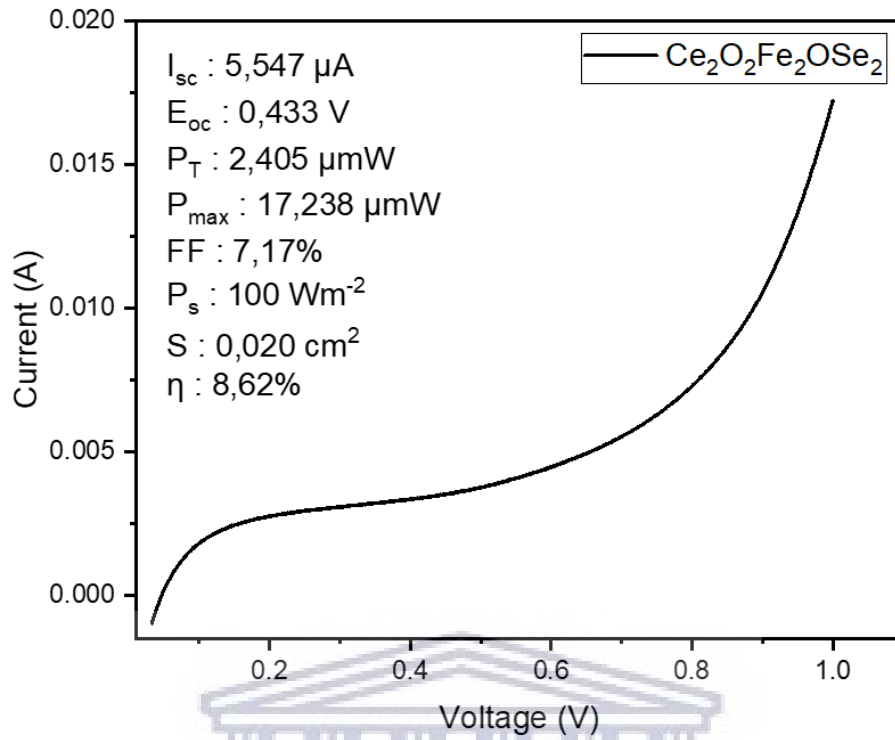
Figure 4.6.3.1: I-V curve of the $Ce_2O_2Fe_2OSe_2$ nanoparticles at a scan rate of 100 mVs.
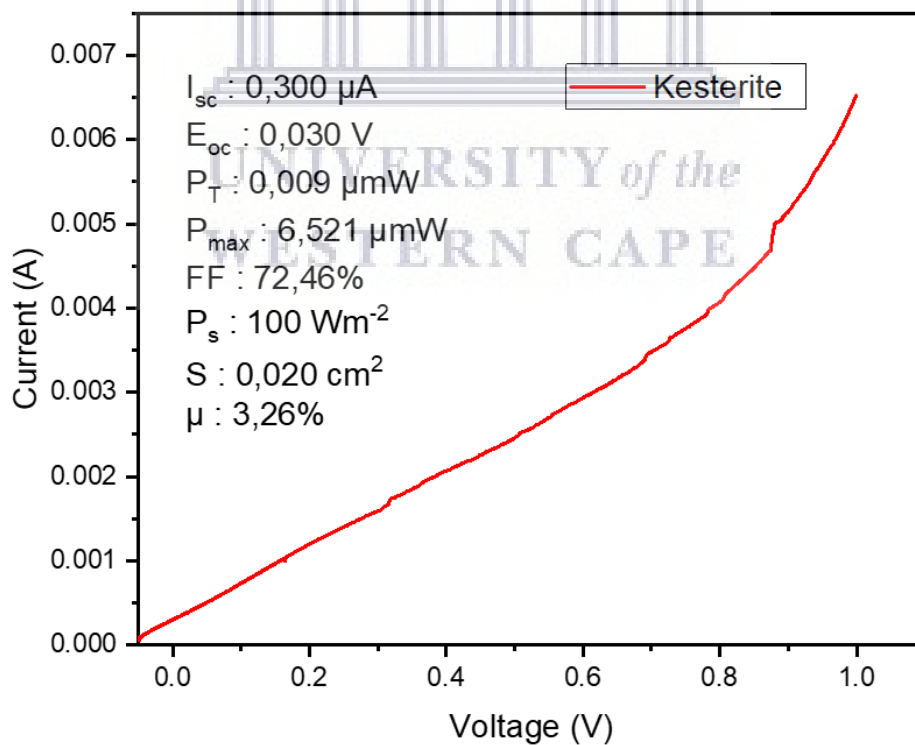
Figure 4.6.3.2: I-V curve of the kesterite nanoparticles at a scan rate of 100 mVs.
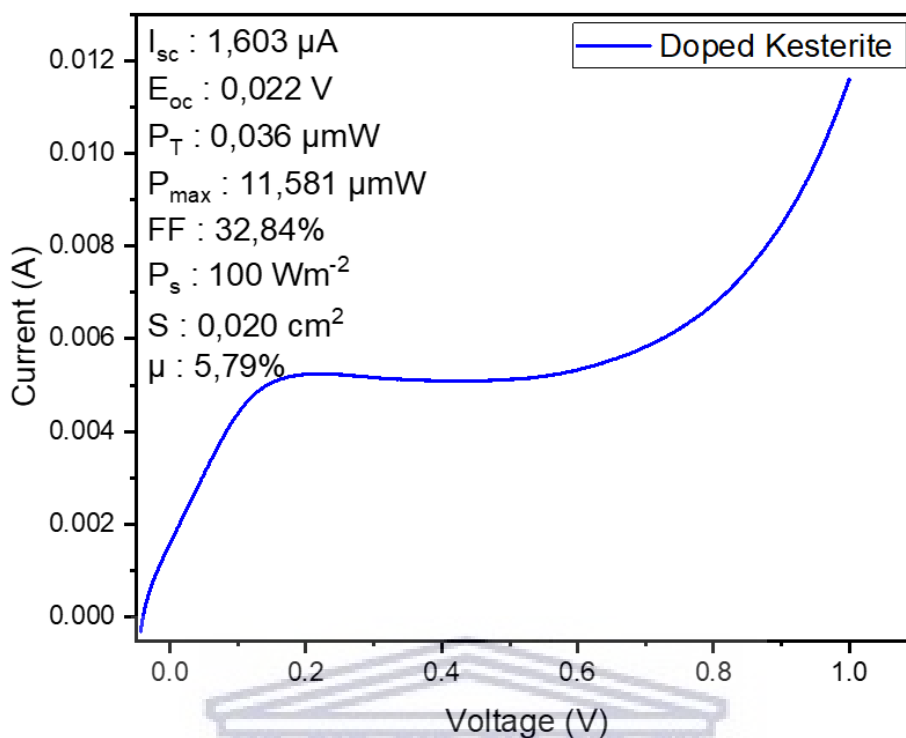
Figure 4.6.3.3: I-V curve of the doped kesterite nanoparticles at a scan rate of 100 mVs.

Table 4.6.3.1 shows the electrochemical efficiencies of the $Ce_2O_2Fe_2OSe_2$ nanoparticles at different scan rates. It is seen that at the scan rate of 100 mV/s the nanoparticles show very good parameters: I_{sc} = 5.547 µA/ cm^2, E_{oc} = 0.433 V, P_T = 2.405 µmW, P_{max} = 17.238 µmW, FF = 7.17 % and an efficiency of η = 8.62 %. As the scan rate decreases the parameters greatly diminish with the results of the scan rate of 10 mV/s being the worst: I_{sc} = 0.477 µA/ cm^2, E_{oc} = 0.451 V, P_T = 0.215 µmW, P_{max} = 4.320 µmW, FF = 20.08 % and an efficiency of η = 2.16 %. This efficiency is very good due to the parameters, with the FF fluctuating as the scan rate increases from 10 to 100 mV/s. The overall efficiency of the $Ce_2O_2Fe_2OSe_2$ dopant nanoparticles is η = 8.62 %, which is very good. Fig 4.6.3.1, shows the I-V curve of the $Ce_2O_2Fe_2OSe_2$ nanoparticles at a scan rate of 100 mVs, the scan rate with the best results and the highest efficiency of η = 8.62 %, which shows that the open circuit voltage 0.433 V of the nanoparticles is lower than the bandgap 0.11 eV. The low FF of 7.17 % can be attributed to a high series resistance resulting from the back contact electrical characteristics [87–95]. Table 4.6.3.2 shows the electrochemical efficiencies of the kesterite nanoparticles at different scan rates. It shows that at the scan rate 10 mV/s the nanoparticles show very poor parameters: I_{sc} = 0.887 µA/ cm^2, E_{oc} = 0.253 V, P_T = 0.224 µmW, P_{max} = 2.060 µmW, FF = 9.19 % and an efficiency of η = 1.03 %. This efficiency is

incredibly low due to the poor parameters, whereas, at the scan rate 100 mV/s the parameters greatly improve: I_{sc} = 0.300 µA cm^2, E_{oc} = 0.030 V, P_T = 0.009 µmW, P_{max} = 6.521 µmW, FF = 72.46 % and an efficiency of η = 3.26 %. The values of the E_{oc} fluctuate while the scan rate increases indicating a potential fault in the characterization run or human error during the synthesis of the kesterite nanoparticles. The overall efficiency of the kesterite nanoparticles is η = 3.26 % which is good. Fig 4.6.3.2, shows the I-V curve of the kesterite nanoparticles at a scan rate of 100 mVs, the scan rate with the best results and the highest efficiency of η = 3.26 %, which shows that the open circuit voltage 0.030 V of the nanoparticles is lower than the bandgap 0.10 eV. This is a problem known as V_{oc} deficit. This problem occurs in solar cells for example at the CdS/ CZTS interface due to dominant recombination [87–95]. Table 4.6.3.3 shows the electrochemical efficiencies of the doped kesterite nanoparticles at different scan rates. It is seen that at the scan rate 10 mV/s the nanoparticles show very poor parameters: I_{sc} = 0.816 µA/ cm^2, E_{oc} = 0.348 V, P_T = 0.284 µmW, P_{max} = 1.524 µmW, FF = 5.36 % and an efficiency of η = 0.762 %. Whereas, at the scan rate 100 mV/s the parameters greatly improve: I_{sc} = 1.603 µA cm^2, E_{oc} = 0.022 V, P_T = 0.036 µmW, P_{max} = 11.581 µmW, FF = 32.84 % and an efficiency of η = 5.79 %. The values of the E_{oc} decrease while the scan rate increases which is unusual and should not happen as the other parameters improved with a greater scan rate. The overall efficiency of the doped kesterite nanoparticles is η = 5.79 %. Fig 4.6.3.3, shows the I-V curve of the doped kesterite nanoparticles at a scan rate of 100 mVs, the scan rate with the best results and the highest efficiency of η = 5.79 %, which shows that the open circuit voltage 0.022 V of the nanoparticles is lower than the bandgap 0.36 eV, indicating a V_{oc} deficit. When comparing the electrochemical properties of the kesterite and doped kesterite, its seen that the doped kesterites electrochemical properties are greatly improved with an overall electrochemical efficiency of η = 5.79 %, which is far greater than the overall electrochemical efficiency of the kesterite nanoparticles η = 3.26 %.Therefore, doping the kesterite material with $Ce_2O_2Fe_2OSe_2$ nanoparticles does improve the materials electrochemical properties, making the doped kesterite material better suited for use in photovoltaic applications. It is known that high recombination losses are a probable cause for the low efficiency of CZTS cells. This possibly results from the carrier trap producing deep defect levels or by interface states. Knowing about the absorber surface properties and defect structure, could lead to possible improvements of the electrical properties of the CZTS material by modifying the surface composition [87–95].

References

[1]   M.M. Ali, H.S. Mahdi, A. Parveen, A. Azam, Optical properties of cerium oxide (CeO$_2$) nanoparticles synthesized by hydroxide mediated method, AIP Conf. Proc. 1953 (2018). doi:10.1063/1.5032379.

[2]   H. Dong, T. Schnabel, E. Ahlswede, C. Feldmann, Polyol-mediated synthesis of Cu$_2$ZnSn(S,Se)$_4$ kesterite nanoparticles and their use in thin-film solar cells, Solid State Sci. 29 (2014) 52–57. doi:10.1016/j.solidstatesciences.2014.01.006.

[3]   M. Patel, I. Mukhopadhyay, A. Ray, Structural, optical and electrical properties of spray-deposited CZTS thin films under a non-equilibrium growth condition, J. Phys. D. Appl. Phys. 45 (2012). doi:10.1088/0022-3727/45/44/445103.

[4]   E.Y. Muslih, K.H. Kim, Characteristics of Cu$_2$ZnSnS$_4$ thin film prepared by calcination and sulfurizing of metal (Cu,Zn,Sn)-ethanolamine precursor complexed from metal (Cu,Zn,Sn)-hydrate, Chalcogenide Lett. 12 (2015) 349–355.

[5]   C. Azanza, M.D. Incau, M. Leoni, P. Scardi, CZTS thin films characterization by XRD, University of Trento, 2010. https://www.enea.it/it/Ricerca_sviluppo/documenti/ricerca-di-sistema-elettrico/celle-fotovoltaiche/8-trento.pdf.

[6]   P.M.P. Salomé, J. Malaquias, P.A. Fernandes, M.S. Ferreira, A.F. Da Cunha, J.P. Leitão, J.C. González, F.M. Matinaga, Growth and characterization of Cu$_2$ZnSn(S,Se)$_4$ thin films for solar cells, Sol. Energy Mater. Sol. Cells. 101 (2012) 147–153. doi:10.1016/j.solmat.2012.02.031.

[7]   E.M. Mkawi, K. Ibrahim, M.K.M. Ali, A.S. Mohamed, Dependence of copper concentration on the properties of Cu$_2$ZnSnS$_4$ thin films prepared by electrochemical method, Int. J. Electrochem. Sci. 8 (2013) 359–368. https://www.researchgate.net/publication/234131523%0ADependence.

[8]   M.Q. Hamzah, A. Hasan Jabbar, S.O. Mezan, N.N. Hasan, M.A. Agam, Energy Gap Investigation and Characterization of Kesterite Cu$_2$ZnSnS$_4$ Thin Film for Solar Cell Applications, Int. J. Tech. Res. Appl. 6 (2018) 2320–8163. www.ijtra.com.

[9]   C. Stock, E.E. McCabe, The magnetic and electronic properties of oxyselenides - Influence of transition metal ions and lanthanides, J. Phys. Condens. Matter. 28 (2016) 1–35. doi:10.1088/0953-8984/28/45/453001.

[10]   A. Le Donne, V. Trifiletti, S. Binetti, New earth-abundant thin film solar cells based on chalcogenides, Front. Chem. 7 (2019). doi:10.3389/fchem.2019.00297.

[11]   A. Apostolopoulou, S. Mahajan, R. Sharma, E. Stathatos, Novel development of nanocrystalline kesterite Cu_2ZnSnS_4 thin film with high photocatalytic activity under visible light illumination, J. Phys. Chem. Solids. 112 (2018) 37–42. doi:10.1016/j.jpcs.2017.09.005.

[12]   D.B. Khadka, J. Kim, Study of structural and optical properties of kesterite Cu_2ZnGeX_4 (X = S, Se) thin films synthesized by chemical spray pyrolysis, CrystEngComm. 15 (2013) 10500–10509. doi:10.1039/c3ce41387j.

[13]   C. Tamin, D. Chaumont, O. Heintz, R. Chassagnon, A. Leray, N. Geoffroy, M. Guerineau, M. Adnane, Investigation of absorber and heterojunction in the pure sulphide kesterite, Bol. La Soc. Esp. Ceram. y Vidr. (2020) 0–11. doi:10.1016/j.bsecv.2020.05.004.

[14]   S.K. Swami, A. Kumar, V. Dutta, Deposition of kesterite Cu_2ZnSnS_4 (CZTS) thin films by spin coating technique for solar cell application, Energy Procedia. 33 (2013) 198–202. doi:10.1016/j.egypro.2013.05.058.

[15]   E.E. McCabe, A.S. Wills, L. Chapon, P. Manuel, J.S.O. Evans, Structural and magnetic characterization of iron oxyselenides $Ce_2O_2Fe_2OSe_2$ and $Nd_2O_2Fe_2OSe_2$, (2014). http://arxiv.org/abs/1410.4990.

[16]   F. Liu, J. Huang, K. Sun, C. Yan, Y. Shen, J. Park, A. Pu, F. Zhou, X. Liu, J.A. Stride, M.A. Green, X. Hao. Beyond 8% ultrathin kesterite Cu_2ZnSnS_4 solar cells by interface reaction route controlling and self-organized nanopattern at the back contact, NPG Asia Mater. 9 (2017). doi:10.1038/am.2017.103.

[17]   B. Pani, S. Padhy, U.P. Singh, A Comparative study of kesterite thin films prepared from different ball milled precursors, Mater. Today Proc. 4 (2017) 12536–12544. doi:10.1016/j.matpr.2017.10.057.

[18]   V.T. Tiong, J. Bell, H. Wang, One-step synthesis of high quality kesterite Cu_2ZnSnS_4 nanocrystals - a hydrothermal approach, Beilstein J. Nanotechnol. 5 (2014) 438–446. doi:10.3762/bjnano.5.51.

[19]   Y. Qu, S.W. Chee, M. Duchamp, S. Campbell, G. Zoppi, V. Barrioz, Y. Giret, T.J. Penfold, A. Chaturvedi, U. Mirsaidov, N.S. Beattie, Real-Time Electron Nanoscopy of Photovoltaic Absorber Formation from Kesterite Nanoparticles, ACS Appl. Energy Mater. 3 (2020) 122–128. doi:10.1021/acsaem.9b01732.

[20]   A. Robert, F. Rubio, TEM characterization of advanced kesterite structures, 2018.

[21]   J.L. Lábár, Consistent indexing of a (set of) single crystal SAED pattern(s) with the ProcessDiffraction program, Ultramicroscopy. 103 (2005) 237–249. doi:10.1016/j.ultramic.2004.12.004.

[22]   E. Isotta, C. Fanciulli, N.M. Pugno, P. Scardi, Effect of the order-disorder transition on the seebeck coefficient of nanostructured thermoelectric Cu_2ZnSnS_4, Nanomaterials. 9 (2019). doi:10.3390/nano9050762.

[23]   M. Fairul, S. Abdul, Z. Zainal, Electrophoretic Deposition and Characterization of Copper Selenide thin films, The Malaysian Journal of Analytical Sciences. 11 (2007) 324–330. http://www.ukm.my/mjas/v11_n1/47-346A3-KB-Za-format-x.pdf

[24]   S. Das, K. Sa, P.C. Mahakul, J. Raiguru, I. Alam, B. Subramanyam, P. Mahanandia, Synthesis of quaternary chalcogenide CZTS nanoparticles by a hydrothermal route, IOP Conf. Ser. Mater. Sci. Eng. 338 (2018). doi:10.1088/1757-899X/338/1/012062.

[25]   C.J. Humphreys, The significance of Braggs law in electron diffraction and microscopy, and Braggs second law, Acta Crystallogr. Sect. A Found. Crystallogr. 69 (2013) 45–50. doi:10.1107/S0108767312047587.

[26]   Y. Kamihara, T. Watanabe, M. Hirano, H. Hosono, Iron-Based Layered Superconductor La $[O_{1-x}F_x]FeAs_{(x)0.05-0.12})$ with Tc) 26 K, (2008) 3296–3297. doi:doi.org/10.1021/ja800073m.

[27]   N. Ni, S. Jia, Q. Huang, E. Climent-Pascual, R.J. Cava, Structural, transport, thermodynamic, and neutron diffraction studies of layered $R_2O_3Fe_2Se_2$ (R = Ce, Pr, Nd,

and Sm), Phys. Rev. B - Condens. Matter Mater. Phys. 83 (2011) 1–7. doi:10.1103/PhysRevB.83.224403.

[28]   D.G. Free, J.S.O. Evans, Low-temperature nuclear and magnetic structures of $La_2O_2Fe_2OSe_2$ from x-ray and neutron diffraction measurements, Phys. Rev. B - Condens. Matter Mater. Phys. 81 (2010) 1–7. doi:10.1103/PhysRevB.81.214433.

[29]   E.E. McCabe, C. Stock, E.E. Rodriguez, A.S. Wills, J.W. Taylor, J.S.O. Evans, Weak spin interactions in Mott insulating $la_2O_2Fe_2OSe_2$, Phys. Rev. B - Condens. Matter Mater. Phys. 89 (2014) 1–5. doi:10.1103/PhysRevB.89.100402.

[30]   S. Schorr, The crystal structure of kesterite type compounds: A neutron and X-ray diffraction study, Sol. Energy Mater. Sol. Cells. 95 (2011) 1482–1488. doi:10.1016/j.solmat.2011.01.002.

[31]   S.R. Hallt, J.T. Szymanski, J.M. Stewart, KESTERITE, $Cu_2(Zn,Fe)SnS_4$, AND STANNITE, $Cu_2(FeZn)SnS_4$, STRUCTURALLY SIMILAR BUT DISTINCT MINERALS, Can. Mineral. 16 (1978) 131–137.

[32]   J. Paier, R. Asahi, A. Nagoya, G. Kresse, Cu_2ZnSnS_4 as a potential photovoltaic material: A hybrid Hartree-Fock density functional theory study, Phys. Rev. B - Condens. Matter Mater. Phys. 79 (2009) 1–8. doi:10.1103/PhysRevB.79.115126.

[33]   S. Schorr, H.-J. Hoebler, M. Tovar, A neutron diffraction study of the stannite-kesterite solid solution series, Eur. J. Mineral. 19 (2007) 65–73. doi:10.1127/0935-1221/2007/0019-0065.

[34]   R.B. Wexler, G.S. Gautam, E.A. Carter, Optimizing kesterite solar cells from Cu_2ZnSnS_4 to $Cu_2CdGe(S,Se)_4$, J. Mater. Chem. A. 9 (2021) 9882–9897. doi:10.1039/d0ta11603c.

[35]   H. Schnablegger, Y. Singh, The SAXS Guide, 3rd ed., Anton Paar GmbH, Austria, 2013.

[36]   A. Craievich, Advanced School on Synchrotron and Free Electron Laser Sources Small-Angle X – ray Scattering by Nanostructured Materials, (2008).

[37]   J. Li, A. Jiao, S. Chen, Z. Wu, E. Xu, Z. Jin, Application of the small-angle X-ray scattering technique for structural analysis studies: A review, J. Mol. Struct. 1165 (2018) 391–400. doi:10.1016/j.molstruc.2017.12.031.

[38]   M. Grawert, D. Svergun, A beginner's guide to solution small-angle X-ray scattering (SAXS), Biochem. 0 (2020) 36–42. doi:10.1042/BIO04201036.

[39]   V. Uvarov, The influence of X-ray diffraction pattern angular range on Rietveld refinement results used for quantitative analysis, crystallite size calculation and unit-cell parameter   refinement,   J.   Appl.   Crystallogr.   52   (2019)   252–261. doi:10.1107/S1600576719000621.

[40]   J. Just, D. Lützenkirchen-Hecht, O. Müller, R. Frahm, T. Unold, Depth distribution of secondary phases in kesterite Cu_2ZnSnS_4 by angle-resolved X-ray absorption spectroscopy, APL Mater. 5 (2017) 1–7. doi:10.1063/1.5000306.

[41]   J. Just, D. Ltzenkirchen-Hecht, R. Frahm, S. Schorr, T. Unold, Determination of secondary phases in kesterite Cu_2ZnSnS_4 thin films by x-ray absorption near edge structure analysis, Appl. Phys. Lett. 99 (2011). doi:10.1063/1.3671994.

[42]   D. Cecchin, D. Poggiali, L. Riccardi, P. Turco, F. Bui, S. De Marchi, Analytical and experimental FWHM of a gamma camera: Theoretical and practical issues, PeerJ. (2015). doi:10.7717/peerj.722.

[43]   Heryanto, Hendri, B. Abdullah, D. Tahir, Analysis of structural properties of X-ray diffraction for composite copper-activated carbon by modified Williamson-Hall and size-strain   plotting   methods,   J.   Phys.   Conf.   Ser.   1080   (2018).   doi:10.1088/1742-6596/1080/1/012007.

[44]   A.O. Bokuniaeva, A.S. Vorokh, Estimation of particle size using the Debye equation and the Scherrer formula for polyphasic TiO_2 powder, J. Phys. Conf. Ser. 1410 (2019). doi:10.1088/1742-6596/1410/1/012057.

[45]   A. Valério, S.L. Morelhão, Usage of Scherrer's formula in X-ray diffraction analysis of size distribution in systems of monocrystalline nanoparticles, ArXiv. (2019) 1-9.

[46]   A. Apostolopoulou, S. Mahajan, R. Sharma, E. Stathatos, Novel development of nanocrystalline kesterite Cu_2ZnSnS_4 thin film with high photocatalytic activity under visible light illumination, J. Phys. Chem. Solids. 112 (2018) 37–42. doi:10.1016/j.jpcs.2017.09.005.

[47]   K. Lejda, Magnetism of Kesterite Cu_2ZnSnS_4 Semiconductor, Materials (Basel). 13 (2020). doi:10.3390/ma13163487.

[48]   M. Rabiei, A. Palevicius, A. Monshi, S. Nasiri, A. Vilkauskas, G. Janusas, Comparing methods for calculating nano crystal size of natural hydroxyapatite using X-ray diffraction, Nanomaterials. 10 (2020) 1–21. doi:10.3390/nano10091627.

[49]   A. Agbabiaka, M. Wiltfong, C. Park, Small Angle X-Ray Scattering Technique for the Particle Size Distribution of Nonporous Nanoparticles, J. Nanoparticles. 2013 (2013) 1–11. doi:10.1155/2013/640436.

[50]   S. Das, I. Alam, J. Raiguru, B.V.R.S. Subramanyam, P. Mahanandia, A facile method to synthesize CZTS quantum dots for solar cell applications, Phys. E Low-Dimensional Syst. Nanostructures. 105 (2019) 19–24. doi:10.1016/j.physe.2018.08.020.

[51]   N. Kattan, B. Hou, D.J. Fermín, D. Cherns, Crystal structure and defects visualization of Cu_2ZnSnS_4 nanoparticles employing transmission electron microscopy and electron diffraction, Appl. Mater. Today. 1 (2015) 52–59. doi:10.1016/j.apmt.2015.08.004.

[52]   D.J. Milliron, D.B. Mitzi, M. Copel, C.E. Murray, Solution-processed metal chalcogenide films for p-type transistors, Chem. Mater. 18 (2006) 581–590. doi:10.1021/cm052300r.

[53]   M. Al-Shakban, P.D. Matthews, N. Savjani, X.L. Zhong, Y. Wang, M. Missous, P. O'Brien, The synthesis and characterization of Cu_2ZnSnS_4 thin films from melt reactions using xanthate precursors, J. Mater. Sci. 52 (2017) 12761–12771. doi:10.1007/s10853-017-1367-0.

[54]   J.-M. Yun, Ternary and quaternary metal chalcogenide nanocrystals: synthesis, properties and applications, J. Mater. Chem. 1 (2013) 3777. doi:10.1039/b000000x.

[55]   O.K. Simya, B. Geetha Priyadarshini, K. Balachander, A.M. Ashok, Formation of a phase pure kesterite CZTSe thin films using multisource hybrid physical vapour deposition, Mater. Res. Express. 7 (2020). doi:10.1088/2053-1591/ab64ee.

[56]   A. Weber, R. Mainz, H.W. Schock, On the Sn loss from thin films of the material system Cu-Zn-Sn-S in high vacuum, J. Appl. Phys. 107 (2010). doi:10.1063/1.3273495.

[57]   S. Siebentritt, G. Rey, A. Finger, D. Regesch, J. Sendler, T.P. Weiss, T. Bertram, What is the bandgap of kesterite?, Sol. Energy Mater. Sol. Cells. 158 (2016) 126–129. doi:10.1016/j.solmat.2015.10.017.

[58]   Z.Y. Xiao, Y.F. Li, B. Yao, R. Deng, Z.H. Ding, T. Wu, G. Yang, C.R. Li, Z.Y. Dong, L. Liu, L.G. Zhang, H.F. Zhao, Bandgap engineering of $Cu_2Cd_xZn_{1-x}SnS_4$ alloy for photovoltaic applications: A complementary experimental and first-principles study, J. Appl. Phys. 114 (2013). doi:10.1063/1.4829457.

[59]   K.J. Yang, D.H. Son, S.J. Sung, J.H. Sim, Y.I. Kim, S.N. Park, D.H. Jeon, J. Kim, D.K. Hwang, C.W. Jeon, D. Nam, H. Cheong, J.K. Kang, D.H. Kim, A band-gap-graded CZTSSe solar cell with 12.3% efficiency, J. Mater. Chem. A. 4 (2016) 10151–10158. doi:10.1039/c6ta01558a.

[60]   I.M. El Radaf, H.Y.S. Al-Zahrani, A.S. Hassanien, Novel synthesis, structural, linear and nonlinear optical properties of p-type kesterite nanosized Cu_2MnGeS_4 thin films, J. Mater. Sci. Mater. Electron. 31 (2020) 8336–8348. doi:10.1007/s10854-020-03369-9.

[61]   J. Henry, K. Mohanraj, G. Sivakumar, Electrical and optical properties of CZTS thin films prepared by SILAR method, J. Asian Ceram. Soc. 4 (2016) 81–84. doi:10.1016/j.jascer.2015.12.003.

[62]   S. Chen, A. Walsh, X.G. Gong, S.H. Wei, Classification of lattice defects in the kesterite Cu_2ZnSnS_4 and $Cu_2ZnSnSe_4$ earth-abundant solar cell absorbers, Adv. Mater. 25 (2013) 1522–1539. doi:10.1002/adma.201203146.

[63]   A. Fairbrother, X. Fontané, V. Izquierdo-Roca, M. Espindola-Rodriguez, S. Lõpez-Marino, M. Placidi, J. Lõpez-García, A. Pérez-Rodríguez, E. Saucedo, Single-step sulfo-

selenization method to synthesize $Cu_2ZnSn(S_ySe_{1-y})_4$ absorbers from metallic stack precursors, ChemPhysChem. 14 (2013) 1836–1843. doi:10.1002/cphc.201300157.

[64]   L. Mg, B. Gr, L. Pu, R. Ab, C. Nb, Electrochemical Synthesis and Characterization of Cu_2ZnSnS_4 Thin Films, J. Mater. Sci. Eng. 5 (2016) 4–9. doi:10.4172/2169-0022.1000261.

[65]   H. Kirou, L. Atourki, L. Essaleh, A. Taleb, M.Y. Messous, K. Bouabid, M. Nya, A. Ihlal, Towards phase pure Kesterite Cu_2ZnSnS_4 thin films via Cu-Zn-Sn electrodeposition under a variable applied potential, J. Alloys Compd. 783 (2019) 524–532. doi:10.1016/j.jallcom.2018.12.269.

[66]   S. Rondiya, A. Rokade, P. Sharma, M. Chaudhary, A. Funde, Y. Jadhav, S. Haram, H. Pathan, S. Jadkar, CZTS/CdS: interface properties and band alignment study towards photovoltaic applications, J. Mater. Sci. Mater. Electron. 29 (2018) 4201–4210. doi:10.1007/s10854-017-8365-5.

[67]   L. Leonat, G. Sbârcea, I.V. Brânzoi, Cyclic voltammetry for energy levels estimation of organic materials, UPB Sci. Bull. Ser. B Chem. Mater. Sci. 75 (2013) 111–118.

[68]   K. Gmucová, V. Nádaždy, F. Schauer, M. Kaiser, E. Majková, Electrochemical Spectroscopic Methods for the Fine Band Gap Electronic Structure Mapping in Organic Semiconductors, J. Phys. Chem. C. 119 (2015) 15933–15934. doi:10.1021/acs.jpcc.5b04378.

[69]   H. Cesiulis, N. Tsyntsaru, A. Ramanavicius, G. Ragoisha, The Study of Thin Films by Electrochemical Impedance Spectroscopy, Springer International Publishing, 2016. doi:10.1007/978-3-319-30198-3.

[70]   S. Sarker, A.J.S. Ahammad, H.W. Seo, D.M. Kim, Electrochemical impedance spectra of dye-sensitized solar cells: Fundamentals and spreadsheet calculation, Int. J. Photoenergy. 2014 (2014). doi:10.1155/2014/851705.

[71]   M.E. Orazem, B. Tribollet, A tutorial on electrochemical impedance spectroscopy, ChemTexts. 6 (2020) 1–9. doi:10.1007/s40828-020-0110-7.

[72]   L. Bardini, EIS 101, an introduction to electrochemical spectroscopy. What was a website is now available as a self-contained PDF, (2018). doi:10.13140/RG.2.1.2248.5600.

[73]   B.A. Mei, O. Munteshari, J. Lau, B. Dunn, L. Pilon, Physical Interpretations of Nyquist Plots for EDLC Electrodes and Devices, J. Phys. Chem. C. 122 (2018) 194–206. doi:10.1021/acs.jpcc.7b10582.

[74]   A. Ghosh, A. Biswas, R. Thangavel, G. Udayabhanu, Photo-electrochemical properties and electronic band structure of kesterite copper chalcogenide Cu_2-II-Sn-S_4 (II = Fe, Co, Ni) thin films, RSC Adv. 6 (2016) 96025–96034. doi:10.1039/c6ra15700a.

[75]   S.J. Patil, V.C. Lokhande, D.W. Lee, C.D. Lokhande, Electrochemical impedance analysis of spray deposited CZTS thin film: Effect of Se introduction, Opt. Mater. (Amst). 58 (2016) 418–425. doi:10.1016/j.optmat.2016.06.011.

[76]   K.M. Lee, P.Y. Chen, C.Y. Hsu, J.H. Huang, W.H. Ho, H.C. Chen, K.C. Ho, A high-performance counter electrode based on poly(3,4-alkylenedioxythiophene) for dye-sensitized solar cells, J. Power Sources. 188 (2009) 313–318. doi:10.1016/j.jpowsour.2008.11.075.

[77]   S.G. Hashmi, T. Moehl, J. Halme, Y. Ma, T. Saukkonen, A. Yella, F. Giordano, J.D. Decoppet, S.M. Zakeeruddin, P. Lund, M. Grätzel, A durable SWCNT/PET polymer foil-based metal free counter electrode for flexible dye-sensitized solar cells, J. Mater. Chem. A. 2 (2014) 19609–19615. doi:10.1039/c4ta03730h.

[78]   Y. Xie, C. Zhang, F. Yue, Y. Zhang, Y. Shi, T. Ma, Morphology dependence of performance of counter electrodes for dye-sensitized solar cells of hydrothermally prepared hierarchical Cu_2ZnSnS_4 nanostructures, RSC Adv. 3 (2013) 23264–23268. doi:10.1039/c3ra43731k.

[79]   K.C. Nwambaekwe, M. Masikini, P. Mathumba, M.E. Ramoroka, S. Duoman, V.S. John-Denk, E.I. Iwuoha, Electronics of anion hot injection-synthesized te-functionalized kesterite nanomaterial, Nanomaterials. 11 (2021) 1–14. doi:10.3390/nano11030794.

[80]   H.D. Shelke, A.M. Patil, A.C. Lokhande, J.H. Kim, C.D. Lokhande, Electrochemical impedance analysis of SILAR deposited Cu_2SnS_3 (CTS) thin film, Int. J.

Eng. Res. Technol. 10 (2017) 578–586. https://www.ripublication.com/irph/ijert_spl17/ijertv10n1spl_111.pdf.

[81] G.K. Gupta, A. Garg, A. Dixit, Electrical and impedance spectroscopy analysis of sol-gel derived spin, J. Appl. Phys. 123 (2018) 013101. doi:10.1016/j.taap.2008.02.004.

[82] A.H.M. Smets, K. Jäger, O. Isabella, R.A. van Swaaij, M. Zeman, Solar Cell Parameters and Equivalent Circuit 9.1 External solar cell parameters, Sol. Energy Phys. Eng. Photovolt. Conversion, Technol. Syst. (2016) 113–121. https://ocw.tudelft.nl/wp-content/uploads/solar_energy_section_9_1_9_3.pdf.

[83] M.T. Patel, M.R. Khan, M.A. Alam, Thermodynamic limit of solar to fuel conversion for generalized photovoltaic-electrochemical systems, IEEE J. Photovoltaics. 8 (2018) 1082–1089. doi:10.1109/JPHOTOV.2018.2831446.

[84] Q. Liu, Y. Jiang, K. Jin, J. Qin, J. Xu, W. Li, J. Xiong, J. Liu, Z. Xiao, K. Sun, S. Yang, X. Zhang, L. Ding, 18% Efficiency organic solar cells, Sci. Bull. 65 (2020) 272–275. doi:10.1016/j.scib.2020.01.001.

[85] J.Z. Mbese, E.L. Meyer, M.A. Agoro, Electrochemical performance of photovoltaic cells using HDA capped-SnS nanocrystal from bis (N-1,4-phenyl-N-morpho-dithiocarbamato) Sn (II) complexes, Nanomaterials. 10 (2020) 1–10. doi:10.3390/nano10030414.

[86] S.K. Wallace, D.B. Mitzi, A. Walsh, The Steady Rise of Kesterite Solar Cells, ACS Energy Lett. 2 (2017) 776–779. doi:10.1021/acsenergylett.7b00131.

[87] S. Ahmed, K.B. Reuter, O. Gunawan, L. Guo, L.T. Romankiw, H. Deligianni, A high efficiency electrodeposited Cu_2ZnSnS_4 solar cell, Adv. Energy Mater. 2 (2012) 253–259. doi:10.1002/aenm.201100526.

[88] M. Azzouzi, A. Cabas-Vidani, S.G. Haass, J.A. Röhr, Y.E. Romanyuk, A.N. Tiwari, J. Nelson, Analysis of the Voltage Losses in CZTSSe Solar Cells of Varying Sn Content, J. Phys. Chem. Lett. (2019) 2829–2835. doi:10.1021/acs.jpclett.9b00506.

[89]   A. Ashery, I.M. El Radaf, M.M.M. Elnasharty, Electrical and Dielectric Characterizations of $Cu_2ZnSnSe_{4/n}$-Si Heterojunction, Silicon. 11 (2019) 2567–2574. doi:10.1007/s12633-018-0047-2.

[90]   G.K. Dalapati, S. Zhuk, S. Masudy-Panah, A. Kushwaha, H.L. Seng, V. Chellappan, V. Suresh, Z. Su, S.K. Batabyal, C.C. Tan, A. Guchhait, L.H. Wong, T.K.S. Wong, S. Tripathy, Impact of molybdenum out diffusion and interface quality on the performance of sputter grown CZTS based solar cells, Sci. Rep. 7 (2017) 1–12. doi:10.1038/s41598-017-01605-7.

[91]   S. Giraldo, Z. Jehl, M. Placidi, V. Izquierdo-Roca, A. Pérez-Rodríguez, E. Saucedo, Progress and Perspectives of Thin Film Kesterite Photovoltaic Technology: A Critical Review, Adv. Mater. 31 (2019). doi:10.1002/adma.201806692.

[92]   K.J. Yang, S. Kim, S.Y. Kim, K. Ahn, D.H. Son, S.H. Kim, S.J. Lee, Y.I. Kim, S.N. Park, S.J. Sung, D.H. Kim, T. Enkhbat, J.H. Kim, C.W. Jeon, J.K. Kang, Flexible $Cu_2ZnSn(S,Se)_4$ solar cells with over 10% efficiency and methods of enlarging the cell area, Nat. Commun. 10 (2019) 1–10. doi:10.1038/s41467-019-10890-x.

[93]   D.B. Mitzi, O. Gunawan, T.K. Todorov, K. Wang, S. Guha, The path towards a high-performance solution-processed kesterite solar cell, Sol. Energy Mater. Sol. Cells. 95 (2011) 1421–1436. doi:10.1016/j.solmat.2010.11.028.

[94]   A.S. Nazligul, M. Wang, K.L. Choy, Recent development in earth-abundant kesterite materials and their applications, Sustain. 12 (2020). doi:10.3390/su12125138.

[95]   M. He, C. Yan, J. Li, M.P. Suryawanshi, J. Kim, M.A. Green, X. Hao, Kesterite Solar Cells: Insights into Current Strategies and Challenges, Adv. Sci. 8 (2021) 1–16. doi:10.1002/advs.202004313.

CHAPTER 5

KESTERITE AND DOPED KESTERITE DEVICE RESULTS AND DISCUSSION

Chapter overview

This chapter describes the fabrication process of the kesterite and doped kesterite solar cells, followed by an analysis of their photovoltaic and electrochemical properties. The various characterizations help determine the various properties exhibited by these fabricated solar cells.
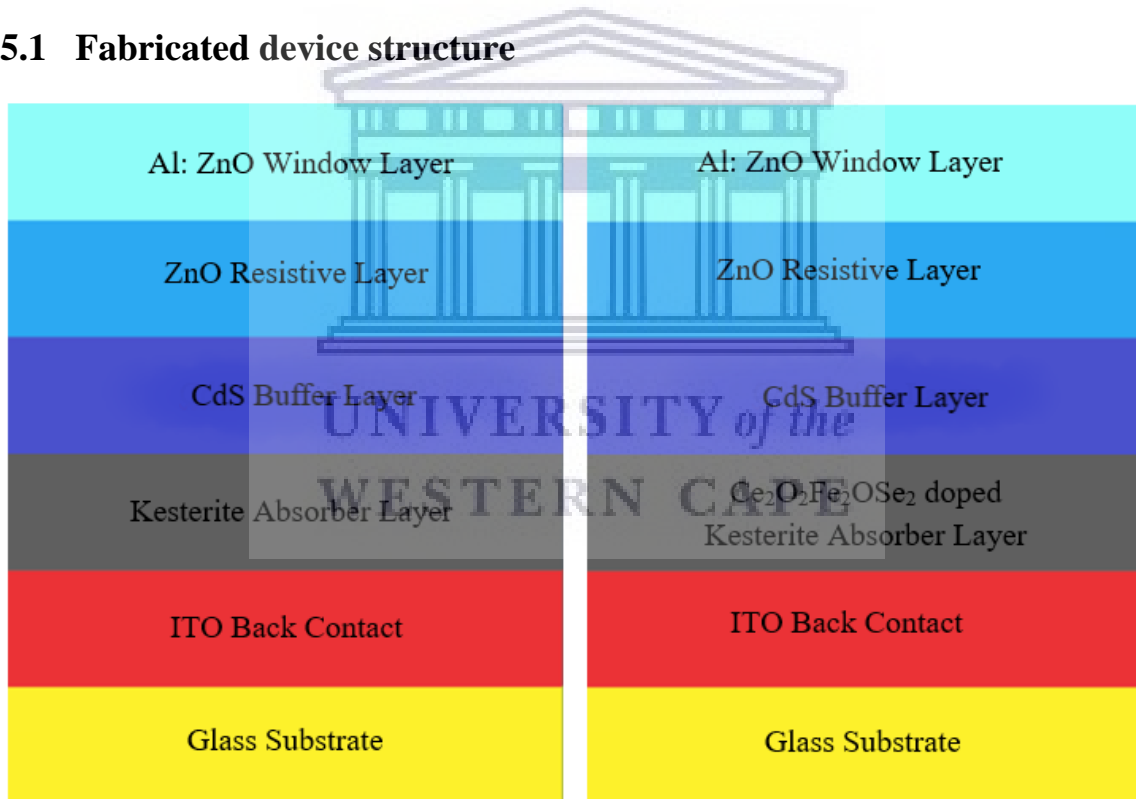
5.1 Fabricated device structure

Figure 5.1: Device architecture of the prepared kesterite and doped kesterite PV cells.

5.2 Device efficiency measurement

The kesterite and doped kesterite device power conversion efficiencies were obtained by I-V curve diode measurement. In order to characterize the performance and efficiencies of solar cells, certain parameters must be determined. These parameters are; "peak power (P_{max}), short-circuit current density (J_{sc}), open circuit voltage (V_{oc}) and the fill factor (FF)", once these parameters are known the conversion efficiency (η) can be determined. The major performance gap between CZTS and CIGS solar cells is the large open circuit voltage deficit. Thus, the "V_{oc} deficit is the key limiting factor" for highly efficient CZTS solar cells. The open-circuit voltage is the maximum voltage that a solar cell can deliver, and is the voltage at which no current flows through the external circuit. The ratio between the "maximum power ($P_{max} = J_{mpp}V_{mpp}$)" of a solar cell and the product of V_{oc} with J_{sc} is known as the fill factor. The ratio between the maximal generated power and the incident power is calculated to determine the conversion efficiency [1–5].

Table 5.2.1: Electrochemical efficiencies of the kesterite solar cell at the different pixels on the cell.

Pixel	PCE (%)	FF (%)	J_{sc} (mA.cm^{-2})	V_{oc} (V)	MP (W)	R_{shunt} (Ohm.cm^2)	R_{series} (Ohm.cm^2)
1 - 1	0.003	33.496	-0.732	0.011	0.003	15.134	15.101
1 - 2	0.003	29.265	-0.763	0.013	0.003	16.469	16.454
1 - 3	0.003	11.686	-0.627	0.004	0.003	7.032	7.048
1 - 4	0.003	12.977	-0.637	0.004	0.003	6.455	6.450
1 - 5	0.003	53.870	-0.706	0.008	0.003	11.018	11.017
1 - 6	0.008	24.816	-0.813	0.043	-0.009	52.569	52.112
1 - 7	0.481	59.459	-0.900	0.900	-0.481	3501.523	112.302
1 - 8	0.003	35.071	-0.755	0.011	0.003	14.402	14.351

Table 5.2.1 shows the electrochemical efficiencies of the different cells in the kesterite photovoltaic cell. The electrochemical performance of the photovoltaic cell is low across the eight cells. Cell 7 has the best electrochemical performance with the greatest efficiency of 0.48%, J_{sc} of -0.90 mA/cm^2, V_{oc} of 0.90 V and an FF of 59.46.
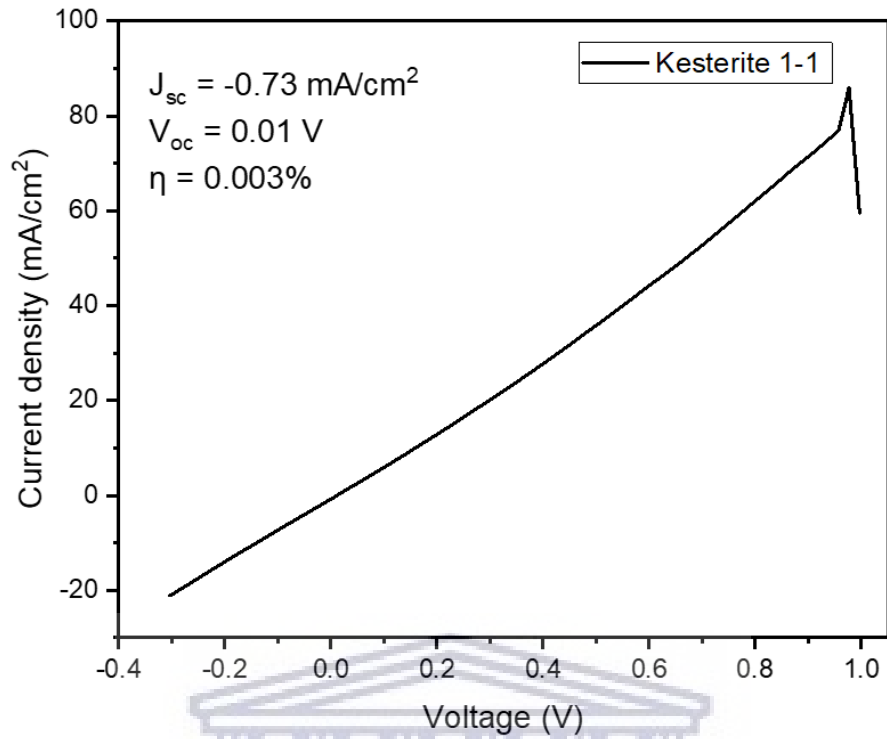
Figure 5.2.1: J-V Curve showing the power conversion efficiency of the kesterite 1-1 photovoltaic cell.

Figure 5.2.2: J-V Curve showing the power conversion efficiency of the kesterite 1-2 photovoltaic cell.

Figure 5.2.3: J-V Curve showing the power conversion efficiency of the kesterite 1-3 photovoltaic cell.

Figure 5.2.4: J-V Curve showing the power conversion efficiency of the kesterite 1-4 photovoltaic cell.

Figure 5.2.5: J-V Curve showing the power conversion efficiency of the kesterite 1-5 photovoltaic cell.

Figure 5.2.6: J-V Curve showing the power conversion efficiency of the kesterite 1-6 photovoltaic cell.

Figure 5.2.7: J-V Curve showing the power conversion efficiency of the kesterite 1-7 photovoltaic cell.
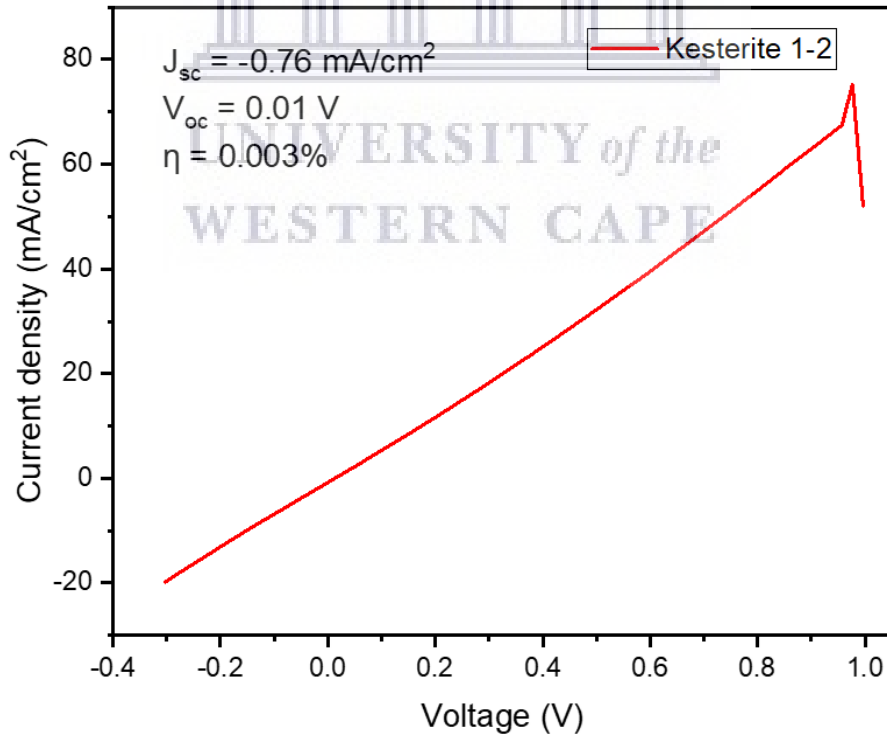

Figure 5.2.8: J-V Curve showing the power conversion efficiency of the kesterite 1-8 photovoltaic cell.
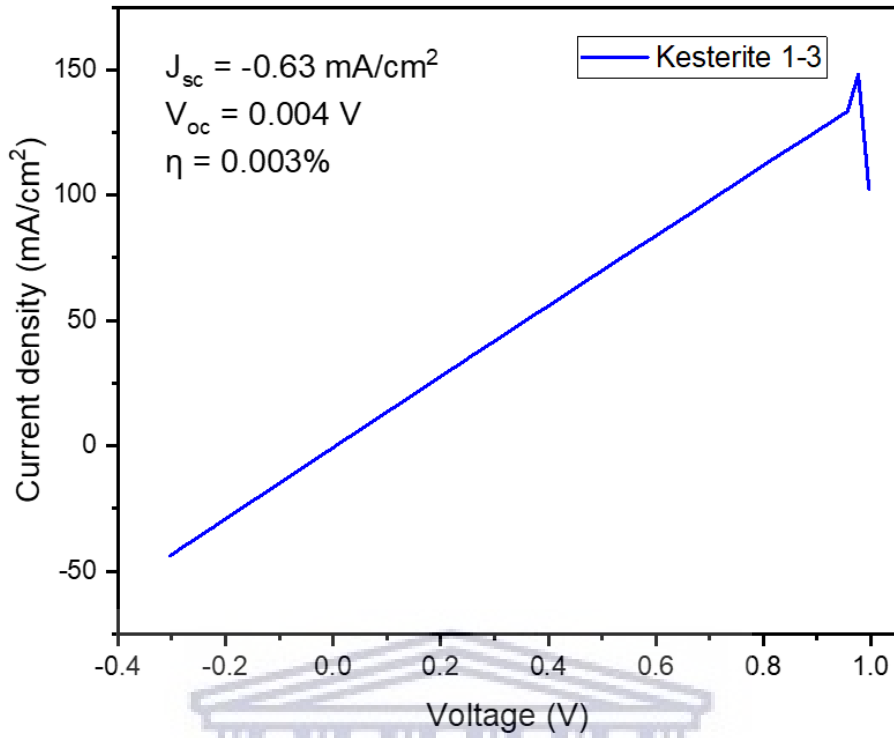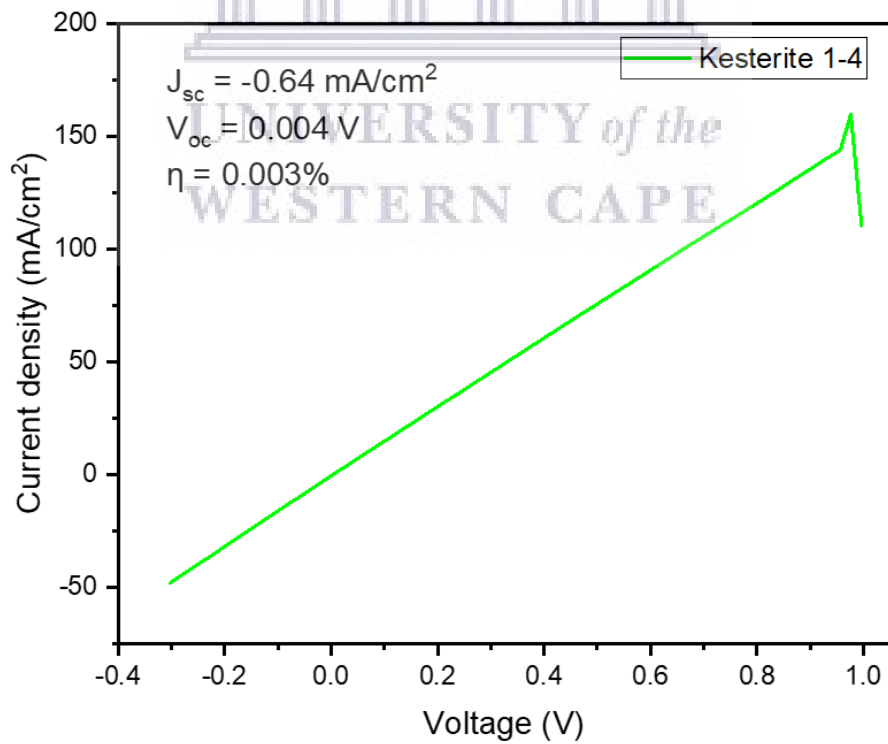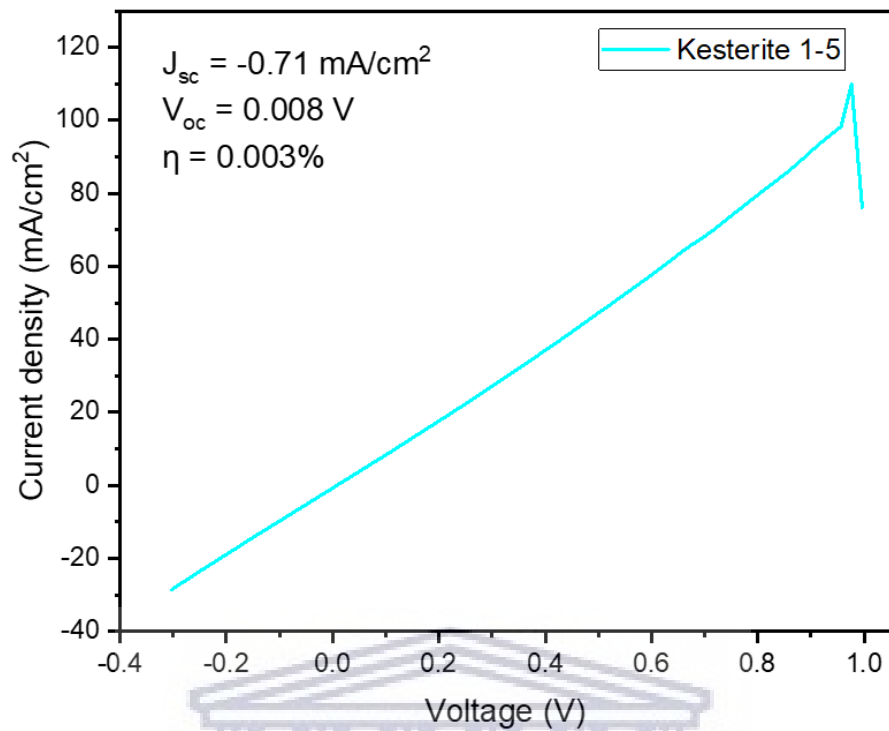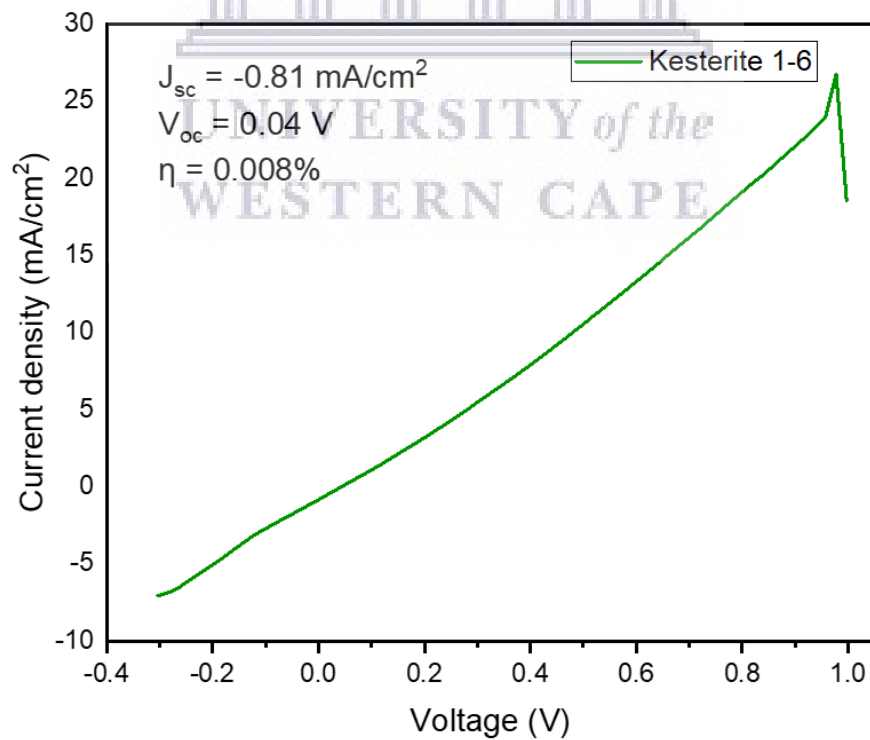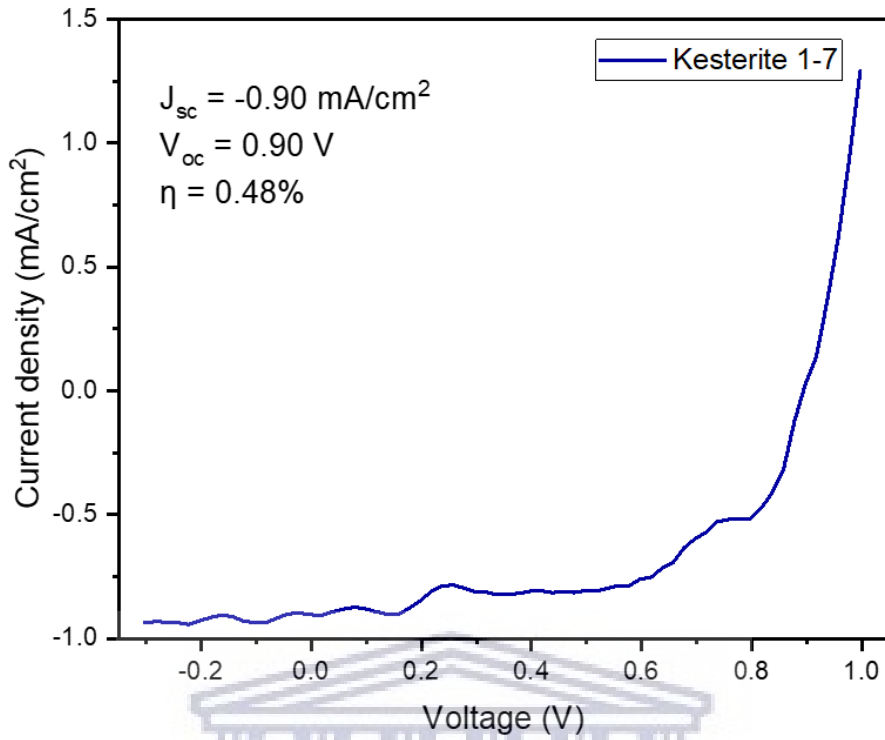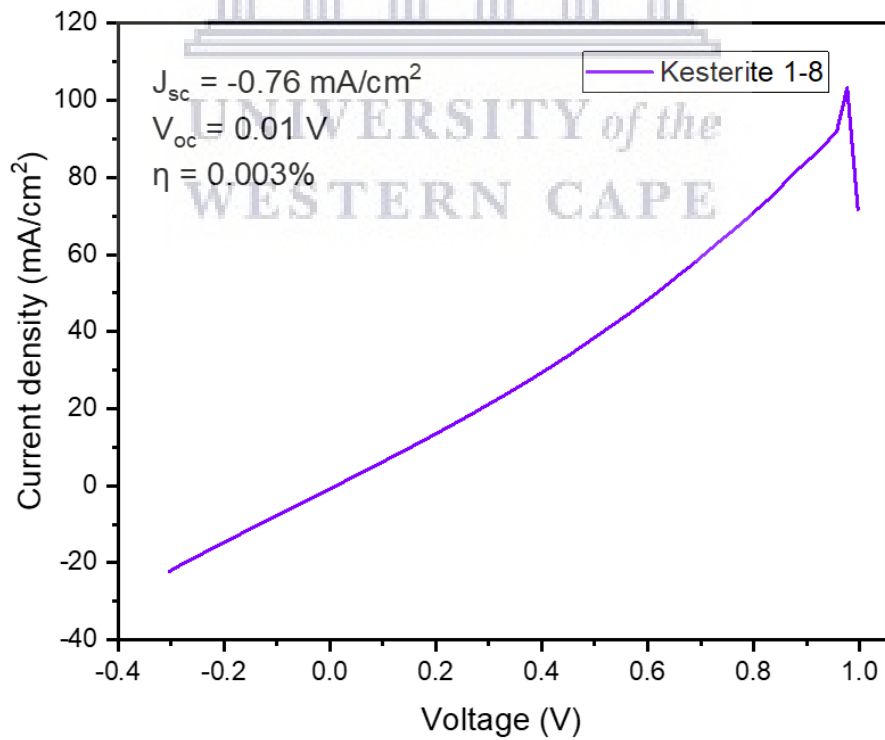
Figure 5.2.9: J-V Curve showing the power conversion efficiency of all the kesterite photovoltaic cells.

Table 5.2.2: Electrochemical efficiencies of the doped kesterite solar cell at the different cells.

Pixel	PCE (%)	FF (%)	J_{sc} (mA.cm^{-2})	V_{oc} (V)	MP (W)	R_{shunt} (Ohm.cm^2)	R_{series} (Ohm.cm^2)
Device 1 - 1	0.004	7.719	-0.158	0.0003	0.004	2.319	2.319
Device 1 - 2	0.004	1.683	-0.107	0.0002	0.004	2.305	2.305
Device 1 - 3	0.003	9.604	-0.327	0.0010	0.003	3.241	3.241
Device 1 - 4	0.003	31.014	-0.467	0.0019	0.003	4.281	4.284
Device 1 - 5	0.003	65.609	-0.955	0.0042	0.003	6.800	6.881
Device 1 - 6	0.003	21.304	-0.585	0.0023	0.003	4.629	4.643
Device 1 - 7	0.003	13.937	-0.540	0.0034	0.003	6.149	6.148
Device 1 - 8	0.003	22.126	-0.495	0.0025	0.003	4.875	4.870

Table 5.2.2 shows the electrochemical efficiencies of the different cells in the doped kesterite photovoltaic cell. The electrochemical performance of the photovoltaic cell is low across the eight cells. Cell 5 has the best electrochemical performance with an efficiency of 0.003%, J_{sc} of -0.96 mA/cm^2, V_{oc} of 0.004 V and an FF of 65.61.

Figure 5.2.10: J-V Curve showing the power conversion efficiency of the doped kesterite 1-1 photovoltaic cell.

Figure 5.2.11: J-V Curve showing the power conversion efficiency of the doped kesterite 1-2 photovoltaic cell.
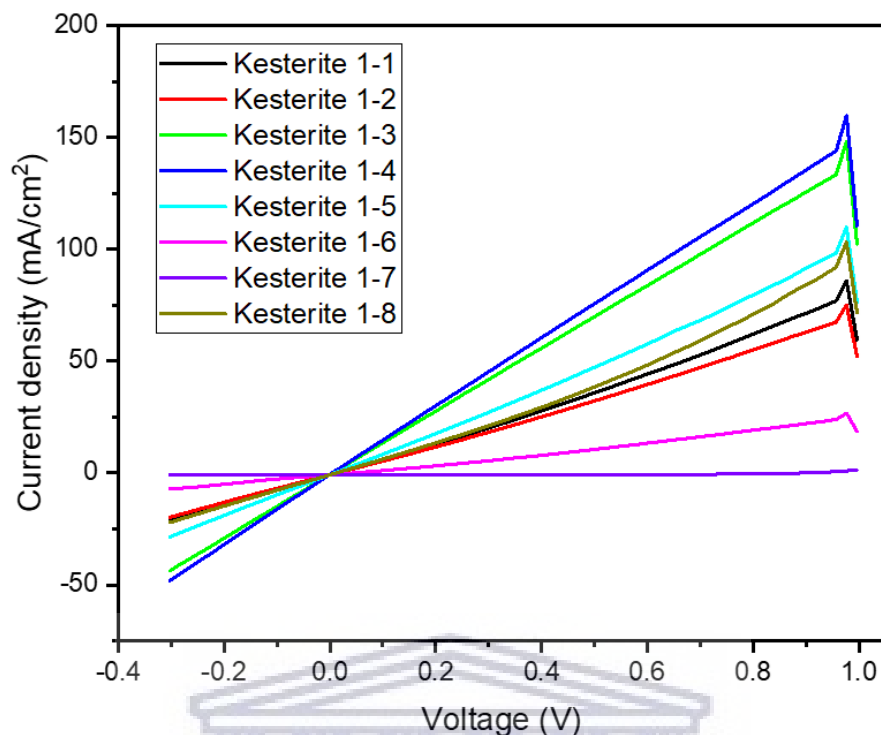
Figure 5.2.12: J-V Curve showing the power conversion efficiency of the doped kesterite 1-3 photovoltaic cell.

Figure 5.2.13: J-V Curve showing the power conversion efficiency of the doped kesterite 1-4 photovoltaic cell.

Figure 5.2.14: J-V Curve showing the power conversion efficiency of the doped kesterite 1-5 photovoltaic cell.

Figure 5.2.15: J-V Curve showing the power conversion efficiency of the doped kesterite 1-6 photovoltaic cell.
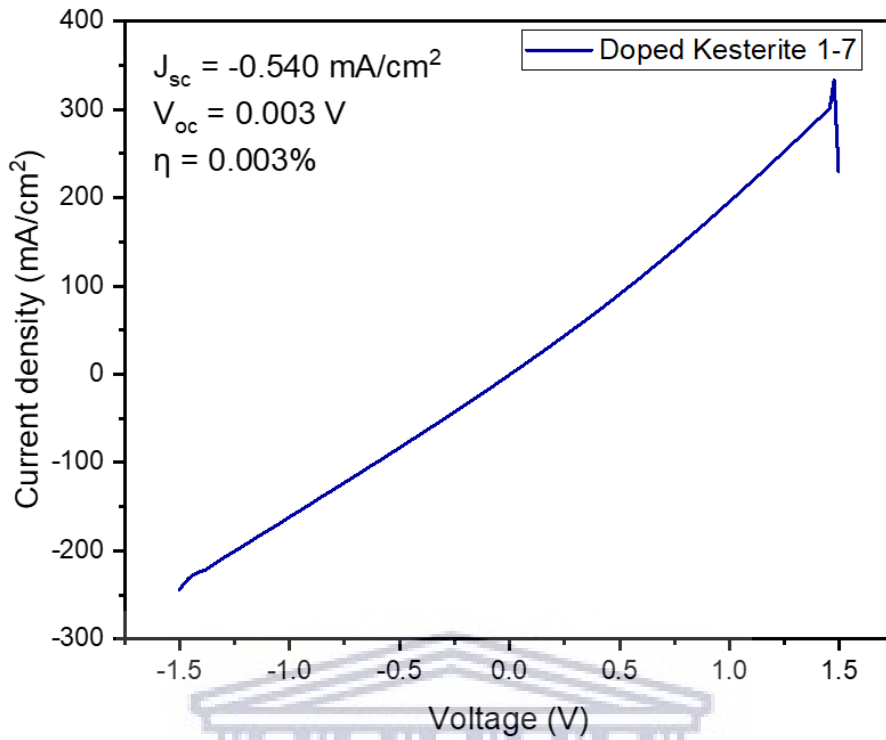
Figure 5.2.16: J-V Curve showing the power conversion efficiency of the doped kesterite 1-7 photovoltaic cell.
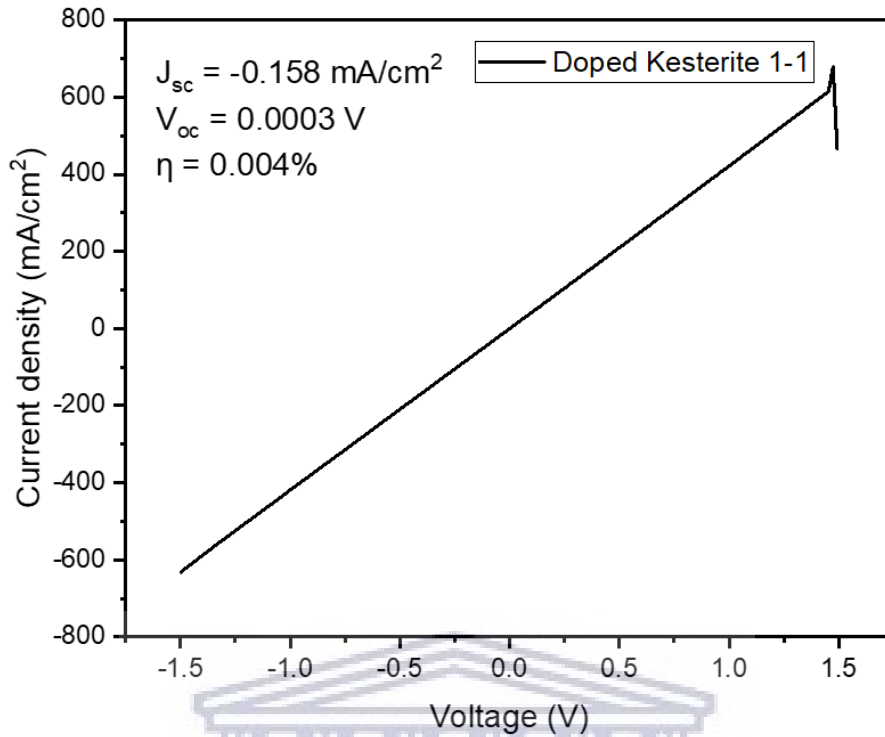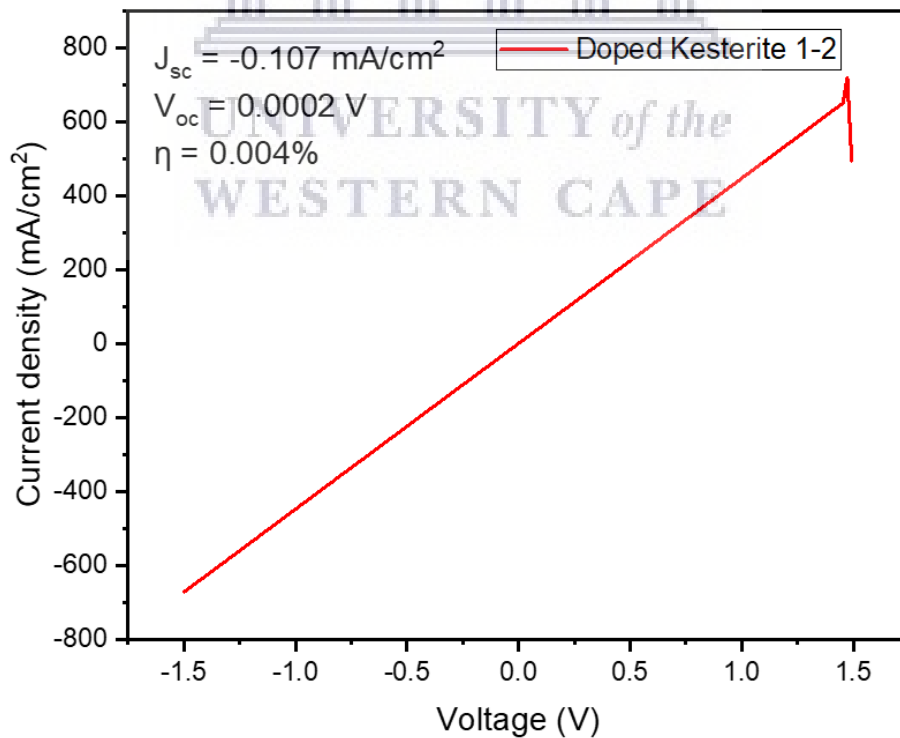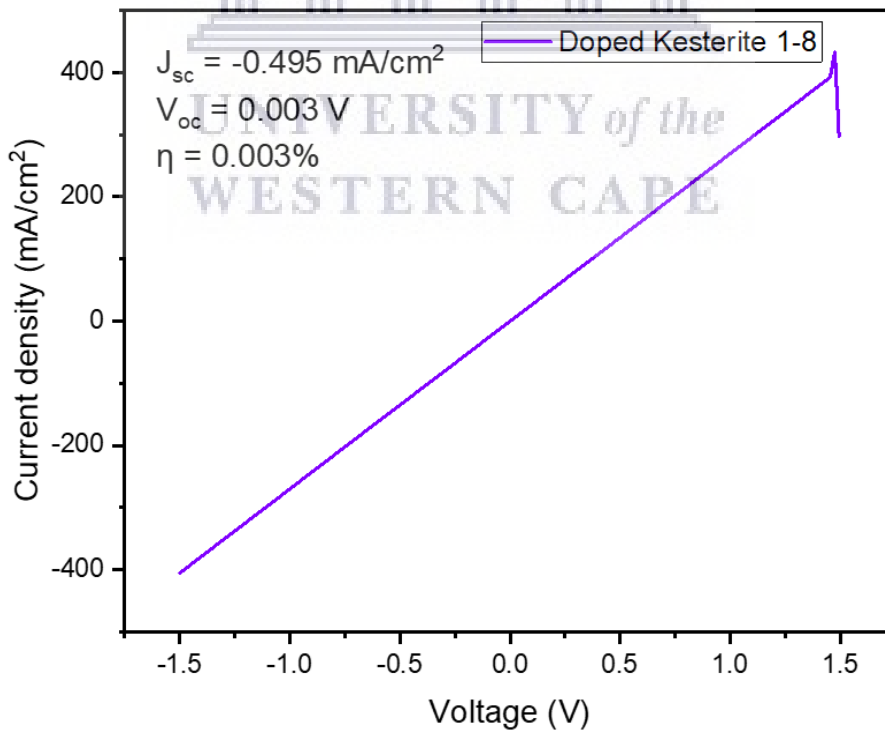

Figure 5.2.17: J-V Curve showing the power conversion efficiency of the doped kesterite 1-8 photovoltaic cell.
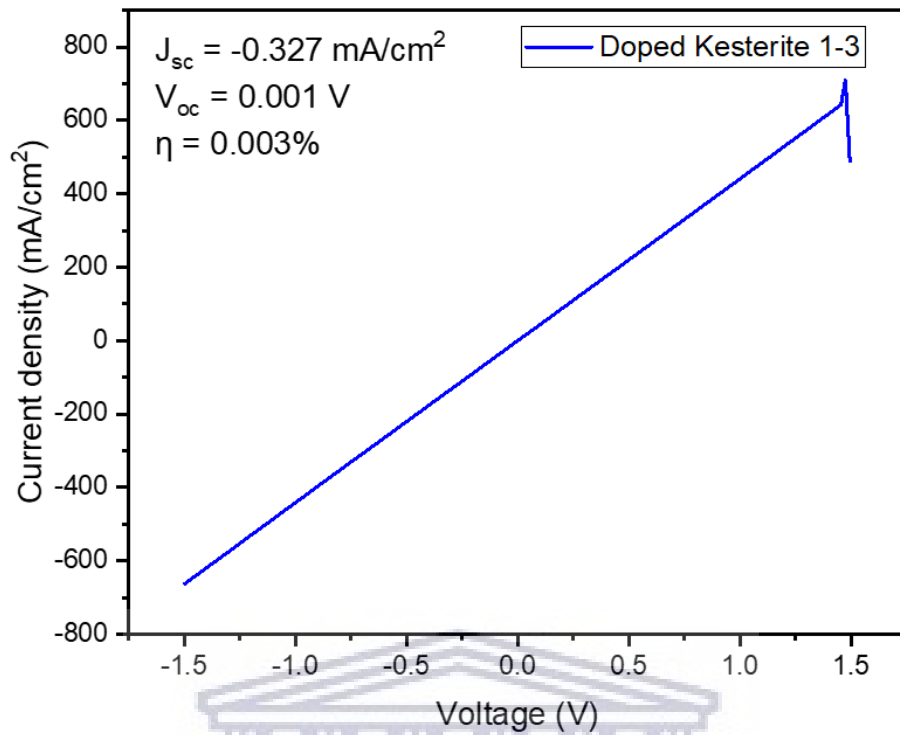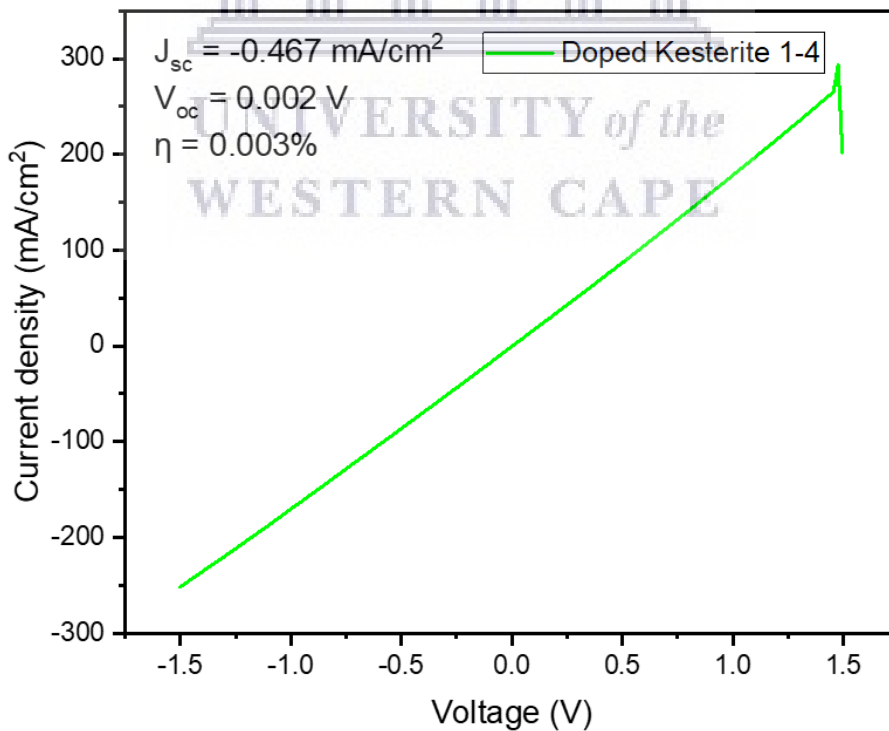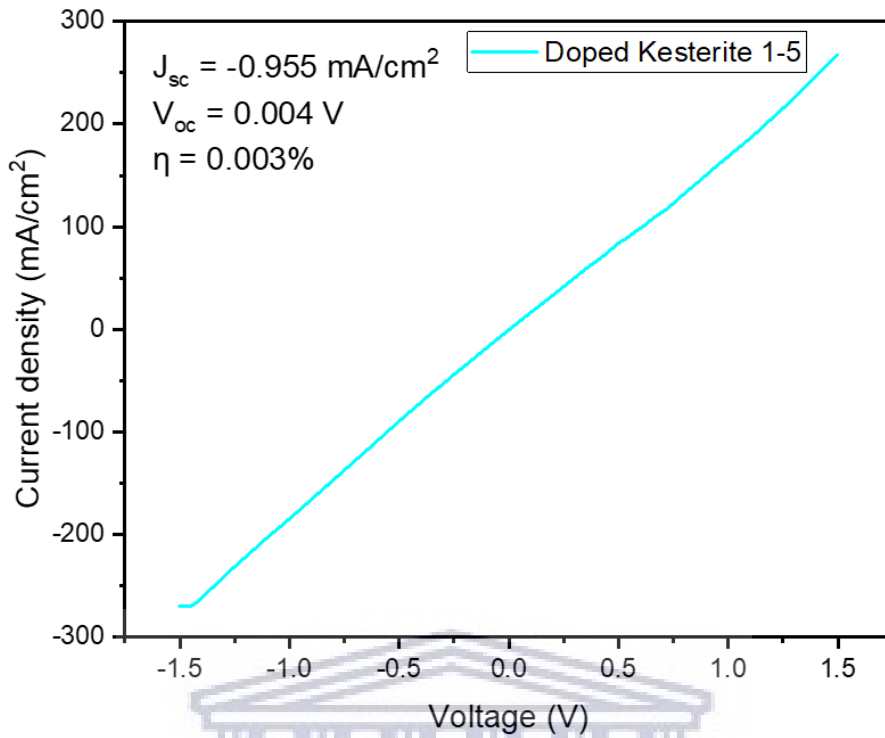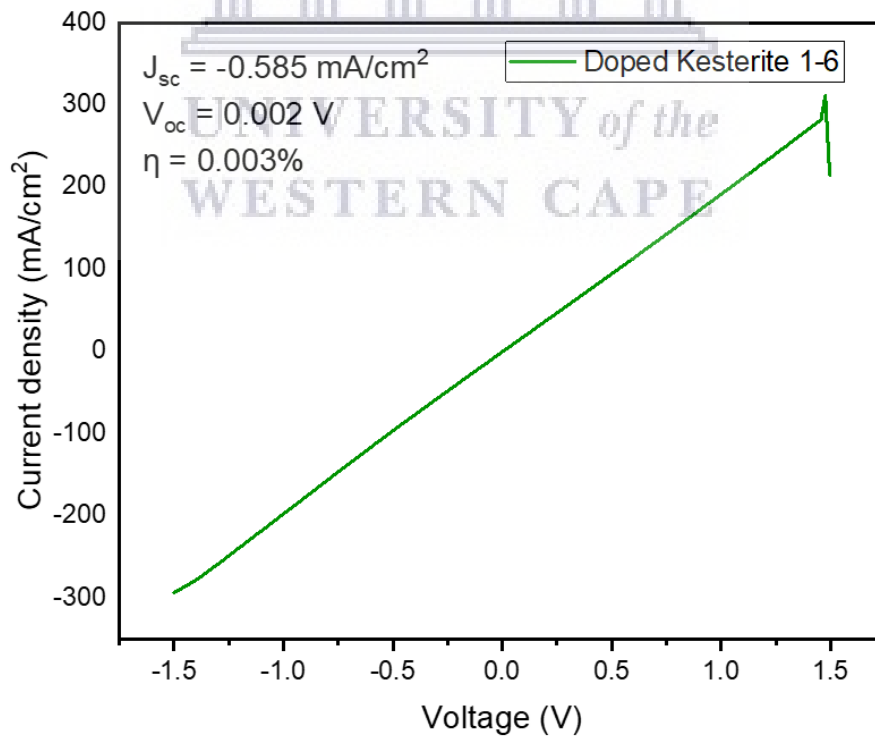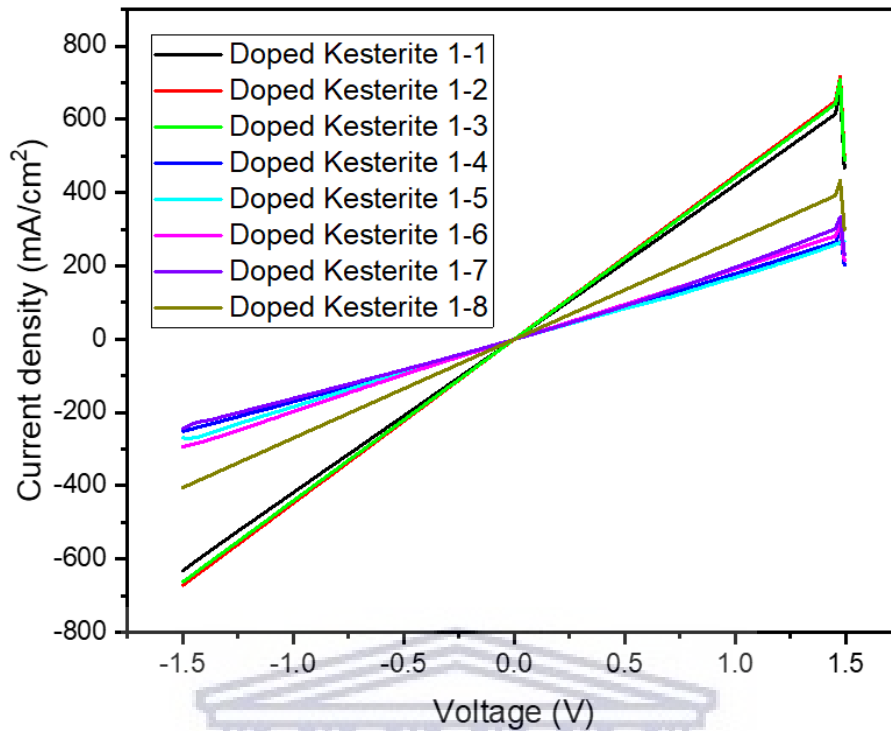
Figure 5.2.18: J-V Curve showing the power conversion efficiency of all the doped kesterite photovoltaic cells.

While analyzing the kesterite solar cells, eight IV-curve characterizations were performed on the eight fabricated kesterite cells. Of these cells only one cell provided a good efficiency. Table 5.2.1 and Fig. 5.2.1 – Fig 5.2.9, presents the electrochemical results for these eight kesterite cells. The kesterite cells 1-1 to 1-6 and the device 1-8, had very poor electrochemical properties such as fill factors (FF) that are very low, the V_{oc} of these devices are not adequate either. This is a problem known as V_{oc} deficit. This problem occurs in solar cells for example at the CdS/ CZTS interface due to dominant recombination. Kesterite cell 1-1, had poor electrochemical properties such as a low FF of 33.495%, J_{sc} of -0.732 mA/cm^2, a poor V_{oc} of 0.011 V and a lackluster efficiency of 0.003%. Kesterite cell 1-2, had poor electrochemical properties such as a low FF of 29.265%, J_{sc} of -0.763 mA/cm^2, a poor V_{oc} of 0.013 V and a low efficiency of 0.003%. Kesterite cell 1-3, had poor electrochemical properties such as a low FF of 11.686%, J_{sc} of -0.627 mA/cm^2, a poor V_{oc} of 0.004 V and a poor efficiency of 0.003%. Kesterite cell 1-4, had poor electrochemical properties such as a low FF of 12.977%, J_{sc} of -0.637 mA/cm^2, a poor V_{oc} of 0.004 V and a lackluster efficiency of 0.003%. Kesterite cell 1-5, had poor electrochemical properties with an average FF of 53.870%, J_{sc} of -0.706 mA/cm^2, a poor

V_{oc} of 0.008 V and a low efficiency of 0.003%. Kesterite cell 1-6, had poor electrochemical properties such as a poor FF of 24.816%, J_{sc} of -0.813 mA/cm^2, a poor V_{oc} of 0.043 V and a low efficiency of 0.008%. Kesterite cell 1-7 had the greatest efficiency of 0.48%, J_{sc} of -0.90 mA/cm^2, V_{oc} of 0.90 V and an FF of 59.46%. Kesterite cell 1-8, had poor electrochemical properties such as a low FF of 35.071%, J_{sc} of -0.755 mA/cm^2, a poor V_{oc} of 0.011 V and a lackluster efficiency of 0.003% [6–15]. Analyzing the doped kesterite solar cells, eight IV-curve characterizations were performed on the eight fabricated doped kesterite cells. Table 5.2.2 and Fig. 5.2.10 – Fig 5.2.18, presents the electrochemical results for these eight kesterite cells. The doped kesterite cells 1-1 to 1-4 and the cells 1-6 to 1-8, had very poor electrochemical properties such as poor FFs, the V_{oc} of these devices are not adequate either. Doped kesterite cell 1-1, had poor electrochemical properties such as a low FF of 7.719%, J_{sc} of -0.158 mA/cm^2, a V_{oc} of 0.0003 V and an efficiency of 0.004%. Doped kesterite cell 1-2, had poor electrochemical properties such as a low FF of 1.683%, J_{sc} of -0.107 mA/cm^2, a V_{oc} of 0.0002 V and an efficiency of 0.004%. Doped kesterite cell 1-3, had poor electrochemical properties such as a low FF of 9.604%, J_{sc} of -0.327 mA/cm^2, a V_{oc} of 0.001 V and an efficiency of 0.003%. Doped kesterite cell 1-4, had poor electrochemical properties such as a low FF of 31.014%, J_{sc} of -0.467 mA/cm^2, a V_{oc} of 0.002 V and an efficiency of 0.003%. Doped kesterite cell 1-5 had the greatest electrochemical properties with an efficiency of 0.003%, J_{sc} of -0.955 mA/cm^2, V_{oc} of 0.004 V and an FF of 65.61%. Doped kesterite cell 1-6, had poor electrochemical properties such as a low FF of 21.304%, J_{sc} of -0.585 mA/cm^2, a V_{oc} of 0.002 V and an efficiency of 0.003%. Doped kesterite cell 1-7, had poor electrochemical properties such as a low FF of 13.937%, J_{sc} of -0.540 mA/cm^2, a V_{oc} of 0.003 V and an efficiency of 0.003%. Doped kesterite cell 1-8, had poor electrochemical properties such as a low FF of 22.126%, J_{sc} of -0.495 mA/cm^2, a V_{oc} of 0.003 V and an efficiency of 0.003% [6–15]. When comparing the electrochemical properties of the kesterite and doped kesterite cells, its seen that the kesterite cell electrochemical properties are greater than those of the doped kesterite cell, suggesting that doping the kesterite with cerium and iron oxyselenides has reduced the photovoltaic applications of the kesterite cell as the efficiency is reduced from 0.48% in the kesterite cell to 0.003% in the doped kesterite cell, this trend can be seen amongst almost all of the eight kesterite cells and doped kesterite cells. There are many factors that are influencing these results, including lack of optimization of the photovoltaic devices. Furthermore, major issues such as a large open-circuit voltage (V_{oc}) deficit; the

presence of the secondary, mid-gap states and band tails are all playing a pivotal role in heavily reducing or hindering the improvements and advancements in CZTS solar cell PCEs [16–19]. Improvements on these low efficiencies can be obtained via various optimization techniques accompanied by further and more advanced research techniques and strategies. For example, a CZTS device with a power conversion efficiency of over 10% was fabricated by Hao, et al. in 2018, by using a heterojunction heating treatment process to reduce heterojunction recombination [20]. It is known that high recombination losses are a probable cause for the low efficiency of CZTS cells. This possibly results from deep defect levels that act as carrier traps or by interface states [21–24]. Having knowledge about the absorber surface properties and defect structure, could lead to possible improvements of the electrical properties of the CZTS material by changing the surface composition [6–13]. Another aspect resulting in the poor electrochemical properties is that the conventional kesterite photovoltaic devices are fabricated on molybdenum coated solar lime glass, but during the fabrication of our device, ITO glass was only available for use in the fabrication which ultimately reduced the electrochemical properties as the molybdenum coated solar lime glass has major advantages over the ITO glass for the cell integration of kesterite solar cells [25,26]. Another factor influencing the performance of these devices is the conduction band of set (CBO) between the absorber and buffer layers (p-CZTS and n-CdS). S. E. Maklavani and S. Mohammadnejad found that the maximum efficiency is obtained with a conduction band offset of ± 0.4 eV after optimizing the absorber and buffer layers' thickness and doping concentration [27]. There would also be a 9% reduction in efficiency resulting from the increase in conduction band offset from 0.4 to 0.7 eV [27–29]. A major drawback of kesterite devices is that they suffer from cation-disordering defects and defect clusters, causing severe potential fluctuation, low minority carrier lifetime as well as unsatisfactory performance. J. Le, et al, have found that an effective way for suppressing detrimental intrinsic defects and activating desirable shallow acceptor Cu vacancies can be obtained by controlling the oxidation states of cations and modifying the local chemical composition, resulting in a confirmed 12.5% device efficiency [30]. From these major negative aspects of the kesterite material, when doping the kesterite material the negative aspects of the material are also influenced and in the case of the $Ce_2O_2Fe_2OSe_2$, the negative aspects of the kesterite material are enhanced which results in the reduced electrochemical and photovoltaic efficiencies of the solar cell.

References

[1]   A.H.M. Smets, K. Jäger, O. Isabella, R.A. van Swaaij, M. Zeman, Solar Cell Parameters and Equivalent Circuit 9.1 External solar cell parameters, Sol. Energy Phys. Eng. Photovolt. Conversion, Technol. Syst. (2016) 113–121. https://ocw.tudelft.nl/wp-content/uploads/solar_energy_section_9_1_9_3.pdf.

[2]   M.T. Patel, M.R. Khan, M.A. Alam, Thermodynamic limit of solar to fuel conversion for generalized photovoltaic-electrochemical systems, IEEE J. Photovoltaics. 8 (2018) 1082–1089. doi:10.1109/JPHOTOV.2018.2831446.

[3]   Q. Liu, Y. Jiang, K. Jin, J. Qin, J. Xu, W. Li, J. Xiong, J. Liu, Z. Xiao, K. Sun, S. Yang, X. Zhang, L. Ding, 18% Efficiency organic solar cells, Sci. Bull. 65 (2020) 272–275. doi:10.1016/j.scib.2020.01.001.

[4]   J.Z. Mbese, E.L. Meyer, M.A. Agoro, Electrochemical performance of photovoltaic cells using HDA capped-SnS nanocrystal from bis (N-1,4-phenyl-N-morpho-dithiocarbamato) Sn(II) complexes, Nanomaterials. 10 (2020) 1–10. doi:10.3390/nano10030414.

[5]   S.K. Wallace, D.B. Mitzi, A. Walsh, The Steady Rise of Kesterite Solar Cells, ACS Energy Lett. 2 (2017) 776–779. doi:10.1021/acsenergylett.7b00131.

[6]   S. Ahmed, K.B. Reuter, O. Gunawan, L. Guo, L.T. Romankiw, H. Deligianni, A high efficiency electrodeposited Cu_2ZnSnS_4 solar cell, Adv. Energy Mater. 2 (2012) 253–259. doi:10.1002/aenm.201100526.

[7]   M. Azzouzi, A. Cabas-Vidani, S.G. Haass, J.A. Röhr, Y.E. Romanyuk, A.N. Tiwari, J. Nelson, Analysis of the Voltage Losses in CZTSSe Solar Cells of Varying Sn Content, J. Phys. Chem. Lett. (2019) 2829–2835. doi:10.1021/acs.jpclett.9b00506.

[8]   A. Ashery, I.M. El Radaf, M.M.M. Elnasharty, Electrical and Dielectric Characterizations of $Cu_2ZnSnSe_{4/n}$-Si Heterojunction, Silicon. 11 (2019) 2567–2574. doi:10.1007/s12633-018-0047-2.

[9]   G.K. Dalapati, S. Zhuk, S. Masudy-Panah, A. Kushwaha, H.L. Seng, V. Chellappan, V. Suresh, Z. Su, S.K. Batabyal, C.C. Tan, A. Guchhait, L.H. Wong, T.K.S.

Wong, S. Tripathy, Impact of molybdenum out diffusion and interface quality on the performance of sputter grown CZTS based solar cells, Sci. Rep. 7 (2017) 1–12. doi:10.1038/s41598-017-01605-7.

[10]   S. Giraldo, Z. Jehl, M. Placidi, V. Izquierdo-Roca, A. Pérez-Rodríguez, E. Saucedo, Progress and Perspectives of Thin Film Kesterite Photovoltaic Technology: A Critical Review, Adv. Mater. 31 (2019) 1–11. doi:10.1002/adma.201806692.

[11]   K.J. Yang, S. Kim, S.Y. Kim, K. Ahn, D.H. Son, S.H. Kim, S.J. Lee, Y.I. Kim, S.N. Park, S.J. Sung, D.H. Kim, T. Enkhbat, J.H. Kim, C.W. Jeon, J.K. Kang, Flexible $Cu_2ZnSn(S,Se)_4$ solar cells with over 10% efficiency and methods of enlarging the cell area, Nat. Commun. 10 (2019) 1–10. doi:10.1038/s41467-019-10890-x.

[12]   D.B. Mitzi, O. Gunawan, T.K. Todorov, K. Wang, S. Guha, The path towards a high-performance solution-processed kesterite solar cell, Sol. Energy Mater. Sol. Cells. 95 (2011) 1421–1436. doi:10.1016/j.solmat.2010.11.028.

[13]   A.S. Nazligul, M. Wang, K.L. Choy, Recent development in earth-abundant kesterite materials and their applications, Sustain. 12 (2020). doi:10.3390/su12125138.

[14]   M. He, C. Yan, J. Li, M.P. Suryawanshi, J. Kim, M.A. Green, X. Hao, Kesterite Solar Cells: Insights into Current Strategies and Challenges, Adv. Sci. 8 (2021) 1–16. doi:10.1002/advs.202004313.

[15]   A. Benmir, Preparation of $Cu_2ZnSn(S,Se)_4$ thin film solar cell by a green and facile solution method, Int. J. Sci. Res. Eng. Technol. 9 (2017) 8–11. http://ipco-co.com/IJSET/vol9/issue-1/2.pdf.

[16]   G. Tseberlidis, V. Trifiletti, A. Le Donne, L. Frioni, M. Acciarri, S. Binetti, Kesterite solar-cells by drop-casting of inorganic sol–gel inks, Sol. Energy. 208 (2020) 532–538. doi:10.1016/j.solener.2020.07.093.

[17]   J. Kois, S. Polivtseva, D. Mamedov, A. Samieipour, S.Z. Karazhanov, Visible light-assisted instability of kesterite Cu_2ZnSnS_4: What are the implications?, Sol. Energy Mater. Sol. Cells. 208 (2020) 110384. doi:10.1016/j.solmat.2019.110384.

[18]   Y. Gong, Y. Zhang, Q. Zhu, Y. Zhou, R. Qiu, C. Niu, W. Yan, W. Huang, H. Xin, Identifying the origin of the: V ocdeficit of kesterite solar cells from the two grain growth mechanisms induced by Sn^{2+} and Sn^{4+} precursors in DMSO solution, Energy Environ. Sci. 14 (2021) 2369–2380. doi:10.1039/d0ee03702h.

[19]   M. Minbashi, A. Ghobadi, E. Yazdani, A. Ahmadkhan Kordbacheh, A. Hajjiah, Efficiency enhancement of CZTSSe solar cells via screening the absorber layer by examining of different possible defects, Sci. Rep. 10 (2020) 1–14. doi:10.1038/s41598-020-75686-2.

[20]   C. Yan, J. Huang, K. Sun, S. Johnston, Y. Zhang, H. Sun, A. Pu, M. He, F. Liu, K. Eder, L. Yang, J.M. Cairney, Z. Hameiri, J.A. Stride, S. Chen, M.A. Green, X. Hao, Cu_2ZnSnS_4 solar cells with over 10% power conversion efficiency enabled by heterojunction heat treatment, Nat. Energy. 3 (2018) 764–772. doi:10.1038/s41560-018-0206-0.

[21]   V. Kosyak, N. Ross, C. Platzer-Björkman, Current-voltage and capacitance study of light-induced metastabilities in $Cu_2ZnSnSSe_4$ thin film solar cells, J. Phys. D. Appl. Phys. 53 (2020) 1–14. doi:10.1088/1361-6463/ab747e.

[22]   M. Courel, J.A. Andrade-Arvizu, O. Vigil-Galán, The role of buffer/kesterite interface recombination and minority carrier lifetime on kesterite thin film solar cells, Mater. Res. Express. 3 (2016) 1–14. doi:10.1088/2053-1591/3/9/095501.

[23]   V. Trifiletti, Kesterite Solar Cells, Mod. Concepts Mater. Sci. 1 (2019) 3–6. doi:10.33552/mcms.2019.01.000524.

[24]   M. He, K. Sun, M.P. Suryawanshi, J. Li, X. Hao, Interface engineering of p-n heterojunction for kesterite photovoltaics: A progress review, J. Energy Chem. 60 (2021) 1–8. doi:10.1016/j.jechem.2020.12.019.

[25]   K. Wang, O. Gunawan, T. Todorov, B. Shin, S.J. Chey, K. Wang, O. Gunawan, T. Todorov, B. Shin, S.J. Chey, N.A. Bojarczuk, D. Mitzi, Thermally evaporated Cu_2ZnSnS_4 solar cells, 143508 (2010) 8–11. doi:10.1063/1.3499284.

[26]   M.I. Khalil, R. Bernasconi, L. Magagnin, CZTS layers for solar cells by an electrodeposition-annealing route, Electrochim. Acta. 145 (2014) 154–158. doi:10.1016/j.electacta.2014.09.001.

[27]   S. Enayati, M. Shahram, Enhancing the open - circuit voltage and efficiency of CZTS thin - film solar cells via band - offset engineering, Opt. Quantum Electron. (2020) 1–22. doi:10.1007/s11082-019-2180-6.

[28]   A.D. Adewoyin, M.A. Olopade, M. Chendo, Prediction and optimization of the performance characteristics of CZTS thin film solar cell using band gap grading, Opt. Quantum Electron. 49 (2017) 1–13. doi:10.1007/s11082-017-1176-3.

[29]   J. Zhou, X. Xu, B. Duan, H. Wu, J. Shi, Y. Luo, D. Li, Q. Meng, Regulating crystal growth via organic lithium salt additive for efficient Kesterite solar cells, Nano Energy. 89 (2021) 106405. doi:10.1016/j.nanoen.2021.106405.

[30]   J. Li, Y. Huang, J. Huang, G. Liang, Y. Zhang, G. Rey, F. Guo, Z. Su, H. Zhu, L. Cai, K. Sun, Y. Sun, F. Liu, S. Chen, X. Hao, Y. Mai, M.A. Green, Defect Control for 12. 5% Efficiency $Cu_2ZnSnSe_4$ Kesterite Thin-Film Solar Cells by Engineering of Local Chemical Environment, Adv. Mater. (2020). doi:10.1002/adma.202005268.

CHAPTER 6

CONCLUSION AND RECOMMENDATIONS

6.1 Conclusion

Kesterite (CZTS) materials have been studied and analyzed for use in photovoltaics in order to harness solar energy and enable the world to lean more towards the use of renewable energy. In this study, selenide kesterites were doped with nanoscopic cerium and iron oxyselenide ($Ce_2O_2Fe_2OSe_2$) as a means to improve the photovoltaic and electrochemical efficiencies of the kesterite material. The pristine kesterite and doped kesterite materials were synthesized via a polyol method, with various calcination steps for the $Ce_2O_2Fe_2OSe_2$ prior to doping the kesterite material. These materials underwent various characterization studies. The FTIR studies showed that the doped kesterite material consisted of the same general vibration stretches across v(O-H), v(C-H), v(C-H$_2$) and v(C-O) as found in the pristine kesterite material. This doped kesterite also possessed similar Ce-O and Fe-O stretching modes of vibration as seen in the $Ce_2O_2Fe_2OSe_2$, confirming the complete incorporation of the $Ce_2O_2Fe_2OSe_2$ into the kesterite framework. XRD studies conducted on these materials showed crystalline patterns and indicated the existence of secondary phases in the kesterite material. The crystalinity of the materials shown by XRD was supported by the SAX results. The HRSEM and HRTEM analysis of the materials highlighted important characteristics of the materials. These investigations presented highly agglomerated spheres with a non-porous, inhomogeneous composition, forming an L like shape with a polycrystalline nature of the $Ce_2O_2Fe_2OSe_2$ nanoparticles. The kesterite nanoparticles possessed an irregular rod and spherical polycrystalline shape with a porous and homogeneous composition with some level of agglomeration. The doped kesterite nanoparticles consists of a porous inhomogeneous composition forming a spherical shape with a high level of agglomeration and polycrystalline in nature. The HRSEM and HRTEM results agree with the SAXs data together with the XRD data, indicating crystal sizes of 10.30 nm, 11.03 nm and 9.45 nm for the $Ce_2O_2Fe_2OSe_2$, kesterite and doped kesterite nanoparticles respectively. The optical analysis from UV-Vis showed the optical band gaps of the $Ce_2O_2Fe_2OSe_2$, kesterite and doped kesterite nanoparticles to be 1.59 eV, 2.25 eV and 2.20 eV respectfully, thus indicating the doped kesterite nanoparticles

superiority over the pristine kesterite nanoparticles for light absorption as well as for photovoltaic applications. According to the electrochemical analysis, the doped kesterite nanoparticles outperformed the pristine kesterite nanoparticles as seen from the various electrochemical characterization techniques performed. According to the CV, both the pristine and doped kesterite nanoparticles had a high peak current in both the forward and reverse reactions but although high, the doped kesterite nanoparticles had lower peak currents than the pristine kesterite nanoparticles. From the CV data, the electrochemical band gaps were obtained being, 0.48 V, 0.67 V, 0.46 V for the $Ce_2O_2Fe_2OSe_2$, kesterite and doped kesterite nanoparticles respectively. EIS studies produced both Nyquist and Bode plots for all the materials, and from these its shown that the $Ce_2O_2Fe_2OSe_2$, kesterite and doped kesterite nanoparticles have a Rct of 84.64 Ω, 625 Ω and 91.44 Ω respectively, suggesting that doping the pristine kesterite material with $Ce_2O_2Fe_2OSe_2$ does significantly reduce the resistance of the kesterite material which proves that the doped kesterite is less resistive thus a better conductor than the pristine kesterite material. The I-V curves of the materials indicated that the $Ce_2O_2Fe_2OSe_2$, kesterite and doped kesterite nanoparticles have efficiencies (η) of 8.62%, 3.26% and 5.79%, respectively. Thus, indicating that the doped kesterite has a greater electrochemical efficiency than the pristine kesterite material and would be best suited for photovoltaic applications. At this point of the study the doped kesterite nanoparticles have proven to be better suited over the pristine kesterite materials for use in photovoltaics. The next section of this study is the fabrication of a pristine and doped kesterite solar cell. The two solar cells were fabricated via a spin coating method. Electrochemical characterization techniques were performed on the cells and the pristine kesterite cell had an efficiency of 0.48% while the doped kesterite cell had an efficiency of 0.003%. These efficiencies were not expected as it contradicts the findings of the materials in their nanoparticle form. A major reason for the obtained efficiencies is due to the poor choice in fabrication methods, as spin coating using nanoparticles does not work due to the nanoparticles being insoluble and rather being suspended in solution. A second reason for the unexpected results is due to the fact that there was no optimization carried out during device fabrication. This study has added invaluable knowledge and importance to the study and use of kesterite materials for use in photovoltaics and/or other electrochemical fields. This work has shown that there is possibility in improving kesterite materials by doping them with nanoscopic cerium and iron oxyselenides or materials of the same family.

6.2 Recommendations

In future works, fabrication methods of the kesterite solar cell should take into consideration the chemistry of nanoparticles and that they are not soluble. Another method of improving kesterite solar cell fabrication is the inclusion of optimization studies which should be done during fabrication as to obtain improved PCE for the novel nanoparticles. This could be achieved by varying the ratio of the materials used, since it's known that kesterite solar cells with slight high zinc ratio perform better. Taking account of various temperature parameters, the kesterite solar cell can be improved as these temperatures will help determine the best temperature that yield an optimal device. Layer thickness can influence the cell as adequate volume of the layers available for absorbing and converting light to useful energy can significantly enhance the efficiency. A fabrication method that would work well is vacuum deposition as it can deliver better results and the process through sputtering of the constituent metals reduces the presence of secondary phase formation in the PV cell. Kesterite nanomaterials have a known phase problem. A method of minimizing the occurrence of secondary phases in the kesterite material is ensuring that the chalcogen being used is in powder form and is correctly reduced in order to be incorporated well into the kesterite phase. Methods for further reducing or preventing secondary phases include the incorporation of chemical bath etching of the kesterite absorber layer.

Appendix

Figure 1.1.1: A comparison of PV capacity projections between IRENA 2019 and WEO 2019 scenarios.

Copywrite permission and license for figure 1.1.1:

Original content from this work may be used under the terms of the Creative Commons Attribution 4.0 license. Any further distribution of this work must maintain attribution to the author(s) and the title of the work, journal citation and DOI.

https://iopscience.iop.org/article/10.1088/1361-6463/ab9c6a

https://creativecommons.org/licenses/by/4.0/

G.M. Wilson, M. Al-Jassim, W.K. Metzger, S.W. Glunz, P. Verlinden, G. Xiong, L.M. Mansfield, B.J. Stanbery, K. Zhu, Y. Yan, J.J. Berry, A.J. Ptak, F. Dimroth, B.M. Kayes, A.C. Tamboli, R. Peibst, K. Catchpole, M.O. Reese, C.S. Klinga, P. Denholm, M. Morjaria, M.G. Deceglie, J.M. Freeman, M.A. Mikofski, D.C. Jordan, G. Tamizhmani, D.B. Sulas-Kern, The 2020 photovoltaic technologies roadmap, J. Phys. D. Appl. Phys. 53 (2020). doi:10.1088/1361-6463/ab9c6a.

Figure 1.1.2: External quantum efficiency (EQE) as a function of the wavelength λ

Copywrite permission and license for figure 1.1.2:

Permissions

No special permission is required to reuse all or part of article published by MDPI, including figures and tables. For articles published under an open access Creative Common CC BY license, any part of the article may be reused without permission provided that the original article is clearly cited. Reuse of an article does not imply endorsement by the authors or MDPI.
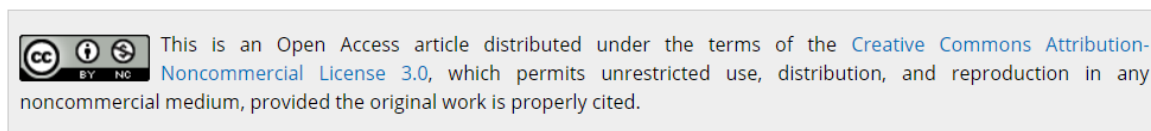
https://www.mdpi.com/about/openaccess

https://www.mdpi.com/1996-1944/5/10/1933

B. Minnaert, P. Veelaert, Guidelines for the bandgap combinations and absorption windows for organic tandem and triple-junction solar cells, Materials (Basel). 5 (2012) 1933–1953. doi:10.3390/ma5101933.

Figure 2.4.1: Kesterite, $Cu_2ZnSn(S,Se)_4$, elemental structure

Copywrite permission and license for figure 2.4.1:

https://www.epj-pv.org/articles/epjpv/abs/2012/01/pv110023/pv110023.html

https://creativecommons.org/licenses/by-nc/3.0/

S. Delbos, Kësterite thin films for photovoltaics: a review, EPJ Photovoltaics. 3 (2012) 35004. doi:10.1051/epjpv/2012008.

Figure 2.4.2: Calculated defect states in CZTS (Red numbers correspond to charge of defect)

Copywrite permission and license for figure 2.4.2:

https://onlinelibrary.wiley.com/doi/10.1002/aenm.201100630

A. Walsh, S. Chen, S.H. Wei, X.G. Gong, Kesterite thin-film solar cells: Advances in materials modelling of Cu 2 ZnSnS 4, Adv. Energy Mater. 2 (2012) 400–409. doi:10.1002/aenm.201100630.